TOWARDS EXPLORING PROTEIN CLUSTERS:
DETERMINING STOICHIOMETRY AND RECRUITMENT KINETICS VIA SINGLE MOLECULE MICROSCOPY

by

STANIMIR ASENOV TASHEV

A thesis submitted to the University of Birmingham for the degree of
DOCTOR OF PHILOSOPHY

Institute of Cardiovascular Sciences
College of Medical and Dental Sciences
University of Birmingham
July 2024

Declaration

I hereby declare that all work presented within this thesis titled "Towards exploring protein clusters: determining stoichiometry and recruitment kinetics via single molecule microscopy." is my own, unless declared in the Acknowledgements or specified in the text. The work was submitted to the Institute of Cardiovascular Sciences, College of Medical and Dental Sciences, University of Birmingham, United Kingdom as the ultimate synopsis and authentic record of the work during my Doctor of Philosophy degree.

- Stanimir Asenov Tashev

Abstract

Cells are dynamic systems, in which proteins regularly form complexes of changing stoichiometry. However, molecular counting techniques are mainly performed on fixed cells, thus losing the temporal aspects of complex formation, which might have revealed additional information of underlying biological processes.

This PhD thesis presents developments to the quantitative microscopy technique Counting by Photon Statistics (CoPS), contributing towards towards making the technique a live cell compatible method. The work involved constructing a microscopy setup with the ability to acquire antibunching data, as well as to support widefield modalities. The microscope characteristics were defined and CoPS measurements on it were validated. A molecular standard with consistent DNA-hybridisation kinetics, the rates of which were defined, was used to test new dynamic versions of CoPS better suited for continuous data. However, photodestruction of the model system was observed with Cy5 labelling, which decreased when labelled with Atto 643.

Experiments on cells were conducted to explore the challenges of *in cellulo* CoPS. The optimal imaging conditions were explored and CoPS experiments were conducted on a cellular molecular standard. The recruitment of the adaptor protein SLP-76 protein was also inspected as a dynamic system of protein recruitment, and the stoichiometry of its clusters was identified. A new technique for determination of the degree of labelling (DOL) was developed to facilitate the accuracy of these measurements.

The limiting factor of live cell CoPS was determined to be the photophysics and photostability of the fluorophores. For the technique to work a further large study of different fluorophores and live cell buffers was identified as a direction of future experiments.

Acknowledgements

First, I want to give my gratitude Dirk-Peter Herten for all the guidance and help throughout this degree. Special thanks to Jonas Euchner and Johan Hummert for both their supervision and friendship. A big "Thank you!" to the other members of the Herten Lab, as well, for all the help and as being good companionship throughout my degree.

I have to acknowledge all of our collaborators from the Tinnefeld lab, the Pressé lab, and the Owen lab for sharing their amazing expertise throughout our shared projects.

I also want to give thanks to all members of the Gemlich lab, which were wonderful neighbours and friends for all these years, for all the help they have provided. My gratitude to Daniel Nieves for making the degree manageable with his expertise and guidance both in the lab and outside. I want to also thank my fellow coffee enjoyer Danielle Lezama for all the help and discussion concerning T cells.

A great deal of gratitude goes to Dylan Marques for making both physics conversations and playing football enjoyable. My appreciation to Caitlin Hall for hosting all the wonderful movie nights that kept the spirits up. I also want to extend my gratitude towards all members of the MDS that have lent their help and knowledge.

A very special thanks to my partner Aleen Baber for all the support and patience, especially during the difficult period of writing this thesis. I couldn’t have done it without her.

Last but not least, I want to thank my friends and family back in Bulgaria for supporting me through all the hard times even all these years later.

This work has been proofread in full or in part by Dirk-Peter Herten, Jonas Euchner, Johan Hummert, and Daniel Nieves.

Table of Contents

Page

List of Figures

List of Tables

List of Abbreviations

2D	2-dimensional
AA	ascorbic acid
ADC	analog-to-digital converter
ADU	analog-to-digital units
AF	Alexa Fluor
AFM	atomic force microscope
AOM	acousto-optic modulator
AOTF	acousto-optic tunable filter
APC	antigen presenting cells
APD	avalanche photodiode
BODIPY	boron-dipyrromethene
BRET	bioluminescence resonance energy transfer
BSA	bovine serum albumin
CCD	charge-coupled device
CI	confidence interval
CMOS	complementary metal–oxide–semiconductor
CoPS	counting by photon statistics
cps	counts per second
CW	continuous wave
Cy	cyanine
DAPI	4’ 6-diamidino-2-phenylindole
DBSCAN	density-based spatial clustering of applications with noise
DIC	differential interference contrast
DM	dichroic mirror

DMEM	Dulbecco's modified eagle medium
DoG	Difference of Gaussian
DOL	degree of labelling
DPSS	diode-pumped solid-state
dsDNA	double stranded DNA
dSTORM	direct stochastic optical reconstruction microscopy
DTT	dithiothreitol
EDTA	ethylenediaminetetraacetic acid
eGFP	enhanced green fluorescent protein
EGTA	ethylene glycol-bis(β-aminoethyl ether)-N,N,N',N'-tetraacetic acid
ELE	effective labelling efficiency
emCCD	electron-multiplying charge-coupled device
EtOH	ethanol
F-actin	filamentous actin
FB	FluoroBrite
FBS	fetal bovine serum
FCCS	fluorescence cross-correlation spectroscopy
FCS	fluorescence correlation spectroscopy
FF	fill factor
FFT	fast Fourier transform
FITC	fluorescein isothiocyanate
FLIM	fluorescence-lifetime imaging microscopy
FLT	fluorescence lifetime
FM	flip mirror
FOV	field of view

FP	fluorescent protein
FRAP	fluorescence recovery after photobleaching
FRET	Förster resonance energy transfer
FWHM	full width at half maximum
GCE	genetic code expansion
GFP	green fluorescent protein
GO	glucose oxidase
HA	haloalcane
hAGT	human O^6-alkylguanine-DNA-alkyltransferase
HCl	hydrochloric acid
HEPES	2-[4-(2-Hydroxyethyl)piperazin-1-yl]ethane-1-sulfonic acid
HF	hydrofluoric acid
HILO	highly inclined and laminated optical sheet
HRP	horseradish peroxidase
IC	internal conversion
IF	immunofluorescence
IRF	instrument response function
IS	immunological synapse
ISC	intersystem crossing
ITC	isothermal titration calorimetry
IU	illumination unit
JF	Janelia Fluor
kb	kilobases
lbFCS	localization-based FCS
LCU	laser combining unit
LFA-1	lymphocyte function-associated antigen

LSCM	laser scanning confocal microscope
MC	microcluster
mDE	multiple detection event
MEA	2-mercaptoethylamine
MeOH	methanol
MHC	major histocompatibility complex
MLE	multi-laser engine
mRNA	messenger ribonucleic acid
NA	numerical aperture
ND	neutral density
NHS	N-hydroxysuccinimide
NPC	nuclear pore complex
NRO	new rectangular origami
nt	nucleotide
PAINT	point accumulation for imaging in nanoscale topography
PALM	photo activated localization microscopy
PBSA	photobleaching step analysis
PCA	protocatechuic acid
PCD	protocatechuate 3,4-dioxygenase
PD	photodiode
PDE	photon detection efficiency
PFA	paraformaldehyde
PIPES	2,2’-(piperazine-1,4-diyl)di(ethane-1-sulfonic acid)
PLL	poly-L-lysine
PMT	photomultiplier tube
POI	protein of interest

ProDOL	protein-tag degree of labelling
PSF	point spread function
PSPL	picosecond pulsed laser
QE	quantum efficiency
qPAINT	quantitative PAINT
qSMLM	quantitative SMLM
quickPBSA	quick-photobleaching step analysis
ROI	region of interest
ROS	reactive oxygen species
ROXS	reducing and oxidising system
RSFP	reversibly switchable fluorescent protein
SC	surface coating
sCMOS	scientific complementary metal–oxide–semiconductor
SD	standard deviation
SDS	sodium dodecyl sulfate
SE	standard error
SiR	silicon rhodamine
SMAC	supramolecular activation complex
SMAP	super-resolution microscopy analysis platform
SMLM	single-molecule localisation microscopy
SNR	signal-to-noise ratio
SPAD	single-photon avalanche diode
SPR	surface plasmon resonance
STORM	stochastic optical reconstruction microscopy
svFCS	spot variation FCS
TBE	TRIS-borate-EDTA

TBST	TRIS-buffered saline with 0.1% Tween 20
TCR	T-cell receptor
TCSPCS	time-correlated single photon counting system
TIR	total internal reflection
TIRF	total internal reflection fluorescence
TIRFM	total internal reflection fluorescence microscopy
TMR	tetramethylrhodamine
TRIS	tris(hydroxymethyl)aminomethane
tRNA	transfer ribonucleic acid
Tyr	tyrosine
UI	user interface
UV	ultraviolet
VR	vibrational relaxation
WB	western blot

Chapter 1

General Introduction

1.1 Motivation

Cells are dynamic systems which continuously receive signals and integrate them before eliciting an appropriate response. This is the basic outline of cell signalling and what underlies most of these dynamic processes are proteins (1). Understanding the interactions between these proteins is vital for drug discovery and the development of medical treatments.

Receptors, mostly found on the surface of the cell, are the proteins at the start of signalling cascade. They receive extracellular signals, some of which composed from as little as a few molecules (2). This level of sensitivity can be accomplished by increasing the number of receptors on the surface or the increase of time a member of the signal chain stays on. The prior is costly for the cell, and both can be difficult to downregulate. Thus in certain processes another method of modulating the signal has evolved over time - clustering. Clustering creates an area with a high concentration of proteins and their ligands, which allows for high sensitivity and amplification by avoiding long-distance diffusion (3), as well as modulation of the response by multiple ligands in an analog fashion (4).

A notable example is T cell activation during the formation of the supramolecular activation complex (SMAC), where proteins are grouped into microclusters (MCs) (5) (see Sec. 5.1.5). The T-cell receptor (TCR) is not the only protein recruited to MCs, but also proteins such as the adaptor SLP-76 (6). Investigation of proteins into MCs can give a better understanding of the T cells as a whole.

There are multiple ways to assay the stoichiometry of protein clusters (7). However, determining the kinetics of recruitment proteins remains a difficult task (8). *In vitro* techniques such as isothermal titration calorimetry (ITC) (9) and surface plasmon resonance (SPR) (10, 11) assays show only bulk measurements and are done in an environment different than what is found inside of cells.

Microscopy, on the other hand, provides a great deal of spatial information and quantitative information. This can be used to assay dynamic processes in live cells. Microscopy techniques have been continuously improving both in their spatial and temporal resolution. However, so far there has not been a technique that combines the accurate determination of protein numbers with the estimation of the protein recruitment rate in live cells. To tackle this issue novel methods need to be explored and developed, which will feature a great deal of understanding of the concepts underlying light, fluorescence and microscopy.

1.2 Fluorescence microscopy

1.2.1 Light microscopy

Light microscopes are instruments featuring a lens or combination of lenses for the purpose of magnifying the image of the specimen. Microscopy has been a staple of biological research since the 1600s when van Leuenhook first observed microorganisms (12) and Robert Hooke first described the small pores he saw inside of cork as "cells" (13). Modern microscopes have a more complex structure with multiple lenses and apertures, and can feature electronic components (Sec. 3.1.1). The most commonly used light microscopy types are brightfield and fluorescence. There is also Raman microscopy which uses light excitation, similar to fluorescence, but relies on different photophysical effect to determine the molecular composition of the sample (14).

Initial versions of light microscopy had white light transmitted through the sample resulting in an image based on the attenuation of light through the denser parts of the sample (15). This method is called brightfield. Most mammalian cells, however, are mostly transparent and lack the contrast to reveal most of their subcellular information (16). To solve this issue techniques, such as differential interference contrast (DIC) and phase-contrast, have been developed (17). The former uses polarised light while the latter uses the phase of the light to create contrast.

Another important aspect of brightfield microscopy is the staining of specific features of the sample. These coloured molecules, called chromophores, provide a spectrally distinct signal which can provide qualitative information for multiple structures. However, one weakness of brightfield microscopy is the inability to isolate the signal from two different chromophores in cases of spatial overlap.

One of the greatest developments in the field of microscopy has been the introduction of fluorescence in the early 1900s (18, 19), which solves this problem. Fluorescence microscopy provides greater multiplexing capabilities by having the ability to detect each different fluorescent label (fluorophore) independently (20). It also provides the signal against a featureless dark background by filtering out the light used to probe the sample (21). These features not only increase the quality of the image given, but also allow for the development of a multitude of different microscopy techniques. The properties of fluorescence are what give fluorescence microscopy its unique advantages.

1.2.2 Fluorescence

Fluorescence is a physical phenomenon in which the excitation of a molecule or an atom (22, 23) from the absorption of light is followed by photon emission during rapid relaxation (24, 25) (Fig. 1.1 a).

At room temperature most atoms and molecules are confined to the ground state (S_0). When a photon is absorbed it causes an electron to migrate to a higher energy state (26). This occurs incredibly quickly (10^{-18} s) (27). The change in energy is equal to the photon's energy E, which is calculated by the Planck equation (Eq. 1.1).

$$E = h\nu \tag{1.1}$$

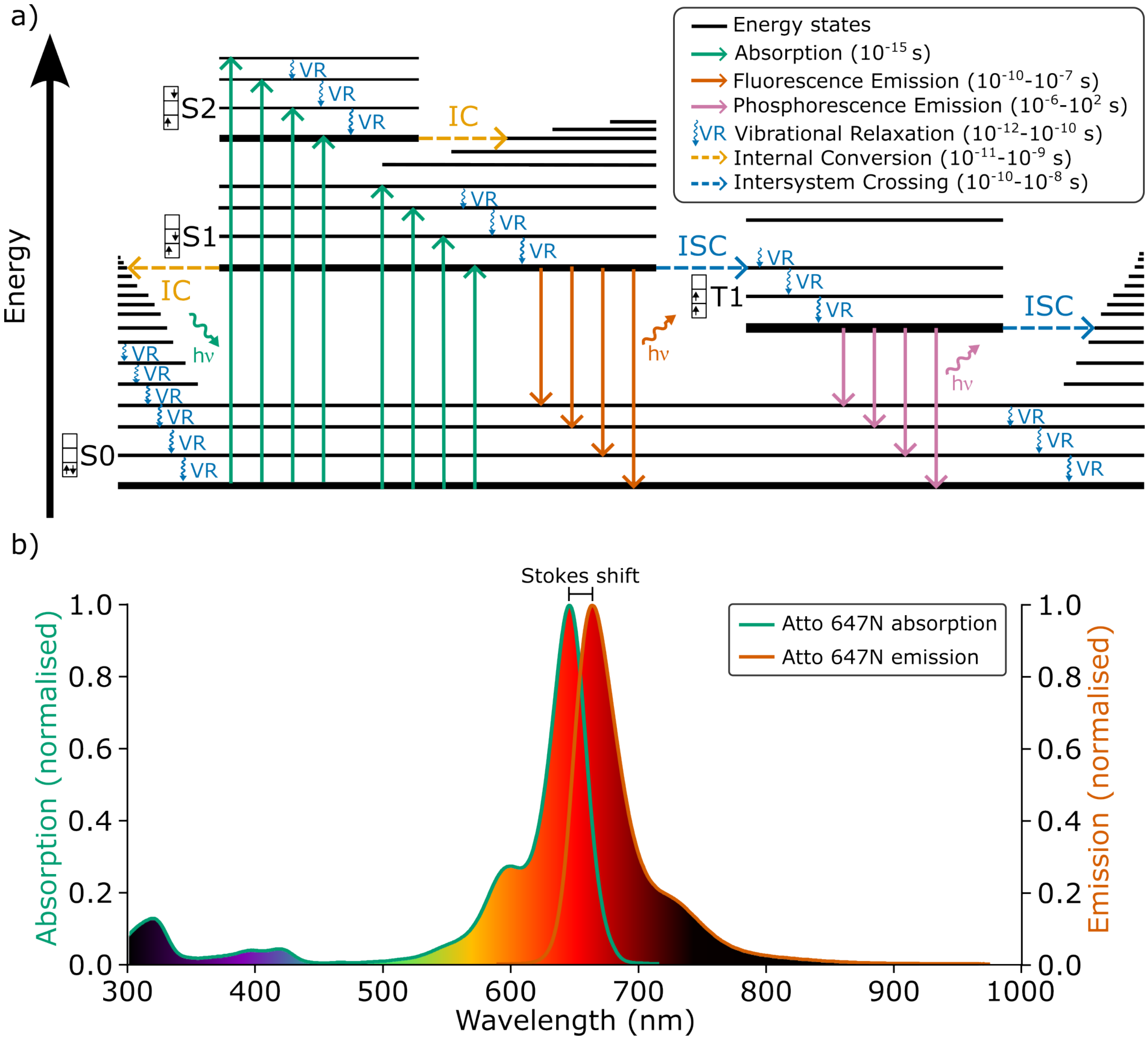

Fig. 1.1: Essentials of fluorescence. a) Jablonski diagram showing the transitions between electronic states and the processes underlying the of fluorescence. b) Absorption (green) and emission (orange) spectrum of Atto647N with the corresponding Stokes shift. IC- internal conversion, VR- vibrational relaxation, ISC- intersystem crossing.

Where h is the Planck constant and ν is the frequency of the electromagnetic radiation. The wavelength λ of that same photon can be calculated by the relation to ν (Eq. 1.2) in regards to the speed of light c.

$$\nu = \frac{c}{\lambda} \tag{1.2}$$

After absorbing the energy of the photon the system is in an excited singlet state (S_1 or S_2) due to the electrons being previously in a pair of opposite spins (21). The "singlet" part is derived from the multiplicity M calculated by Eq. 1.3 (28, 29).

$$M = 2S + 1 \tag{1.3}$$

S is the total spin angular momentum where each individual electron contributes either $-1/2$ or $+1/2$, for down spin and up spin, respectively. After the absorption some of the energy is lost as vibrational relaxation (VR), which leads the electron to a lower vibrational states. The electron can also transition from one electronic state to a high vibrational state of a lower energy electronic state without the loss of energy in a phenomena known as internal conversion (IC). Vibrational relaxation and internal conversion are both non-radiative and bring the system to the lower energy level of S_1. In most cases, fluorescence occurs from S_1 to any of the electronic states of S_0 with an emission of a photon. In organic molecules the excitation-emission cycle takes approximately 10^{-8} s, with the final emission step being the slowest.

A population of excited molecules n relaxes in an exponential decay fashion. The time that it takes for the decay to reach n/e is called the fluorescence lifetime (FLT) (30). The value of this parameter depends not only on the fluorophore, but also on the environmental factors, such as hydrophobicity, temperature, and the presence of fluorescent quenchers (30).

Due to the loss of energy from non-radiative transitions, the wavelength of the emitted photons is longer than the absorbed ones, except in the case of a multi-photon excitation. The former results in a difference between the absorption and emission spectra, called a Stokes shift (Fig.1.1 b). This gives the ability of fluorescence microscopy to minimize the contributions of the excitation laser in the detected signal via spectral filtering (see Sec. 3.1.1).

In most cases the excitation and emission spectra appear as mirrored versions of each other. This is because electronic excitation does not change the nuclear geometry. Thus, the spacing of the energy states in the S_0 and S_1 are similar (31). These states are determined by the structure. Therefore, the two spectra are specific for the molecule or atom. This allows for the separation of differently labelled features even if they spatially overlap (see Sec. 3.1.1).

The excited singlet systems can also undergo intersystem crossing (ISC) by inverting the spin of the promoted electron and results in a triplet state, in which two single electrons are in a single spin orientation. As with singlet energy states, energy is lost by vibrational relaxation and internal conversion until a stable level T_1 is reached. In the final relaxation to S_0, called phosphorescence, the system needs to undergo a "forbidden" triplet-to-singlet transition and in the process releases a photon. This unlikely event is the reason for the relatively long relaxation times (10^{-6} s - 10^{2} s). This transition time and non-radiative relaxation to S_0 (e.g. quenching) can result in a dimming of the fluorescence by removing the fluorophore from the excitable state (32). Triplet states tend to be lower than their corresponding singlet states meaning the phosphorescence spectra is red shifted in terms of the fluorescence one.

Interestingly molecular oxygen (O_2) is in a triplet state in its ground state which makes it less reactive due to a high activation barrier. However, it is also a prominent triplet state quencher (33). The quenching of triplet states of aromatic molecules generates a singlet oxygen (34). This can, in turn, result in the creation of reactive oxygen species (ROS). These can cause the chemical transformation in fluorescent dyes, called photobleaching, and in cells can lead to phototoxicity.

1.2.3 Fluorophores

Fluorescent molecules, also called fluorophores, can be divided into intrinsic and extrinsic (31). Intrinsic fluorophores are ones that can be found naturally in cells and their fluorescence is referred to as autofluorescence (35). These include coenzymes, such as NADH and FAD, as well as the aromatic containing amino acids tryptophan, phenylalanine and tyrosine. These account for the majority of autofluorescence in cells, but certain pigments, porphirins and retinol can also act as intrinsic fluorophores (36). Extrinsic fluorophores are probes introduced into the experimental system with the purpose of specifically labelling a target or probing the environment they exist in.

The smallest extrinsic fluorophores are small organic molecules which are only around a nanometre in diameter (37). These fluorescent dyes are conjugated systems of alternating single and double bonds, and often feature an aromatic structures in which the electrons in the π bonds are distributed into a larger area (21, 38). This serves to lower the energy gap between the S_0 and S_1. In general, the energy gap between the two lowers with the addition of more conjugated bonds, red-shifting both the excitation and emission spectra (39). The spectra can be further modified by the addition of either electron donating or electron withdrawing chemical groups, or a heteroatom (40).

Another photophysical property effected by the double bonds is the quantum yield ϕ. This is the probability of an excited molecule to emit a photon. It has a theoretical maximum of one and increases with the number of double bonds (31). Another photophysical property is the molar extinction coefficient, ϵ and it is measured in $M^{-1}cm^{-1}$, which shows the ability to absorb photons (21). The luminescence of fluorescence detected by a certain system $L_f(\lambda)$ for wavelength λ is calculated by Eq. 1.4 (41).

$$L_f(\lambda) = \Omega N \phi \epsilon_\lambda I_0 \tag{1.4}$$

This includes the Ω factor which is a factor specific for the optical setup, the extinction coefficient for the specific wavelength ϵ_λ, the number of the fluorophores N, and the intensity of the incident light I_0. The amount of photons that a fluorescent molecule can emit before bleaching can also be calculated using the quantum yield and the inverse of the photobleaching quantum yield $\phi_B{}^{-1} = \mu$ (Eq. 1.5) (42).

$$\text{Total photons emitted} = \phi\mu \tag{1.5}$$

The photobleaching quantum yield µ is another characteristic, which represents average number of excitation cycles a fluorophore can undergo before being destroyed by photobleaching.

Organic dyes can be divided into groups based on their scaffold molecule: coumarin, rhodamine, boron-dipyrromethene (BODIPY), cyanine (Cy), etc (40). This project includes the use of cyanine 5 (Cy5), AlexaFluor647 (AF647), which are based on cyanine, as well as Atto542, Atto565, Atto647N, and silicon rhodamine (SiR), which are based on rhodamine. Cyanine dyes tend to have higher excitation coefficients, but low quantum yield, while the rhodamine dyes have higher brightness (43).

1.2.4 Fluorescent labelling

Some fluorophores readily bind specific targets in the cell due to their shape, lipophilicity or charge. For instance, 4’6-diamidino-2-phenylindole (DAPI) and Hoechst stain the chromosomes in the nucleus of the cell by fitting inside the minor groove of double stranded DNA (dsDNA) (44). Another example are dyes such as Mitotracker and Lysotracker, which localise to mitochondria and lysosomes, respectively, function based on the charges of the fluorophores drawing them to the inside of the lumen of these organelles, which have an opposite charge (45). Due to the heteropolymer nature of proteins multiple proteins share a lot of their secondary structure, therefore labelling a specific epitope can be quite challenging.

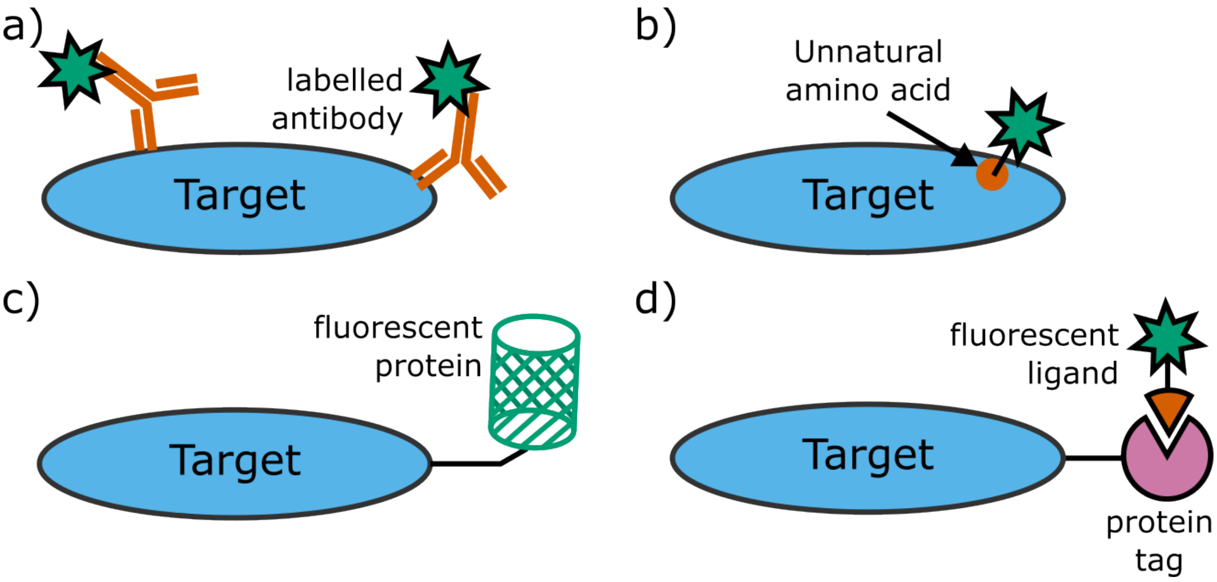

Fig. 1.2: Protein labelling strategies. Schematics of different strategies for attaching a fluorescent label (green) to a protein target (blue). a) Affinity labels (direct antibody labelling shown). b) Unnatural amino acid addition. c) Fluorescent protein chimerisation. d) Genetic addition of a protein tag and subsequent staining with a ligand.

Developments in fluorescence labelling have allowed multiple different ways to accomplish this task (Fig. 1.2). One way is conjugating fluorescent molecules to an affinity probe, which act as the previously mentioned cell dyes, but they have increased specificity to a particular part of the protein of interest (POI) called epitope. These include immunolabels, such as antibodies, Fab fragments and nanobodies, as well as aptermers, nucleic acid or peptide oligomers that bind to the POI (46–48). Another type of affinity labels are protein-specific small molecules. Often these are drugs developed for specific diseases or naturally occurring toxins. One such molecule is the mycotoxin phalloidin originally found in *Amanita phalloides*, which binds to filamentous actin (F-actin) (49).

Another way to specifically label proteins is to change one of the amino acids of its sequence to an unnatural one allowing for *in cellulo* click chemistry (Fig. 1.2b). This process involves inserting a stop UAG codon in the messenger ribonucleic acid (mRNA) of the POI, as well as genetic code expansion (GCE), which involves adding the transfer ribonucleic acid (tRNA) and the tRNA-transferase machinery, as well as the addition of the unnatural amino acid to the growth media (50). This is a highly involved process and it might prove toxic to the cell.

A simpler labelling strategy in which the protein is genetically modified is the addition of a fluorescent protein (FP) (Fig. 1.2c). After the first isolation of green fluorescent protein (GFP) in 1962 from the jellyfish *A. victoria* (51), fluorescent proteins became an important tool in the assaying of live cells, because it does not require a ligand and it does not disturb the folding of the native protein (52). FPs structurally similar to GFP, with β-barrel structure of anti-parallel strands with an α-helix inside them (53) are called prototypical. Inside of the barrel there are three amino acids which are post-translationally modified to create the fluorophore. Development and discoveries of new FPs have given us better photophysical properties and a bigger choice of emission spectra (54). Certain FPs are able to change their photophysical properties upon excitation with violet or blue light (55, 56). These can be separated into three categories: photoactivatable, photoconvertable and photoswitchable. Photoactivatable FPs are in a low fluorescence state before transitioning to a high fluorescence state upon irradiation violet light or ultraviolet (UV) light. In contrast, photoconvertable FPs already emit a high degree of fluorescence, however, their absorption and emission spectra changes upon UV irradiation. Both photoactivation and photoswitching FPs are irreversible, while photoswitching is reversible. Reversibly switchable fluorescent proteins (RSFPs) can be switched between bright and dark states for multiple excitation-emission cycles by illumination with two different wavelengths. These can be used in advanced microscopy techniques such as photo activated localization microscopy (PALM) (see Sec. 1.2.7) and Förster resonance energy transfer (FRET) (see Sec. 4.1.1).

An alternative way to label protein by chimerisation is the addition of a self-labelling protein tag to the POI's gene, and then an addition of a fluorescent ligand which binds to the tag (Fig. 1.2d). Protein tags are genetically modified enzymes which have been engineered to have an increased affinity to a specific small molecule (Tab. 1.1). For instance, both CLIP-tag and SNAP-tag originate from human O^6-alkylguanine-DNA-alkyltransferase (hAGT), but have been modified to bind to a slightly different ligand (57, 58). Protein tags come with the flexibility of choosing the fluorophore, and having control of the percentage of the molecules labelled. This is percentage is called degree of labelling (DOL).

Tab. 1.1: Common protein tags. Protein tags with their origin and corresponding ligand.

Name	Original enzyme	Ligand	
HaloTag	haloalkane dehalogenase	haloalcane (HA)	(59)
SNAP-tag	O^6-alkylguanine-DNA alkyltransferase	O^6-benzylguanine (BG)	(57)
CLIP-tag	O^6-alkylguanine-DNA-alkyltransferase	O^2-benzylcytosine (BC)	(58)

1.2.5 Quantitative fluorescence microscopy

The specific labelling of multiple different structures in the cell allowed for the better understanding of the cellular processes by studying structure-function relationship (60). Beyond just visualising structures, different microscopy techniques emerged. For instance, fluorescence correlation spectroscopy (FCS) and fluorescence recovery after photobleaching FRAP could determine the diffusion speeds of molecules, while Förster resonance energy transfer (FRET) allowed to determine the colocalisation of molecules down to the nanometer level. FLT was also used in combination with microscopy in a method called fluorescence-lifetime imaging microscopy (FLIM). This is a powerful technique that can assay the inner environments of cells, as well as their metabolic processes (61, 62). However, prior to the development of single-molecule imaging (see Sec. 1.2.7) these techniques were restricted to ensemble measurements, and could not gain information for molecular subpopulations, such as molecular clusters (63). For microscopy techniques to be able to determine the number of emitters inside molecular complexes, there were several issues that needed to be addressed.

1.2.6 Challenges with molecular counting

Quantitative microscopy has a multitude of issues that require solutions if the protein number is to be accurately estimated. These can be divided into the photophysical and physical challenges, the degree of labelling determination. In cases of live cells there are additional issues with molecular counting.

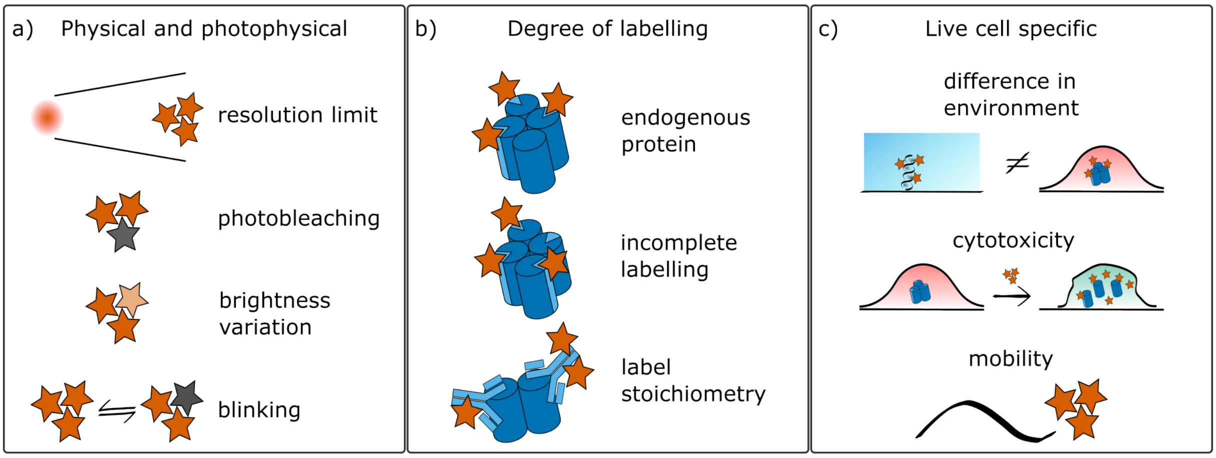

Fig. 1.3: Issues with molecular counting. Illustration of the problems that quantitative microscopy needs to tackle. a) Physical and photophysical properties of the dye. b) Degree of labelling differences. c) Issues relating to live cell imaging. Fluorophores shown as orange stars. Adapted from Hummert, *et al.* 2021 (7).

The properties of light and fluorescent labels are a constant concern in all fluorescence microscopy (Fig. 1.3a). The main issue with the molecular counting stems from the resolution limit making it impossible to distinguish the individual molecules in clusters smaller than a certain size. This limitations comes from the physical properties of the light mainly the diffraction limit of light (64). The diffraction limit describes the limits of how small a focus spot can be based on the ability of a medium to bend light (65). For a single perfect lens this is not a circular spot, but an Airy disk, which contains a central peak of light intensity surrounded by dimmer rings moving away from the centre (19). In microscopy, such a small point results in a shape determined by the interaction of the optical components, called a point spread function (PSF) (66). The formula for the minimum distance d at which you can resolve two points was given by Ernst Abbe in 1873 (67) and is calculated by Eq. 1.6.

$$\mathrm{d} = \frac{\lambda}{2\, n \sin(\theta)} \tag{1.6}$$

λ is the wavelength of the light diffracted, n is the index of refraction and θ is half of the maximal angle of light collection for a lens. In microscopes, the element collecting the the emission initially, and thus determining the resolution limit, is most commonly the objective. The objectives ability to bend light is specified by the manufacturer and is described by the numerical aperture (NA).

$$\text{NA} = n\sin(\theta) \tag{1.7}$$

Combining Eq. 1.6 and Eq. 1.7 results in:

$$\text{d} = \frac{\lambda}{2\,\text{NA}} \tag{1.8}$$

Points situated in a proximity less than the resolution limit cannot theoretically be distinguished. In practice, the PSF is approximated to a Gaussian function and estimates for resolution is mostly done by the radius of the full width at half maximum (FWHM) of the function, which is slightly larger than Abbe's resolution limit (68).

$$R_{\text{FWHM}} = 0.51\frac{\lambda}{\text{NA}} \tag{1.9}$$

In the past three decades, however, developments in microscopy have made it possible to obtain spatial information about the amount of proteins inside diffraction limited clusters (Fig. 1.4) (60, 69–71). These are expanded on in Sec. 1.2.7

The photophysical properties of the dyes can also prove to be an obstacle to accurate quantitation by molecular brightness. These include the bleaching of the dyes, as well as changes due to photoblinking or brightness variation. These challenges are mainly caused by the transition to a triplet states (see Sec. 1.2.2). As previously said, these reduce fluorescence and can generate reactive oxygen species (ROS) leading to photoblinking and photobleaching, respectively.

Another issue is the label number to protein number ratio, which depends on the labelling parameters and method (Fig. 1.3b). For instance, labelling methods that rely on genetic modification can be susceptible to miscalculations if there is an endogenous protein that has not been modified. This can be taken one step further in the cases where the label fails to attach. A technique addressing this issue has been developed during this project and is described in Chap. 5. Immunolabelling can also suffer from a difference in the ratio of labels to affinity tags, which is exacerbated in indirect immunolabelling. Determination of labelling efficiency is vital for molecular counting experiments if absolute copy number of targets is to be determined. This topic is expanded on in Sec. 5.1.1.1.

A more specific challenge to molecular counting stems from the complex cellular environment where the target protein is located (Fig. 1.3c). Not only that, but also the issue with the semi-permeability of the plasma membrane. This can prevent both the infiltration of labels, as well as the components of the imaging buffer (see Sec. 5.1.2). This means that live-cell imaging is only possible with membrane-permeable fluorophores and buffer components. These components need to also be non-toxic, both in their ground state and in their excited state. An oxygen depletion system can also not be utilised if the experiments are to be biologically relevant. The final consideration for live cells is the fact that cells are dynamic moving systems. This means that the sample can move away from its original position during recording. This can be due to the movement of the molecular cluster, as well as motility of the entire cell itself.

Development of molecular counting microscopy techniques involves solving one or multiple of these issues.

1.2.7 Development of counting techniques

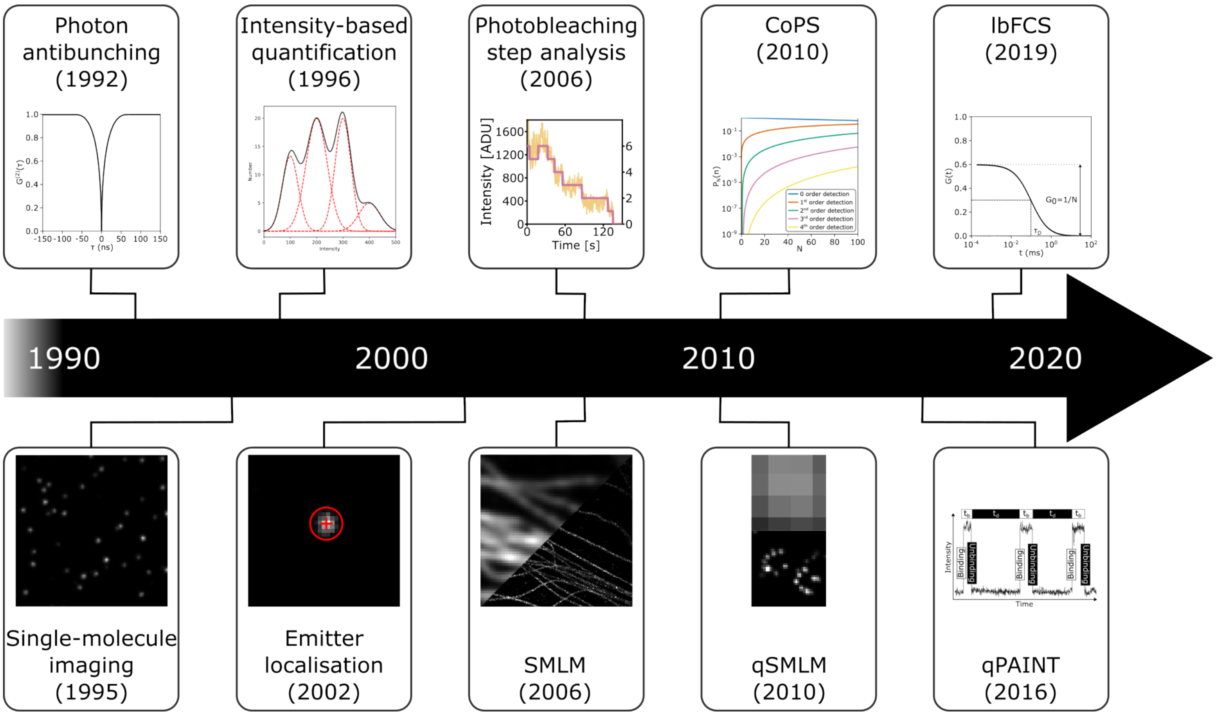

Fig. 1.4: Timeline of single-molecule microscopy developments. Quantitative microscopy techniques and time of first publication. This figure was adapted from Grussmayer, et.al. 2019 (60).

Initial imaging experiments on single molecule systems were conducted in the mid-1990s to study enzymatic reactions (72, 73). The first attempts at molecular counting were based on the fluorescence intensity of molecular clusters smaller than the diffraction limit (74). Despite the advances in intensity-based counting, the main issue with these techniques remains the necessity for calibration with a molecular standard of known stoichiometry, whose intensity is used to calculate the protein number in other clusters (75, 76). One way to circumvent that is to exploit the step-like decrease in fluorescence intensity during bleaching (77, 78). This method has become a viable way to count fluorophores with the addition of automatic fitting of the photobleaching steps (79), giving the name of this group of methods - photobleaching step analysis (PBSA). Another important development was the introduction of the reducing and oxidising system (ROXS) buffer which controls photophysical effects (7, 80, 81). These include oxygen scavenger systems, which reduce ROS generation, reducing molecules, which act as triplet quenchers, or a combination of the two. Another improvement came with the addition of Bayesian modelling of the steps detected (7, 82).

A major development in molecular quantification was the ability to surpass the diffraction limit. One way to do this is to split the emission of molecules in time and determine the centre of the PSF (66). The group of these techniques is called single-molecule localisation microscopy (SMLM) and have allowed for the estimation of the location of emitters down to several nanometer (83). The temporal split can be done by photo switching of the fluorophores different brightness states as in stochastic optical reconstruction microscopy (STORM) (71) and photo activated localization microscopy (PALM) (83), or by the immobilisation of free labels at only parts of the structure of interest at a single point in time as is the case in point accumulation for imaging in nanoscale topography (PAINT) (84). Quantitative SMLM (qSMLM) techniques frequently start with combining the localisations into clusters followed by examinations of the number of localisations per clusters. For STORM and PALM, the kinetics and quantity of the blinking can be used to assume the fluorophore count (85). In a similar manner quantitative PAINT (qPAINT), a subset of DNA-PAINT, uses the kinetics of binding and unbinding of a labelled DNA strand (69). These methods also require a monomeric standard for calibration with either a known amount of localisations per molecule or known binding kinetics, for qSMLM or qPAINT. An expansion of qPAINT called localization-based FCS (lbFCS) also utilises the molecular brightness to give an estimate of the binding and unbinding rates based on fluorescence fluctuation without the need of a standard. A downside to qSMLM methods rely on the homogeneity of the sample and are limited to static systems, such as fixed cells as they cannot deal with sample movement.

Another type of calibration free methods are ones based on a characteristic of fluorescence called photon antibunching (60). Photon antibunching means that the emission of photons shows a sub-Poissonian distribution, i.e. the variance is less than the mean (86). This regularity in the emission comes from the fact that a fluorophore can only emit a maximum of a single photon per excitation-emittion cycle (Fig. 1.5a). By inspecting the second order correlation function $G^{(2)}(\tau)$ for the intensity I with delay time τ, antibunching can be observed (87).

$$G^{(2)}(\tau) = \frac{\langle I(t)I(t+\tau)\rangle}{\langle I(t)\rangle\langle I(t+\tau)\rangle} \tag{1.10}$$

Nowadays single-photon avalanche diodes (SPADs) and a time-correlated single photon counting system (TCSPCS) are used in combination with picosecond pulsed lasers (PSPL) are used for quantitative antibunching measurements. With these the difference in the arrival times of two subsequent photons can be determined. This transforms Eq. 1.10 into:

$$G^{(2)}(\tau) = \frac{\langle n_1(t)n_2(t+\tau)\rangle}{\langle n_1(t)\rangle\langle n_2(t+\tau)\rangle} \tag{1.11}$$

where $n_i(t)$ is the number of detected photons by detector i at time t (88).

When using a PSPL $G^{(2)}(\tau)$ resembles a series of peaks with a distance between them being the time between the pulses and a slope dependent on the fluorescence lifetime (87). With a small number of emitters, the second order correlation function $G^{(2)}(\tau)$ shows a dip of the peak at τ = 0 (Fig. 1.5b). With a single emitter $G^{(2)}(0) = 0$, which is a sign of antibunching. When using a PSPL the number of emitters n can be estimated from the ratio of the surface area of the central peak N_c to the mean of the surface areas of the lateral peaks $\overline{N}_l$ (89):

$$\frac{1}{n} = 1 - \frac{N_c}{\overline{N}_l} \tag{1.12}$$

When use a continuous wave (CW) laser the $G^{(2)}(\tau)$ function can only show the consistent emission of fluorophores (Fig. SI 1). However, the dip at $G^{(2)}(0)$ is still visible in low fluorophore numbers and the number of emitters can be calculated by the inverse of that dip (90).

The problem with using the value of $G^{(2)}(0)$ is that its values plateau and start to merge with experimental noise at about 4 emitters (Fig. 1.5c). Beyond that point errors in emitter estimation will occur.

Counting by photon statistics (CoPS) was developed as an extended method for molecular counting and utilises multiple SPADs with the same detection probability. It relies

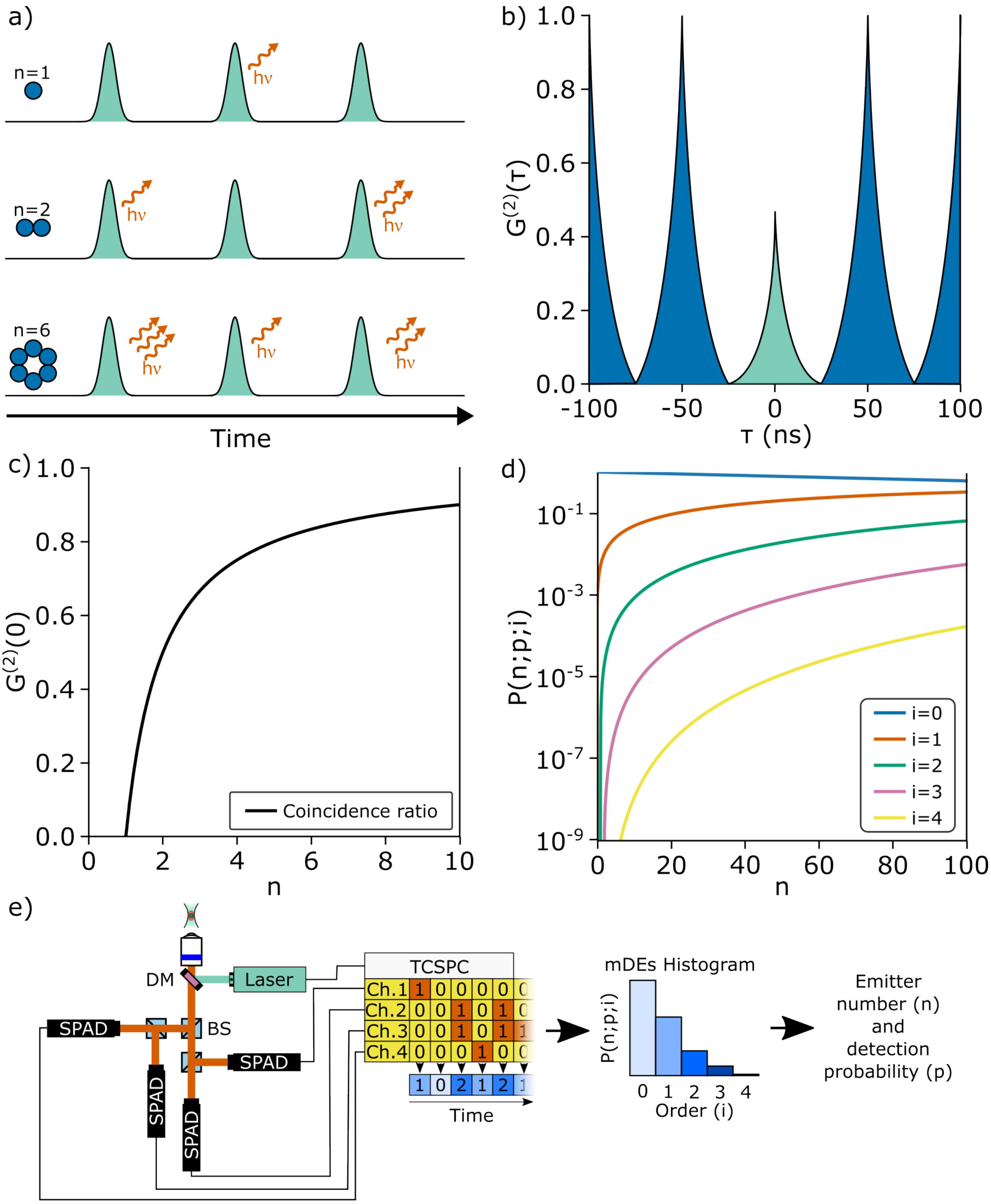

Fig. 1.5: Fluorescence antibunching. a) Cartoon of emission of photons after pulsed laser excitation. Examples given for n=1, 2 and 6 emitters (top, middle and bottom panel). b) Second order correlation function $G^{(2)}(\tau)$ of a two emitters excited with a picosecond pulsed laser (PSPL). The distance between peaks represent the time between laser pulses. The dip at the central peak at τ = 0 is typical for photon antibunching. The surface area of the central peak N_c (green) and the mean of lateral peak surface areas $\overline{N}_l$ (blue) can be used to estimate the emitter number (Eq. 1.12). c) Values of the $G^{(2)}(0)$ for different numbers of emitters (n). d) Distribution of probabilities of different orders of detection (i) per pulse given at different numbers of emitters (n). These values are also dependent on the detection probability per pulse for a single emitter p, which for this example was set to 0.005. e. counting by photon statistics (CoPS) analysis pipeline.

on the difference in probability of multiple detection events (mDE) (91). mDE are a way to classify the laser pulses depending on the number of photons detected after them, thus separating them into orders. The order i of the mDE range from zero to the total number of detectors, in a single laser pulse. Fig. 1.5d shows an model probabilities demonstrates the increase in the range of quantification. CoPS analysis normally begins by grouping the detection events of single channels into a mDE time trace, then using that to create a histogram of mDE probabilities (Fig. 1.5e). The probability of having a mDE $P(n;p;i)$ of order i for emitter number n, where p is the probability of detection of a photon from a single fluorophore per pulse, is calculated by Eq. 1.13 (91).

$$P(n;p;i) = \begin{cases} (1-p)^n & ,\ i=0 \\ \binom{n}{m}\left(i\frac{p}{m}+1-p\right)^n - \sum_{k=0}^{i-1}\frac{\binom{n}{m}}{\binom{m}{k}}P(n;p;k) & ,\ i>0 \end{cases} \tag{1.13}$$

m is the number of detectors and in most cases this would be four. This mathematical model is then fitted to the histogram to estimate the n and p. p is highly dependent on the luminescence of fluorescence detected by a the microscope system (Eq. 1.4). CoPS is not only calibration free, but also does not rely on bleaching and can theoretically work in dynamic systems, which makes it appropriate for live cell experiments. This, however, has not been attempted yet. This project was focused on determining the challenges, as well as defining the limits of dynamic CoPS.

1.3 Aims

The ultimate goal is transitioning CoPS from a technique used in static samples, such as fixed cells, to one that is able to be used on live cells. This method would then be used to determine the number of molecules inside cell clusters *in vivo* and would hopefully contribute to measuring the recruitment kinetics of proteins.

This work focuses on moving towards this goal and determining the challenges that come along the way.

Conducting these experiments would require building a microscope setup, with the architecture to support the antibunching measurements and the ability to detect mDEs. This microscope will require initial validation to ensure the validity of the experiments conducted with it.

The software used for CoPS analysis will also require modification to facilitate the new analysis method. After that a dynamic system needs to be chosen and the kinetics of it need to be determined, before being assayed with the dynamic version of CoPS. The experiments should be conducted to determine the challenges and limits of this technique.

Finally, the method will need to be attempted in live cells, and the challenges of imaging live cells need to be established and addressed. Initially, this can be done in a relatively stationary system. Then an appropriate dynamic system needs to be determined and characterised. Then, finally, attempts to quantify the kinetics of it needs to be made with the dynamic version of CoPS.

Chapter 2

Material and Methods

2.1 Material

2.1.1 Biological materials

Cell lines

Tab. 2.1 shows all the eukaryotic cell lines used in this thesis. COS-7, Hela and U2OS are adherent cell lines, while Jurkat cells are grown in suspension. The HeLa cells stably expressing the ProDOL construct were generated by Florian Schwörer, while the Jurkat stable cell lines were made by Wioleta Chmielewicz *et al.* (92).

Tab. 2.1: List of cell lines.

Cell line	Transfection	ATCC/CLS code	Supplier
COS-7 (Cercopithecus aethiops, fibroblast)	-	CRL-1651	ATCC
HeLa (Homo sapiens, epithelial)	-	CCL-2	ATCC
HeLa (Homo sapiens, epithelial)	ProDOL construct	-	Herten-Lab
U2OS (Homo sapiens, epithelial)	-	300364	CLS
U2OS (Homo sapiens, epithelial)	Nup107-SNAP	300294	CLS
Jurkat (Homo sapien, CD4 T-cell)	-	-	Fackler-Lab
Jurkat (Homo sapiens, CD4 T-cell)	ProDOL construct	-	Herten-Lab
Jurakt (Homo sapiens, CD4 T-cell)	LynG construct	-	Herten-Lab
Jurkat (Homo sapiens, CD4 T-cell)	SLP76-Halo	-	Herten-Lab

Plasmids

This thesis contains two plasmids used in the determination of tag labelling and non-specific binding, ProDOL and LynG respectively. Both of these constructs were generated by Siegfried Hänselmann in the Herten lab (Fig. SI 2). The ProDOL construct is a fusion protein containing Lyn kinase anchor, enhanced green fluorescent protein (eGFP), HaloTag, and SNAP-tag (92). The LynG probe only contains only the Lyn kinase anchor and the eGFP.

Antibodies, protein-tag ligands and fluorescent labels

Tables 2.2, 2.3 and 2.4 show the antibodies, protein-tag ligands and fluorophores used within this thesis, respectively. Tags that were produced in the lab were purchased as N-hydroxysuccinimide (NHS)-ester versions of the fluorescent dyes after which they were functionalised with a HaloTag-ligand or SNAP-tag ligand based on manufacturer's protocol. These tags were then purified by HPLC (30 to 70% H_2O/acetonitrile with 0.1% trifluoroacetic acid over 30 min) by Jonas Euchner.

For microscope validation experiments, TetraSpeck with 200 nm diameter or Dark Red FluoSpheres with 20 nm diameter were used (ThermoFisher).

Tab. 2.2: List of antibodies. Antibodies were split into aliquots of 10 µl and the number of freeze-thaw cycles was recorded on each vial. Immunofluorescence (IF), western blot (WB), surface coating (SC).

Primary

Antigen	Host	Clone	Fluorophore	Concentration	Clonality	Use
pCD3	Mouse	K25-407.69	AlexaFluor 488/640	1:5	Monoclonal	IF
SLP76	Rabbit	-	-	1:500	Polyclonal	WB
GAPDH	Mouse	1D4	-	1:500	Monoclonal	WB
CD3	Mouse	HIT3a	-	1:50	Monoclonal	SC
CD90	Mouse	eBio5E10 (5E10)	-	1:50	Monoclonal	SC
CD28	Mouse	CD28.2	-	1:50	Monoclonal	SC

Secondary

Antigen	Host	Clone	Fluorophore	Concentration	Clonality	Use
Mouse IgG	Goat	-	DyLight™ 680	1:5000	Polyclonal	WB
Rabbit IgG	Goat	-	DyLight™ 800	1:5000	Polyclonal	WB

Tab. 2.3: List of tag ligands. Alexa Fluor (AF), silicon rhodamine (SiR), tetramethylrhodamine (TMR).

Ligand	Modification	Item number	Source
Halo	SiR	-	Herten Lab
SNAP	SiR	S9102S	NEB
Halo	TMR	G8251	Promega
SNAP	TMR	S9105S	NEB
SNAP	AF647	-	Ries Lab

Tab. 2.4: List of organic fluorophores. 4’6-diamidino-2-phenylindole (DAPI), Alexa Fluor (AF), fluorescein isothiocyanate (FITC).

Fluorophores and cell stains
DAPI
Phalloidin-Atto565
phalloidin-AF647
FITC
Atto655

DNA origami and oligonucleotides

DNA origami of the new rectangular origami (NRO) structure was generously provided by Michael Scheckenbach from the lab of Prof Philip Tinnefeld (LMU Munich, Germany) in three variations- 1 (1xS1), 2 (2xS1), and 5 binding sites (5xS1) containing the S1-docking sequence and three reference labels bound to the S2 binding sequence.

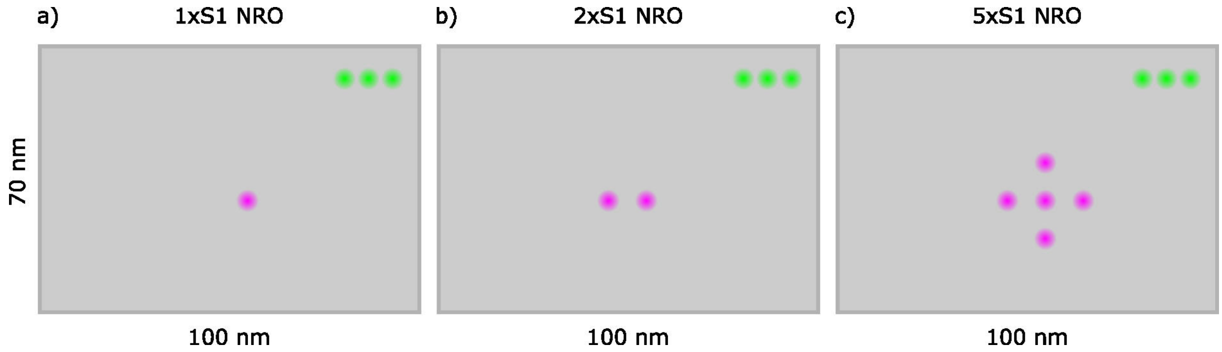

Fig. 2.1: DNA origami design. Design of the three NRO. All of them have three S2 docking sites (green) with Atto542 labels. Each has a different number of S1 docking sites (magenta): a) 1xS1, b) 2xS1 and c) 5xS1.

The DNA origami is made from p7249 (M13mp18) DNA bend by staple stands (Tab. SI 2). The origami has two types of docking sites with 3’-end single-strand overhangs- S1 and S2. S1 bind to different imager strands (Tab. SI 3) and S2 binds Atto 542 modified strands for reference (Tab. SI 1). Imager strands for the S1 sequence were purchased from commercial sources as stated in Tab. 2.5. Both DNA origami and imager strands were aliquoted to prolong shelf life.

Tab. 2.5: List of labelled oligonucleotides. DNA sequences match on their 3' so that they all bind with the conjugated fluorophore towards the DNA origami.Cyanine (Cy), nucleotides (nt).

Sequence (5' to 3')	Length (nt)	3'-modification	Source
TAG AGG AA	8	Cy5	IDT
GTA GAG GAA	9	Cy5	IDT
GGT AGA GGA A	10	Cy5	IDT
GTG ATG TAG GTG GTA GAG GA	21	Cy5	IDT
GTA GAG GAA	9	Atto643	Biomers.net
GTG ATG TAG GTG GTA GAG GAA	21	Atto643	Biomers.net

Biological Products

Biological products were purchased from the commercial sources in Tab. 2.6 and were stored in accordance with manufacturers guidelines.

Tab. 2.6: Biological products. Fetal bovine serum (FBS), glucose oxidase (GO), protocatechuate 3,4-dioxygenase (PCD).

Compound	Supplier	Final concentration
Catalase	Sigma-Aldrich	40 µg/ml
FBS	Thermo Fisher	10%
GO	Sigma-Aldrich	500 µg/ml
PCD	Sigma-Aldrich	50 nM

Cell media and buffers

Media

Cell media were prepared from phenol-red-free Dulbecco's modified eagle medium (DMEM) or RPMI 1640 according to Tab. 2.7 for adherent or suspension cells, respectively.

Tab. 2.7: Cell media. Cell media composition for culturing mammalian cells.

Adherent cell media		Suspension cell media	
DMEM		RPMI 1640	
FBS	10%	FBS	10%
GlutaMAX	50 ng/ml	GlutaMAX	50 ng/ml
Sodium pyruvate	50 ng/ml	Sodium pyruvate	50 ng/ml
Penicillin	50 U/ml	Penicillin	50 U/ml
Streptomycin	50 µg/ml	Streptomycin	50 µg/ml

Buffers

Where appropriate buffers were purchased from commercially available sources.

Tab. 2.8 shows custom buffers. dSTORM buffer was prepared according to Jimenez *et al.* (93) and was adjusted to pH=8.0.

Tab. 2.8: Common buffers. tris(hydroxymethyl)aminomethane (TRIS), 2-mercaptoethylamine (MEA), 2,2'-(piperazine-1,4-diyl)di(ethane-1-sulfonic acid) (PIPES), ethylene glycol-bis(β-aminoethyl ether)-N,N,N',N'-tetraacetic acid (EGTA).

dSTORM		ROXS Blue base		ROXS Red base	
TRIS	50 mM	PBS	5 ×	PBS	2 ×
NaCl	10 mM	MV	1 mM	MV	1 mM
Glucose	10%	AA	2.1 mM	AA	2.1 mM
MEA	40 µg/ml	PCA	2.5 mM	PCA	2.5 mM
GO	500 µg/ml	PCD	50 nM	PCD	50 nM
Catalase	40 µg/ml	Glycerin	12.5%	NaCl	500 mM
				Tween 20	0.05%

Two different reducing and oxidising system (ROXS) were used. One using glucose oxidase (GO) and catalase (93), and another using protocatechuate 3,4-dioxygenase (PCD) and protocatechuic acid (PCA) (7). The enzymes in these imaging buffers were stored as specified in Tab. 2.9.

Tab. 2.9: Enzyme storage buffers. tris(hydroxymethyl)aminomethane (TRIS), 2,2'-(piperazine-1,4-diyl)di(ethane-1-sulfonic acid) (PIPES), ethylene glycol-bis(β-aminoethyl ether)-N,N,N',N'-tetraacetic acid (EGTA),ethylenediaminetetraacetic acid (EDTA).

GO storage		PCD storage	
PIPES	12 mM	TRIS-HCl	100 mM
EGTA	1 mM	Glycerol	50%
MgCl2	2 mM	KCl	50 mM
Glycerol	50%	EDTA	1 mM
	pH=6.8		pH=8

2.1.2 Chemicals and consumables

Chemical and consumables where purchased from Sigma-Aldrich/Merck if available. Reagents for cell culture where purchased from Thermo Fisher Scientifc unless otherwise stated.

2.1.3 Microscope systems

Laser scanning confocal and widefield microscope setup

More details about the positioning of the components of the microscope in Chap. 3. The custom microscope setup consists of a Nikon Eclipse Ti body with a motorised XY-stage (Märzhäuser) and a PFS2 autofocus system. All imaging was done with an Apo TIRF 100× 1.49 NA oil immersion objective (Nikon).

The left port of the body is a laser scanning confocal microscope (LSCM) with a FLIMBee scanner (PicoQuant). Excitation is provided via a picosecond pulsed source at 640 nm (LDH P-C-640B, PicoQuant), 532 nm (P-FA-530XL, PicoQuant) and 470 nm (P-C-470M, PicoQuant) coupled into a single-mode polarisation maintaining fibre (Schäfter Kirchhof). Signal was detected by four single-photon avalanche diode (SPADs) (Perkin-Elmer). A dichroic mirror (z532/640, Chroma) separated the emission and excitation pathways. The emitted signal was filtered using a quad notch filter with additional spatial filtering using a 100 µm pinhole (P100K, Thorlabs) placed in the focal plane between two 75 mm achromatic doublet lenses (AC254-075-A-ML, Thorlabs). All emission was split into four equal intensity paths using 50:50 beamsplitter cubes (BS013, Thorlabs) and focused on the four SPADs by a 200 mm achromatic doublet (AC254-200-A-ML, Thorlabs). Signals were combined by a multichannel time-correlated single photon counting system (TCSPCS) (HydraHarp 400, PicoQuant). The microscope was operated using SymPhoTime 64. The exposure settings, and the illumination intensities were each tuned for each individual sample.

The right port of the body leads to a motorised filter wheel (FW102C, Thorlabs) with bandpass filters (525/50, 605/70, and 690/70 nm), after which an OptoSplit II (Cairn) was installed. The detection was done by an iXon Ultra 897 back-illuminated emCCD camera (Andor). A multi-laser engine (MLE; TOPTICA Photonics), equipped with 405 488, 561, and 640 nm laser lines is coupled to the body. A quadband dichroic mirror was used separate the paths of the emission and excitation paths. The microscope was operated using µManager 1.439. The exposure times, the electron-multiplying gain factor g, and the illumination intensities were each adjusted for each experiment.

Fluorescence microscope for widefield microscopy

For dSTORM experiments a widefield microscope with an ASI RAMM body fitted with a Nikon 100X 1.49 NA immersion oil objective was used. It was fitted wth a motorised stage and autofocus system (CRISP, ASI). Illumination was provided by four laser lines (405 nm, 488 nm, 561 nm and 647 nm) controlled by an acousto-optic tunable filter (AOTF) or direct laser control. A uniform excitation across the field of view was ensured by a refractive field mapping device (piShaper, AdlOptica). Signal was detected on two scientific complementary metal–oxide–semiconductor (sCMOS) cameras (Prime95B, Photometrics). A dichroic mirror (405/488/561/640, Chroma) separated the emission from the excitation before the prior being filtered using a notch-filter (405/488/532/635 or 561 Semrock), as well as an additional band-pass filter depending on the channel (470/24, 525/50, 593/46, 685/70, or 731/137, Chroma and Semrock). This microscope setup was controlled using µManager 2.0 (94). Exposure time, laser power and number of frames were adapted for each sample.

2.1.4 Optics and optomechanical components

All optical optomechanical components in Sec. 2.1.3 were purchased from Thorlabs, unless otherwise stated. Optical filters used in the microscopes described in Sec. 2.1.3 were purchase from Chroma or Semrock. Optical tables and dampening equipment were purchase from Newport.

2.1.5 Electronics

All electronic components, microcontrollers and cables were purchased from RS Components, respectively unless otherwise stated in the text.

2.1.6 Software

Software

Tab. 2.10: Software. List of commonly used software together with their versions.

Software		Programming Language	
Chimera	1.1	Arduino (C++)	1.8.5
GraphPad Prism		ImageJ Macro	-
Fiji	2.14	MATLAB	2021b
ImageJ	1.54f	Python	3.7
µManager	1.4 and 2.0	Java	1.8.0
Anaconda	2.4.0		
Spyder	5.2		
Jupyter Notebook	6.4		

Code The custom libraries pycromove and PynamicMeasurements were created for this work and can be provided upon request.

Tab. 2.11: Code base. List of commonly used scripts, libraries and modules with version number.

Java/Fiji		MatLab		Python	
MultiStackReg	1.46.5	ProDOL	1.1	pycops	update 2023.03.20
ProDOL	1.1	SMAP	201217	PynamicMeasurements	update 2023.09.06
ThunderSTORM	1.3			quickPBSA	2020.0.1
Weka Segmentaion	3.2.34			pycromove	update 2023.03.17

2.2 Methods

2.2.1 Cell culture

Mammalian cell lines were cultured from frozen stock by quick thawing of the vial in a 37° C water bath, followed by addition of the cells to 9 ml of prewarmed media. After 3 min centrifugation at 200×g the supernatant is discarded and the cell pellet is resuspended into 5 ml of fresh media before being transfered to a T25 flask. Cells were kept in culture until passage 20, unless morphological or growth abnormalities were detected. All cell lines were cultured at 37° C, in a high humidity and 5% CO$_2$ incubator.

Adherent cell lines were grown in T25 or T75 filled with the adherent cell media specified in Sec. 2.1.1. Cells were passaged when having reaching 80% confluency and were seeded into a new flask. To split the cells, the old media was discarded, the cells were quickly washed with PBS, followed by addition of 80 µL/cm^2 TrypLE (depending on the flask surface area). Once cells were completely detached, 2 times the volume of DMEM was added to the cell suspension and cells were pelleted at 200×g for 3 min. After the supernatant was discarded cells were resuspended to in 1 or 3ml of prewarmed growth media for T25 or T75 flask, respectively. A prewarmed flask with 0.2 ml/cm^2 of media was prepared to which the appropriate cell count was added to reach approximately 1.0-1.2×10^4 cells/cm^2.

Suspension cells were cultured in RPMI-based media as specified in Sec. 2.1.1. Cells were grown in non-coated T25 or T75 flasks and split when 0.8-1.0×10^6 cells/ml density was reached. The SLP76-HaloTag Jurkat cell lines expressed a puromycin resistance gene so they were grown in selection media containing 1.5 µg/ml puromycin. Cells were passaged by splitting of a certain volume and adding the appropriate amount of fresh media to reach a concentration of 2×10^5 cells/ml.

2.2.2 Biochemical Techniques

Agarose gel electrophoresis

Gel preparation

A 1% agarose gel was prepared by adding 5 g of agarose in 500 ml of water and microwaving the solution at 5 s intervals until all powder is dissolved. Then 50 µl of ×10^4 SYBR™ Safe stain was added to the gel solution. After which the gel was poured into a mold and a 10-channel comb was inserted. The gel was left to cool after which the comb was removed.

Electrophoresis

Gel was placed in a Owl EasyCast B1 Mini gel electrophoresis system (ThermoFisher) after which it was submerged in TRIS-borate-EDTA (TBE) buffer. 20 fmol of each DNA origami mixed 1:10 with 21 nucleotide long Cy5 imager starnds were topped up to 10 µl with purple loading dye (NEB).The origami and MP13 was loaded into the gel, as well as 4 µl of DNA ladder (Quick-Load® Purple 1 kb DNA Ladder, NEB). The electrophoresis was performed by a PowerPacBasic (BioRad) power supply at 120 V for 90 min. Imaging was done via Odessey Fc imager(Li-Cor).

Western blotting

Sample preparation

Cells were counted with a hemocytometer before 1×10^7 cells were taken out from suspension and spundown at 200×g. After the supernatant was discarded the samples were washed once with prewarmed PBS. The cells were then pelleted at 200×g and the supernatant was discarded. 50 µl of 2× running buffer was added to the pellet and mixed until homogenous. The samples were then heated to 95° C for 3 min, after which they were transferred to a ice box. After cooling samples were sonicated at 40% intensity by amplitude for 2 s. Finally, samples were spun down and stored at - 20° C.

Electrophoresis and Western Blotting

10 µl of each cell samples and 4 µl of protein ladder were loaded into 10% precast polyacrylamide gel (Mini-PROTEAN® TGX™, BioRad) with empty chambers being loaded with 2× running buffer. The electrophoresis was and ran at 90 V for 90 min by a PowerPacBasic (BioRad) power supply. Next, the gel was carefully removed and placed in a Novex Mini (Invitrogen) nitrocellulose transfer stack and ran for 7 min at 20 V in an iBlot 2 (Invitrogen) transfer device. After that, the nitrocellulose membrane was cut into shape and washed three times in TBST buffer for 5 min.

Tab. 2.12: Running buffer components. Final concentration for a 1× concentration of the running buffer. The buffer is adjusted to pH=6.7. tris(hydroxymethyl)aminomethane (TRIS), sodium dodecyl sulfate (SDS), dithiothreitol (DTT).

Component	Concentration
TRIS-HCl	35 mM
SDS	40 mM
DTT	60 mM
Glycerol	3.6%
Bromophenol blue	0.002%

Membrane labelling and imaging

The membrane was blocked using 5% powdered milk in TRIS-buffered saline with 0.1% Tween 20 (TBST) for 1 hour in room temperature after followed by overnight incubation with a 1:500 dilution of the primary antibodies in 5% powdered milk in TBST at 4° C. Next the membrane is washed twice quickly in TBST followed by two 5 min washes in TBST to remove the primary antibodies. The membrane is the incubated with a 1:5000 dilution of the secondary antibodies in 1% powdered milk in TBST for 1 hour in room temperature in the dark. The membrane was then washed twice quickly and twice for 5 min in TBST before being imaged by an Odessey Fc imager (Li-Cor).

2.2.3 Flow cytometry

An aliquot of 2×10^6 Jurkat cell clones were stained with 1 nM HA-SiR for 30 min in RPMI before being washed three times in RPMI for 15 min and then once for 40 min. The cells were then pelleted and resuspended in 100 µl of RPMI. The samples were put on ice and then stained with 7-AAD to determine viability before being inspected in a CytoFLEX S (Beckman Coulter). Measurements were peformed by Danielle Lezama. The SiR signal was detected in the APC channel and the 7-AAD in its own. The signal for the SiR was corrected for the 7-AAD bleedthrough by a sample unlabelled with HA-SiR. The gating was determined based on Jurkat wild type measurements.

2.2.4 Microscopy sample preparation

Surface Treatment and Coating

Cleaning with hydrofluoric acid

All glass coverslips and glass surfaces used were cleaned with 0.1 M hydrofluoric acid. The acid was administered twice to the coverslip after each time followed by two washes with sterile H_2O. Finally, the surfaces were incubated with PBS for 5 min before being used.

Coating with biotin-bovine serum albumin (BSA), streptavidin and DNA origami

Samples were prepared in chambered coverslips (Nunc™ Lab-Tek™ I, ThermoFisher Scientific) which were cleaned with hydrofluoric acid. After that, coverslips coated with 1 mg/ml biotin-BSA overnight before being washed three times in PBS. Next, 0.2 mg/ml streptavidin was incubated for 30 min before three washes with Red Base prepared as specified in Tab. 2.8. In each chamber 10 fmol of the new rectangular origami (NRO) in Red Base was incubated for 30 min, before being washed three times in Red Base. The samples were inspected for sufficient DNA origami coverage and in cases of low coverage the DNA origami was reintroduced before being washed three times in Red Base.

Each chamber of the coverslips was then filled with imaging buffer and encapsulated with self-sealing Parafilm(M). The imaging buffer contained 2.1 mM ascorbic acid (AA), 1 mM methyl viologen (MV), 2.5 mM protocatechuic acid (PCA) and 50 nM protocatechuate 3,4-dioxygenase (PCD) in Red Base. Different concentrations of Cy5-conjugated oligonucleotides were achieved by substituting Red Base with 1 µM imager strand diluted in Red Base.

Poly-L-lysine (PLL) coating and antibody coating

For T cell cell experiments a modified version of the Bunnell *et al.* 2001 method was used (95). The hydrofluoric acid cleaned coverslips were incubated with 0.01% PLL in PBS for 10 min. Afterwards the solution was taken out and the coverslips were left to dry. Depending on the experiment, antibodies from Tab. 2.2 were diluted 1:50 (20 µg/ml) in PBS after which the sample was incubated for more than 3 hours at 37° C.

Bead samples

The bottle of 660 nm excited 20 nm FluoSpheres Carboxylate-Modified Microspheres (F8783, ThermoFisher), were sonicated, before creating a 1:10000 dilution. 20 µl were then pipetted into a well made from a glass slide and parafilm. A #1.5 coverslip was placed on top and the sample was sealed with nail polish.

Fluorescent dye dilution series

A dilution series of Atto655 from 5 pM to 100 nM in H_2O with 0.05% Tween20 was prepared. Afterwards 200 µl of each concentration was pipettes in chambered slides (Nunc™ Lab-Tek™ I, ThermoFisher Scientific).

Cell seeding

Adherent cells seeding

Adherent cells were removed from the growth flask by Tryple, counted and seeded at 0.5-1.0$\times10^4$ cells/cm^2 and incubated for at least 10 h before further use.

Suspension cell seeding

All suspension cells were seeded on poly-L-lysine (PLL) and antibody coated coverslips, unless otherwise specified. Unless specified otherwise suspension cells were seeded at 1.0-1.2$\times10^4$ cells/cm^2 for 10-15 min after which cells were fixed in 4% paraformaldehyde (PFA) in PBS.

For syncronised activation experiments the cells were resuspended in PBS at 2$\times10^6$ cells/100 µl. After which 100 µl of the cell suspension was pipetted into a chamber of a chambered coverslip and then removed after approximately 3 s. The slip was gently washed once PBS and after which the cells were left to incubated for a desired activation time period before being fixed in 4% PFA in PBS.

Fixation and labelling

SNAP-tag labelling with AF647 for cross validation of DOL

The labelling protocol was adapted from Thevathasan *et al.* (76). U2OS cells were prefixed in pre-heated 2.4% PFA in PBS for 30 sec after which they were permeabilised with 0.4% Triton X-100 in PBS for 3 min. The cells were then fixed using 2.4% PFA in PBS for 30 min. Next, the samples were quenched using 100 mM ammonium chloride in PBS for 5 min. Samples were incubated with Image-iT FX for 30 min. Samples were then stained with a solution containing containing 1 µM BG-AF647 ligand, 1 µM dithiothreitol and 0.5% BSA in PBS for 2 h. Samples were washed twice for 30 min and once for 60 min in PBS.

SNAP-tag labelling with SiR for cross validation of DOL

The sample processing was adapted from Hummert (7). U2OS cells were incubated with 200 nM SiR SNAP-tag ligand at 37° C for 2 hours. Samples were then washed twice quickly, after which twice for 30 min and once for 1 hour with warm growth media at 37° C. Next cells were fixed for 20 min with prewarmed 3.7% PFA in PBS. Finally, the sample was washed twice for 5 min in PBS.

ProDOL labelling

For ProDOL experiments, the cells were seeded in chambered coverslips. For quantitative experiments cells were processes according to the experiment specific protocol. In the case of the optimisation of labelling experiment in Jurkat cells, the concentration and incubation time were systematically varied varied between 100 pM and 250 nM and between 15 min to 16 hours, respectively. Next, the cells were washed three times in prewarmed RPMI growth media for 15 min and once for 40 min. Finally, cells were washed for 5 min in prewarmed PBS after which cells were seeded and fixed. All washes were done at 37° C.

SLP76-HaloTag labelling

SLP76-HaloTag expressing Jurkat cells were labelled with 1 nM HaloTag ligand for 30 min, unless otherwise specified. The cells were then washed as described above.

phospho-CD3 labelling

Cells were permeabilised with 0.1% Triton for 5 min after which the cell was washed three with PBS for 5 min. The sample was incubated with 5% bovine serum albumin (BSA) to block non-specific binding. Next the sample was stained with the anti-phospho-CD3 antibody specified in Tab.2.2 at a 1:5 dilution for 20 min. The sample was then washed three times in PBS for 10 min. Samples were post-fixed with 4% PFA in PBS for 20 min followed by two washes for 5 min in PBS.

Phalloidin labelling

Samples were stained with 100 nM fluorescently labelled phalloidin in PBS for 15 min after which the samples were washed three times with PBS for 5 min. Samples stained with phalloidin were imaged on the same day.

2.2.5 Microscopy techniques

All samples were imaged with the laser scanning confocal microscope specified in Sec. 2.1.3, unless specified otherwise.

Light microscopy for camera calibration

Samples were illuminated with the halogen lamp from the illumination pillar of the Nikon Ti specified in Sec. 2.1.3. The intensity, gain and exposure was adjusted according to the experiment. 100 frames were acquired per condition.

Bead tracking

Fluorescent bead samples were imaged for 8000 frames at 20 ms exposure and 5 multiplication gain factor g, in frame-transfer mode, with 9.5 W/cm^2 640 nm illumination.

For dampening measurements the same FOV was imaged multiple times with changes of the pressure of the pneumatic dampeners.

Fluorescence cross-correlation spectroscopy

Three 5 min traces were recorded per concentration at 5 µm above the surface of the coverslip. The confocal volume was excited with a 640 nm pulsed laser with an average illumination of 21 kW/cm^2 at 40 MHz repetition rate.

Diffraction-limited microscopy

Samples for qualitative diffraction-limited microscopy images were acquired in PBS, or in ROXS buffer for the Jurkat SLP-76-HaloTag experiments which used CoPS, using the appropriate laser line and filters on the widefield microscope in TIRF mode using the BatchImager script.

ProDOL

Samples imaged for determination of DOL with the protein-tag degree of labelling (ProDOL) method were imaged under total internal reflection fluorescence (TIRF) for 10 frames at 640 nm , 561 nm and 488 nm with 9.3 W/cm^2, 9.3 W/cm^2 and 10 W/cm^2 laser power, respectively.

Photobleaching step analysis

For PBSA, samples were acquired using a laser power of 30 W/cm^2 at 640 nm or 50 W/cm^2 at 561 nm with 50-200 ms exposure time, until all fluorescence was bleached (typically 2000-8000 frames) according to (7). Samples were filled with ROXS blue buffer and sealed with Parafilm before being imaged.

Dynamic DNA origami measurements

Measurements of DNA origami were performed in ROXS Red buffer specified in Tab. 2.8, unless stated otherwise. Samples were scanned in the 561 nm channel to ensure proper density of DNA origami. After four fields of view were selected per sample 10 frames taken in the 561 nm channel for reference. Finally, 8000 frames were recorded in the 640 nm channel first with 193 W/cm^2 and then with 96.4 W/cm^2.

dSTORM

Samples were imaged in STORM buffer (Sec. 2.1.1) with 30-40 mM of MEA adjusted according emitter density by Jonas Euchner. The 647 nm CW laser line was used at 100% laser power, corresponding to 3.5 kW/cm^2. 405 nm illumination was exponentially increased to maintain a constant density of localisations suitable for SMLM. Optimal parameters were selected after preliminary imaging and inspection. The exposure time was between 30-100 ms, frame count between 1.0-8.0$\times$10^4 and 405 nm was increased exponentially until reaching 40 W/cm^2.

CoPS

Samples were imaged in a air-tight imaging chamber with ROXS Blue buffer specified in Tab. 2.8. An overview scan was performed with 15 kW/cm^2 peak laser power at 20 MHz with a 100 nm pixel size and 10 µs exposure. The molecular clusters were localised in ThunderSTORM, and their coordinates were transferred into SymPhoTime64 with a custom Python script. A point measurement was taken with a 640 nm pulsed excitation with an average of 6.25 kW/cm^2 set to 20 MHz. The length of the trace was changed depending on the experiment.

Live U2OS cell imaging

Cells were incubated for at least 30 min with the imaging media before imaging. For imaging media DMEM, RPMI-1640, or FluoroBrite (FB) were used. Certain samples had 100 µM AA or 100 µM AA and 20 mM HEPES.

Live T cell cell imaging

After staining cells were kept at 37° C before imaging. Cells were pipetted into chambers coated with poly-L-lysine and antibodies as outlined in Sec. 2.2.4. Cells were selected as they were depositing on the glass surface by brightfield microscopy. After selection the cells were imaged with 100 ms exposure at 9.1 W/cm^2 for either 8000 frames or stroboscopically via a custom µManager code for approximately 15 min at different intervals.

2.2.6 Image and data analysis

Gain calibration

For gain calibration image stacks were inspected in pairs of subsequent frames. The mean and variation of the frames were calculated frame-wide. The mean of these values was plotted. A linear regression with an offset was fitted via scipy.optimize.curve_fit weighted by the standard deviation of the values of the variances (96), unless otherwise specified.

Stability measurements and single particle tracking

Image stacks were analysed with the TrackMate plugin in Fiji (97) using the Difference of Gaussian (DoG) with 0.4 µm diameter, 5 initial quality filter and sub-pixel localisation. The traces were estimated using a Simple LAP tracker with 0.3 µm linking distance and 0.3 µm gap closing distance, with 5 frame gap closing. The localisations present from first frames were inspected. The frame-to-frame deviations of the localisation were used as an input for a fast Fourier transform (FFT) to generate the frequency space. Both of them were plotted in a double plot via matplotlib.pyplot.

For T cells the initial quality filter for the DoG was set to 50, the size to 0.4 nM and the sub-pixel localisation on. The LAP tracker was used with 0.4 µm linking distance, 0.4 µm gap closing with 5 frame gap closing, with merging and combining set to 0.8 µm.

SPAD dark count measurements

Different light conditions were explored by recording 30 s timetraces at 20 MHz. The laser on setting was a 640 nm pulsed excitation with an average of 6.25 kW/cm^2 set to 20 MHz. Three 30 s traces were recorded per condition.

Fluorescence Cross-Correlation Spectroscopy

Analysis of FCCS intensity traces was done via the SymPhoTime64 software between channels 2 and 3. The resulting $G(\tau)$ function was fitted as a single dye simple diffusion.

The data was then extracted as .txt files. The intensity as counts/s for the background correction were extracted via the read_ptu function in pycops. The χ^2 was calculated as:

$$\chi^2 = (1 + \frac{\langle b \rangle}{\langle f \rangle})^2 \tag{2.1}$$

With $\langle b \rangle$ being the average background rate and $\langle f \rangle$ being the count rate due to fluorescence, which is calculated by the formula $\langle f \rangle = \langle F \rangle - \langle b \rangle$, where $\langle F \rangle$ is the average count rate for the trace.

The corrected average number of molecules in the volume $\langle N_c \rangle$ is then calculated by :

$$\langle N_c \rangle = \langle N_u \rangle / \chi^2 \tag{2.2}$$

Where $\langle N_u \rangle$ is the uncorrected average number of molecules from the confocal volume. V_{eff} was calculated by dividing $\langle N_c \rangle$ by the concentration. The SymPhoTime software was also used to calculate the width and eccentricity of the confocal volume from a diffusion rate.

Fluorescence lifetime determination

Fluorescence lifetime was analysised by the dynamic CoPS traces via SymPhoTime64. The Lifetime Trace analysis was used and the traces were filtered to only include the data from during a binding event. The FLIM was fitted past the instrument response function (IRF), which on average was 0.34 ns. The data was then combined and plotted via a custom Python script.

Dynamic DNA origami Data

The localisation, filtering, drift-correction and rendering of dynamic binding of imager strands was performed in super-resolution microscopy analysis platform (SMAP) (98). The fit_fastsimple workflow was chosen with parameters determined in Sec. 3.2.2.2. As peak finder a difference of Gaussian of 1.2 and a dynamic factor of 1.5. A "PSF free" fitting algorithm was chosen with a asymmetry calculation. The localisations were drift corrected twice by dividing the image sequence in 11 and then in 12. Then the localisations were grouped within 35 nm if in subsequent frames.

The grouped data was then clustered by DBSCAN algorithm with 35 nm distance and at least three members per cluster via a Python script in the PynamicMeasurements library. Another custom Python script then registers the coordinates of the binding to the coordinates of the reference channel via a transformation matrix generated by MultiStackReg analysis of the maximum projection images of the two channels. These groups were then filtered if the average localisation of the cluster was more than 200 nm of a reference localisation. The numberInGroup of the kinetics data was then used as the bright times and the dark times was calculated by the time between groups. These reciprocal of these was taken as the rates per DNA origami.

Quantitative microscopy

Cell size and relative brightness

Relative brightness measurements were conducted on the maximum intensity projection of the image stack, followed by a Weka segmentation (99) of the cells based on the phalloidin stain. The size of the cell is determined by the generated mask, which is then used to isolate only the cell for further analysis. The intensities were calculated by using ThunderSTORM plugin in Fiji with the multiplication gain factor g set to 2.3 e^-/ADU and an offset of 187 ADU.

CoPS

The first 0.5-1.0$\times 10^7$ excitation cycles during CoPS acquisition were used to generate a histogram of mDEs (1 to 4 detection events). These histograms were then fitted to the analytical model described in Eq.1.13 to estimate the of number of emitters n and the probability of detection p. An additional background component was added as a single emitter with probability p_{bg} to account for out of focus fluorescence signal. The resulting equations are shown in Sec. 8.1.1. A Levenberg-Marquardt algorithm was used to fit the parameters to the observed probabilities (from unpublished work by Johan Hummert). Ten bootstrap cycles were applied to minimize the probability of outlier events. The results were filtered based on the results for p to eliminate failures to fit.

State inference for stepwise CoPS analysis

The counts are grouped a for 10 ms to give the brightness. The Steve Presse lab produced a Python script, which takes the brightness trace $\boldsymbol{x}_{1:N}$, where x_n is the brightness at time n, as input and outputs the state trace $\boldsymbol{b}_{1:N}$. This is done working inside of the Bayessian paradigm when taking into account the following parameters: fluorophore brightness μ_f, background brightness μ_b, the noiseσ^2, array of starting probabilities $\boldsymbol{\pi}_0$, and the state transition matrix $\boldsymbol{\pi}$. The state trace $\boldsymbol{b}_{1:N}$ is calculated by optimizing for the highest $\mathcal{P}\left(\boldsymbol{\Theta}\right)$:

$$\begin{aligned}\mathcal{P}(\boldsymbol{\Theta}) =& \mathcal{P}\left(\mu_f, \mu_b, \sigma^2, \boldsymbol{\pi}_0, \boldsymbol{\pi}\right) \\ =& \mathcal{P}(\mu_f)\,\mathcal{P}(\mu_b)\,\mathcal{P}\left(\sigma^2\right)\mathcal{P}(\boldsymbol{\pi}_0)\,\mathcal{P}(\boldsymbol{\pi})\end{aligned} \tag{2.3}$$

where the individual priors are given by

$$\mathcal{P}(\mu_f) = \textbf{Normal}\left(\mu_f; \alpha_{\mu_f}, \beta_{\mu_f}\right) \tag{2.4}$$

$$\mathcal{P}(\mu_b) = \textbf{Normal}\left(\mu_b; \alpha_{\mu_b}, \beta_{\mu_b}\right) \tag{2.5}$$

$$\mathcal{P}\left(\sigma^2\right) = \textbf{InvGamma}\left(\sigma^2; \alpha_{\sigma^2}, \beta_{\sigma^2}\right) \tag{2.6}$$

$$\mathcal{P}(\boldsymbol{\pi}_0) = \textbf{Dirichlet}\left(\boldsymbol{\pi}_0; \boldsymbol{\alpha}_0\right) \tag{2.7}$$

$$\mathcal{P}(\boldsymbol{\pi}_i) = \textbf{Dirichlet}\left(\boldsymbol{\pi}_i; \boldsymbol{\alpha}_i\right) \tag{2.8}$$

and where the α and β are hyperparameters- variables used in learning model training.

ELE

Effective labelling efficiency (ELE) analysis was performed as described by Thevathasan *et al.* (76). The orientation of the nuclear pore complex was fitted based on the observed localisation pattern. Each sector of a nuclear pore complex (NPC) with at least 2 localisation was deemed labelled. The degree of labelling was determined by a binomial distribution fitted to the number of labelled sectors for the NPC to the probability that best represents the observed distribution of up to 8 labelled sector.

quickPBSA

Quick-photobleaching step analysis (quickPBSA) was performed as described by Hummert *et al.* (7). Initially, a diffraction-limited molecular localisation is performed on a maximum intensity projection of the first five frames in ThunderSTORM. For each localisation, the intensity of the central region is determined as well as a background intensity for each frame. The two are subtracted and the resulting intensity trace is analysed to detect the final bleaching step. Certain traces are filtered based on the intensity of this step size, the rest are inspected going back and fitted with single photobleaching events. The filter is set around 60% of a manually observed bleaching step. The number of emitters is then determined by a Bayesian model, allowing for multiple emitter bleaching and blinking of fluorophores. The maximum bleaching events are set in the quickpbsa_analysis function and the input is atleast twice more than the maximum number of molecules expected.

ProDOL

Protein-tag degree of labelling (ProDOL) was performed as described by Tashev *et al.* (92). Multichannel recordings were performed in the reference and target channel for 10 frames. The average projection of these were taken before. A mask was generated by a "Triangle" thresholding algorithm in ImageJ. The localisation analysis was performed in ThunderSTORM. An affine transformation limited to 3 pixel shift, 5° rotation and 5% scaling was performed to register the two channels. A cut off T for the spatial mismatch was determined by inspecting random localisations, generated by rotating the target channel 90°, and maximizing the specific colocalisations to the random ones. After that, a density correction is performed to minimize the effects of false positive colocalisations and multiple detection events. The result is a corrected degree of labelling calculated in a cell-wide basis. See Fig. 5.2 for visual representation.

2.2.7 Statistical analysis

All statistical analysis was performed in the respective programming language for that analysis. The analysis of the ELE and dSTORM data, as well as ProDOL were performed in MATLAB. The gain analysis was performed in Java/Fiji, and all others were performed in Python. 3D leaf plots were performed made in GraphPadPrism. Linear regression and curve fitting was performed by the scipy.optimize.curve_fit function in Python (96). Statistical tests were done in Python, unless otherwise sepcified. For two sample comparative analysis t tests or Mann–Whitney U tests were performed based on the normality. Similarly, for multiple analysis ANOVA or Kruskal-Wallis tests were performed with an appropriate post hoc test. All results are quoted as the mean or median with their corresponding standard deviation (SD), standard error $(\mathrm{SE})_{mean}$, and confidence interval (CI). R^2 or p-value are shown where appropriate. Boxplots show the quartiles as well as the range of values of the sample.

Chapter 3

Design and construction of a single-photon correlation microscope

Author contributions:
J.H. created the initial designed of the microscope. S.A.T. and J.H. constructed the microscope. S.A.T. conceived and designed the supplementary 3D-printed components, while J.E. manufactured them. J.H. developed the original automated point picking code. S.A.T. expanded the code into the Pycromanager library. S.A.T. carried out the validation of the microscope setup. D-P.H., J.H. and J.E. supervised, and contributed with ideas and concepts.

3.1 Introduction

Using antibunching counting techniques, such as counting by photon statistics (CoPS), requires a highly specialised microscope system that has the ability to detect photon correlation and contains multiple single-photon sensitive detectors, as mentioned in Sec. 1.2.7. Not only that, but to build a robust histogram of multiple detection events (mDEs) the system requires a great number of picosecond laser pulses (91). This means that for the measurements to be performed in a reasonable time frame the single-photon detector and the picosecond pulsed laser must operate at the megahertz scale.

There are two main options for obtaining a microscope setup: building a system from modular components or purchasing a complete commercial system. There has been an increasing choice of modular systems (92, 100–102). These provide a cheaper option with a high degree of modification sometimes costing only a few thousand pounds (102). Modular microscopes offer added flexibility, however, but it can be difficult to integrate the multiple components both physically and in terms of software control. Another issue can be the collection of dust in open compartments. Modern fully commercial systems are fully enclosed and mostly fully automated. They also come with a beginner-friendly user interface (UI). Commercial systems can be quite bulky, and additional or replacement parts can be expensive.

Until only recently, photon correlation microscopy was constrained to only custom builds (91, 103). Thus, this project featured building a custom microscope setup, which has the ability to quickly gather antibunching data to facilitate live cell imaging. This task requires the understanding of the components and principles behind microscopy.

3.1.1 Fluorescence microscope anatomy

Microscopes are complex systems of a multitude of different components. Arguably the most important component of a microscope setup is the objective. When paired with the correct tube lens, the distance between the two is "infinity corrected", and allows for the addition of auxiliary components to the system with minimal aberration to the image. This allows for different filters to be placed in the light path (Fig. 3.1).

The first necessity in fluorescence microscopy is to separate the emitted light from the excitation light, which is much brighter (64). This can be done spectrally due to the Stokes shift (see Sec. 1.2.2). To separate the emission and excitation spatially in most modern microscopes a dichroic mirror is used, which reflects either one, while allowing the other one to pass through. Then, an emission filter blocking the excitation light's wavelength can be placed before the detection to remove its contribution. This provides images of the target against a black background. An excitation filter can also be added to narrow the excitation wavelength. The two filters and the dichroic mirror are often grouped in a cube formation inside most commercial systems, and in combination with the excitation source, define different spectral channels. The ability to spectrally separate differently labelled structures is one of the benefits of fluorescence microscopy.

Modern fluorescence microscope setups also have movable stages for lateral (XY) and axial (Z) movement, which allow for the accurate positioning of the region of interest (ROI) at the focus plane and aligned axially with the objective. In most cases, these stages are motorized for greater automation. These allow movement of the sample with a sub-micron step size. For single-molecule microscopes there is the need for stabilisation of the axial distance to the sample to maintain focus. Therefore, autofocus

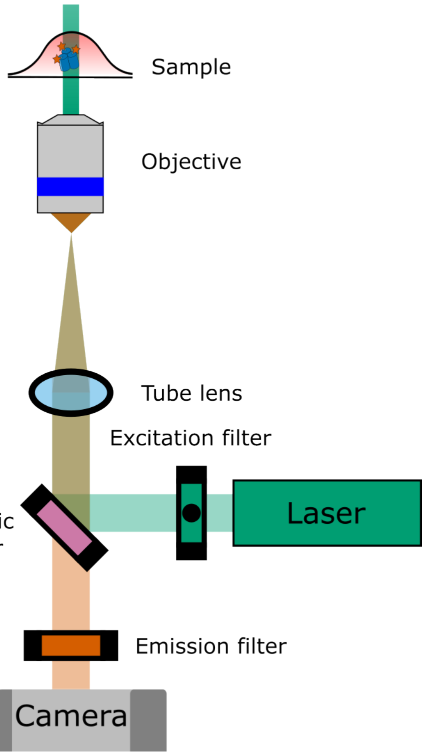

Fig. 3.1: Simplified model of a fluorescence microscope. Simple fluorescence microscopy setup featuring laser excitation (green) and a camera for the detection of fluorescence emission (orange). The two are separated by the dichroic mirror (pink) which separates reflects the excitation light and transmits the emission light. The two each has a filter to reduce the unwanted wavelengths.

stabilisation systems are needed to control the Z-axis stage. For lateral stabilisation, dampening tables are most often used, although certain super resolution setups have active dampening by movement dictated by fiducial markers in the sample (104). More important than these, however, is the combination of optical elements in the light paths of the excitation and emission. These can give rise to different modes of microscopy called microscope modalities.

3.1.2 Fluorescence microscope modalities

Each fluorescence microscope modality comes with specific benefits and limitations. One example of fluorescence microscope modality is the confocal microscope. In this imaging modality the excitation light enters the back aperture of the objective collimated and gets focused at a point in front of the objective (Fig. 3.2a) (64). The emission from that point gets collected by the same objective, but out of focus light gets blocked later in the system by a pinhole, which defines the confocal volume (105, 106). This allows for optical sectioning deep inside the sample. The axial component of the confocal volume is defined by the size of the pinhole. The ratio between the lateral and axial diameter of the confocal spot is called eccentricity. An example of the optical pathway of a confocal microscope is given in Fig. 3.11b.

The confocal volume can be measured in two different ways by Z-scanning or by fluorescence correlation spectroscopy (FCS) (107). FCS is a technique which can determine the number of molecules inside of the confocal volume. FCS is further discussed in Sec. 3.1.3.2. It can be used in a combination with a known concentration to calculate the volume. A more direct way to determine the confocal volume is via scanning a diffraction limited bead and fitting a 2-dimensional (2D) Gaussian over the intensity values of the orthogonal sections of each axis.

In confocal microscopy information only comes from the confocal spot generating only a point value. For an image to be created, the confocal spot needs to be moved across the sample, as in laser scanning confocal microscopes (LSCMs), or vice versa.

Despite the benefits of confocal, if simultaneous spatial information is required, a widefield microscope modality is required, in which large sections of the samples are imaged. This can be brightfield microscopy or it can be used with fluorescence techniques. Regular fluorescence widefield microscopy, also called epifluorescence, has the incident light focused by a tube lens at the back focal plane of the objective, which then collimates the excitation light, which in turn passes through the sample

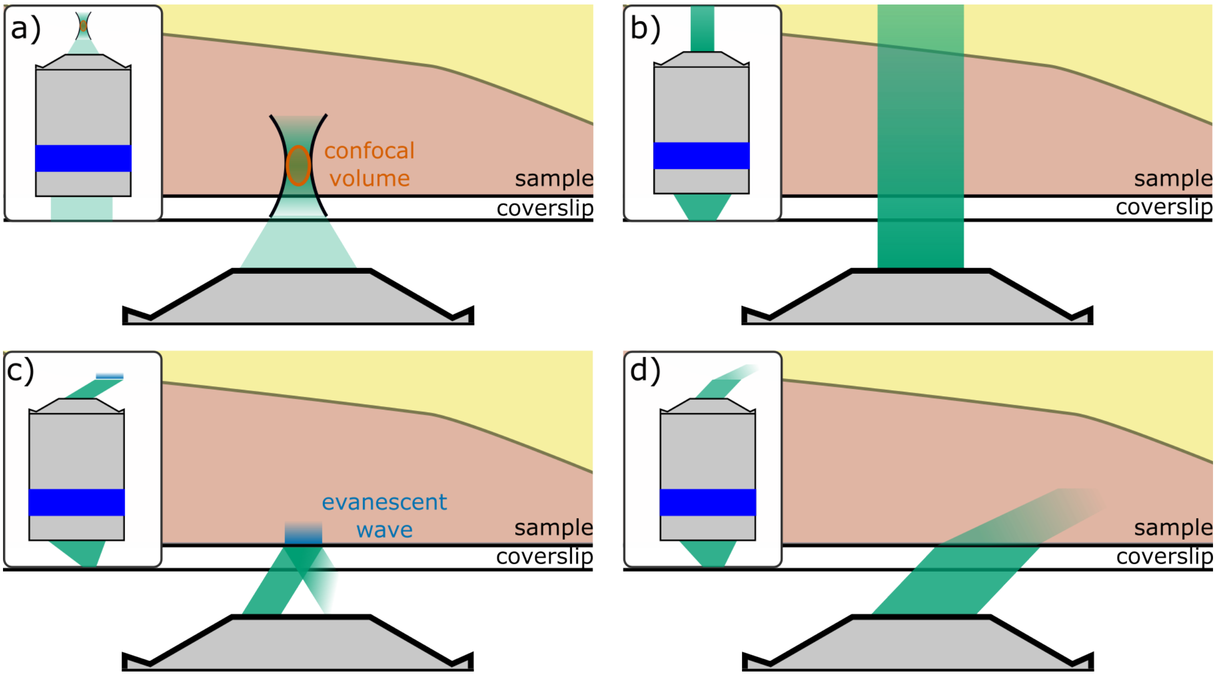

Fig. 3.2: Fluorescence microscopy modalities. Schematics of the illuminations modes of different microscopy modalities. a) Confocal microscope features a confocal volume (orange) which optically sections the sample. b) Epifluorescence microscopy passes a collimated beam through the sample. c) In total internal reflection fluorescence (TIRF) microscopes the excitation light hits the coverslip at an angle at which no light passes but generates an evanescent wave (blue). d) HILO microscopy generates a thin light beam across the field of view. The zoom out shows how the excitation beam enters the objective.

(Fig. 3.2b) (108). The emission gets collected from the focal plane of the objective, but some of the out of focus fluorescence gets collected as well. This can be problematic in single-molecule experiments. Signal-to-noise ratio (SNR) can be increased by limiting the excitation only to the wanted depth.

A preferred way of reducing out of focus light in single-molecule microscopy is using total internal reflection fluorescence (TIRF) microscopy (Fig. 3.2c) (72). In total internal reflection (TIR) the incident light hits the cover slip above the so called critical angle (θ_c). The critical angle is the angle at which point its refraction direction becomes parallel to the interface between the coverslip and the sample (109). The light excitation light itself does not pass through the coverslip, however, it generates an electromagnetic field called an evanescent wave. The evanescent wave decreases exponentially and excites less than 200 nm into the sample giving a much lower out of focus excitation, and thus lower background signal. TIRF is however, limited to the very bottom of the sample, and in cell samples it limits measurements to the basal plasma membrane. A technique combining the optical sectioning of TIRF and the ability of imaging into the sample has also been developed, called highly inclined and laminated optical sheet (HILO) (110) (Fig. 3.2d). Unfortunately this technique has the downside of unequal illumination across the field of view (FOV).

With the current level of technology CoPS is restricted to single-point detectors which are best utilised by confocal microscopy (see Sec. 3.1.3.2). However, the other modalities allow for a variety of microscopy techniques. They would greatly expand the capabilities of a microscope setup, and imaging an entire field of view (FOV) can help with the utility of the system. However, widefield imaging requires a multi-pixel camera that can detect small amounts of light and then amplify that signal (see Sec. 3.1.4).

3.1.3 Single photon sensitive detectors

3.1.3.1 Photomultiplier tube

Microscopes for antibunching microscopy techniques, such as CoPS, require a single photon sensitive detectors. Photomultiplier tubes (PMTs) were the preferred choice of detectors in early iterations of single photon sensitive microscopes (90, 111, 112). First patented in 1923 by Joseph Slepian (113, 114), multiplier tubes became valuable tools for single photon microscopy after the addition of a photocathode.

The photocathode releases electrons when struck with photons (115, 116). This is called the photoelectric effect, and the electrons that leave the photocathode - photoelectrons. It was discovered by Einstein in 1905 that this phenomenon is a quantum in nature and that a single incident photon transfers its energy to a single electron (117). The ratio between incident photons and photoelectrons is called quantum efficiency (QE) and is specific for wavelength λ. The QE is determined by the amount of incident light reflected and absorbed, as well as the probabilities of an electron to get excited and escape into the vacuum tube (116).

Inside a PMT, the photoelectrons collide with a series of electrodes, called dynodes, exponentially increasing the signal via generation of secondary electrons (118). The amplification of the photoelectron signal is called gain and PMTs have the ability to amplify the initial signal up to 10^8 times. However, PMTs have a relatively large size and a low QE in the red to far-red spectra (119).

3.1.3.2 Single-photon avalanche detector

With the developments of semi-conductors, solid state detectors were created with similar gain as PMTs. These detectors used reverse-biased p-n photodiodes to induce a multiplication of the signal (120) (Fig. 3.3a).

The reverse-bias results in the linear amplification of signal in avalanche photodiodes (APDs) (Fig. 3.3b). If the reverse bias voltage (V_A) is greater than the breakdown voltage (V_B), the photodiode's operation mode turns into Geiger-mode. In that mode a single photon can result in a single detection event, giving the name single-photon avalanche diode (SPAD) (119). The absorption of a photon in a SPAD, which is biased beyond V_B, results in a runaway process which increases the current greatly giving near infinite gain, if not for the space-charge effect (Fig. 3.3b i). This amplification, however, would damage the detector so a passive quenching system of resistors are

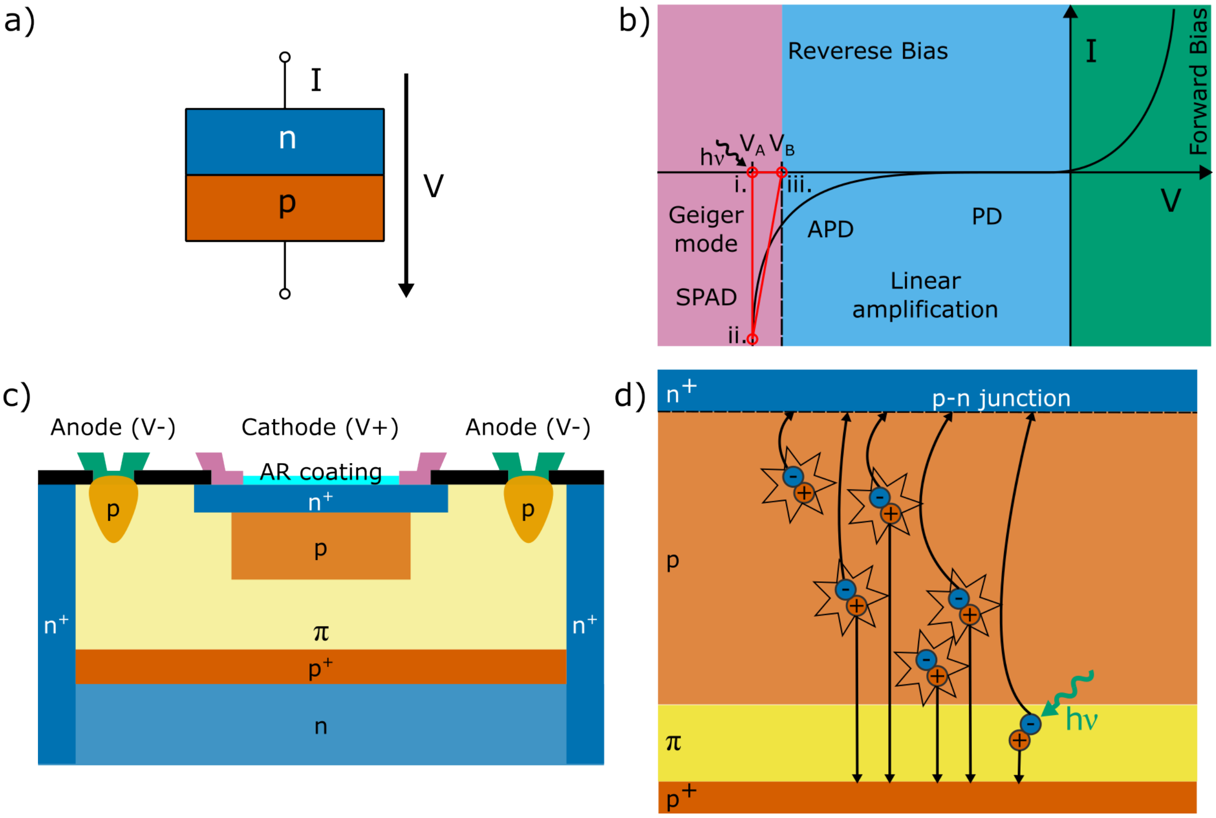

Fig. 3.3: Photodiodes and single-photon avalanche detectors. a) A schematic of a diode which is in a circuit with a voltage V and through which a current I passes. b) Graph of the current (I) in relation to the voltage (V). Forward (green) biasing allows current to pass easier. Reverse biasing allows for linear amplification (blue) and can be used in photodiodes (PDs) and avalanche photodiodes (APDs). When biasing beyond the breakdown voltage (V_B) the diode is in a Geiger mode (pink). SPADs are reverse biased beyond the V_B at a V_A. During the function of the SPAD (red) it accepts a photon allowing current to pass (i.), following quenching(ii.), and then a recharging (iii.). c) Illustrations of the general structure of SPADs. d) Mechanism of action of SPADs via an electron-hole pair generation avalanche.

used to decrease the voltage to V_B (Fig. 3.3b ii). The diode then needs to be recharge back to V_A (Fig. 3.3b iii). Thus, after the detection of a photon there is a dead time when no signal can be detected. The photon detection efficiency has been shown to increase with the increase in V_A (121, 122). However, with the increase in the voltage, the possibility that a charge carrier is generated increases and this could result in a photon independent dark count. The dark count rate also increases with temperature. The ability of SPADs to limit the dark counts comes from the structural differences from APDs. Both APDs and SPADs have a their p-element connected to the cathode, and the n-element to the anode (Fig. 3.3c). When a photon reaches their π layer they create electron-hole pairs, with each charge particle moving to their corresponding electrode.

The electrons passing through the p region generate additional charge particles by impact ionisation and leads to the avalanche of charge (Fig. 3.3d). In SPADs, this avalanche is diverging and self-sustained resulting in a detection event (123). SPADs have a thin π layer. This results in fewer dark counts and a quicker average response time than APDs (119). The sunk p-anodes act as guard-rings and can be used to control V_B.

One problem with SPADs is the ability of some charge carriers to get stuck in different energy levels, which can result in delayed avalanche triggering (124). This phenomenon is called afterpulsing and can result in time correlated signals meaning that this effect can be detrimental to methods like fluorescence correlation spectroscopy (FCS), which rely on the fluctiation of the signal.

Normally FCS is used to determine the kinetic rate of dynamic processes, as well as the average number of molecules inside of a certain volume. It utilises the differences in intensity fluctuations F from the mean between different time intervals τ to calculate the correlation $G(\tau)$ 3.1.

$$G(\tau) = \frac{\langle F(t)F(t+\tau)\rangle}{\langle F(t)\rangle^2} \tag{3.1}$$

Where t is different time points in an intensity trace and the angular brackets show the average of the components inside. For a simple one species diffusion, the value of $G(0)$ is inversely proportional to the number of molecules inside the confocal volume and the diffusion rate can be calculated from the average time spent in the confocal volume τ_D (Fig. 3.4a).

To perform FCS measurements the afterpulsing needs to be classified and then decoupled, or a fluorescence cross-correlation spectroscopy (FCCS) analysis between

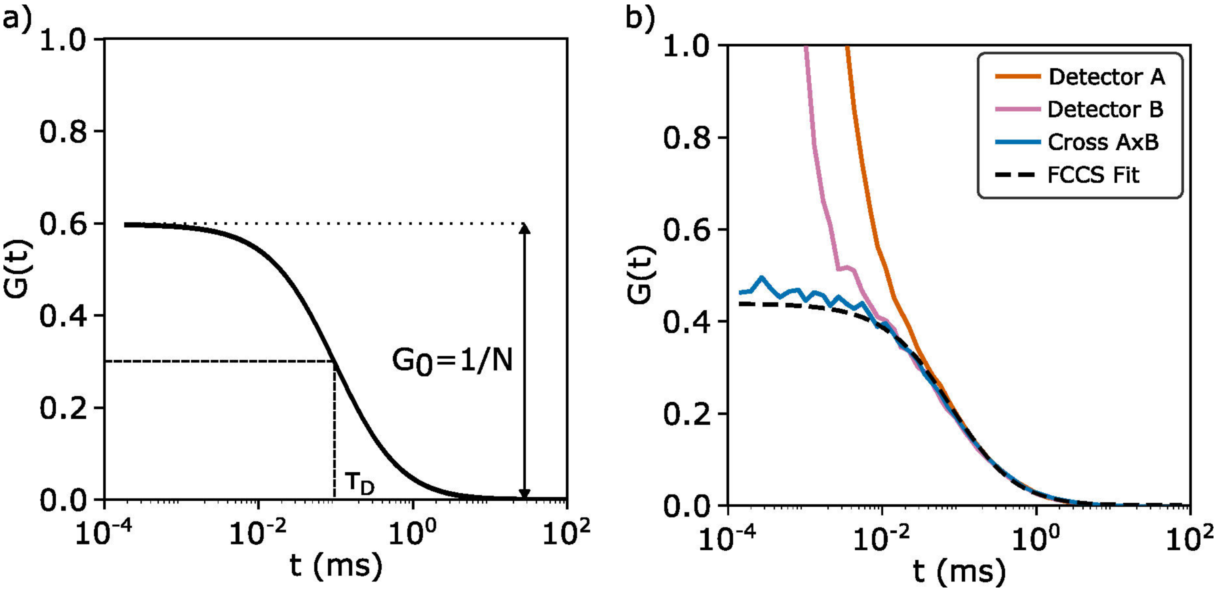

Fig. 3.4: Fluorescence correlation spectroscopy and afterpulsing. a) Representation correlation curve from a FCS analysis. The τ_D is the rate off diffusion while the $G(0)$ is inversely proportional to the number of fluorophores. b) Representative FCCS curve from a 1 nM Atto655 sample between two SPAD detectors.

two different detectors needs to be performed. In that case, the correlation is performed between the two detectors (A and B) and the formula changes to:

$$G(\tau) = \frac{\langle F_A(t) F_B(t+\tau) \rangle}{\langle F(t)_A F(t)_B \rangle} \tag{3.2}$$

The afterpulsing between two SPADs will not correlate, thus the effect should be diminished (Fig. 3.4b). An important characteristic of afterpulsing is that it increases with decreased temperature and with increased charge.

Historically SPADs have been a single point measurement, but recently there have been significant developments in arranging individual SPADs into arrays. These come in different shapes and sizes (125).

One problem inherent to SPAD arrays is crosstalk between two neighbouring detectors, resulting from secondary photons emitted from the charge carriers flowing through a triggered pixel, resulting in an avalanche in another (126). To fix that the individual SPADs are placed further apart, however, this lowers the fill factor (FF) of the chip - the percentage area that detects light. To fix these micro-lens arrays can be used to focus the light (125). Individual SPADs in the array can also malfunction giving higher or lower counts resulting into cold and hot pixels, respectively. These pixels are typically disabled.

Another problem is the large amount of digital data derived from larger arrays. This is because according to the Nyquist-Shannon criterion to gain the complete spatial information of a point it requires for that point to be sampled at least twice (127, 128), which means for a sufficient FOV with a diffraction limited resolution a large array of pixels is required to image tens of microns. Different manufacturers have dealt with that in a variety of ways. Some change between two modes, pixel-by-pixel or frame-wide, for low counts or high counts, respectively. Modern large SPAD arrays come with on-chip processing to decrease the amount of data output. However, for photon antibunching SPAD arrays are not yet appropriate. This is due to the low photon detection efficiency (PDE), resulting from the product of the FF and the QE, and the low frame rate for large detectors ($\sim 10^5$ fps). This means for most samples single-point detection would be better for antibunching measurements.

3.1.3.3 FLIM and instrument response

The fluorescent lifetime can be measured by a time-correlated single photon counting system (TCSPCS) using SPADs and a picosecond pulsed laser (Fig. 3.5a). However, every detection system will have its own instrument response function (IRF) (Fig. 3.5b). This will include multiple components, e.g. the laser pulse duration, photon travel time, propagation delay in electronics, etc. Fluorescence lifetime (FLT) measurements will result in a convolution between the ground truth and the IRF (Fig. 3.5c). The lifetime can be extracted by deconvolution with a reference measurement or by taking the latter part of the recorded lifetime after the influence of the IRF.

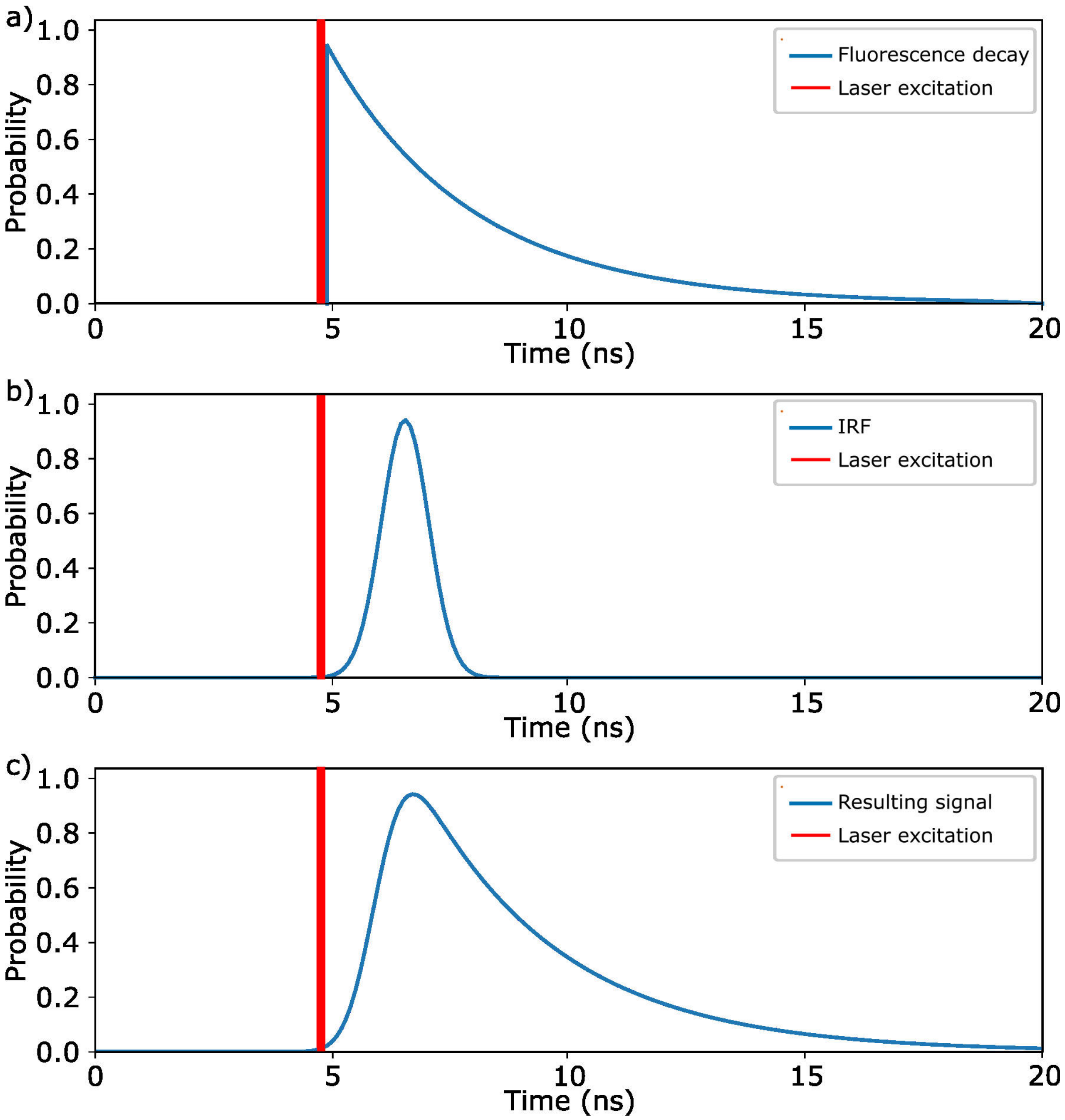

Fig. 3.5: Fluorescence lifetime and instrument response function. Mockup of a fluorescence lifetime function (a) and an instrument response function (IRF) (b). In actual measurements the interaction between the two define the result (c). The signals are shown in blue while the laser excitation is shown in red.

3.1.4 Microscope cameras

Microscope setups require highly sensitive cameras for single molecule imaging. As already mentioned previously, SPAD arrays are still in their infancy with plenty of problems needed to be solved before becoming viable for most samples or techniques. This leaves us with two types of cameras defined by their detectors - complementary metal–oxide–semiconductor (CMOS) or charge-coupled device (CCD).

In CCD cameras during exposure photoelectrons fill capacity wells on the sensor area and then are shifted down one row at a time until the row reaches the serial register (Fig. 3.6 left) (129).

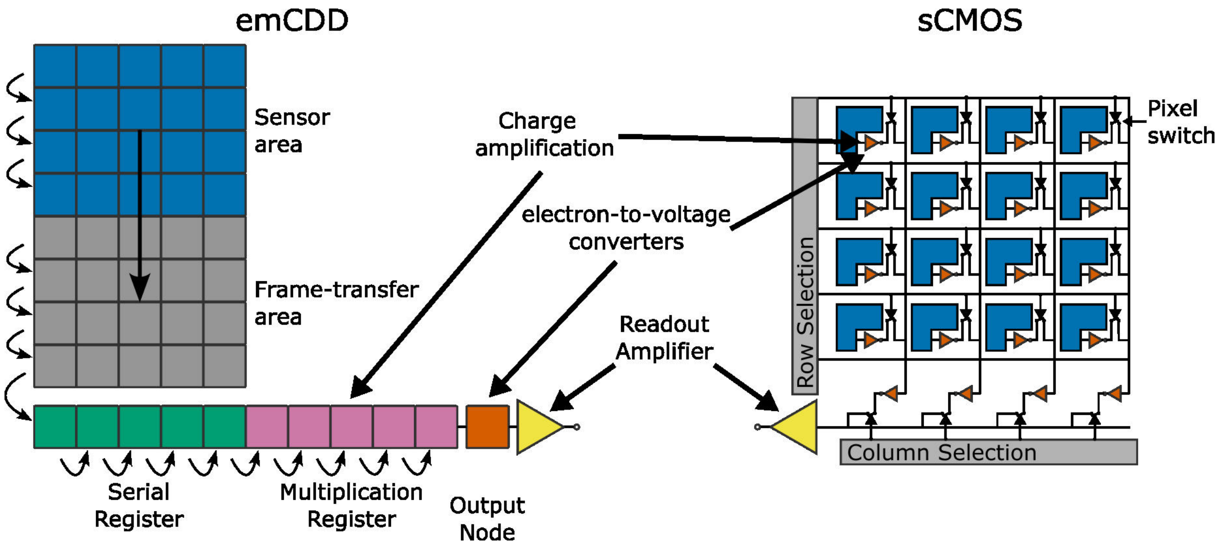

Fig. 3.6: Microscopy camera options. Schematics of the two types of camera chips commercially available- emCCD (left), and CMOS (right). The light detecting parts which define the pixel intensity are in blue, while the electron-to-voltage converters and the readout amplifiers are in orange and yellow, respectively.

These wells, however, can get overfilled and this can result in CCD blooming, in which the charge gets leaks up and down the column resulting in streaks. CCD cameras have a high QE (> 80%). Some CCD chips have the ability to frame-transfer the data to another opaque region which serves to store the charge while the sensor are recording new information information (130). The opaque area is then read out independently.

This, in combination with limiting the number of rows read out, is used to increases the rate of acquisition. The sensitivity on the camera can be increased by the addition of a multiplication register resulting in an electron-multiplying charge-coupled device (emCCD). Moving through the multiplication register results in an exponential increase of the signal with each step. The increase can be regulated with the change of voltage and is described by the multiplication gain factor g set in software. The electrons are then converted to voltage and this voltage gets a final multiplication by a readout amplifier. Finally, the readout is transformed by an analog-to-digital converter (ADC) before giving the data to a computer, which receives the signal as analog-to-digital units (ADU).

CMOS cameras have a readout amplifier and an ADC (131) (Fig. 3.6). However, in CMOS cameras each pixel independently generates photoelectrons, amplifies the charge and then transforms them into a voltage (132). This allows for faster acquisition rates and, in turn, allows for larger pixel arrays. Which rows or columns of pixels is read out can be selected as well, adding some flexibility to the measurement.

New developments have given rise to scientific complementary metal–oxide–semiconductor (sCMOS) cameras. These include the use of photodiodes (PDs) for photon detection, as well as optimisation of the electronics, which increase the PDE and lower the noise. This results in sCMOS cameras having a higher SNR than emCCDs in higher photon counts (133). However, in signal below 100 photons the emCCD proves to be superior. This is due to the low FF in sCMOS cameras, resulting from the fact that some of the circuitry takes a part of the light detecting region, as well as the low QE (<70%). sCMOS cameras, also require a thorough gain calibration due to differences in pixels, called fixed pattern noise (σ_F), while CCD cameras calibration can be done for the entire chip. There is also the dark current noise σ_D, which is a thermal phenomenon in which electrons are generated inside the chip of the camera. In emCCD cameras this would lower significantly the SNR, as it would be amplified before readout. For that reason, modern emCCD cameras are cooled below -70 ° C, which reduces the dark count noise to a negligible amount (134). Gain calibration can be performed by a mean-variance relationships (135). The total noise of a camera σ is calculated by Eq. 3.3 from the readout noise σ_R and the shot noise σ_S, which comes from quantum nature of the emission of light and the detection (Fig. 3.7), as well as the dark current noise which arises due to heat.

$$\sigma^2 = \sigma_R^2 + \sigma_S^2 \tag{3.3}$$

The shot noise is known to increase with the intensity of the signal, while the readout noise is generated from electronic conversion and is temperature dependent. The shot noise follows a Poisson distribution meaning that the variance σ_S^2 correlates with the mean signal $\langle S \rangle$. The ratio between the two gives the ADU conversion factor ϕ:

$$\phi = \frac{\langle S \rangle}{\sigma_S^2} \tag{3.4}$$

ϕ is measured in photoelectrons/ADU (e$^-$/ADU) and can be calculated by using the reciprical of the slope of the total noise (Fig. 3.7). The quantum efficiency for the wavelength can also be used for further correction.

For CMOS cameras the gain equals ϕ, but in emCCD cameras the total system gain also includes the multiplication gain factor g and can be calculated by (129):

$$\text{gain} = \frac{\phi}{g} \tag{3.5}$$

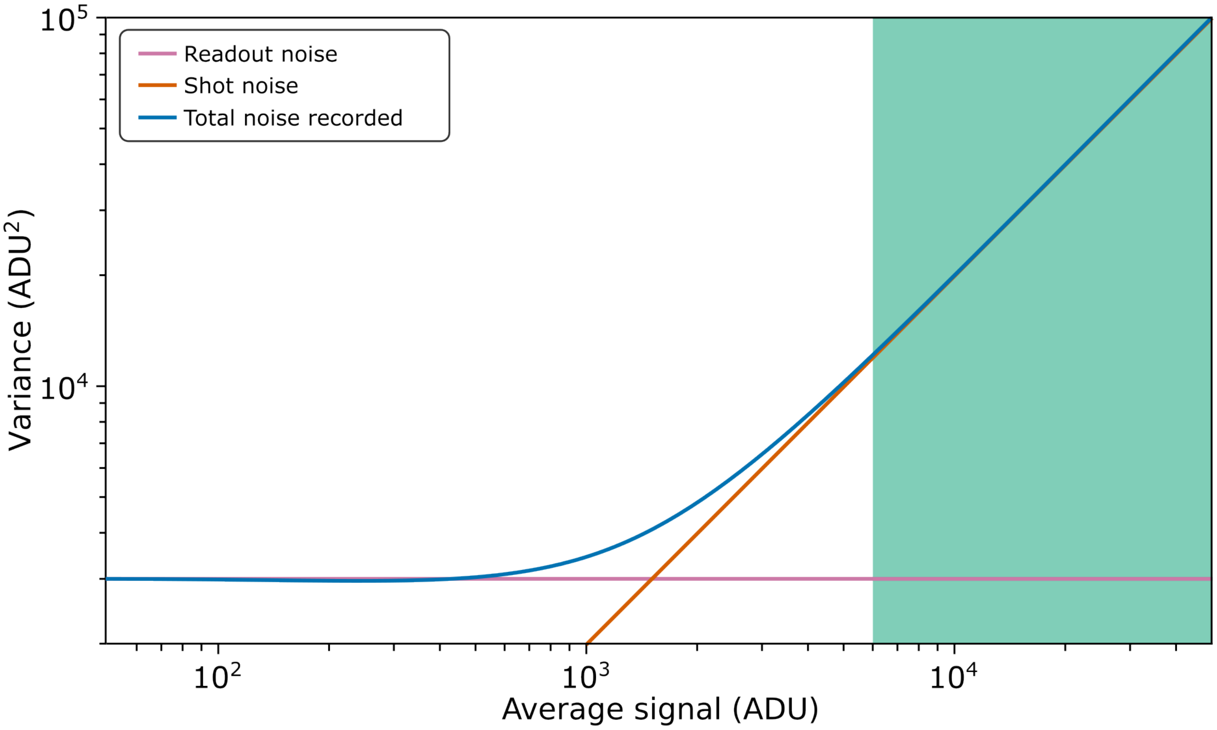

Fig. 3.7: Gain calibration. Simplified schematic of the mean-variance relationship found in cameras. Modified from (135). The conversion factor ϕ is calculated by the inverse of the slope of the total recorded noise (blue) in the linear area (green), resulting from the addition of the readout noise (pink) and the shot noise (orange).

Meaning that the for higher g the ADU values corresponds to less photoelectrons.

To optimise the system for low signal experiments we will proceed with an emCCD detector with the caveat that in the future a sCMOS camera might be more appropriate.

3.1.5 Microscopy technique validation

3.1.5.1 Quantitative microscopy standards

Once built, a microscope the techniques performed on it require validation. On way is to validate the measurements via molecular standards labelled with a known stoichiometry (60). These can vary in range from small DNA oligomers labelled with fluorescent molecules to large molecular complexes such as the nuclear pore complex (3.8). For high molecular counting even viral particles could be used as standards. Protein complex standards have the benefit of being used in a cellular context. These are very limited in

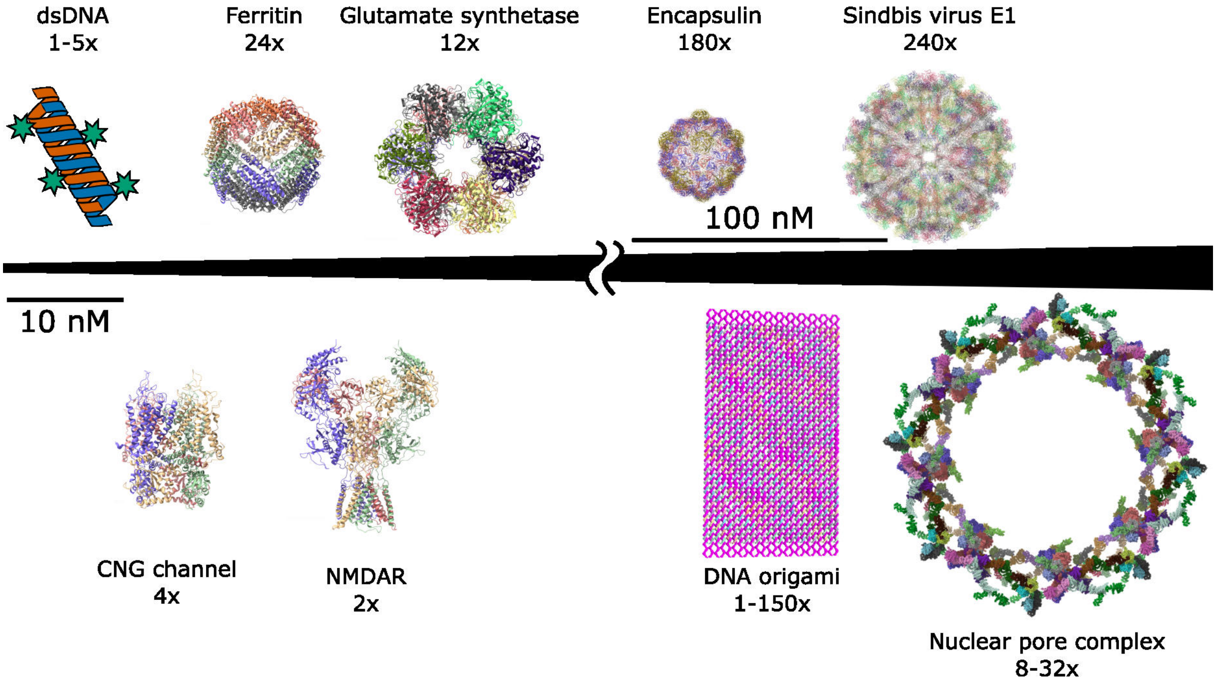

Fig. 3.8: Molecular counting standards. Standards used for molecular counting arranged from smallest to largest with their stoichiometries specified below their names. All structures except the double-stranded DNA (dsDNA) were all rendered in ChimeraX. Structures are coloured based on amino acid chains or DNA strands. Protein structures were structures with accession numbers 5iou (NMDAR), 5h3o (CNG), 1fpy (Glutamine synthetase), 1eum (Ferritin), 4pt2 (Encapsulin), 3j0f (Sindbis virus), 5a9q (Nuclear pore complex) taken from PDB. The DNA origami structure was generated via the Aksimantiev group online tool (https://bionano.physics.illinois.edu/cadnano2pdb) using the sequence file of the origami. Figure adapted from Grussmayer, *et al.* 2019 (60).

range and very few complexes have been found to have a consistent stoichiometry. DNA origami on the other hand are artificial constructs, which use DNA oligomers, called staple strands, to bind and bend a circular DNA into almost any shape wanted (136). This provides programmability as well as flexibility. For fluorescent labelling the only requirement is substituting some of the staple strands with either labelled imager strands or with docking strands that extend as single-stranded sections from the nanostructure and provides sites for imager strand binding.

3.1.5.2 Cross validation via photobleaching step analysis

Another way to validate a technique or an instrument is via an independent experimental technique. For CoPS, cross validation can be done via another molecular counting technique. One such technique is photobleaching step analysis (PBSA), a version of which was developed by Hummert, *et al.* in 2010 and was part of this project (7). This extracts the traces from diffraction limit clusters and a doughnut shape is drawn around each localisation (Fig. 3.9). The intensity of the bleaching and the background are extracted from the mean intensities of the centre and doughnut, respectively and a corrected intensity trace is generated by subtracting the latter. The photobleaching steps are then fitted to that trace by using Bayesian statistics. The fluorophore number is given by counting back the steps for each cluster.

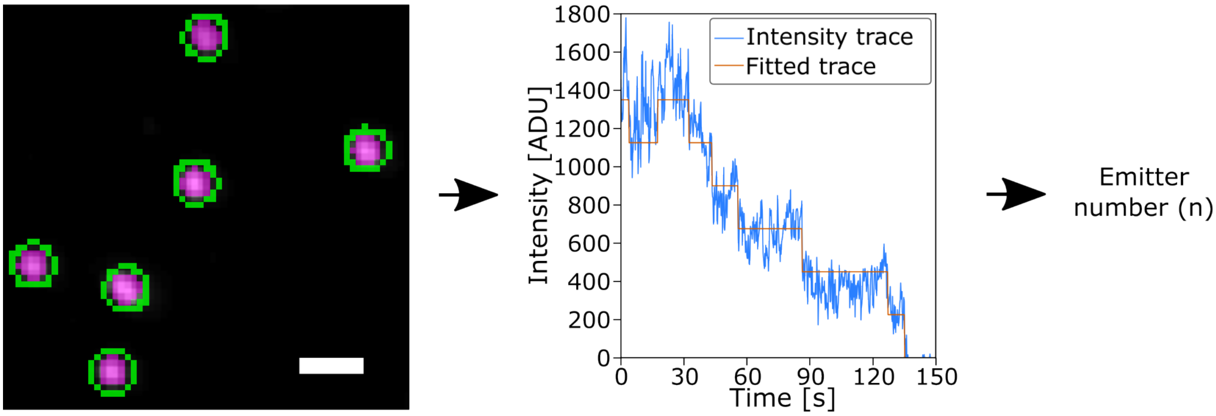

Fig. 3.9: Photobleaching step analysis pipeline. Simplified pipeline of the photobleaching step analysis. The localisation of the single point images are used to define an area of interest (magenta) and an area for background. The intensity traces of the means values of pixels inside both are taken and then the background is subtracted. Photobleaching steps are then determined. The number of molecules n are determined by counting back the steps. More detailed information in Chap. 2.

3.2 Results

3.2.1 Microscope design and construction

For the purposes of performing CoPS there was no complete commercial anti-bunching LSCM options at the start of this project. However, the automation and the presence of multiple additional features, directed us to use a commercial microscope body. The inverted Nikon Ti-E body was chosen due to its three light port (including an eye-piece) options and its integrated autofocus system (Fig. 3.10). The former allows us to have both a confocal and a widefield system, while the latter allows for long acquisition experiments without the need to refocus. The setup also requires lateral stabilisation, which in most systems are performed by dampening tables. Our setup includes a 180 cm×120 cm Newport RS-2000 passive dampened table with pneumatic vibration insulator legs PL-2000. An additional stabilisation by active dampening or piezo motors was deemed unnecessary and too expensive for the purposes of this project.

The microscope was also equipped with a Märzhäuser XY-stage, as well as a Nikon Z-stage. The Nikon tube lens inside the body has a focal length of 200 mm and requires a Nikon microscope objective for the magnification specified on the latter to be correct. For our purposes we require a high NA objective to obtain high resolution (Eq. 1.8). The CFI Apo TIRF 100× oil-immersion objective gives the wanted specifications as corrections ensuring consistent illumination across the field of view (FOV). For that objective the PSF of the widefield path will have a radius of the full width at half maximum (FWHM) calculated by Eq. 1.9. R_{FWHM} results in:

$$R_{\text{FWHM}} = 0.51 \frac{450\,nm}{1.49} \approx 154\,nm \tag{3.6}$$

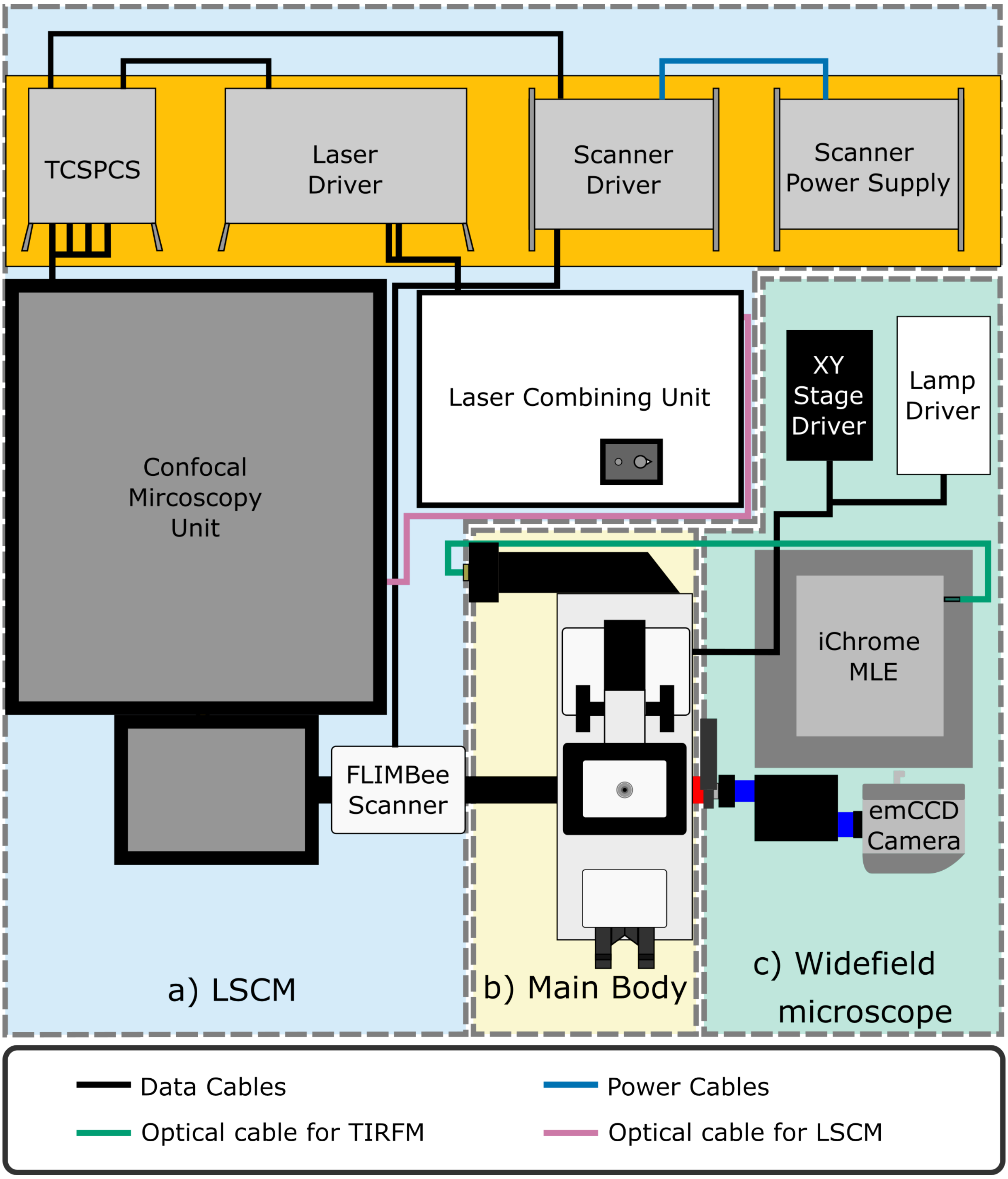

Fig. 3.10: Microscope setup. Schematic of the dual purpose - LSCM and a widefield microscope. Main microscope body (yellow) which combined the LSCM and widefield microscope via the left and right light ports, respectively. LSCM system (blue) included the laser combining unit, the FLIMBee scanner and the corresponding drivers and power supplies, as well as the optical path inside the confocal microscopy unit. All confocal elements were synchronised by the TCSPCS. Light from the laser combining unit (LCU) to the confocal microscope unit via a single mode optical fibre (pink). The widefield part of the setup (green) contained the iChrome MLE which is connected to the body by a single mode fibre (green). The emission passes through a filter wheel and an Optosplit before being detected by an iXon Ultra 897 emCCD camera. Data cables and power cables between components are shown in black and blue, respectively. Cables connecting to the operating computer and direct power supply cables are not shown. The red component was 3D printed from plastic.

And to get all of the spatial information we need to sample according to the Nyquist-Shannon criterion:

$$\text{Optimal pixel size} = \frac{450\ nm}{2 \times 1.49} \approx 151\ nm/pixel \tag{3.7}$$

Meaning that the final pixel size needs to be below 151 nm if we want to be diffraction limited for the entirety of the spectrum.

The left port of the objective led to the LSCM pathway, which has the single-photon capability. PicoQuant was selected as the main supplier of components in the antibunching setup, as they provide them together with software integration. This included the FLIMBee scanner, the laser combining unit (LCU), containing the picosecond pulsed laser (PSPL), and the confocal microscopy unit housing most of the optical components and the SPADs. The confocal microscopy unit was enclosed by a custom made optical enclosure. This together with a 3D printed skirt sitting beneath the stage (Fig. SI 3c) resulted in an almost complete optical insulation. These components required integration and time stamping of the detection events, which is performed by the HydraHarp time-correlated single photon counting system (TCSPCS). The TCSPCS received signals from the SPADs, the PDL 828 Sepia II laser driver and the scanner driver. Information is communicated between the TCSPCS and the SymPhoTime64 software. The right port of the main body led to the emCCD camera for widefield imaging. The widefield setup also included the iChrome multi-laser engine (MLE), the driver for the lamp on the illumination column, and microcontroller which serve for triggering the laser. More details given in the next chapters.

3.2.1.1 Confocal microscope

CoPS requires excitation by picosecond pulsed lasers (PSPLs) controlled by the TC-SPCS. In our setup they are housed in the LCU, containing three PSPL: 470 nm (P-C-470, PicoQuant), 532 nm (P-FA-530XL, PicoQuant) and a 640 nm (P-C-640B, PicoQuant), each with their own thin band pass filter only permitting that specific wavelength. (Fig. 3.11a). The LCU which features a neutral density (ND) filters, which block a portion of the light that passes through it regardless of wavelength, thus tuning the excitation power. The laser light is directed by dichroic mirrors (DMs), as well as small optical glass windows allowing for fine tuning the lasers' path.

The laser light is taken from the LCU to the confocal microscopy unit via a single-mode optical fibre with a coupler on each side. To ensure the homogeneous excitation of the fluorophores at a different dipole angle inside the confocal volume the laser light was initially filtered by polarisation, and then its polarisation was circularised by a quarter-wave (λ/4) plate. The excitation light is then directed to the FLIMBee scanner by a bandpass dichroic mirror (z532/640, CHROMA). The mirror is on a switchable mount if other wavelengths are needed. Inside the laser scanner three galvo mirrors change the position of both the excitation and emission light. From the perspective of the excitation light the scan lens focuses the laser at the different position in the intermediate plane, and therefore the illumination light at the imaging plane.

From the emission light point of view, the light is collected from the objective at the imaging plane and is collimated by the objective (Fig. 3.11b). The tube lens then focuses that light creating an image at its focal plane, which is called the intermediate image plane. The scanner lens picks up the light from anywhere within the intermediate image

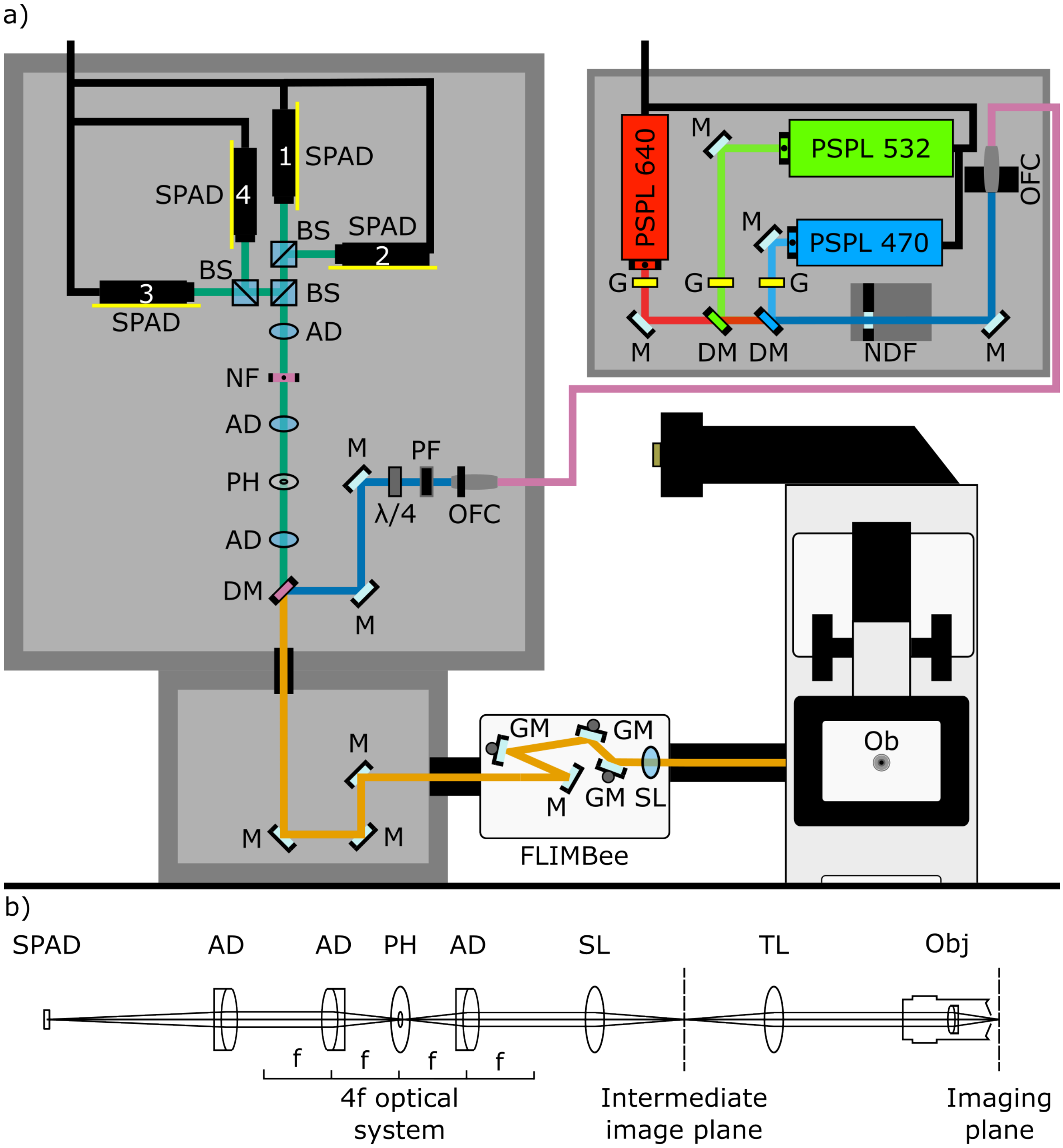

Fig. 3.11: LSCM pathway. a) Schematic of the LSCM pathway. The LCU contains three picosecond pulsed lasers (PSPL). The lasers are guided into an optical fibre coupler (OFC) by mirrors (M), dichroic mirrors (DM) and optical windows (G). The lasers are modulated by a neutral density filter (NDF) wheel before being put through an optical fibre coupler. The light coming out of the single mode optical fibre (pink) is then filtered with a polarisation filter PF and circularised by a $\lambda/4$ plate ($\lambda/4$). The excitation (blue) and emission (green) pathways are divided by a DM. Inside the FLIMBee three galvo mirrors (GM) and a scanning lens (SL) are used to change the incidence angle of the light for both pathways (orange). The emission passes through a 4f system made from two achromatic doublets (AD) with a pinhole in the middle before being focused and split into the four SPADs by 50:50 beam splitters (BS). Laser lines are coloured based on wavelength and the SPADs have the number of the channel written on them. b) Simplified model of the optical assembly of the detection system. The emission is collected from the image plane by the objective (Obj) before the tube lens (TL) creats an image of the emission into the intermediate image plane. This is then scanned by the scan lens (SL) which collimates the light before the 4f system. The lenses of the 4f system focuses the light coming from the image plane through the pinhole, and then collimates it again. The signal is then focused onto the SPADs.

plane and then collimates it. If aligned properly the emission signal should match the pathway of the excitation laser. The emission is transmitted by the dichroic and enters a

4f system. A 4f system is an optical relay that usually consists of two positive lenses and represents a cascade of two Fourier transforms (137). The magnification is found to be equal to $-\frac{f_2}{f_1}$ where f_2 and f_1 is the focal lengths of the lenses. If both are equal the resulting image is an inverted replica of the input. In confocal microscopes a pinhole is used to restrict the out of focus light. In our case, we have two 75 mm achromatic doublets with a 50 µm pinhole in between.

Despite the dichroic mirror reflecting about 95% of the laser light away from the detectors, the remainder is high enough to damage the SPAD. Notch filters have a high attenuation factor for a really thin band. Our setup requires blocking of all three wavelengths, for that we use a 640/532 and a 470 notch filters in the same mount. Light is finally focused by a 200 mm doublet and split by four 50:50 beamsplitters between four SPADs. The SPADs are positioned equidistant in relation to the doublet and each is mounted on a three-axis manual stages for alignment together with a copper heat sink to prevent additional dark counts due to increases in heat during acquisition.

3.2.1.2 Widefield microscope

Widefield microscopes require strong continuous wave (CW) lasers for the illumination of the larger surface area. The iChrome MLE provides an enclosed small footprint option with multiple choice of laser lines. For our system we have chosen three diode lasers - 640 nm, 488 nm and 405 nm, as well as a diode-pumped solid-state (DPSS) 561 nm laser (Fig. 3.12).

DPSS lasers take time to fully charge, thus it is always emitting and requires modulation by an acousto-optic modulator (AOM), which acts as a shutter or modulator of intensity.

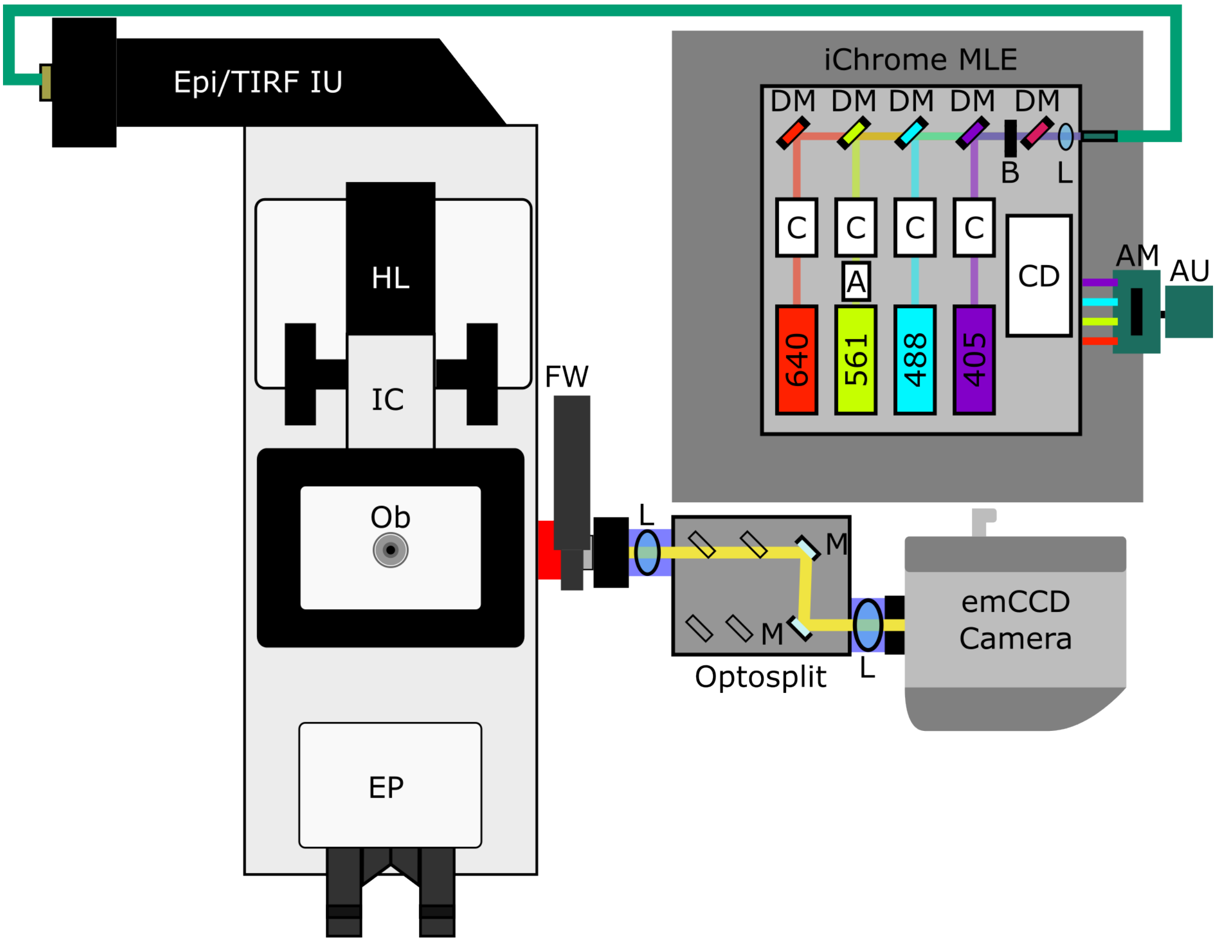

Fig. 3.12: Widefield system. The Widefield setup contains the iChrome MLE, which houses four CW lasers in a single box. These lasers are auto aligned by the COOL^{AC} sytem containing the alignment elements (C) and the detector (CD). The 561 nm laser has an additional acousto-optic modulator (A). The lasers' light is focused by a lens (L) into a single-mode fibre to which is coupled into the Epi/TIRF illumination unit (IU). The light is send by a dichroic mirror to the objective. The right exit port is used to send emission light (yellow) to the filter wheel. The emission is then collected by a lens (L) and then passed through a set of mirrors (M). Dichroic mirrors can be arranged in the place of the empty boxes to optically split the image into multiple channels and then another lens would focus those on different sections of the camera. In this work, only two ordinary mirrors were used to direct the signal into an emCCD camera. The camera and lasers can be synchronised by the use of Arduino Uno (AU) and Arduino Mega (AM) microcontrollers. The system also has an illumination column (IC) equipped with a halogen lamp (HL) and eyepieces (EP) allowing for examination of the sample prior to fluorescence illumination. Laser lines and corresponding cables coloured based on wavelength.

These wavelengths would allow us to cover most fluorophores in the visible spectrum. The laser light is then directed by dichroic mirror (DM), which have variable transmission based on the wavelength of the light to a lens, which leads to a single-mode optical fibre. A lens at the exit of the The MLE also has a the COOL^{AC} system which uses alignment elements and a detector to align the lasers into the fibre coupler. This can be done in three ways. Internal with a flip mirror (FM), external by inserting the other end of the optical fibre back into the body, or by the signal from an external power meter.

The optical fibre is coupled into the Epi/TIRF illumination unit illumination unit (IU) of the Nikon Ti-E body. This component has adjustment knobs which can change the angle with which the laser light enters the objective giving the ability to change between epifluorescence, HILO and TIRF. The IU also features multiple neutral density (ND) filters. Inside of the Nikon body the light gets directed up to the objective by a quadruple bandpass dichroic (ZET405/488/561/640), which only reflects the excitation wavelength. The emission passes through it and gets directed with a mirror to the right port. The emission is then passes through a ThorLabs FW102C filter wheel, tuned on one of four emission mirrors: 525/50 nm, 605/70 nm, and 690/70 nm. Emission filters are required to remove any unwanted signal from the remnants of the laser light and unspecific fluorescence. This adds an additional length to the optical pathway, which needed to be offset by a shorter camera adaptor, which was 3D modelled and printed (Fig. SI 3a). The emission then passes through an OptoSplit II, which has the ability to split the light into multiple channels allowing for parallel multiplexing imaging. That is done by the addition of DMs inside a 4f system to split the emission, however, this is not present in this work. Finally, the second lens of the OptoSplit focuses the image into the sensor of an iXon Ultra 897 emCCD camera.

3.2.1.3 Microscope control and automation

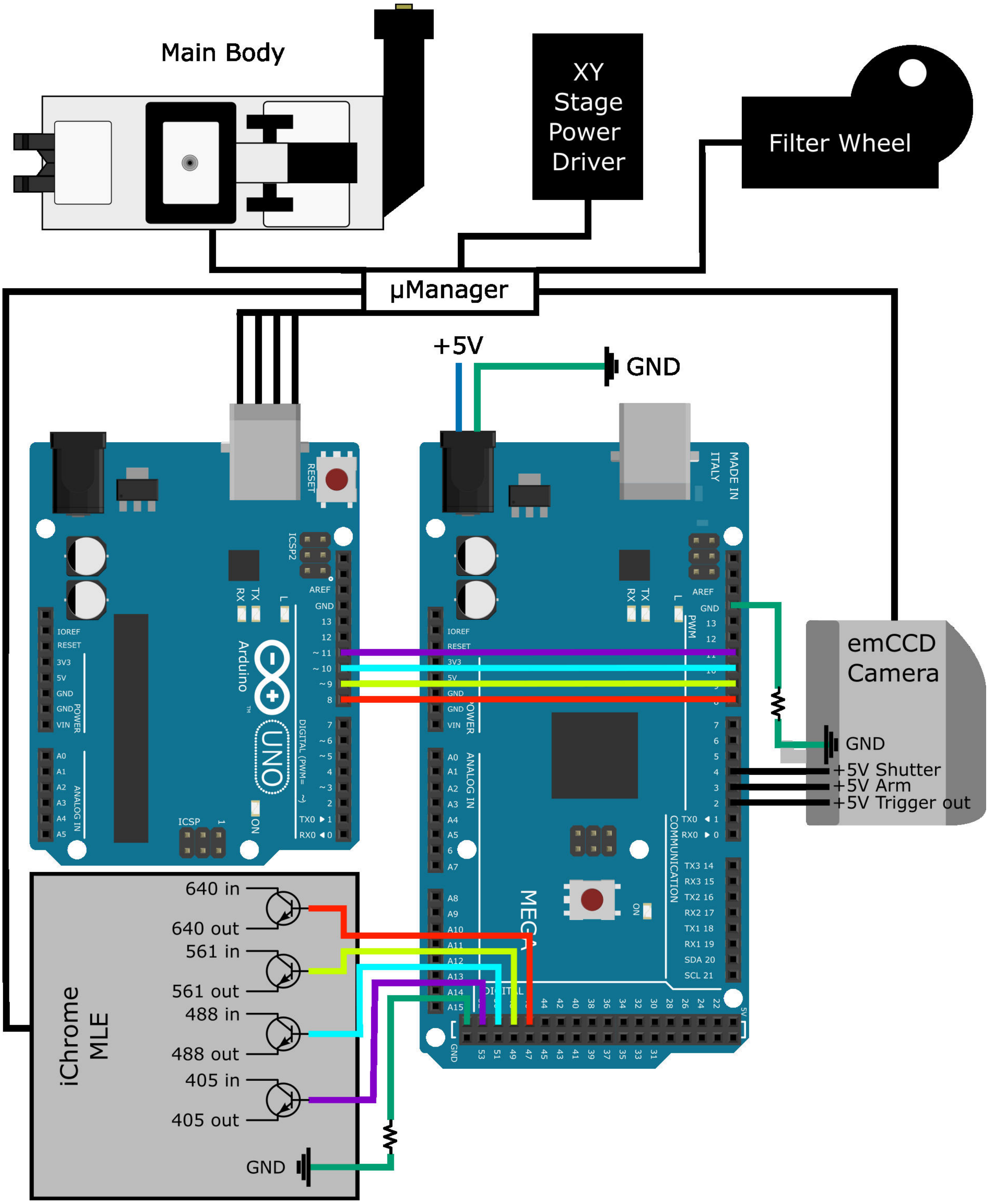

Fig. 3.13: µManager configuration. The body, camera, stages, filter wheel and camera were controlled by the µManager software. µManager also controled an Arduino Uno, which conveyed signals to an Arduino Mega, which communicated between the multi-laser engine and the camera. Power supply cables and data cables are shown in the dark blue and black, respectively. Cables responsible for triggering lasers are coloured based on the corresponding wavelength. Green cables connect grounds (GND) between components and have a pulldown resistor.

As mentioned before, despite individual parts having software, custom microscope setups require third party automation software to combine all components of the setup. Simpler microscopy setups could be controlled by a custom in-house written code via direct port manipulation. However, the added flexibility does not justify the time investment. Fortunately in the last 20 years open source microscopy software options have become available (94, 138). In our setup µManager was used to control the main body with the XY- and Z-stages, the filter wheel, the camera and the MLE (Fig. 3.13). To decrease the bleaching and phototoxicity the MLE can be triggered by the camera, or vice versa, to limit illumination only during exposure time. Communication of these was established via an Arduino Uno microcontroller transmitting signals from µManager about which laser should be triggered to an Arduino Mega. That microcontroller then communicated with the camera and the multi-laser engine about when the laser should be on (trigger out) or a frame should be triggered (shutter). This allowed acquisitions to be specified via custom µManager scripts.

Unfortunately, the components of the LSCM do not have a plug-in µManager and can only be controlled in SymPhoTime64. To resolve this a Python library was written, called Pycromanager, which communicated with µManager via a socket connection and the Windows UI. This provided the ability to perform automatic Z-stack imaging, automatic acquisition at different positions and a combination of the two. It also included a point-picking code which was written originally by Johan Hummert, and then later modified to fit the microscope setup by Stanimir Asenov Tashev. This used the ThunderSTORM plug-in in Fiji and a Python code interacting with Windows UI, and gave the ability to select points from an image and then choose them on SymPhoTime64 before starting an acquisition automatically. This allowed for more consistent measurements, and increased the throughput of experiments significantly.

3.2.2 Microscope characterisation and validation

3.2.2.1 Pixel size determination

To assess the scale at which we observed samples the pixel size needed to be determined. The pixel size of the setup was calibrated by the use of the Pixel Calibrator plugin of µManager, where features are detected and their change in space is registered upon exact movements with the stage. For the 1x magnification on the body the resulting pixel size was 156.8 nm. This is right on the theoretical resolution limit, but to gain the full information a higher sampling is required. Thus, for most widefield experiments we would use the 1.5× magnification on the Nikon body. This led to a pixel size of 105.6 nm. In epifluorescence the illunminated diameter was shown to be around 150 µm by projecting the transmitted image of a microruler. This meant that even at the lower magnification the entire field of view, which is around 80 µm, will be illuminated.

3.2.2.2 emCCD camera calibration

For accurate determination of the brightness, parameters such as the noise and the gain needed to be determined. Thus, calibration of camera noise and gain was performed on a chip-wide scale by imaging with different parameters. For calibration of the heating effect during acquisition brightfield imaging was performed with the same illumination with increasing exposure times (Fig. 3.14a).

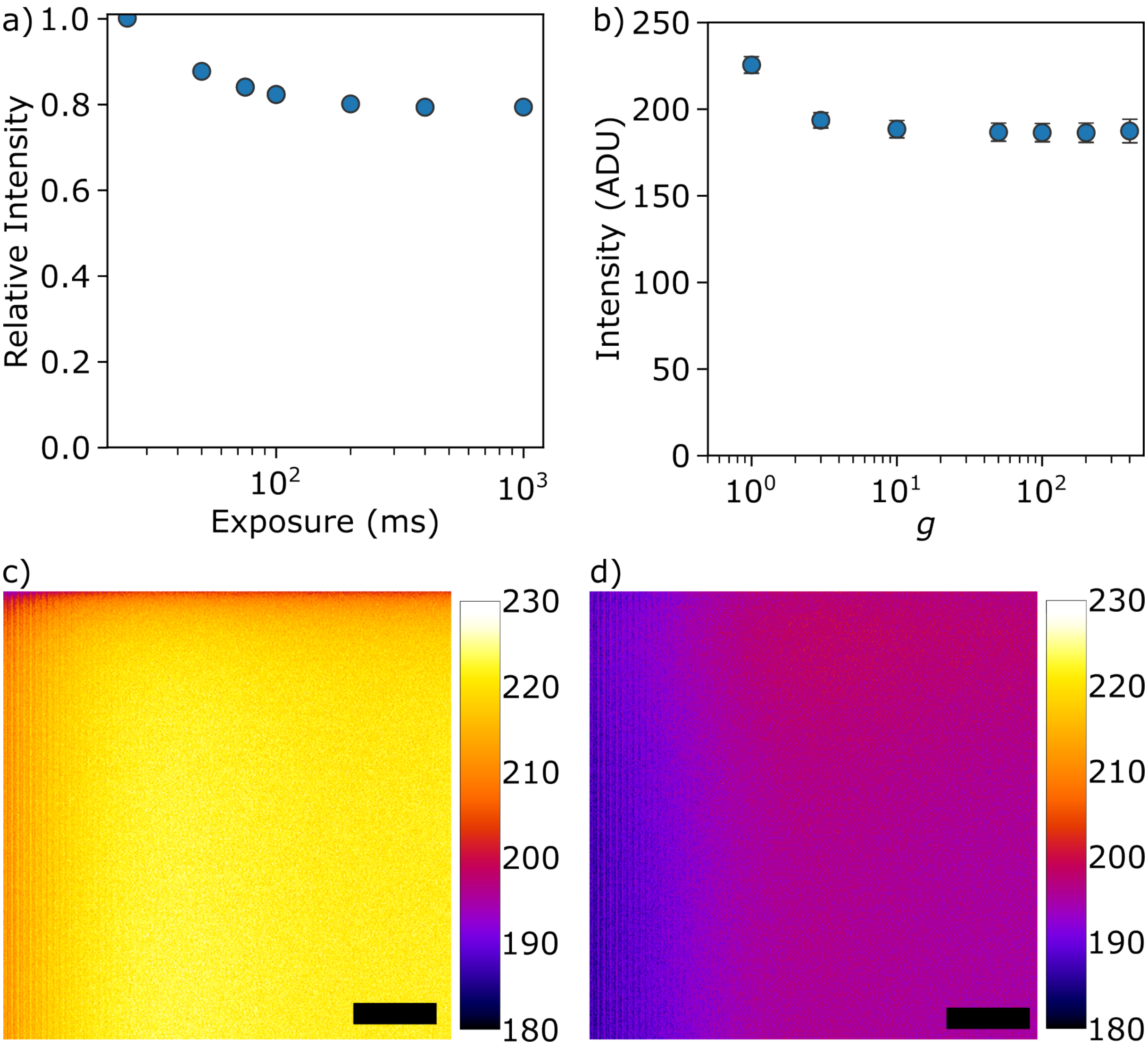

Fig. 3.14: Effects of heat and gain on intensity. a) Relative intensity across the camera chip across exposure time. The intensity was normalised from the 25 ms measurement. b) Dark counts from the chip at different emGain settings. The point at emGain 1 was taken with emGain off. Averaged image from the camera taken without emGain (c) and with g 10 (d). Both c) and d) have been false coloured and scaled as the look-up table shown at the side. Scale bars 95 pixels. Dot plots feature mean with standard deviation (SD).

The average intensity was normalised by the exposure time and by the average intensity for 20 ms exposure time. The relative intensity decreased down to 80% of the values seen from the 20 ms time, meaning that heat has a strong effect in the imaging. The dark counts of the camera were also investigated with different emGain settings with the shutter of the camera closed. The dark noise showed a decrease upon turning on the emGain (Fig. 3.14b). The dark counts seemed to decrease when emGain was turned on, from 225.3±4.8 ADU to 187.3±6.8 ADU at g 100. The average projection of the camera without emGain exhibited a stripped pattern on the left side of the chip (Fig. 3.14c), this was also observed with the 10 emGain multiplication factor (Fig. 3.14d). The ADU conversion factor ϕ of the emCCD also required calibration to accurately calculate the photons from the ADU. Initially the gain calibration was performed without the use of emGain with the multiplication coming just from the readout amplifier. The signal to variance ratio showed a linear relationship with a slope 0.238±0.00 (mean±95% CI) ADU/photoelectrons (ADU/e$^-$) (Fig. 3.15a), which results in a ϕ of about 4.2 Subsequently experiments were conducted with gain multiplication factors g set to 10, 20 and 50 (Fig. 3.15b-d). These too produced linear relationships with slopes for g 10 3.80±0.10 ADU/e$^-$, for g 20 8.23±0.12 ADU/e$^-$, and for g 50 20.2±0.2 ADU/e$^-$. We can see that the increase of the g is proportional to the ADU/e$^-$ conversion. To estimate the gain resulting from the software set g value a linear regression was calculated to show that relation (Fig. 3.15e). The resulting in 0.413±0.025 ADU/e$^-$ or a ϕ of around 2.3 e$^-$/ADU.

When operating the camera the significant difference is seen upon turning the emGain on. Thus, it is safe to say that the amplification register of the emGain required calibration.

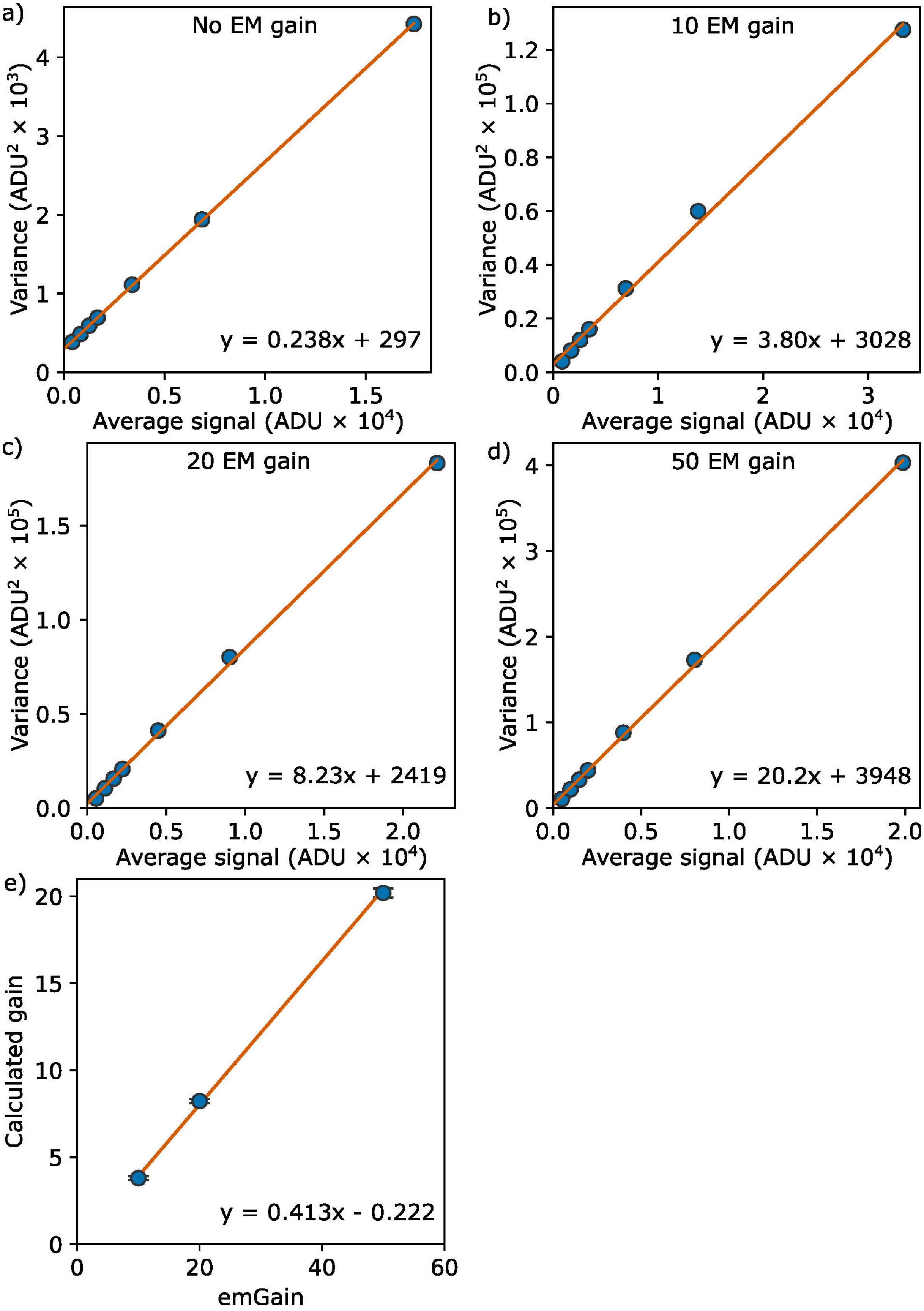

Fig. 3.15: Gain calibration. Calibration of the gain of the camera at no emGain (a), as well as g 10 (b), g 20 (c) and g 50 (d) emGain. Relation between variation and average signal at 25 ms, 50 ms, 100 ms, 200 ms, 400 ms and 1000 ms. Linear regressions (orange) was fitted to the data sets. e) Gain with different g values. Data is mean with SD. R > 0.99 for all fits.

3.2.2.3 Stability measurements

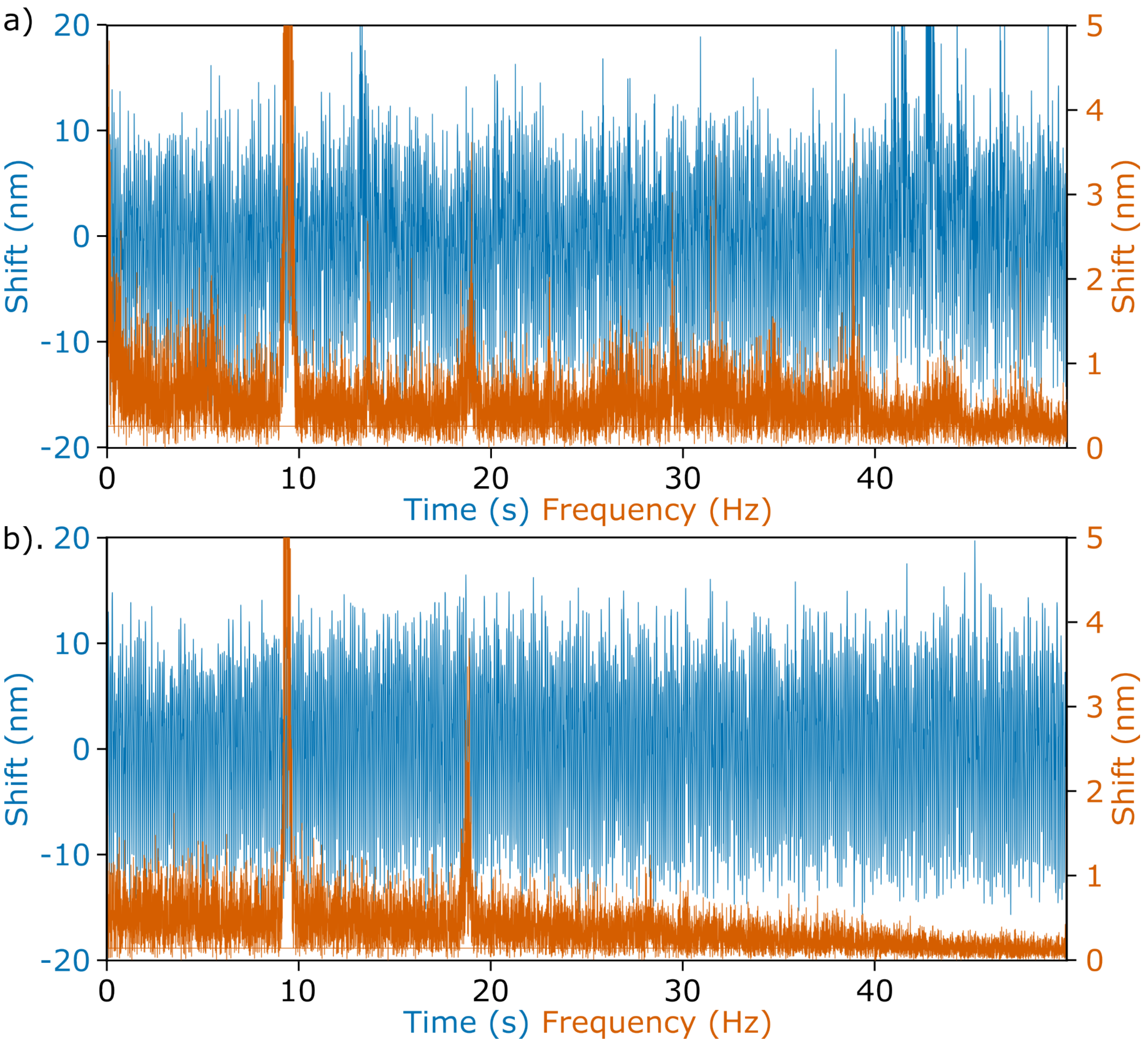

Fig. 3.16: Stabilisation by passive dampening. Representative data from single molecule tracking of diffraction limited beads. Dual plots of the shift of the sub-pixel localisaitons (blue) on the left and the frequency of the vibrations detected (orange) on the right. Data was recorded without the dampening (a) and with the dampening present (b).

The effect of the dampening table on the vibrations experienced by the microscope was characterised by single particle tracking of sub-diffraction-sized beads. The dampening was inspected with a control where the table legs were not pumped against one where they were according to manufacturers guideline. The frame-to-frame shift in localisation of one of the beads is shown in Fig. 3.16, together with a fast Fourier transform performed to show the frequency of vibrations. All measurements showed spikes around 9 Hz and

18 Hz. The control shows additional spikes around 13 Hz and 23 Hz. As claimed by the manufacturer dampening was seen in frequencies higher than 10 Hz.

The dampening was sufficient and the shift seen between frames was below that which can be determined by the sub-pixel localisation algorithms. This maked the microscope appropriate for super resolution techniques and single-molecule microscopy techniques.

3.2.2.4 Confocal volume determination

To assess the resolution limit of the LSCM the size and shape of the confocal volume needed to be determined. Both FCS on a dilution series of a fluorophore and Z-scanning of diffraction limited beads were performed to calculate the confocal volume.

A dilution series of Atto655 between 5 pM and 100 nM was used. The estimated average number of molecules $\langle N_u \rangle$ in the confocal volume was multiplied by the correction factor χ^2, calculated from the average intensity of the trace compared to a no dye control (see Sec. 2.2.6). χ^2 decreases to 1 as the background contributes less (Fig. 3.17a). The average number of fluorophores $\langle N_c \rangle$ showed a linear correlation with the concentration of Atto655 (Fig. 3.17b). The linear regression shows 2.20±0.13 molecules/nM inside of the confocal volume. V_{eff} was then calculated to 3.65±0.22 fl by dividing the number of molecules by the concentration (139).

For a direct intensity estimation diffraction limited beads were Z-scanned with the 640 nm with voxel size 20 nm $\times$ 20 nm $\times$ 50 nm. Images from the sum of all detectors were used to create a Z-stack. The orthogonal sections in XY, XZ and YZ were fitted with a 2D Gaussian (Fig 3.18a, d, and g). The 0.9 $\times$ I_{max}, the 0.5 $\times$ I_{max}, and the $1/e^2 \times I_{\text{max}}$ were extracted, where I_{max} is the maximum intensity of the Gaussian function (Fig 3.18b,e,

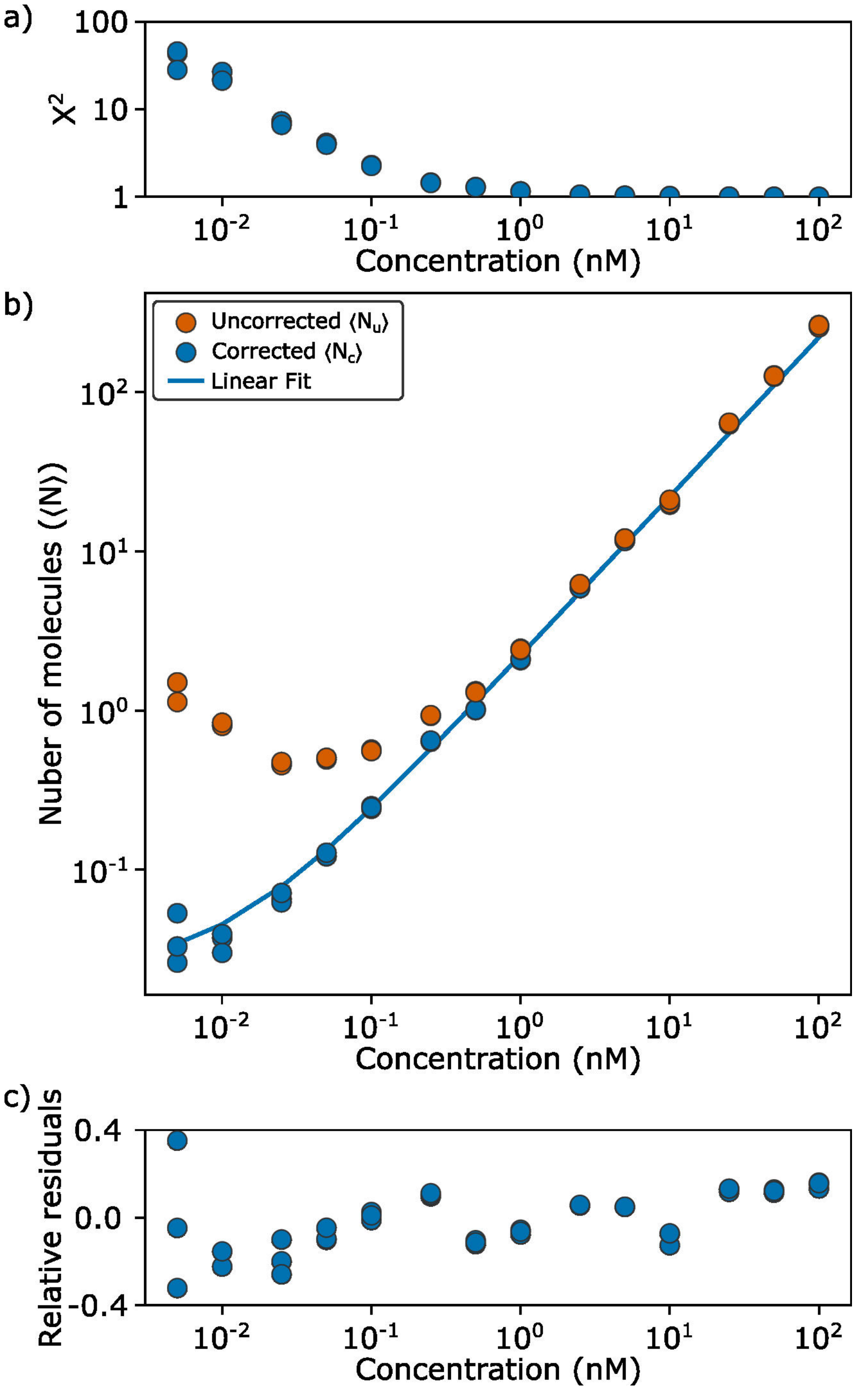

Fig. 3.17: FCS measurements on Atto655 dilutions. Data from a serial dilution from 0.05 pM to 100 nM of Atto655. a) Correction factor X^2 calculated from the average intensity values and corrected by pure solvent. b) The average number of molecules $\langle N_u \rangle$ (orange) estimated by FCS measurements and the corrected values $\langle N_c \rangle$ (blue) with the fitted linear regression weighted logarithmically. c) The relative residuals of the linear regression fit. n=3 traces per concentration

and h). To calculate V_{eff} the average values of the radii of the $1/e^2 \times I_{\text{max}}$ for the three dimensions, w_x, w_y, and w_y was used (107, 139)(Table 3.1).

$$V_{eff} = \pi^{\frac{3}{2}} w_x w_y w_y \tag{3.8}$$

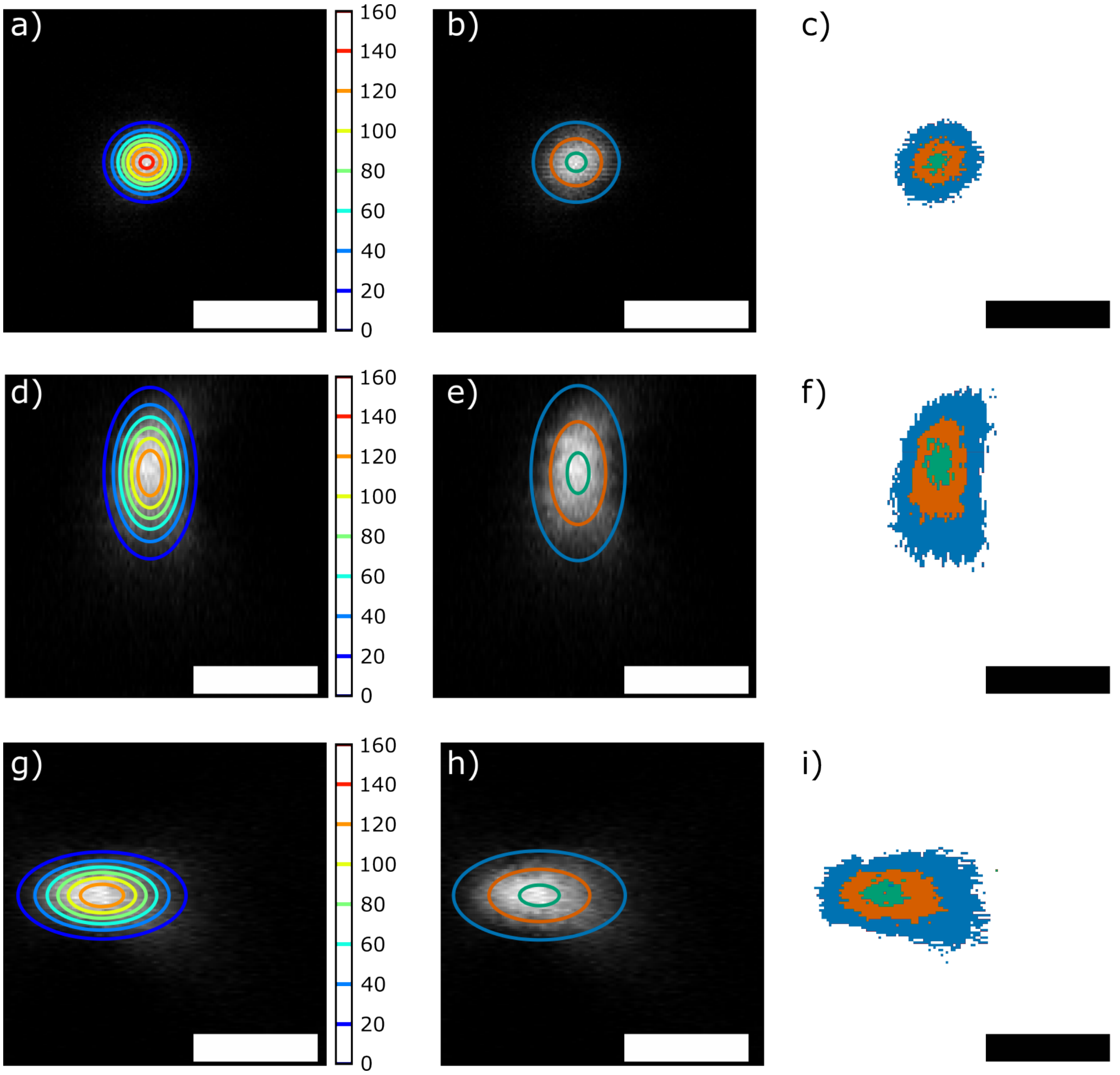

Fig. 3.18: 3D bead scanning. Orthogonal sections of a 3D scan of a sub-diffraction-sized bead. Images a)-c) show the XY section at the focus plane, d)-f) represent the XZ section through the middle of the point spread function, and g-i depict the YZ equivalent. Images a), d), and g) show the values of the 2D Gaussian fitted to the intensity values of the orthogonal section. b, e, and h the 0.9 $\times$ I_{max} (green), the 0.5 $\times$ I_{max} (orange), and the $1/e^2$ $\times$ I_{max} (blue) levels, with I_{max} being the maximum intensity of the fitted 2D Gaussian. c), f), and i. PSF with the pixel values above the three limits specified in their corresponding images to the left. Scale bars 1 µm.

V_{eff} was calculated to be 0.5 fl. The estimated values for the three radii seem to be in agreement with the general size, but the shape of the PSF is less regular than the theoretical (Fig 3.18c,f, and i). For single molecule experiments the density of emitters will need to be below a 2 per micron squared to limit contribution of neighbouring emitters to CoPS analysis.

Tab. 3.1: PSF width measurements. Radii of width at the $1/e^2 \times I_{\max}$ estimated from fitting a 2D Gaussian function on the orthogonal sections shown in Fig. 3.18. Independent scans n=4.

section	w_x (nm)	w_y (nm)	w_z (nm)
xy	341±5 nm	321±8 nm	-
xz	370±8 nm	-	773±57 nm
yz	-	362±4 nm	704±58 nm
Mean	355±14 nm	342±20 nm	739±35 nm

3.2.3 Validation of antibunching quantification

3.2.3.1 Signal distribution and light insulation

For CoPS to work, the measurements needed to fit the mathematical model. Thus, the emission of light needed to be evenly split between the four detectors. To assess the intensity detection distribution for each detector, the emission for each second from a 1 nM Atto655 solution over 5 min was assessed (Fig. 3.19a). The intensity of detector 1 showed 2182±77 counts per second (cps), which was a decrease in the intensity from the other detectors, 2391±85 cps, 2515±90 cps, 2477±83 cps, for detectors 2, 3, and 4, respectively. This resulted in a spread of 23:25:26:26% (Fig. 3.19b). The dark counts of the detectors were also investigated in different light conditions. The lights in the room showed a significant increase of the dark counts ($p<0.05$) from 1138±6 cps to 1613±3 cps, unlike the autofocus system which only resulted in 1162±6 cps (Fig. 3.19c). However, this was overshadowed by the reflection of the laser light, which despite the Notch filter, significantly increased the counts ($p<0.01$) up to 3644±270 cps. The effects of light on the emCCD camera was also examined with different exposures and no significant difference was found (Fig. 3.19d).

The effects of the difference in the distribution of the signal between the channels on CoPS analysis was further investigated in Sec. 3.2.3.3. The contribution on the ambient

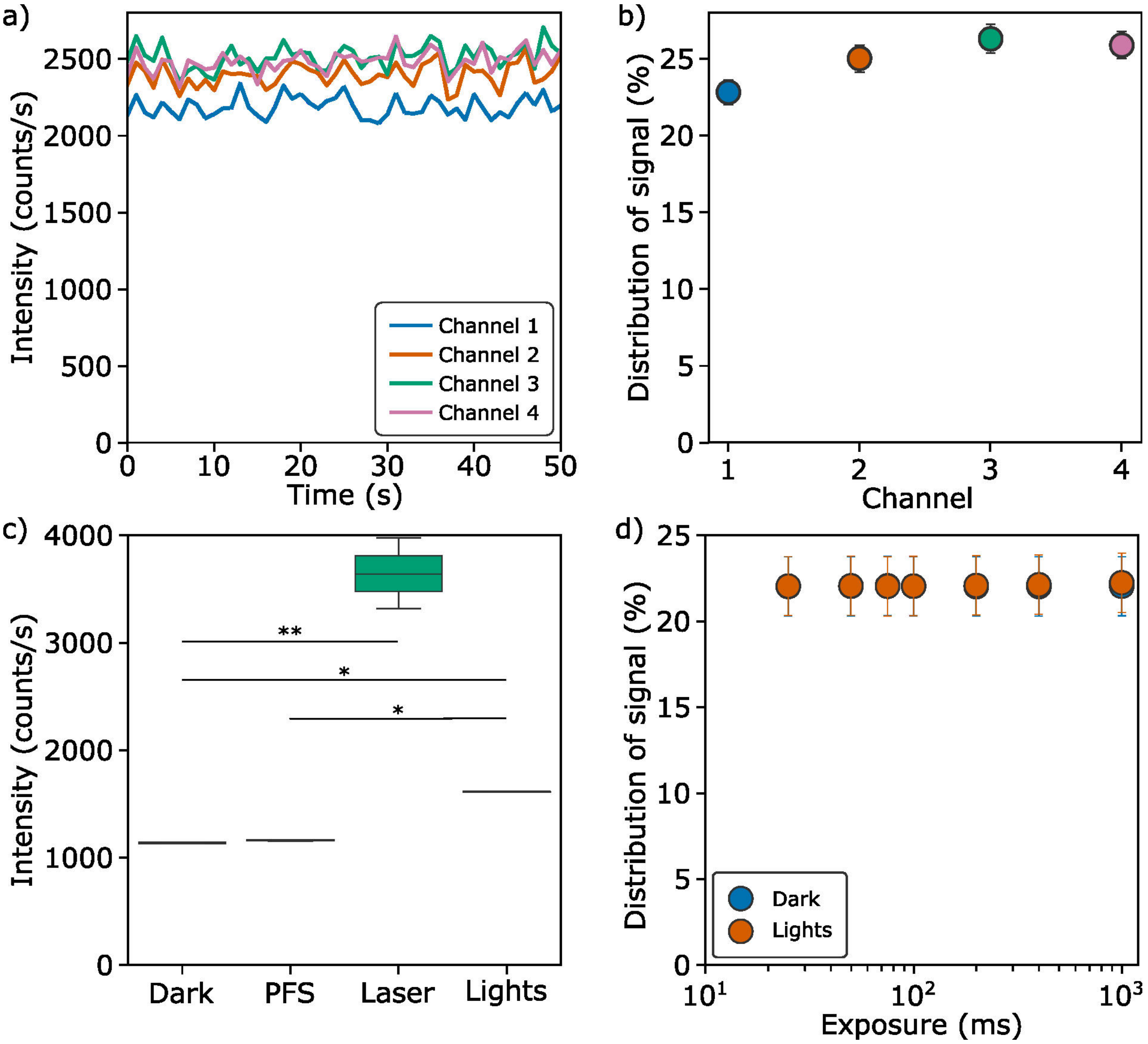

Fig. 3.19: Distribution of signal and effects of light conditions. a) Intensity trace of the four separate detectors with a second time resolution for 50 s. b) Distribution of the signal between the four channels for 10 min, thus n=600 bins of a second for each detector. c) Effects of the different light conditions on the SPAD detection compared with a Dunn's test. n=3 30 s traces for each condition. d) Effects of overhead lights on the emCCD camera recorded in the same way as the heat contribution measurements. Dot plots feature mean with (SD). Boxplots shows the three quartiles with the whiskers representing 1.5× IQR. Significance shown as: *-$p<0.05$, **-$p<0.01$, ***-$p<0.001$.

light in the room was shown to have little effect on the overall signal. Thus, it was deemed possible for measurements to be done with the lights on.

3.2.3.2 Synchronisation of detectors

Certain microscopy techniques, e.g. FLIM, require the accurate estimation of photon arrival time. In the case of our microscopy setup there are four separate detectors. To ensure the accuracy of measeurements the photon arrival time between them must be synchronised.

For this calibration the fluorescence from fluorescent beads were recorded and the fluorescence decay are plotted in Fig. 3.20a. These were shown to have a slightly different start of the arrival times from each other with the biggest difference being between detector 1 and 3. An offset was applied by the SymPhoTime64 software based on the arrival times. For detector 1 to 4 the following delays were applied: -2000 ps, -5000 ps, -4000 ps, -2500 ps. This resulted in the synchronised instrument response times shown in Fig. 3.20b.

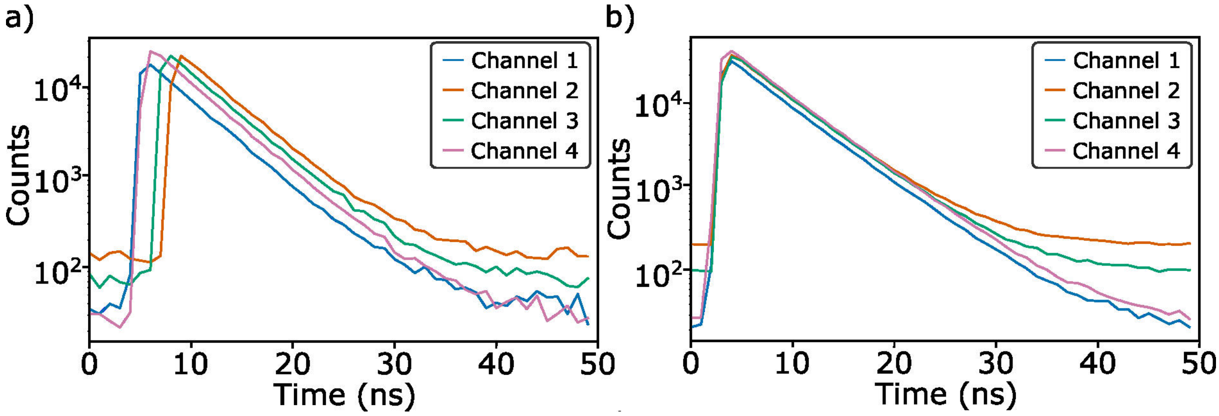

Fig. 3.20: Synchronisation of the four SPADs. a) The fluorescence decay plot from 1 nM Atto655 solution of each of the detectors before synchronisation. b) The fluorescence decay curves of the same solution upon adding the correct offsets to each channel.

3.2.3.3 Validation of CoPS measurements

To validate the antibunching character of the microscope we have cross validated CoPS with another quantitative microscopy technique, photobleaching step analysis (PBSA). DNA origami labelled with Atto647N or with Atto565, at 9, 20 or 35 binding sites with approximately 70% labelling efficiency specified by the manufacturer (7)(Fig. 3.21a, d and g). The fluorophore number was derived by both CoPS and PBSA, and a Gaussian function was fitted on the results. The results are shown in Tab. 3.2.

Tab. 3.2: Results from cross validation experiments. The different type of DNA origami with their expected average stoichiometry. The mean±SD of the number of fluorophores estimated by using either CoPS or PBSA. The DNA origami are named after their label and number of binding sites.

DNA Origami	Expected stoichiometry	PBSA result	CoPS result
9×Atto647N	6.3	7.1±4.1	7.3±3.1
9×Atto565	6.3	5.9±2.7	6.6±3.1
20×Atto647N	14	14.2±12.7	11.9±6.3
20×Atto565	14	14.4±5.6	15.1±7.3
35×Atto647N	20	20.8±14.9	14.3±10.4
35×Atto565	20	22.1±12.4	29.2±15.7

For 9×Atto647N both the CoPS and the PBSA resulted in a number higher than the expected one, 7.3±3.1 and 7.1±4.1 respectively. On the other hand for 9×Atto565 the fluorophore numbers estimated; 6.6±3.1 with CoPS and 5.9±2.7 with PBSA, seem to be closer to the 6.3 given by the manufacturer. For 20×Atto647N origami the PBSA measurement resulted in a large spread with a median close to the expected value (14.2±12.7), while CoPS showed lower accuracy, but higher precision (11.9±6.3). The results of the measurements of the 20×Atto565 standard showed agreement for both techniques (CoPS - 15.1±7.3 and PBSA - 14.4±5.6), as well as compared to the given labelling efficiency. For 35 binding site origami, CoPS seem to show deviation from the expected value with 14.3±10.4 and 29.2±15.7 for Atto647N and Atto565, respectively. On the other hand the fluorophore numbers resulting from PBSA were 20.8±14.9 and 22.1±12.4 for Atto647N and Atto565, respectively, which closer resembles the expected results.

Both techniques showed the ability to estimate upwards of 14 emitters as shown by the 20×Atto565 and 20×Atto647N origami experiments. CoPS has showed greater deviation from the manufacturers specifications above 20 emitters, which might be due to the photobleaching during the recording. The PBSA exhibited greater spread of the data, which could be attributed to the multiple photobleaching step fitting incorrectly determining the stoichiometry. The 9×Atto565 showed a lower density upon immobilisation to the coverslip even when additional DNA origami was incubated. An instability of the origami could explain that and the increase of 1 emitter estimation by both techniques.

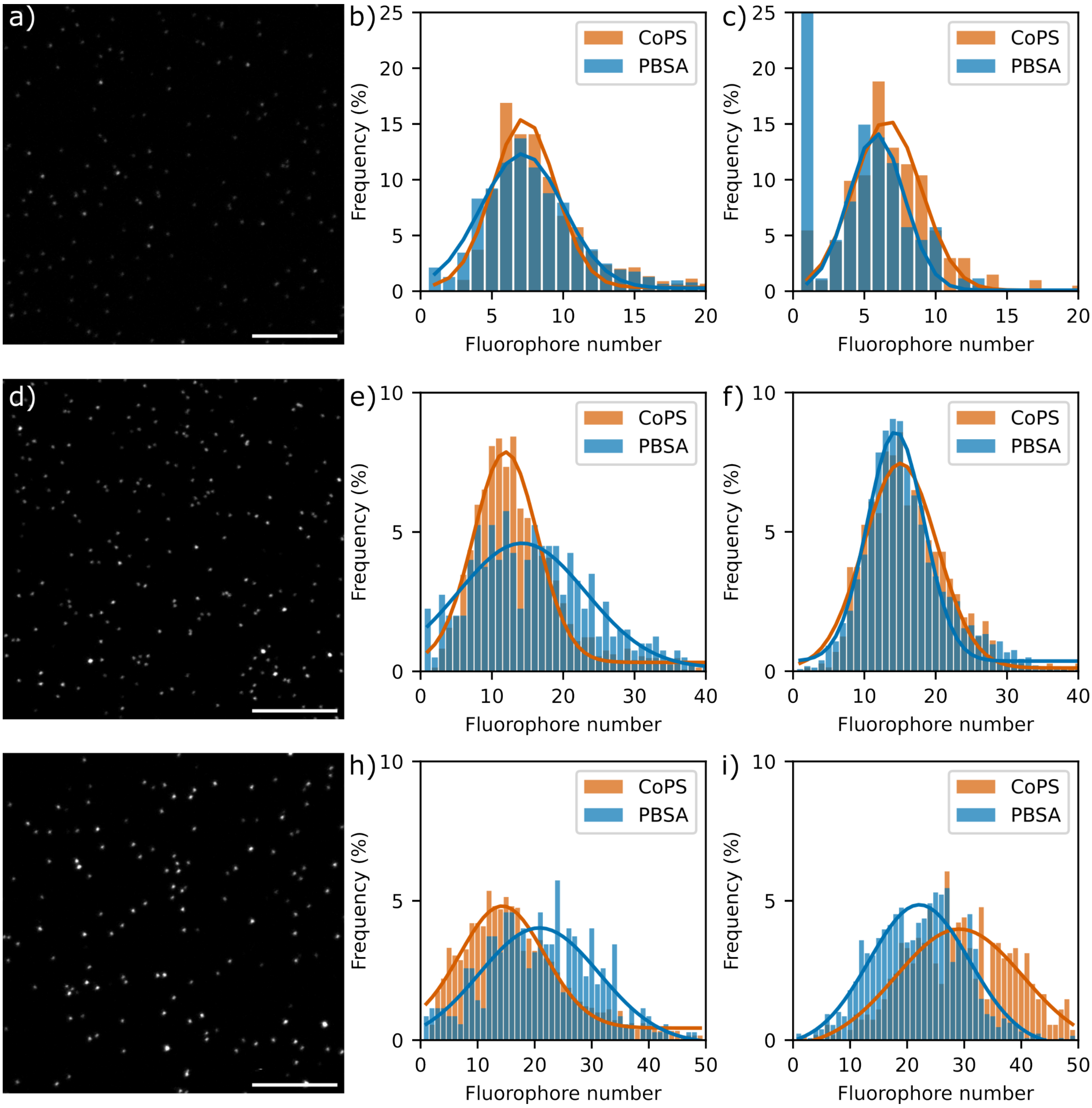

Fig. 3.21: Cross validation of CoPS and PBSA using DNA origami. a), d), g) are representitive images of immobilised DNA origami labelled with Atto565 with 9, 20 and 35 binding sites. Scale bars 1 µm. The other subplots show the histograms of the fluorescent emitters estimated by CoPS (orange) and PBSA (blue) for the different DNA origami with a Gaussian fit over the values: b) 9×Atto647N, c) 9×Atto565, e) 20×Atto647N, f) 20×Atto565, h) 35×Atto647N, and i) 35×Atto565. n in DNA origami written first for CoPS, then PBSA: b) 888, 1649, c) 202, 87, e) 1500, 400, f) 725, 3823, h) 1870, 35, i) 564, 1290.

3.3 Discussion

Construction of a new microscope setup is a time-consuming endeavour and custom microscope setups require validation, which in our case took about a year in total. Even with prior optics-building experience building a system can take more than half an year (140). The confocal-widefield hybrid style which we chose for this project has flexibility in modalities, giving it the ability to perform a wide array of microscopy techniques. However, it is prone to misalignment, and operation requires both experience and a high degree of computer literacy.

During this project a commercially available system, called Luminosa, has been developed by PicoQuant similar to the one described in this chapter (141). It has the ability to perform antibunching experiments, as well as other confocal microscope techniques, with a high degree of automation. Regardless, this system will still cost an order of magnitude more than our single-photon correlation microscope setup.

Another matter is the maintenance of the individual components of this setup. The emCCD camera calibration setup showed a discrepancy of the multiplication gain factor shown in the software versus the one calculated. The dark counts also seemed to decrease when the emGain is turned on. Unfortunately time constraints prevented us from sending the camera back to the manufacturer. Instead, calculations of the photon count when the emGain is turned on will use a conversion factor ϕ of 2.3 e^-/ADU and a 187 ADU offset. The stripped pattern, however, needs to be corrected if super resolution imaging was to be performed. In our case the sub-pixel localisation of molecules was not of interest, and any localisation's based on these aberrations was going to be discarded during filtering. If necessary a cropping of the field of view down to the leftmost 80% of the camera can be done post acquisition.

Other than this issue, the dampening of the vibrations showed that single-molecule localisation microscopy techniques can be performed on this table. The enclosure of the microscope is also seen to have worked sufficiently to allow CoPS to work in a general purpose lab, and not a dark room.

The distribution of signal being unequal can be attributed to the fact that the beam splitters do not split equally depending on the polarisation of light. Thus, using two beam splitters consecutively can lead to unequal signal. The differences, despite statistically significant, are small enough to still use the equal distribution model. This is observed by the ability of the microscope to conduct as shown by the comparison between CoPS and PBSA performed on DNA origami with low number fluorescent molecules. To count to a higher number of fluorescent molecules fluorophores with higher photobleaching quantum yield to build the mDE histogram is needed, and thus in these cases PBSA might be more appropriate.

For the confocal volume the bead scanning result of 0.5 fl were determined to be more reliable as it is a direct measurement from the intensity measured. While the measurement might stem from a incorrect dilution of the initial stock of the dye, it is more likely that the disparity was due to the optical mismatch between the aqueous medium and the immersion oil. This effect is increased by the depth at which the measurement is taken.

After the thorough validation of the microscope the project continued to the development of the CoPS analysis, as well as validating it with a dynamic system.

Chapter 4

Quantitative microscopy: from static to dynamic

This work is currently in preparation for submission and publication: J. B. Shep IV*, **S. A. Tashev*,** M. Fazel, M.Scheckenbach, P. Tinnefeld, D.-P. Herten, S. Pressé, *"Bayesian Inference of Binding Kinetics from Fluorescence Microscopy Experiments."*

Author contributions:
DNA origami was created and initially validated by M.S. from the lab of Prof Philip Tinnefeld, LMU Munich, Germany. State inference and Bayessian analysis was written by J.B.S. and M. F. from the lab of Steve Pressé, ASU, USA. All other work was done by S.A.T.

4.1 Introduction

A large portion of the proteins inside of cells are grouped together in complexes to carry out their function (142). This grouping can have biological functions related to control of signalling (143). One such example are receptors on the surface of the cell which bind extracellular ligands. An extreme example of this is the formation of clusters where hundreds or thousands of proteins aggregate together (144). Certain systems, such as T cells, form microclusters (MCs) with a sub-resolution size. The study of the formation of such clusters can reveal interesting aspects of cell signalling. One characteristic of recruitment is the the kinetics of assembly and disassembly. Studying these can reveal the biding affinities of proteins, as well as the mechanisms of MC formation.

4.1.1 Determination of molecular kinetics

There are a number of ways to assay the formation of molecular complexes. For instance plenty of in vitro techniques, such as surface plasmon resonance (SPR) and isothermal titration calorimetry (ITC), have been used for protein-protein interaction kinetics (145–147). These, however, require large amounts of highly concentrated proteins, and are not compatible with live cell experiments (148).

There are also various fluorescence microscopy methods used to assay protein-protein interactions each with their benefits and limitations. Two common techniques are Förster resonance energy transfer (FRET) and bioluminescence resonance energy transfer (BRET), in which energy is transferred from a donor molecule to an acceptor fluorophore when the two are within the Förster distance. The difference between the two is that in FRET the donor is another fluorophore while in BRET the donor is a bioluminescent enzyme (149). There have recently been developments which can allow the ability to determine the kinetics of binding of these proteins (150). Although this could potentially be used in live cells this hasn not been demonstrated, and would require a knowledge of the structure of the proteins' structure.

As mentioned before, fluorescence correlation spectroscopy (FCS) can be used for determination of the diffusion of molecules, but the mathematical formula for correlation can be modified to determine the kinetics of molecular recruitment (151). This, however, does not work in every system, as shown in a study by Anita Mouttou, *et al.* on the recruitment of proteins to the plasma membrane by a combination of computer modeling and spot variation FCS (svFCS) (152). This model has so far not been shown to work on other systems.

Single-molecule localisation microscopy (SMLM) has also been used to determine the kinetics. A common use is the determination of binding kinetics of nucleotides and studies of epigenetic modifications (69, 153). These techniques are derivative of DNA-PAINT, where a fluorescently labelled strand of DNA called an imager binds to a docking strand, which can be located on a DNA orgami or a labelled protein (69).

In them the recruitment kinetics are determined based on the steplike increase or decrease in fluorescence that occurs upon binding or unbinding, respectively. Most commonly localisation analysis is performed on TIRFM data to determine the presence of a localisation, which corresponds to the bright state. These are grouped in consecutive frames to show the length of the bright times (τ_b). From the mean of the bright times $\langle\tau_b\rangle$ the rate of unbinding k_{off} can be calculated.

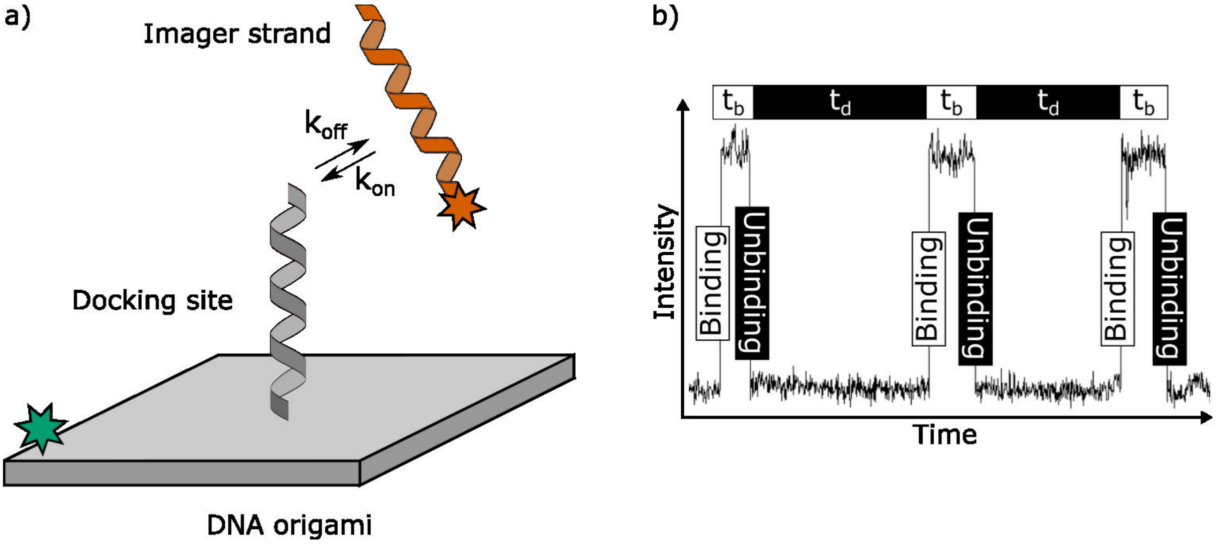

Fig. 4.1: Determination of kinetics via PAINT. Example of the determination of the kinetics of a DNA origami system via PAINT. a) Schematic of a simple DNA origami with one docking site binding to an imager strand (orange). DNA origami can be folded with a strand linked to a fluorophore (green) embedded in them as a reference. b) PAINT measurements are done via TIRFM and result in intensity traces of steplike increases and decreases upon binding and unbinding,respectively. Thus the trace can be divided into bright (τ_b) and dark (τ_d) times.

$$k_{off} \propto \frac{1}{\langle \tau_b \rangle} \tag{4.1}$$

Clustering algorithms are then used to connect the bright states in a sub-pixel radius. These could include simple ones, which only connect the localisations from the binding of imager strands in a radius around the reference signal. This, however, would include the non-specific binding that just so happens to be in that location. Geometric features of the localisations inside the imager strands can be used to reduce the influence of non-specific binding.

One such one is density-based spatial clustering of applications with noise (DBSCAN). This technique examines the distance between neighbouring localisations and forms clusters if the distance between localisations are within a certain radius (154). Clusters are then filtered if there are enough members inside them. This method is used within this work.

Clustering would then gives the dark times τ_d as the time between different localisations. The kinetics of binding k_{on} can then be calculated by:

$$k_{on}c \propto \frac{1}{\langle \tau_d \rangle} \tag{4.2}$$

where $\langle \tau_d \rangle$ is the mean of the dark times.

An important thing to remember is that the rate of unbinding k_{off} should be a constant across concentrations thus it also corresponds to the unbinding rate constant k'_{off}. On the other hand, the rate of binding k_{on} is linearly dependent on the concentrations. To get the rate constant for binding k'_{on}, k_{on} needs to be divided by the concentration.

Peptide-PAINT has also been developed where the kinetics of the binding of peptides to proteins (155), as well as LIVE-PAINT in which sub-pixel resolution is achieved in live cells by protein-protein interactions (156). However, the combination of these where protein interaction kinetics are determined *in vivo* remains a difficult task. This is because as the interactions need to be in a stationary cluster for the clustering of localisations to work. There is also the difficulty with the heterogeneity of the cell creating differences in the binding kinetics between clusters. The kinetics and stoichiometry of the protein also needs to be right for there to be sufficient amount of bright and dark times detectable by microscopy.

Despite these techniques being powerful tools for the study of biological studies, the needs of a cell-compatible technique remains unanswered. To try to solve this, this project has involved an attempt to address this discrepancy via a modified version of CoPS. However, this will initially require validation via a molecular standard, which itself will require characterisation.

For that a dynamic model system needed to be examined and the kinetics of binding and unbinding inside it needs to be determined. This system will then be examined via the regular CoPS analysis, as well as the modified versions of the analysis. The ability of the different analyses to accurately determine the fluorophore count will be determined to examine the benefits of each.

4.2 Results

4.2.1 Determination of binding kinetics

4.2.1.1 Validation of DNA origami

To examine the binding kinetics three different DNA origami were folded by Michael Scheckenbach (LMU Munich, Germany) each with a different amount of docking strands, which would bind the imager strands. These were named 1xS1 2xS1, and 5xS1, which correspond to 1, 2 and 5 binding sites. All of these origami had the new rectangular origami (NRO) basic shape, and also contained three sites on which Atto542-labelled strands were incorporated as a reference signal.

After folding the NRO it required inspection to ensure correct folding, as well as to examine if any clumping between different DNA origami occurred. With that reasoning the three different DNA origami were immobilised on BSA-biotin-streptavidin coated coverslips and imaged via atomic force microscope (AFM) (Fig. 4.2a-c). The origami were observed in the expected rectangular form for which the NRO are named. There were also no linear attachment or clumping between individual origami.

After transportation from LMU Munich, Germany to University of Birmingham, UK, and storage the three origami were also inspected via agarose gel electrophoresis (Fig. 4.2d). As a control, the scaffold DNA (p7249) used to create the NRO was used. All four samples showed a single band, however, not in the position corresponding their length. The scaffold's band was at the 1.75 kilobases (kb) position, while all of the DNA origami bands were positioned at 2 kb. These results were likely caused by the secondary structures of the DNA in these samples.

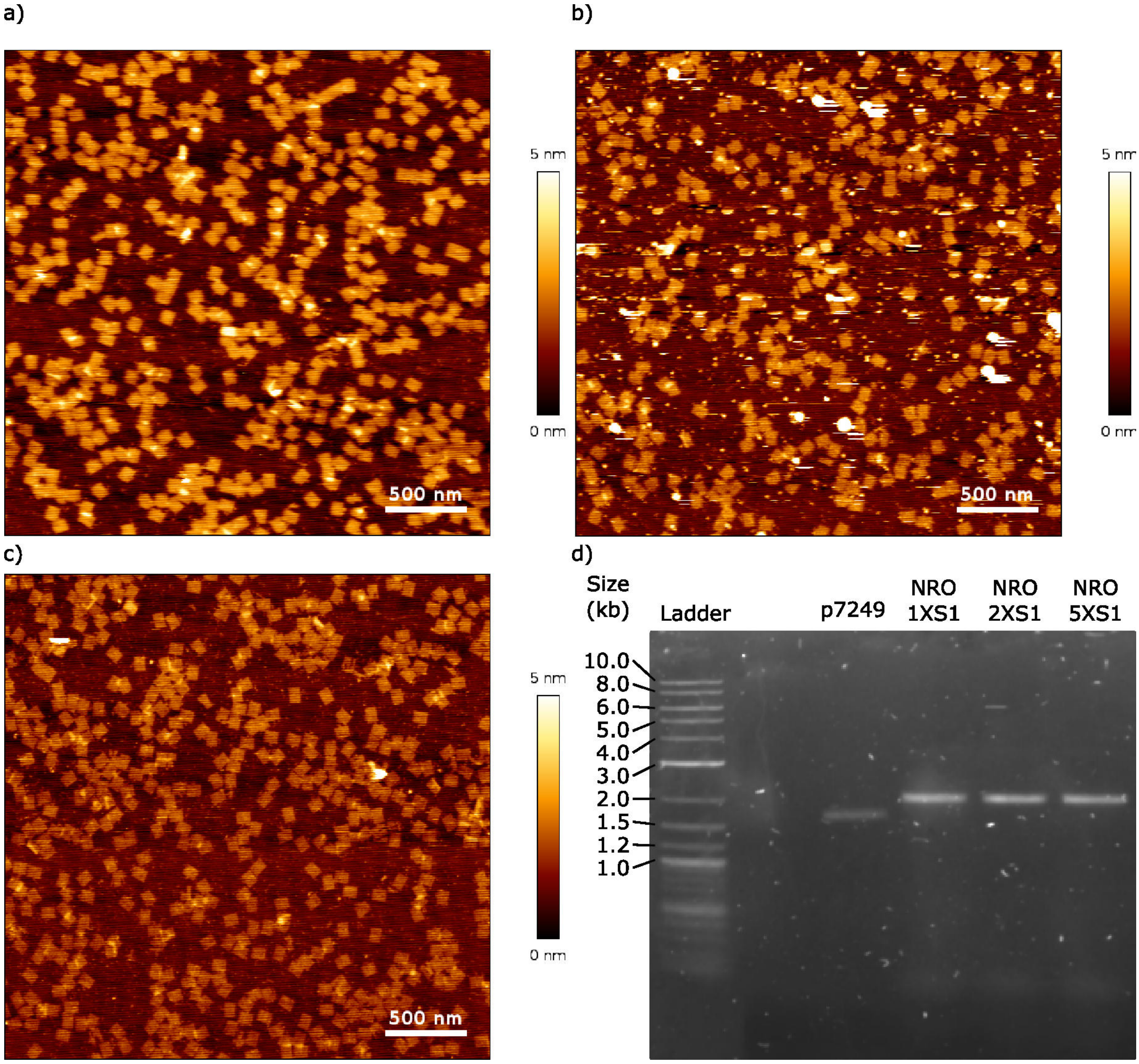

Fig. 4.2: Validation of NRO folding. Atomic force microscopy of NRO 1xS1 (a), 2xS1 (b) and 5xS1 (c) performed by Michael Scheckenbach (LMU Munich, Germany). The scale bar is 500 nm and the colour scale is between 0 nm and 5 nm of elevation. d) Agarose gel electrophoresis of the NRO samples as well as the scaffold. The first well features 4 µl of 1 kb ladder. An unedited image of the entire gel can be seen in Fig. SI 4.

The DNA origami showed correct folding and a high degree of stability even after freezing, which made them viable for dynamic binding experiments.

4.2.1.2 Surface cleaning

Sample preparation of single molecule experiments involves the cleaning of the glass coverslip from fluorescent contaminants. However, some protocols can change the hydrophobicity of the surface of the glass coverslip.

To inspect if the substance used for cleaning affected the non-specific biding of the imager strand or the ability of the DNA origami to be immobilised four cleaning solutions were examined: ethanol (EtOH), hydrofluoric acid (HF) and hydrochloric acid (HCl) in methanol (MeOH). These were compared to a water acting as control. Cleaning was done via an incubation for five minutes followed by two rinses with water. After that the samples were then coated with BSA-biotin and streptavidin as described in Sec. 2.2.4, and inspected at 640 nm via total internal reflection fluorescence microscopy (TIRFM). All treatments showed a significant reduction of fluorescent contaminants at the coverslip surface compared to the control ($p<0.001$) (Fig. 4.3a). The halogen acids showed a greater decrease in contamination than just the EtOH. The HF showed the lowest density of fluorescent contaminants at 0.015±0.001 μm^{-2}, which is significantly less than even the HCl plus MeOH treatment, which had a density of 0.029±0.002 μm^{-2} ($p<0.05$). To investigate the non-specific binding the coverlips were imaged for 30 min during an incubation with 1 nM of 21 nucleotide (nt) long imager strands labelled with Cy5 in PBS (Fig. 4.3b). The only significant change ($p<0.01$) was the MeOH-HCl treatment with 0.86±0.03 μm^{-2}, which showed a decrease in the non-specific binding. The cleaning solutions were also assayed for the ability of the surface to then bind the DNA origami (Fig. 4.3c). The DNA origami was deposited onto the cleaned and coated coverslips. The origami were detected by their reference signal by imaging at 561 nm. The treatments seemed to have significantly decreased the amount of origami bound to the coverslip ($p<0.001$). The density for DNA origami was 0.362±0.007 μm^{-2} and 0.171±0.004 μm^{-2}, for the EtOH and MeOH-HCl, respectively. The HF cleaning on the other hand remained close to the control at 1.654±0.019 μm^{-2}.

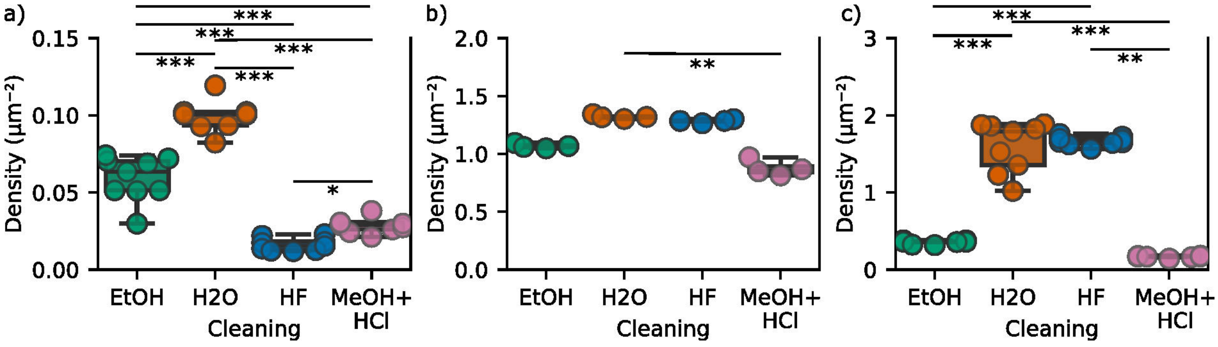

Fig. 4.3: Effects of surface cleaning. a) Densities of the fluorescent contaminants inspected at 640 nm after cleaning. b) Density of the cumilative non-specific binding of 21 nt imager strand labelled with Cy5 after 30 min of incubation. c) Density of the DNA origami immobilised on the glass coverslip determined by the reference channel. n=4 for each condition. Kruskal-Wallis test was performed followed by a Dunn's test. The results of the post-hoc tests shown as: *-p<0.05, **-p<0.01, ***-p<0.001.

Overall, HF showed the best characteristics and was deemed the optimal cleaning solution due to the the low contaminant level, as well as the a high level of DNA origami immobilisation. The alcohol containing cleaning protocols seemed to also decrease fluorescent contaminants, however, the decrease in DNA origami immobilisation points towards disruption of the ability to coat with BSA-biotin-streptavidin.

4.2.1.3 Buffer effects on kinetic determination

Studies of the hybridisaiton of DNA via fluorescence require an imaging buffer that does not cause non-specific binding of the imager strands to the coverslip while still increasing the photostability of the fluorescent signal. To examine the appropriate buffer for imaging the non-specific binding of 9 nt long imager strands labelled with Cy5 was determined by imaging with fast imaging with 21 ms frametime for 3.5 min. Two different buffers were examined made of two different bases-Blue base and Red base. The contents of the two are described in Tab. 2.8. Notable is the increased Na^+ concentration, as well as the addition of Tween20 and removal of glycerol in the Red buffer. The data was analysed with the SMLM analysis software SMAP and the molecules already bound to the coverslip at the start were filtered out.

The density of the non-specific binding found over 3.5 min showed a significantly higher ($p<0.05$) in the Blue buffer than the Red buffer with 282±15 μm^{-2} and 244±6 μm^{-2} (mean±SD), respectively (Fig 4.4a).

The duration of non-specific binding was also examined by grouping the localisations of the imager strand within 50 nm of each other and allowing for a single dark frame in between localisations. The mean duration of localisation within a FOV are shown in Fig 4.4b. The Red buffer showed a small but significant decrease ($p<0.05$) in the immobilisation time of non-specific binding, from 0.468±0.002 s in the Blue buffer to 0.454±0.009 s.

Thus, the Red buffer exhibits better characteristics for DNA binding experiments due to the decrease in frequency and duration of the non-specific binding of the imager strands to the coverslip. Following this experiment the Red buffer was used in future dynamic experiments.

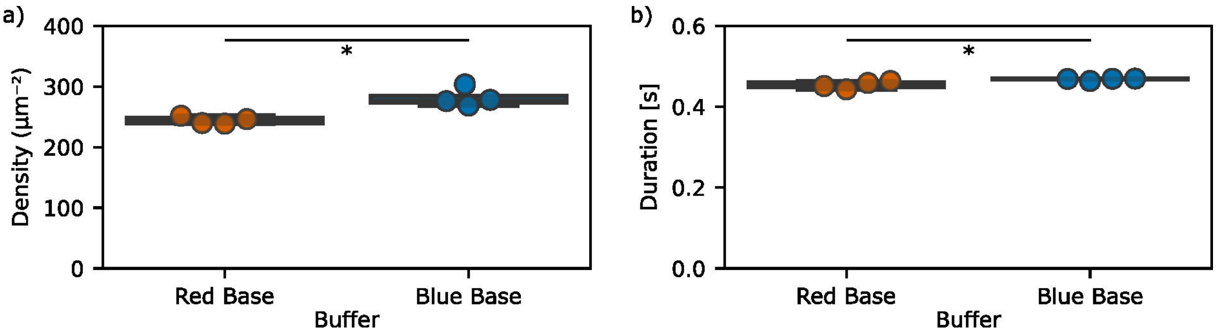

Fig. 4.4: Effects of buffer base on the non-specific biding. a) Density of non-specific binding during 3.5 min of binding of 9 nt long imager strands labelled with Cy5. b) Mean duration of the binding per FOV. The first well features 4 µl of 1kb ladder. The results of Mann-Whitney tests are shown as: *-$p<0.05$, **-$p<0.01$, ***-$p<0.001$. Data was analysed with SMAP and the results are shown on a FOV basis (n=4).

4.2.1.4 Rate determination via localisation

CoPS has a fast rate of determining the number of fluorophores, but due to it being restricted to single point measurements there is no drift correction that can be done post measurements. Thus, the molecular standard's binding kinetics needs to be quick enough that the rates can be sampled atleast 4-5 times for a time measurement of 5 min.

To inspect the kinetics of hybridisation 1xS1 NRO were incubated with 9 nt long imager strand labelled with Cy5 at 1 nM, 2 nM, 5 nM, and 10 nM inside of the Red buffer. The sample was imaged with two different laser powers- 193 W/cm^2 and then with 96.4 W/cm^2, to investigate the effects of laser power on kinetics, as photobleaching can skew the results. The kinetic rates themselves were calculated from the average bright times and dark times as shown in Fig. 4.1. The rate constants are then determined by fitting a linear fit with a (0,0) intercept for k'_{off} (see Eq. 4.1) and a constant for k'_{on} (see Eq. 4.2).

The lower laser power measurement from 1 to 5 nM together resulted in a off rate constant k'_{off} of 1.26±0.24 s^{-} (mean±95% CI) (Fig 4.5a). The 10 nM shows a visible higher result of 2.43±0.09 s^{-}. This brings the estimated k'_{off} to 1.55±0.60 s^{-}. A similar thing is observed with the higher laser power measurements (Fig 4.5b). Prior to 10 nM the value of k'_{off} was 1.39±0.64 s^{-}, while considering the contribution of that dataset it increases to 1.61±0.45 s^{-}.

The on rate constant k'_{on} calculated for the lower laser power was 0.08±0.01 s^{-}nM^{-}. For the high laser power the k'_{on} was 0.06±0.02 s^{-}nM^{-}. There appears to be a small kink of the k_{on} values at the 1 nM. These deviations of k_{on} and k_{off} for the 1 nM and 10 nM

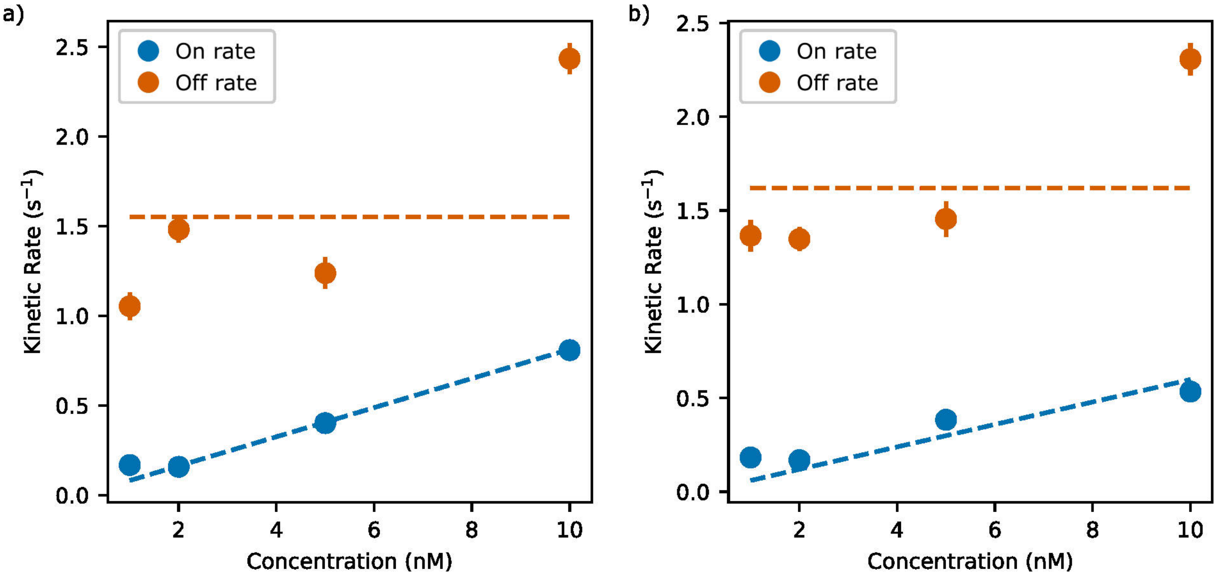

Fig. 4.5: Kinetics of binding of 9 nt long Cy5 imager strands. Binding (blue) and unbinding (orange) kinetic rates of 9-nucleotide-long imager strands to 1xS1 NRO against concentration. a) DNA origami imaged with 96.4 W/cm^2 640 nm illumination. b) DNA origami imaged with 193 W/cm^2 640 nm illumination. Data is the mean±95% CI of the kinetics measured for each origami. Data collected from two independent repeats. For k_{off} a constant value was fitted, while for k_{on} a linear function was fitted with a (0,0) intercept.

values suggest that the kinetics are close to the limits that this technique can assay with the set frame time and number of frames.

To examine the effects of dyes on the binding kinetics Atto643 was also examined the same way as Cy5, by imaging 1xS1 NRO in the presence of 9 nt long imager strands for 15 min at 0.125 ms frametime (Fig. 4.6). The off rate constant k'_{off} of these strands was lower than the ones of Cy5 at 0.87±0.22 s^{-} for the lower laser power (Fig. 4.6a). However, using Atto643 as the imager strand with the higher laser power showed an increase in the k'_{off} 1.09±0.17 s^{-} (Fig. 4.6b). This is likely due to photobleaching. The rate binding k_{on} was also different from that of Cy5. It was observed that it did not follow the linear model with a (0,0) intercept that was expected from the model system. The gradient of the linear fitting for the binding rate constant k'_{on} were 0.02±0.03 $s^{-}nM^{-}$ and 0.04±0.03 $s^{-}nM^{-}$ for the 96.4 W/cm^2 and the 193 W/cm^2 laser power, respectively. This is likely also due to the imager strand being still bound to the binding site without it fluorescing, and thus remaining undetected.

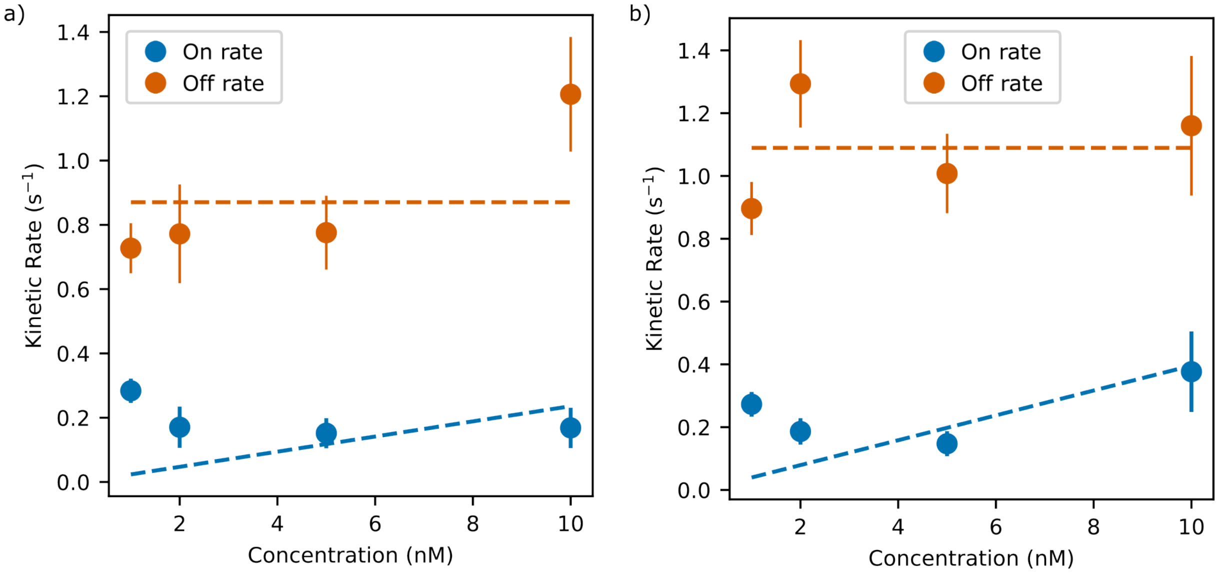

Fig. 4.6: Kinetics of binding of 9 nt long Atto643 imager strands. Binding (blue) and unbinding (orange) kinetic rates of 9-nucleotide-long imager strands to 1xS1 NRO against concentration. a) DNA origami imaged with 96.4 W/cm^2 640 nm illumination. b) DNA origami imaged with 193 W/cm^2 640 nm illumination. Data is the mean±95%CI of the kinetics measured for each origami. For k_{off} a constant value was fitted, while for k_{on} a linear function was fitted with a (0,0) intercept.

The average time of binding would have taken was around 1 s and the time spend between binding events would be between 14 s and 50 s for 1 nM solutions for Cy5 and Atto643, respectively. Thus, the kinetics of the model system is appropriate for attempts of dynamic CoPS measurements.

4.2.2 Dynamic Counting by Photon Statistics

4.2.2.1 Development of dynamic CoPS code

As mentioned before, the CoPS analysis works by fitting the probability of a certain order multiple detection event (mDE) to a mathematical model. To improve the data, fitting the CoPS analysis was updated to a trust region reflective algorithm, which allows for the establishment of boundaries for the number of emitters n and the probability of detection p. With the limitations of the number of binding sites we can expect higher accuracy of the fitting and decrease mistakes due to failure to fit.

To improve CoPS further, new modes of analysis were developed based on what section of the mDE traces is included to better suit the dynamic factor in measurements. The standard CoPS analysis the mDE time trace is divided into equally sized bins of a set amount of pulses (Fig. 4.7a i). For fixed cell experiments, this is appropriate as only the first time bin is analysed to minimize the photobleaching effect that might occur later on in the acquisition. This, however, might lead to errors in the estimation of emitters if a bin contains data from different emitter numbers, which is the case when a molecule binds or unbinds in the duration of a bin.

To solve this a new version of the binning was created, which separates the mDE time trace at timepoints of biding or unbinding. To do that the intensity trace is used to infer state changes of binding and unbinding during recordings (Fig. 4.7a ii). The state inference is done by Bayesian fitting of probabilities developed by the Steve Pressé lab (Arizona State University) (see Sec. 2.2.6). The code was used to determine the timepoints at which binding/unbinding occurs by inspecting the stepwise changes in the intensity trace based on probability (see Sec. 2.2.6). These results are then used in CoPS analysis to separate the mDE traces into different sized bins where the fluorophore number is considered to be consistent. This method, however, is based around the stepwise change in the intensity trace, which might not be possible to distinguish in higher fluorophore numbers.

For that purpose a sliding window analysis has also been developed (Fig. 4.7a iii). This method does not rely on the intensity, but has a greater sampling rate while maintaining the amount of the data that goes into the analysis. In this version of the analysis the bin is moved with a sub-bin sized step, which allows for better sampling of the data without

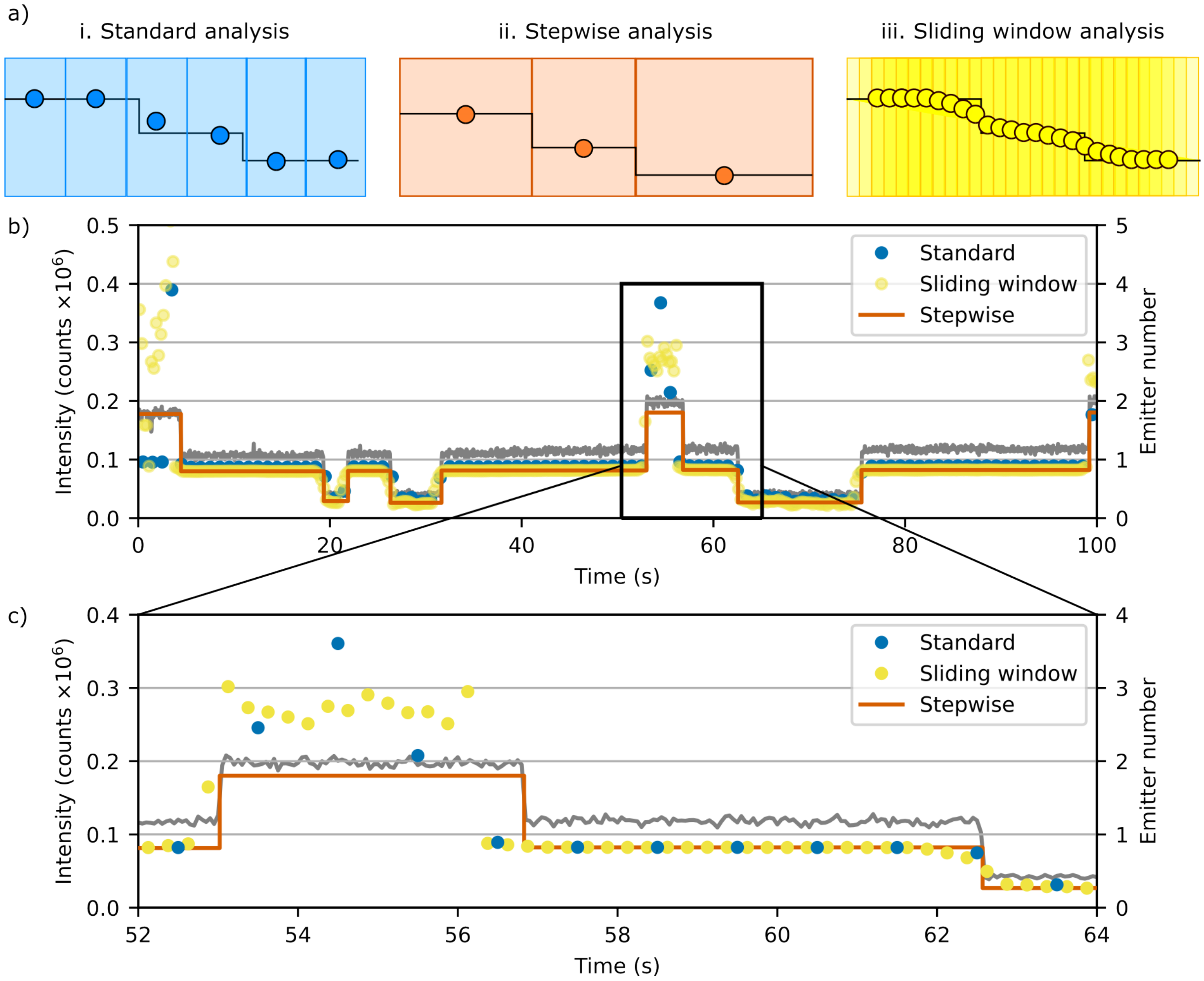

Fig. 4.7: Dynamic CoPS analysis. a) Illustrations of the different analysis methods for dynamic CoPS: i. standard analysis, ii. stepwise analysis, iii. sliding window analysis. b. Example of dynamic CoPS on a 2xS1 NRO recording of 5 nM Cy5 labelling. The intensity trace is shown in gray with the values on the left axis, while CoPS results are plotted against the right axis. The results from the standard (blue) and sliding window (yellow) analysis were done with 1 s binning and 0.1 s step for the sliding analysis and are shown as a scatterplot. The stepwise analysis is shown as a lineplot (orange). c) Zoomed in version of the plot in b) between the 52 s and the 64 s timepoints of the measurement.

making the bins smaller, which can be problematic with a high number of fluorophores. These three techniques have been tested on data from 2xS1 DNA origami data with 5 nM Cy5-labelled 9 nt long imager strands (Fig. 4.7b). The standard analysis was set with a 1 s bin, the sliding window analysis had the same bin moving with a step of 0.1 s. All of the different methods are able to determine the presence of a fluorophore upon binding. However, there is a difference in the results between the transition of on and off states (Fig. 4.7c). For, the standard analysis there were errors in the calculated values at the timepoints of binding and unbinding. These, however, were rare as the rates of binding and unbinding were slow enough. The sliding window analysis yielded similar values, but the sampling over the timepoints where state change occurred lead to a "smudging" of the results.

These methods seemed to perform as expected and the stepwise and sliding window analysis could be valuable in accessing the changes in stoichiometry inside dynamic clusters.

4.2.2.2 Photo destruction

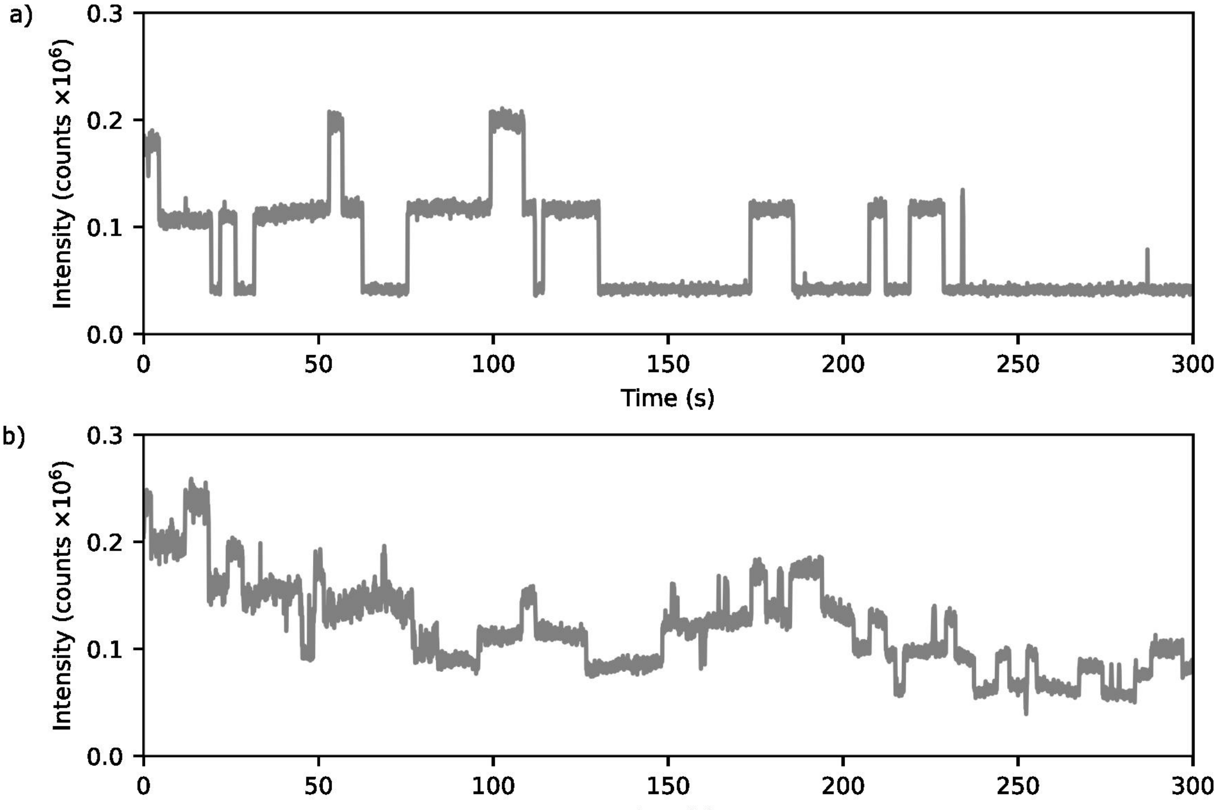

Fig. 4.8: Intensity traces showing photodamage. Intensity traces from 1xS1 (a) and 5xS1 (b) origami labelled with 5 nM 9 nt long Cy5-labelled imager strands. The origami were imaged for 5 min with an average of 6.25 kW/cm^2 laser power.

Despite the ability to assess stoichiometry, observation of longer traces revealed a tendency of the frequency of state changes to decrease in frequency over a period of 5 min when imaged with a pulsed laser at average of 6.25 kW/cm^2 (Fig. 4.8). This was observed in the intensity traces of both the 1xS1 (Fig. 4.8a), as well as the 5xS1

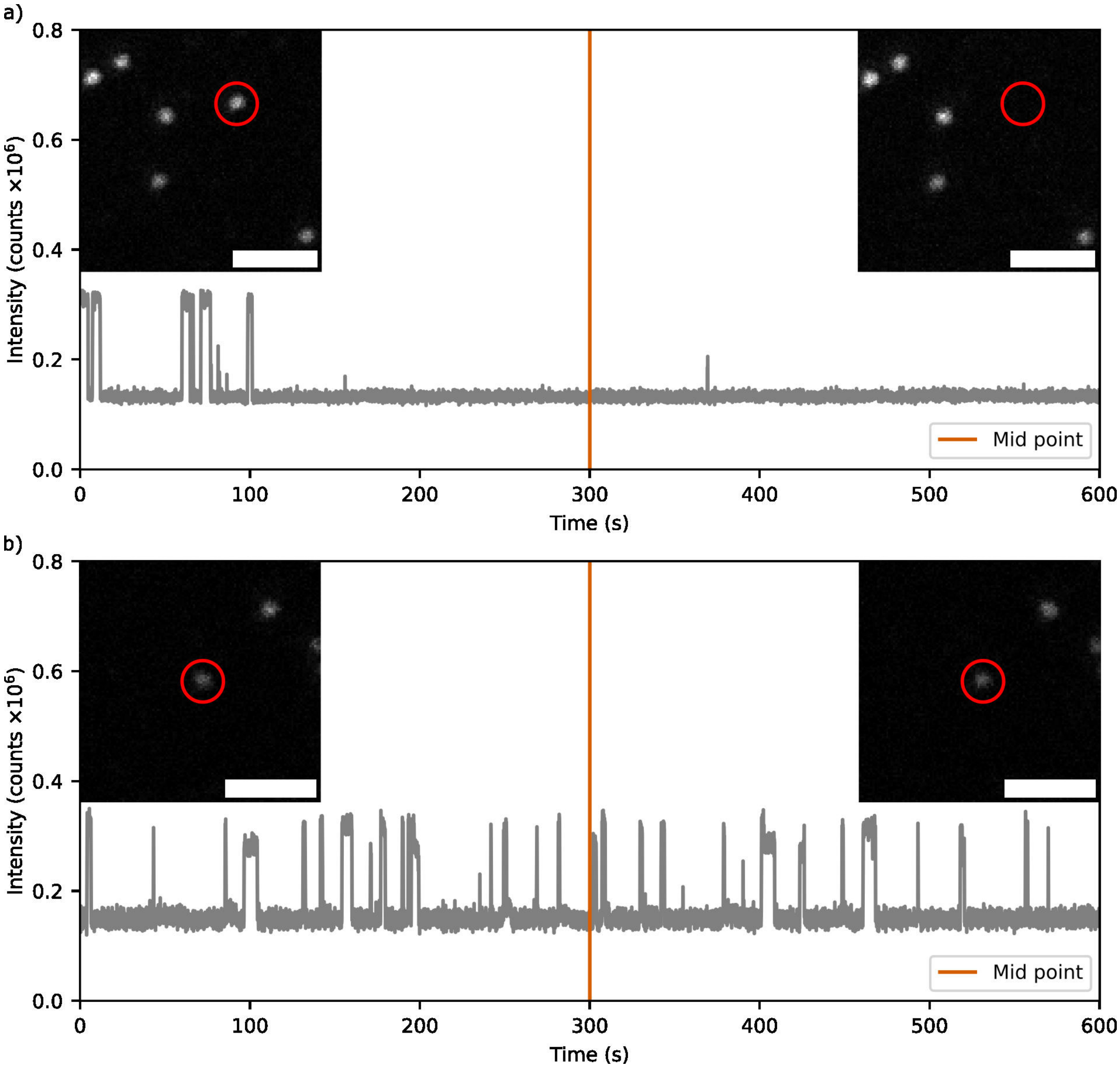

Fig. 4.9: Comparison between the effects of imaging Cy5 and Atto643 imager strands on 1xS1 NRO. Intensity traces from 1xS1 NRO incubated with 1 nM 9 nt long imager strands labelled with either Cy5 (a) and Atto643 (b). Traces are shown in gray and the halfway point in orange. Images of the reference channel before and after the trace was recorded is shown with the origami from which the data was collected circled in red.

(Fig. 4.8b), incubated with 5 nM Cy5-labelled 9 nt long imager strand. To inspect this further a set of experiments were conducted with the same laser power for 10 min. The effects of the fluorophore with which the imager strand were labelled were inspected. For this Atto643, a fluorophore previously used for single molecule DNA-PAINT experiments (157, 158), was compared to Cy5 when used as a label in the imager strand. Experiments were conducted with 10 nM 9 nt long imager strands. Data was gathered for 10 min when imaged with a pulsed laser at average of 6.25 kW/cm^2 for both 1xS1 and 5xS1.

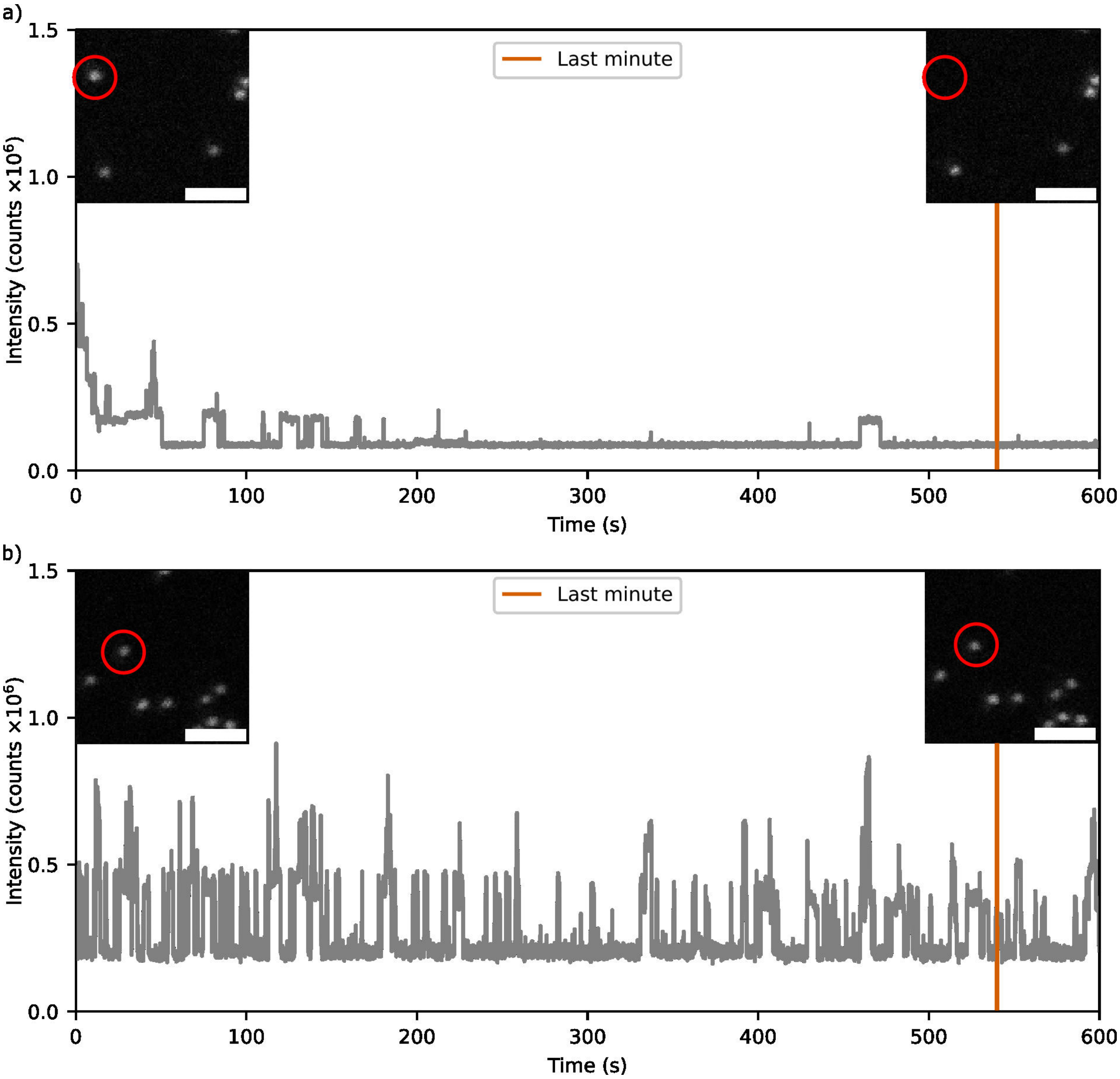

Fig. 4.10: Comparison between the effects of imaging Cy5 and Atto643 imager strands on 5xS1 NRO. Intensity traces from 5xS1 NRO incubated with 1 nM 9 nt long imager strands labelled with either Cy5 (a) and Atto643 (b). Traces are shown in gray and the last minute point in orange. Images of the reference channel before and after the trace was recorded is shown with the origami from which the data was collected circled in red.

Visual inspection of 1xS1 NRO the traces showed that only 25% (n=8) of origami labelled with the Cy5 still exhibited state changes after 5 min (Fig. 4.9a). In comparison, 44% (n=9) of the origami labelled with Atto643 showed state changes after the halfway mark (Fig. 4.9b).

A similar result is shown upon inspection of the 5xS1 NRO with the two dyes (Fig. 4.10). An important thing to point out is the fact that there were state changes in the later half of all traces regardless of fluorophore, in contrast to the 1xS1 NRO. This means that the damage might be done on a docking site basis, and not altogether for the entire NRO. Thus, due to the higher number of binding sites the 5xS1 NRO, traces were inspected for state changes after 9 min. This longer time was determined to provide more time due to the additional binding sites. For the origami labelled with the Cy5 strand 27% (n=11) showed state changes, while the origami labelled with the Atto643 had more surviving origami 44% (n=9).

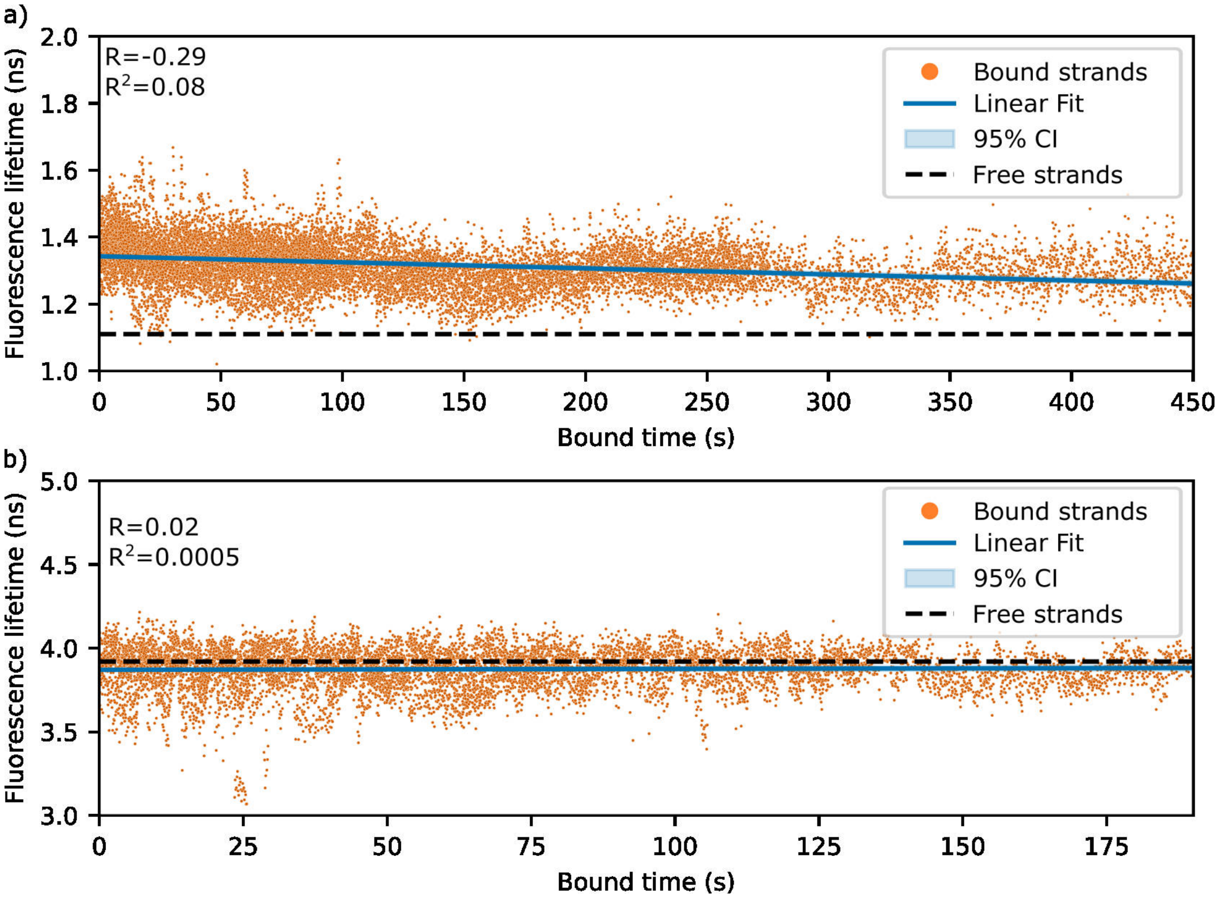

Fig. 4.11: Effects of irradiation of imager strands on fluorescence lifetime. Fluorescence lifetimes (orange) of Cy5 (a) and Atto643 (b) labelled imager strands upon binding of the DNA origami plotted against the time at least one imager was bound and irradiated on the origami. A linear fit was given as well as the 95% CI (blue). The R and R^2 for the fit were given. The lifetime of the free imager strands in the same solution is shown as a black dashed line. a) n=9, b) n=11.

The reference signals of the DNA origami from the Atto542-labelled S2 binding sites signals were also inspected before and after the acquisition. The traces which did not show state changes by the end of recording, also lacked a reference signal. This was observed even when the imager strand was labelled with Atto643 (Fig. SI 5).

The fluorescence lifetime (FLT) of the 5xS1 traces were determined to analyse the potential changes in the environment around the DNA origami. The data from when at least one fluorophore was bound was extracted and the FLT was fitted past the instrument response function (IRF). The two fluorophores had different lifetimes when in solution (Fig. SI 6). The FLT for Cy5 was 1.11±0.01 ns in the buffer, while the Atto643 had a FLT of 3.92±0.01 ns. The lifetime of the Cy5 increased when bound to the DNA origami with values around 1.34 ns, which decreased with the amount of time there was an emitting fluorophore resulting in 1.27 ns at the 400 s mark (Fig. 4.11a). On the other hand, Atto643 had a decrease in its FLT to 3.87 ns, which remained stable during imaging (Fig. 4.11b).

These experiments showed Atto643 might be better suited the high laser power imaging if its higher rate of photobleaching can be overcome. The components of the imaging buffer might need to be explored if there are better alternatives.

4.3 Discussion

The DNA origami provided by the Tinnefeld lab has been shown to be stable and can be immobilised to a glass coverslip functionalised with BSA-biotin and then streptavidin. The best preparation of the coverslip was shown to be HF acid, both due to the thorough cleaning, and the ability to retain the DNA origami binding. This could be due to the modification of the surface of the glass allowing for better BSA-biotin-streptavidin functionalisation. Future experiments can explore HF acid treatment to plasma cleaning of the coverslips, as this would significantly decrease the danger of corrosive damage. Two different buffers were compared and the Red buffer was established as the preferred choice for the dynamic DNA origami experiments due to its lower density of non-specific binding, as well as the amount of time that each non-specific binding lasts. This could be a result of the lower Mg^{+2} concentration or the inclusion of the Tween20.

The kinetics of the 9 nt long imager strand were determined by imaging with approximately 125 ms frame time. Concentration between 2 nM and 5 nM of the imager seemed to yield the best results for imaging as the kinetics of binding was quick enough for short periods where the imager was unbound, while also contributing less background fluorescence.

Developing dynamic versions of CoPS yielded the two new methods of dividing the mDE data- the stepwise analysis and the sliding window analysis. The stepwise analysis can be used on data with lower emitter number and slower kinetics, while the sliding window analysis can be used to monitor the trends of more complex systems.

After the comparison of Cy5- and Atto643-labelled imager strands, the latter showed less photodamage. However, it is not altogether better suited for experiments with the high laser power necessary for CoPS due to its rate of photobleaching. Thus, studies of more fluorophores and imaging buffers need to be conducted, but this was beyond the scope of this project, and thus we proceeded to cell measurements.

Chapter 5

Quantitative *in cellulo* microscopy

This work is currently in preparation for submission and publication: **S. A. Tashev***, J. Euchner*, K. Yserentant*, S. Hänselmann, F. Hild, W. Chmielewicz, J. Hummert, F. Schwörer, N. Tsopoulidis, S. Germer, Z. Saßmannshausen, O. T. Fackler, U. Klingmüller, D.-P. Herten, *“ProDOL: A general method to determine the degree of labelling for staining optimisation and molecular counting.”*

Author contributions:
S.H., J.E. and K.Y. created the ProDOL code. J.E. created performed the dSTORM imaging and analysis, and assisted with 3D structures and plots. W.C. created the single-cell clones. K.M. maintained the stocks of the ProDOL and LynG plasmids, and created the ZAP70-HaloTag plasmid. D.L. performed the flow cytometry. All other work was performed by S.T.

5.1 Introduction

Live cell microscopy is an important tool for analysing biological processes in their natural environment, and it can provide real time information about cellular functions (159). Thus, molecular counting techniques can greatly be improved by the ability to assay live cells. Most counting techniques, however, are not live-cell compatible. One limitation is the time it takes for the measurements, like in single-molecule localisation microscopy (SMLM) or photobleaching step analysis (PBSA). CoPS measurements on the other hand do not require long acquisition times, and thus the analysis can be adapted for live cells, as was described in the previous chapter.

However, any fluorescence imaging can be damaging to the cell due to phototoxicity, thus lower irradiation times and excitation intensities are required to keep the cells viable (160, 161). The wavelength of imaging needs to also be considered due to both the higher background at shorter wavelengths, as well as the higher generation of ROS. Modalities that decrease the region of illumination also limit the amount of the cell exposed to the excitation light.

There are also practical limitations during the imaging of live cells, for example, the necessity for a consistent temperature and 5% CO_2 concentration, as well as specialised media (162). Moreover, components within the media required for optimal conditions must not add to the background fluorescence in the sample.

Not only is live cells imaging challenging, but as mentioned in Sec. 1.2.6, quantitative imaging inside live cells is more difficult still. It requires not only the investigations of the labelling stoichiometry, but also the effects of the cellular environment on the fluorescence. Additionally, microscopy of living cells means the imaging of a dynamic and mobile system, with target proteins within the cells able to form and break down complexes. Thus, picking an appropriate target protein and model organism, can be vital to the success of live cell experiments. All of these issues must be examined before protein counting inside living cells via CoPS is possible.

5.1.1 Degree of labelling determination

As discussed in Sec. 1.2.7, there exist multiple methods that can perform molecular counting. However, it is important to distinguish between the number of fluorescent emitters and the number of protein of interest (POI). In Sec. 1.2.6 the multiple different factors that can effect the fluorophore:POI ratio were covered. To successfully count protein copy number inside of cells, the relationship between label and protein numbers needs to be determined. When it comes to immunolabelling there are two factors to consider, the stoichiometry of fluorescent labels per antibody and their binding affinity (see Sec 1.2.4). When it comes to protein tag labelling, the binding stoichiometry can be at most 1:1, i.e., 1 tag to 1 fluorophore, which leaves the labelling efficiency dependent on the reaction between the ligand and the expressed tag.

Previously, degree of labelling (DOL) determination required a calibration standard of known stoichiometry. One such technique, called effective labelling efficiency (ELE), was introduced in Thevathasan, *et al.* 2019 (76), where the nuclear pore complex (NPC) was used as an intracellular standard (Fig. 5.1a). ELE relies on the structure and the 8-fold symmetry of nucleoporins inside of the NPC. Direct stochastic optical reconstruction microscopy (dSTORM) is used to resolve the structure of the NPC (Fig. 5.1b). After individual NPCs are identified, the radial symmetry is fitted to the localisations (Fig. 5.1c).

Each sector is then inspected and if it contains at least two localisations it is labelled. The number of sectors stained are then fitted into a binomial distribution of the probability of labelling a sector to give the DOL, which is one of the parameters in that distribution. This analysis depends on all copies of the nucleoporin to be linked to a protein-tag. This limits the flexibility of the technique to certain CRISPR-transformed cell lines.

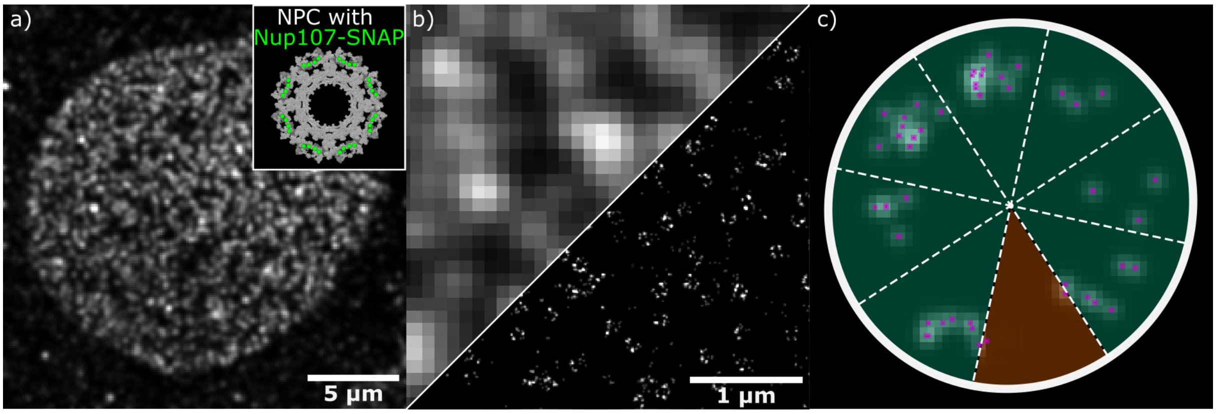

Fig. 5.1: Effective labelling efficiency. a) The effective labelling efficiency analysis starts with the aqcuisition of TIRF/HILO images of the nucleus. The structure of the NPC is shown in the box on the left with the Nup107 nucleoporin in green. b) Localisation analysis and reconstruction of the NPCs. c) Fitting of the 8-fold symmetry and counting the labelled sectors (green). The unlabelled sectors are in orange and the localisations themselves in magenta.

In the past year there have been two independent papers addressing these concerns in the exact same way- colocalisation analysis (92, 163). While Hellmaier, *et al.* 2024 allows for the determination of labelling efficiency for antibodies, Tashev, *et al.* 2023 is focused on protein-tag labelling. The latter became a part of this work and was named protein-tag degree of labelling (ProDOL).

5.1.1.1 ProDOL

The ProDOL method relies on the sub-pixel colocalisation of spectrally different fluorophores. One of these serves as a reference, while the other one is the labelling of the protein tags. The ProDOL method is separated into two parts: the probe and the analysis software (Fig. 5.2). The probe is a single polypeptide chain sequestered to the plasma membrane via post-translational modifications on the N-terminal, which is a segment of the kinase Lyn (Fig. 5.2a). This is directly followed by enhanced green fluorescent protein (eGFP), which serves as a fluorescent reference signal. In this version of the protein, the reference is followed by a HaloTag and SNAP-tag connected a via short linker. The probe also features a His-Tag for purification purposes. To complement this probe a control probe was also designed, which features only the Lyn-Anchor and the eGFP. This probe was called LynG and can be used to determine non-specific binding. Determination of the ProDOL comes from the colocalistion of the tag signal to the reference signal divided by the total reference signal (Fig. 5.2b).

The ProDOL analysis can be split into seven steps which turn the localisation of signal to a corrected DOL value (Fig. 5.2c). First, multiplexed single-molecule images are acquired by total internal reflection fluorescence microscopy (TIRFM) (i), then a segmentation mask is created from the image in the reference channel to exclude non-specific signalling from outside of cells (ii). The signals from all channels are localised using ThunderSTORM to give subpixel localisation (iii). An affine transformation matrix is applied to the coordinates of the localisations to correct for chromatic aberration and other optical artefacts (iv). Next, an initial colocalisation value is calculated (v) by determining a cut-off distance threshold T at which specific colocalisation is maximised, while random colocalisation is kept to a minimum. The colocalisation is then adjusted for emitter density to avoid factors which would lead to underestimation of the degree of labelling (DOL) (vi). The DOL is then determined on a cell-wide basis and the results for each tag are grouped and presented into box plots (vii).

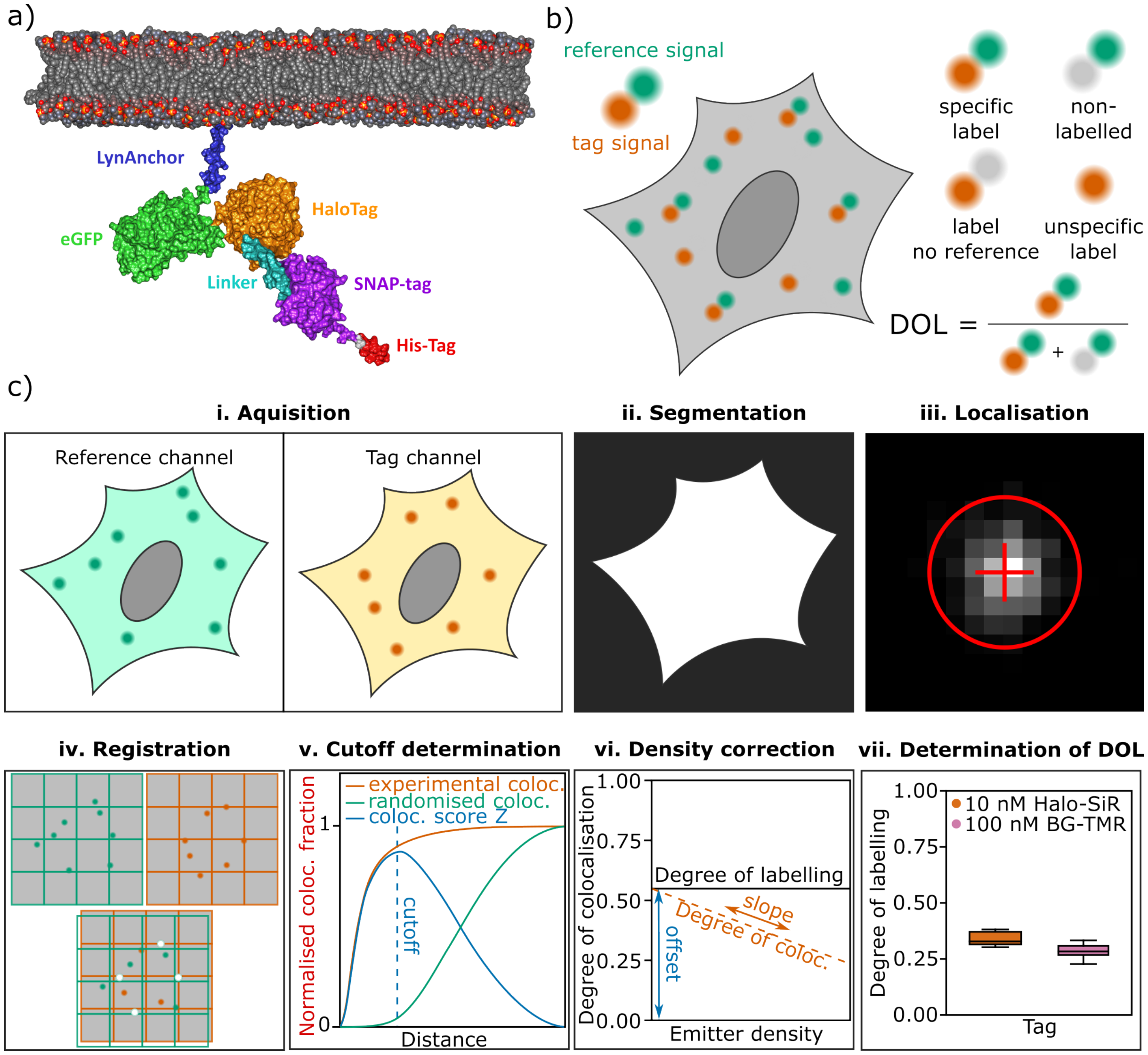

Fig. 5.2: The ProDOL concept. a) ProDOL probe attached to a lipid bilayer via a Lyn-Anchor (blue), and contains eGFP as a reference (green), Halo-tag (orange) and SNAP-tag (magenta) with a linker inbetween. The construct also has a His-tag (red). b) The concept of ProDOL determining labelling degree by colocalisation. c) A step-by-step breakdown of the ProDOL analysis pipeline. Adapted from Tashev, *et al.* 2023.

5.1.2 Live cell imaging buffers

As previously stated, excitation of molecules can create reactive oxygen species (ROS) via their triplet state, which can result in phototoxicity. Another cause of phototoxicity can be the dye itself reacting with biological molecules (164). Thus, excitation of any intensity causes a certain amount of phototoxicity (161). Part of the solution is using the least amount of irradiation as possible, as well as using dyes in the red or far red spectrum to avoid excitation of natural fluorophores.

However, for CoPS to work one of the requirements is the consistent fluorescence emission of each fluorophore meaning the triplet states need to be addressed. In fixed-cell imaging reducing and oxidising system (ROXS) buffers regularly use an oxygen depletion component together with a triplet quencher to reduce photophysical effects (7, 76, 92, 165). Although, oxygen can be reduced while maintaining some cellular functions (166, 167), it could reduce the biological relevance of the results. However, triplet quenchers can still be utilized to reduce ROS generation. Certain cell media, such as FluoroBrite (FB), were created specifically for fluorescence microscopy of live cells (168). It exhibits less background fluorescence due to the removal of certain vitamins. Some of these vitamins however, could be used as triplet quenchers. One example is ascorbic acid (AA). AA was has been found to alleviate disruptions in the mitotic cycle caused by phototoxicity when imaging live cells (169).

Further changes stem from a decrease of CO_2 concentration in the imaging system compared to the 5% inside of the incubator, causing a significant change in the pH. To tackle this 10-25 mM of 2-[4-(2-Hydroxyethyl)piperazin-1-yl]ethane-1-sulfonic acid (HEPES) can be added to the imaging medium for compensate, giving superior pH stability. (162, 166, 170). This, however, needs to be balanced with other components in the media so to not change the pH of the media (171).

The base media, as well as the additives need to be examined to determine the best combination for cell viability and fluorescence imaging results.

5.1.3 The immune synapse

T cells are a part of the adaptive immune response and are responsible for the recognition of antigens on antigen presenting cellss (APCs). Upon contact of the two cells an immunological synapse (IS) is formed between them (5, 172). Detection of non-self antigenic material by the T cell causes the cell to become activated and the signalling molecules at the contact surface are reorganised into a "bullseye" pattern, called the supramolecular activation complex (SMAC) (Fig. 5.3). The SMAC, as defined by Kupfer, is divided into central (cSMAC), peripheral (pSMAC), and distal (dSMAC) (5). The cSMAC is composed by T-cell receptor (TCR)-CD3 complexes, as well as co-receptors, such as the CD4 or CD8, CD28 and CD2, while the pSMAC consists of attachment molecules, such as lymphocyte function-associated antigen (LFA-1) and other integrins. The dSMAC is easily distinguishable by the high density of F-actin, forming an actin ring at the periphery of the synapse (173), and contains proteins with large ectodomains, such as CD43 and CD45, and filamentous actin (F-actin) (174) (Fig. 5.3b). dSMAC is similar in function to a lamellipodium, extending and contracting, while the pSMAC acts as a lamellum. During activation the IS is relatively constant, but elements of the SMAC are dynamic and are continuously renewed (e.g, TCR and LAT recycling, and SLP-76 and ZAP70 recruitment) (175).

5.1.4 T cell activation

The classical T cell signalling pathway starts with the recognition of an antigen-presenting major histocompatibility complex (MHC) complex (Fig. 5.4). The stable bond allows for the CD4 co-receptor to bind, releasing Lck, a Src kinase homologue

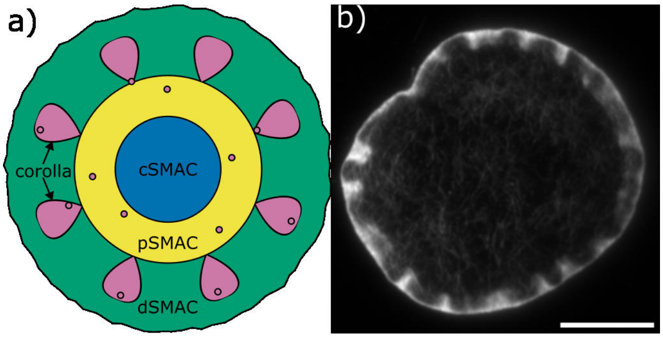

Fig. 5.3: Structure of the SMAC. a) Illustration of SMAC with the central (blue), peripheral (yellow) and distal (green) regions shown. Also included are the CD2 corolla (pink). b) Actin ring organisation of activated Jurkat cells stained with phalloidin-AF647. Scale bar 5 µm.

(176). The Lck phosphorylates tyrosine (Tyr) residues on ITAM motifs of the CD3 complex(177), made up from the δ, ε, γ, and ζ chains. Phosphorylation of CD3 ζ leads to the recruitment of the Zap-70 kinase which also gets phosphorylated by Lck (178). This activates Zap-70, which in turn phosphorylates LAT, a scaffold protein, and the SLP-76 adaptor protein. These two proteins interact with the downstream proteins of the pathway leading to the cellular response.

One of these proteins, PLCγ1, together with co-stimulation from CD28, a transmembrane co-receptor, leads to the calcium release in the cytoplasm of the T cell (179). CD28 also plays a vital role for transcriptional changes, and cytoskeletal remodeling (180). Meanwhile, another co-receptor, CD2, affects the phosphorylation of members of the signalling cascade proximal to the TCR (181). SLP-76 phosphorylation also allows cytoskeletal remodeling via recruitment of Vav and NCK (182), and disruption of this pathway prevents the formation of the actin ring.

5.1.5 Clustering in T cells

T cell function requires them to be sensitive to the small reserve of the APC's MHC-antigen complex (2), in addition to a potentially weak affinity interactions between the

TCR-antigen connection (183). As mentioned in Chap. 1, one way to increase the sensitivity to ligands is clustering. In T cell activation, the initial signal is amplified via TCR clustering (184). While the initial stoichiometry of TCRs prior to activation is in dispute (185), it is known that seconds after the TCR's form sub-micron assemblies called microclusters microclusters (MCs). It has been shown that MCs increase in size and stoichiometry as they travel to the cSMAC (186, 187). CD3 is also a integral component MCs and CD3ζ is shown to trigger T cell activation in a ligand-independent manner when clustered (188). The formation of MC containing downstream molecules has also been observed, however, each of them exhibit different behaviour in both kinetics and localisation (189). The ZAP70 and the SLP-76 are both cytosolic proteins that get recruited into clusters on the plasma membrane, thus acting similarly to the recruitment of imager strands to the DNA-origami in the previous chapter. Thus we decided to investigate the recruitment of SLP-76 to MCs.

In this chapter, the optimal conditions for inspecting SLP-76 in live cells were determined. This included the live cell imaging buffer, which required validation in a stable system for CoPS measurements. The suitability of NPC for these measurements was determined. The SLP-76 cluster stoichiometry was determined in fixed cell in combination with the ProDOL, which was also validated. Following that SLP-76 clusters were also examined in live cell experiments.

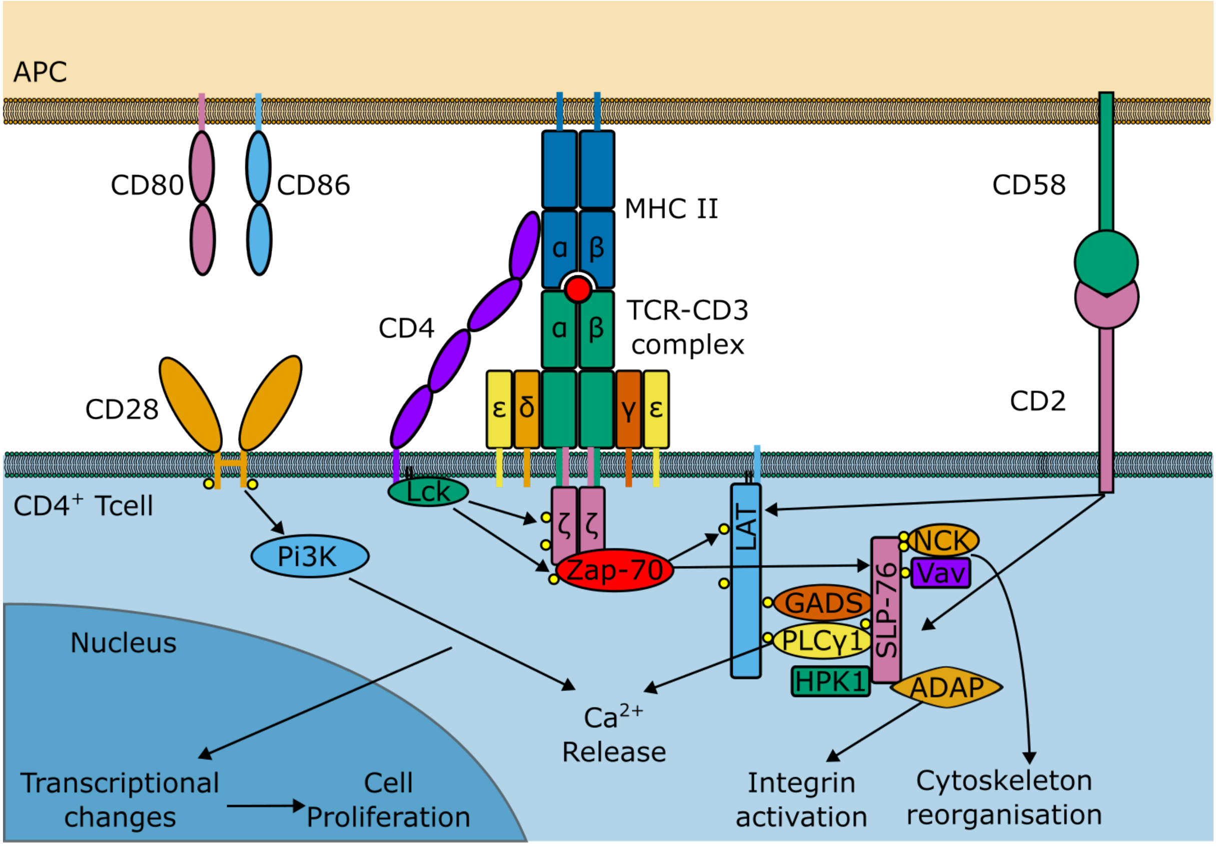

Fig. 5.4: T cell activation pathway. Illustration of the classical pathway of T cell (blue) activation by an APC (orange). The case is shown for CD4$^+$ T cells, which specifically recognise an MHCII-antigen complex.

5.2 Results

5.2.1 Validation and application of the ProDOL approach

5.2.1.1 Validation of ProDOL approach

The ProDOL analysis is a powerful tool for determining the degree of labelling. However, to determine its accuracy it needed to be validated in its ability to estimate the DOL of protein tag labelling by comparison other techniques, e.g. ELE. For all approaches, U2OS cells were labelled with 1 µM BG-AF647. For ELE, dSTORM was utilised to assay the labelling efficiency of a Nup107-SNAP-tag in an NPC. The cell line had both alleles of Nup107 switched with the tagged version. On the same cell line, CoPS and PBSA were used to determine the number of fluorophores per NPC, then divided by the expected stoichiometry of Nup107 per NPC (i.e., 32 copies). ProDOL was conducted on U2OS cells transfected with the ProDOL construct processed the same way. ProDOL analysis resulted in a DOL of 42.6±5.3 % (median±SD). This is consistent with the other methods which utilized the NPC labelling where the efficiencies were determined to be 42.2±4.1%, 40.6±5.8% and 40.5±4.9% for ELE, quickPBSA, and CoPS, respectively (Fig. 5.5a). All methods showed a high degree of statistical agreement (p=0.330, Kruskal-Wallis). To validate the method for live-cell staining, cell were stained with 200 nM BG-SiR, and both ProDOL and CoPS were compared to determine the respective measured labelling efficiencies, i.e., 36.1±12.0% and 36.3±7.9%, respectively. There was no statistical significance between the ProDOL and CoPS measurements (p= 0.707).

These set of experiments confirmed the ability of ProDOL to measure the DOL accurately upon both pre- and post-fixation cell labelling.

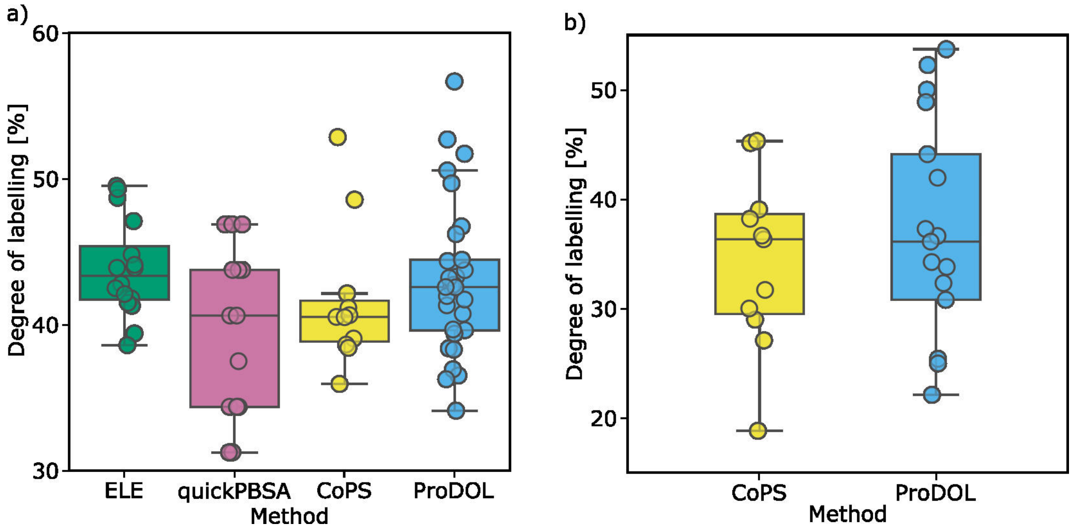

Fig. 5.5: Cross validation of the ProDOL approach. a) Cross-validation of the ProDOL after post-fixation labelling with 200 nM BG-Alexa Fluor647. Box and whisker plot of cell-wide DOLs determined by the indicated methods. N=16, 15, 11, 29 cells were analysed with ELE, quickPBSA, CoPS and ProDOL, respectively. b) Cross-validation of ProDOL after pre-fixation labelling with 200 nM BG-SiR. Box and whisker plot of cell wide DOLs after pre-fixation labelling determined by DOL (n=17 cells) and CoPS (n=11 cells). The ELE, CoPS and PBSA were performed in U2OS cells with two CRISPR-modified alleles attaching SNAP-tag to Nup107. The ProDOL was performed on U2OS expressing the construct. ELE was performed by Jonas Euchner.

5.2.1.2 Degree of labelling in Jurkat cells

For single molecule measurements to be performed the parameters for staining, i.e. concentration and incubation time, need to be adapted to determine the optimal conditions for the required experiment. To investigate the labelling of proteins inside Jurkat cells, staining was performed with HA-SiR at different incubation times and concentrations. Initially, to determine the non-specific labelling, cells expressing the LynG construct (see Sec. 5.1.1.1) were labelled with 0.1 to 100 nM of HA-SiR for 15 min to 16 h. There was very little signal present in the cells showing an non-specific binding inside of cells (Fig. 5.6a). This also resulted in DOL values of less than 10% across all parameters (Fig. 5.6b). ProDOL analysis on the cells expressing the full probe shows a steady increase in labelling until plateauing at approximately 50%, with the exception of the 16h incubation which reached approximately 75% (Fig. 5.6c).

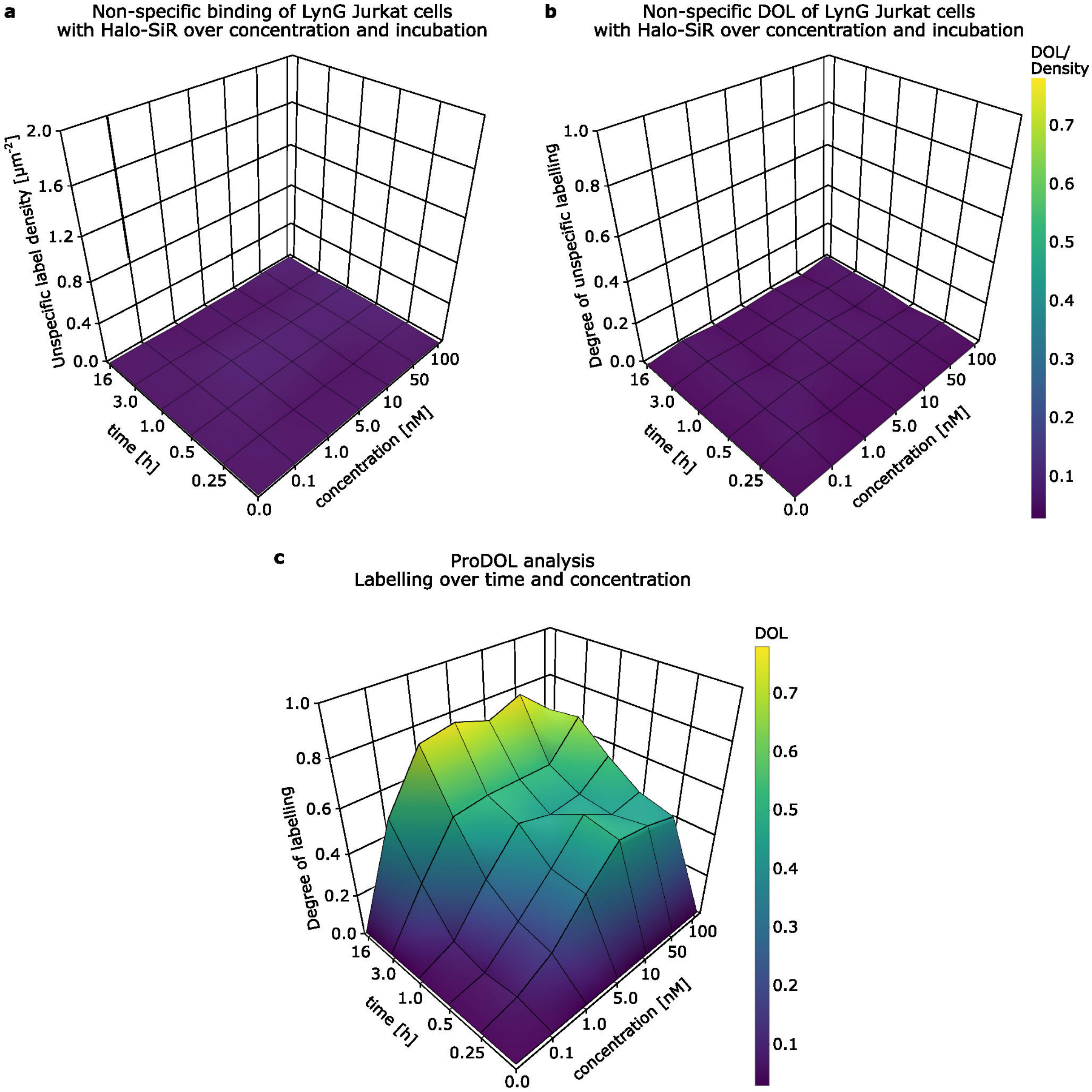

Fig. 5.6: Degree of labelling of ProDOL constructs in Jurkat cells. Cells expressing either the LynG or the ProDOL probe were stained with HA-SiR with different parameters. a) Non-specific labelling density found in Jurkat cells expressing the LynG probe after staining. b) The DOL values from the ProDOL analysis in Jurkat cells expressing the LynG probe. c) The DOL values from the ProDOL analysis in Jurkat cells expressing the ProDOL probe. The values shown in the 3D plots are the medians for each labelling condition. The values are given in a cell-wide fashion. $30 \leq n \leq 50$.

The ProDOL method shows accurate estimation of the degree of labelling of protein tags across different labelling protocols. The method was also established by assaying the effects of concentration and incubation time on labelling efficiency in Jurkat cells.

5.2.2 CoPS in live cells

5.2.2.1 Effects of imaging media on fluorescence

Before proceeding with live cell quantitative imaging, the optimal conditions for fluorescence measurement needed to be established. To determine those, imaging experiments with a diverse range of cell media compositions was conducted and the effect on fluorophore behaviour was inspected.

Here, U2OS cells expressing the NUP107-SNAP-tag were used as a model to determine effect of media composition on the photophysical characteristics of SiR (Fig. 5.7a). The photobleaching rate of SiR was determined by measuring the decrease of the intensity of the individual NPCs. These are then summed and normalised, before an exponential decay is fitted. The fluorescence half-life $t_{1/2}$ was then determined by:

$$I(t) = I_0 \left(\frac{1}{2}\right)^{\frac{t}{t_{1/2}}} \tag{5.1}$$

where I_0 is the initial intensity and $I(t)$ is the intensity at time t (Fig. 5.7b). Three different base media were used- Dulbecco's modified eagle medium (DMEM), RPMI-1640 and FluoroBrite (FB) (Fig. 5.7c). The addition of ascorbic acid (AA), and AA with 2-[4-(2-Hydroxyethyl)piperazin-1-yl]ethane-1-sulfonic acid (HEPES) to base media were examined.

The fluorescence half-life showed a statistically significant difference ($p<0.05$, Kruskal-Wallis). However, the post-hoc Dunn's test resulted in no statistically significant values after Bonferroni correction with most values being between 1.5 s and 2.5 s. Notably, the addition of AA, seemed to increase the bleaching rate except for in FB where the

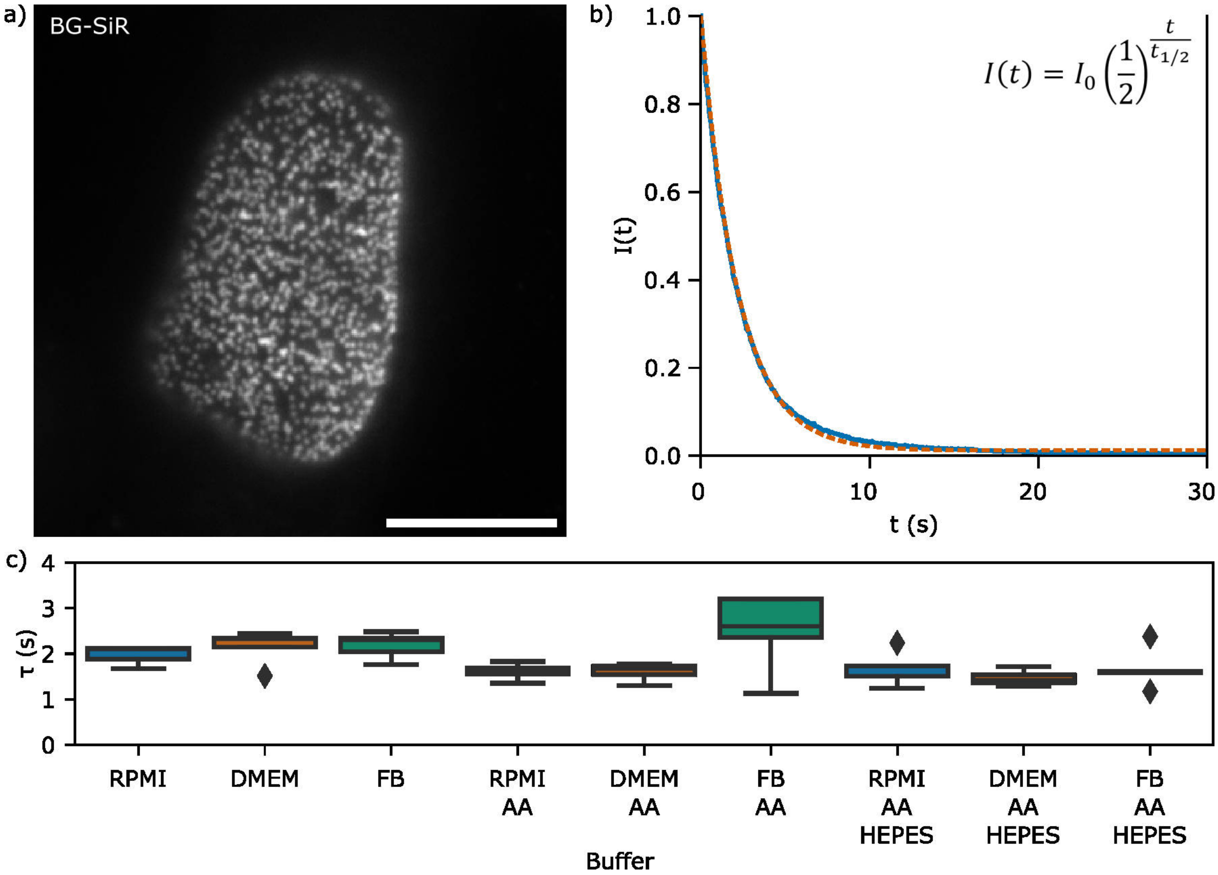

Fig. 5.7: Buffer effects on photobleaching rate. a) Representative highly inclined and laminated optical sheet (HILO) image of U2OS cell expressing Nup107-SNAP-tag stained with 200 nM BG-SiR. b) Example bleaching curve (blue) from a single cell imaged in RPMI fitted with an exponential decay function (orange). c) Fluorescence half-life $t_{1/2}$ of SiR in live U2OS cells imaged in different buffers. n=5 cells for each condition. Scale bar is 10 µm.

bleaching was lower overall. However, the cells in that sample also had morphological aberrations (Fig. SI 7). A smaller trend observed is the increase in photobleaching seen in RPMI base media samples where slightly lower bleaching rates were observed except for the sample containing AA.

Visually inspecting the traces, no photobleaching steps could be distinguish when imaging in DMEM (Fig. 5.8a). In comparison, the media containing AA exhibited some step-like patterns and showed smaller fluctuations in intensity (Fig. 5.8b). Similar properties could be found when imaging in DMEM supplemented with both AA and HEPES (Fig. 5.8c). These two, however, showed a greater degree of intensity fluctuation than fixed cell samples, which were imaged in ROXS buffer (Fig. 5.8d).

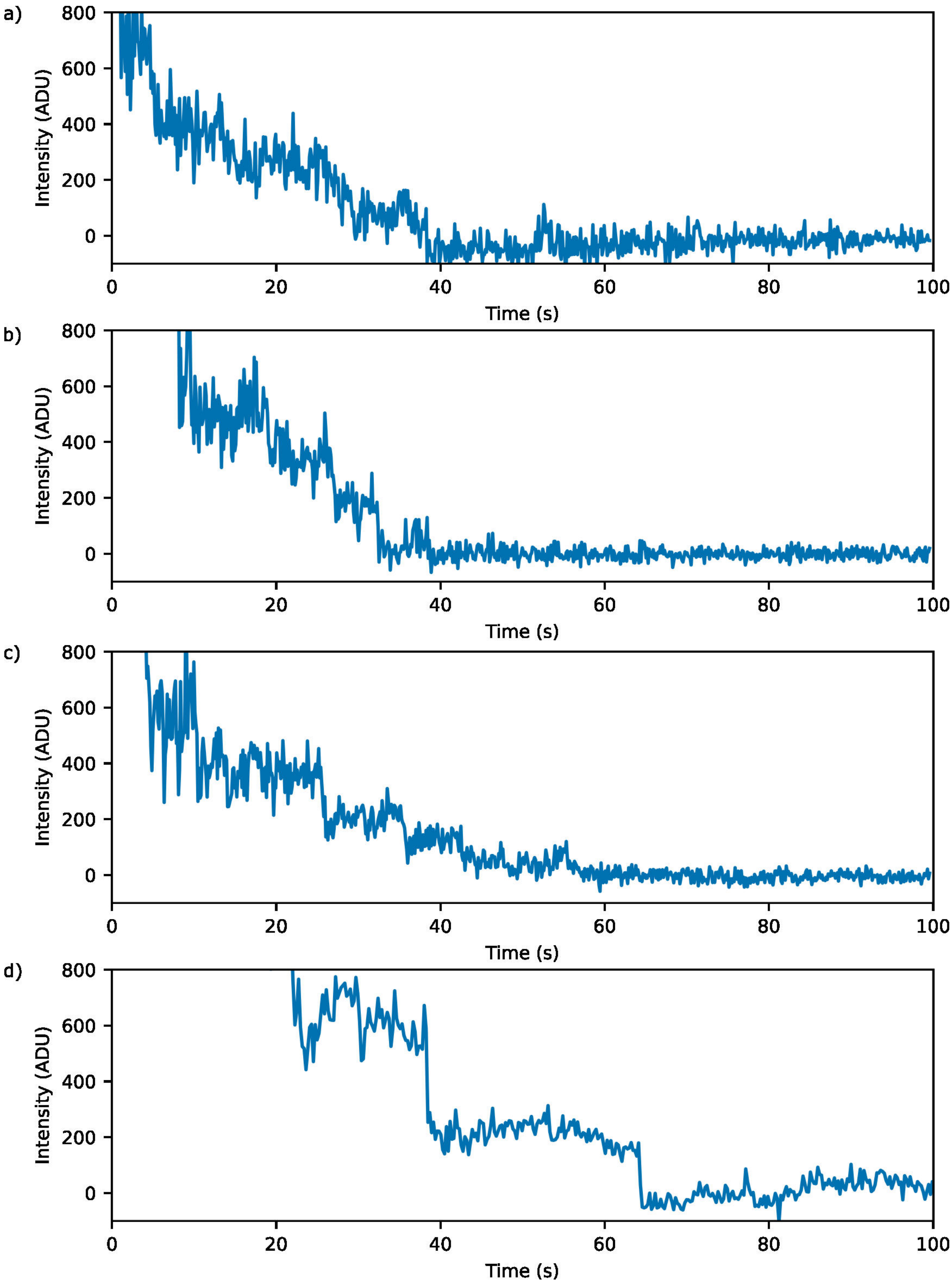

Fig. 5.8: Intensity fluctuations in different imaging media. Zoom in of representative intensity traces of the SiR-labelled Nup107-SNAP-tag. a) DMEM, b) DMEM with the addition of AA, c) DMEM with AA and HEPES, d) ROXS buffer. Examples of full intensity traces can be found in Fig. SI 8.

The inclusion of the AA showed a stabilising effect on photoblinking, which was promising enough to proceed to live cell CoPS.

5.2.2.2 Sample drift in live cells

After determining the suitability of the buffer, Nup107-SNAP-tag was inspected to determine its suitability for single-point measurements, such as CoPS. Movement of the diffraction limited clusters would have a significant effect on the ability to perform the single-point measurements required for CoPS. As a large structural component of the nuclear membrane, the NPC is relatively immobile, thus the only movement expected is the movement of the cell itself and not diffusion of the complex. To examine the applicability of CoPS on NPCs inside live cells, both fixed and live U2OS cells were examined after staining under the same conditions. The fixed cells were imaged in ROXS buffer while the live cells were imaged in DMEM. Single particle analysis was performed and traces less than 150 s were examined to ensure equal time windows despite the effects of the different buffers on photobleaching (Fig. 5.9).

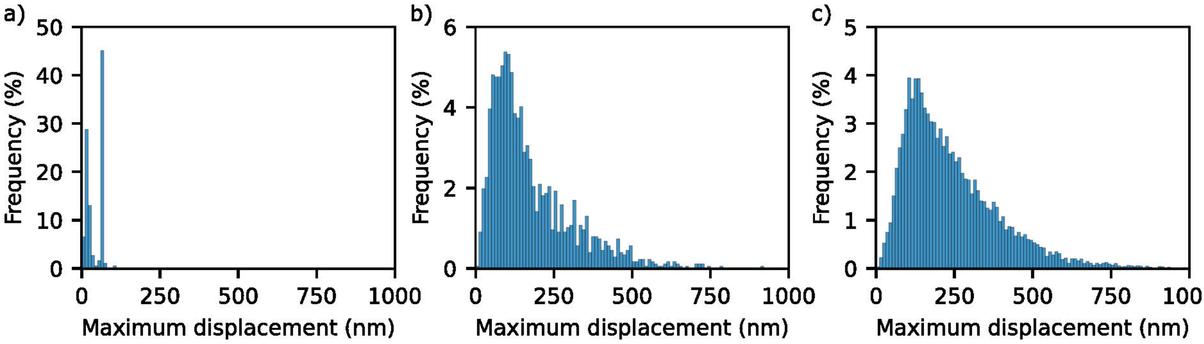

Fig. 5.9: Maximum displacement comparison in different samples. Histograms of the maximum displacement of a) a bead sample, b) fixed U2OS cells, c) live U2OS cells. Cell samples had their Nup107-SNAP-tag stained under the same conditions- 200 nM BGSiR . Traces were extracted and those less then 150 s long were examined to ensure equal time windows. a) n=184 traces, b) n=18662 traces, c) n=3222 traces.

Additionally, bead samples were imaged in PBS as a bright stationary standard. The maximum displacement was plotted in Fig. 5.9a to show the best case scenario of sample drift. The bead sample showed smaller maximum displacement (37±2 nm, median±SE) compared to the cell samples, likely due to the reduced uncertainty of the localisations compromising the traces. This stems from the high fluorescence intensity of the beads. The cell samples had larger distributions of maximum displacement with 205±1 nm in live cells and 137±3 nm in fixed cells (Fig. 5.9b and c). Given the radius of the FWHM of the confocal spot is around 300 nm, recording of NPCs in live cells is feasible without needing to account for drift in the sample at short recording times.

5.2.2.3 Live cell CoPS measurements of NUP107-SNAP-tag

Live cell CoPS, in this iteration, requires discrete protein complexes with little diffusion of those complexes. NPCs are large molecular structures that are relatively immobile with a stable protein stoichiometry, making them an ideal initial target. To determine the ability of CoPS to count the number of proteins inside of molecular clusters U2OS cells were used as a standard expressing Nup107-SNAP-tag. These were stained with BG-SiR and CoPS, as well as PBSA, were used to determine the number of fluorophores per NPC, after which using ProDOL the stoichiometry of the complex was determined and compared to the expected stoichiometry - 32 copies per NPC.

Two independent repeats of these experiments were conducted with 36.1±1.9% and 40.2±2.0% DOL as determined by ProDOL. As controls for the live cell quantification, both PBSA and CoPS were used on fixed cells stained under the same conditions, and then imaged in ROXS buffer. In fixed cells, the PBSA analysis determined 33.8±0.2

copies of the nucleoporin per NPC, which was close to the CoPS results (29.8±0.6 copies/NPC), which were also recorded in the same sample.

In live cells DMEM alone, or supplemented with AA and HEPES, was used as a live cell imaging buffer. Using CoPS, the estimated stoichiometry for cells imaged in DMEM was 67.1±2.1 Nup107 per complex. Interestingly, with the addition of the AA and HEPES the estimated number of Nup107 per cluster decreased to 59.5±2.5. Only the fixed sample assayed with CoPS does not deviate significantly from the expected value of 32 copies (p=0.82, one sample t-test). The significant deviations in live cells could be due to the photoblinking observed in Sec. 5.2.2.1.

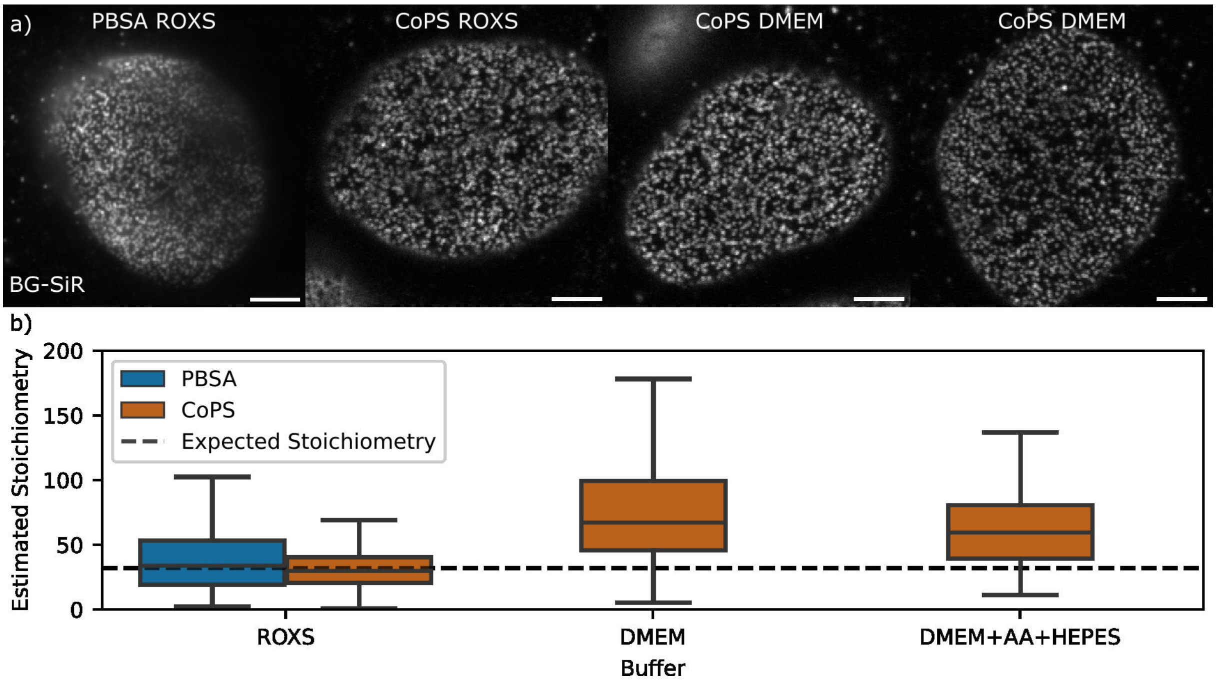

Fig. 5.10: Live cell CoPS on Nup107-SNAP-tag. a) Representative HILO images of U2OS cell expressing Nup107-SNAP-tag stained with 200 nM BG-SiR taken with TIRFM, or confocal for CoPS. b) Results of PBSA (blue) and CoPS (orange) analysis corrected with the DOL results from ProDOL analysis. Data gathered from two independent experiments. n in clusters from left to right: 12765, 572, 398, 139. Scale bars are 5 µm.

5.2.3 Quantification of SLP-76 inside microclusters

5.2.3.1 T cell activation on functionalised coverslips

Inspection of the formation of the IS requires for the T cells to be activated. This is regularly done by an anti-CD3 antibody. To ensure that the Jurkat cells were properly activated, within the timescales of imaging, the phosphorylation of CD3 and the size of the immunological synapse (IS) were observed. To allow imaging of T cells a surface coating can be prepared that not only activates, i.e., induces signaling, but also adheres the cells to the glass coverslip. Coverslips were functionalised with different coatings to determine their activatory effects. The phosphorylation of CD3 was determined by an anti-pCD3 antibody conjugated to a fluorophore, while the size of the IS was determined by TIRF imaging of the cytoskeleton on the basal side of the cell.

Initially, experiments were conducted to observe the effects of the PLL coating on signalling and attachment. However, these revealed difficulties for the attachment of Jurkat cells to the glass coverslip as shown by a low cell density on the coverslip (Fig. SI 11). The few adhered cell were imaged and the results shown in Fig. SI 11f.

Activation was determined via anti-pCD3 staining intensity and cell adherence by the area of the actin ring (Fig. 5.11a). The IS area when bound to a PLL-coated coverslip increased significantly with anti-CD3 antibody from 101±40 µm^2 to 287± 20 µm^2 (median+SE) ($p<0.05$), while no significant increase was observed when CD90 was bound to the coverslip (215±33 µm^2) (Fig. 5.11b). The addition of the anti-CD28 antibody resulted in a further increase to 346±28 µm^2 ($p<0.001$).

The amount of CD3 phosphorylation found in MC has been found to follow a similar pattern with the addition of CD3 showing a significant increase from around 319±36 pho-

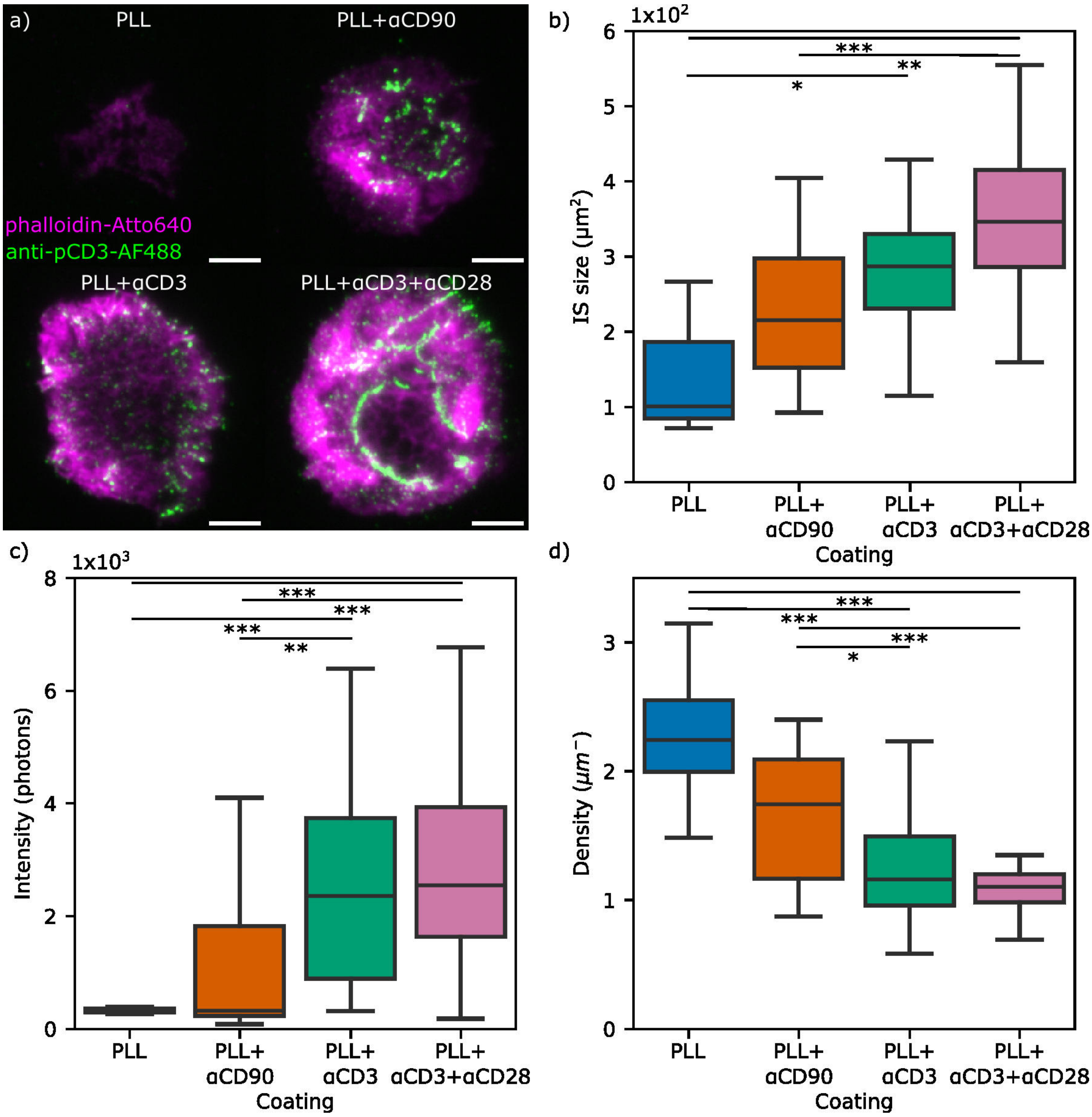

Fig. 5.11: T cell activation by different coverslip coating. a) Representative total internal reflection fluorescence microscopy (TIRFM) images of Jurkat cells activated by different coverslip surface coatings. Activation was determined by the intensity of staining by an anti-pY145-CD3 antibody conjugated to Alexa Fluor488 (AF488) (green) with a phalloidin-AF647 (magenta) to label F-actin. b) Area of the IS on different coverslips coatings determined by the actin stain. c) Intensity of the pCD3 signal determined by localisation software (ThunderSTORM). d) Density of the pCD3 clusters determined by dividing the number of localisations by the area of the IS. a) Scale bars are 5 μm. Boxplots show the values on a cell wide basis with sample number in cells equaling 11, 25, 39, and 31 for the different coating left to right. Results of Dunn's test (post-hoc after Kruskal-Wallis test) with Bonferroni correction shown as: *-$p<0.05$, **-$p<0.01$, ***-$p<0.001$.

tons to 2357±314 photons ($p<0.001$), with almost no additional increase with anti-CD28 antibody 2547±325 photons ($p<0.001$) (Fig. 5.11c). The CD90 antibody did not result in additional activation when considering the phosphorylation of CD3 (322±316 photons). Interestingly, the density of the MCs seem to follow the opposite relation with the addition of the anti-CD3 antibody with it dropping dropping from 2.24±0.15 to 1.10±0.05 μm^{-2}

when both antibodies are immobilised on the coverslip. The differences in CD3 alone and with the addition of the anti-CD28 antibody was statistically insignificant. Thus, to maintain consistency for more direct comparison to the CD90 antibody, the activatory CD3 antibody was used alone.

5.2.3.2 T cell clone characterisation

For single-molecule microscopy, the clusters need to be distinct and in a size lower than the resolution limit. These also have to be a consistent stoichiometry. In the case of our measurements, the SLP-76 clusters require a consistent ratio of the Halo-tagged to the native protein. Thus, stable cell lines have been generated previously by Wioleta Chmielewicz from single cell clones that express SLP-76-HaloTag for quantitative studies. Each of these cell clones have different expression of the SLP-76-HaloTag. For molecular counting experiments the clusters of SLP-76-HaloTag need to be distinct and diffraction limited. To determine the best combination of cell clone and labelling conditions experiments were conducted in combination with ProDOL calibration.

Each cell line was stained, in combination with a phalloidin stain post-fixation, for 15 min at 0.1, 0.5, 1, and 5 nM which yielded 1.9±0.2%, 6.5±0.4%, 9.4±0.7%, and 15.5±1.2% DOL, respectively.(Fig. 5.12a). The IS area of the D8 clone showed a significant increase across labelling conditions spanning about 1×10^3 µm^2 (Fig. 5.12b). Interestingly, the actin ring of the B8V clone showed an actin ring thicker than the rest of the clones. The increasing concentration of the HA-SiR labelling resulted in a higher intensity inside of the SLP-76 clusters across all cell lines. Across all labelling conditions the B3 showed a significantly higher amount of labelled SLP-76 ($p<0.001$), while the B8V showed the

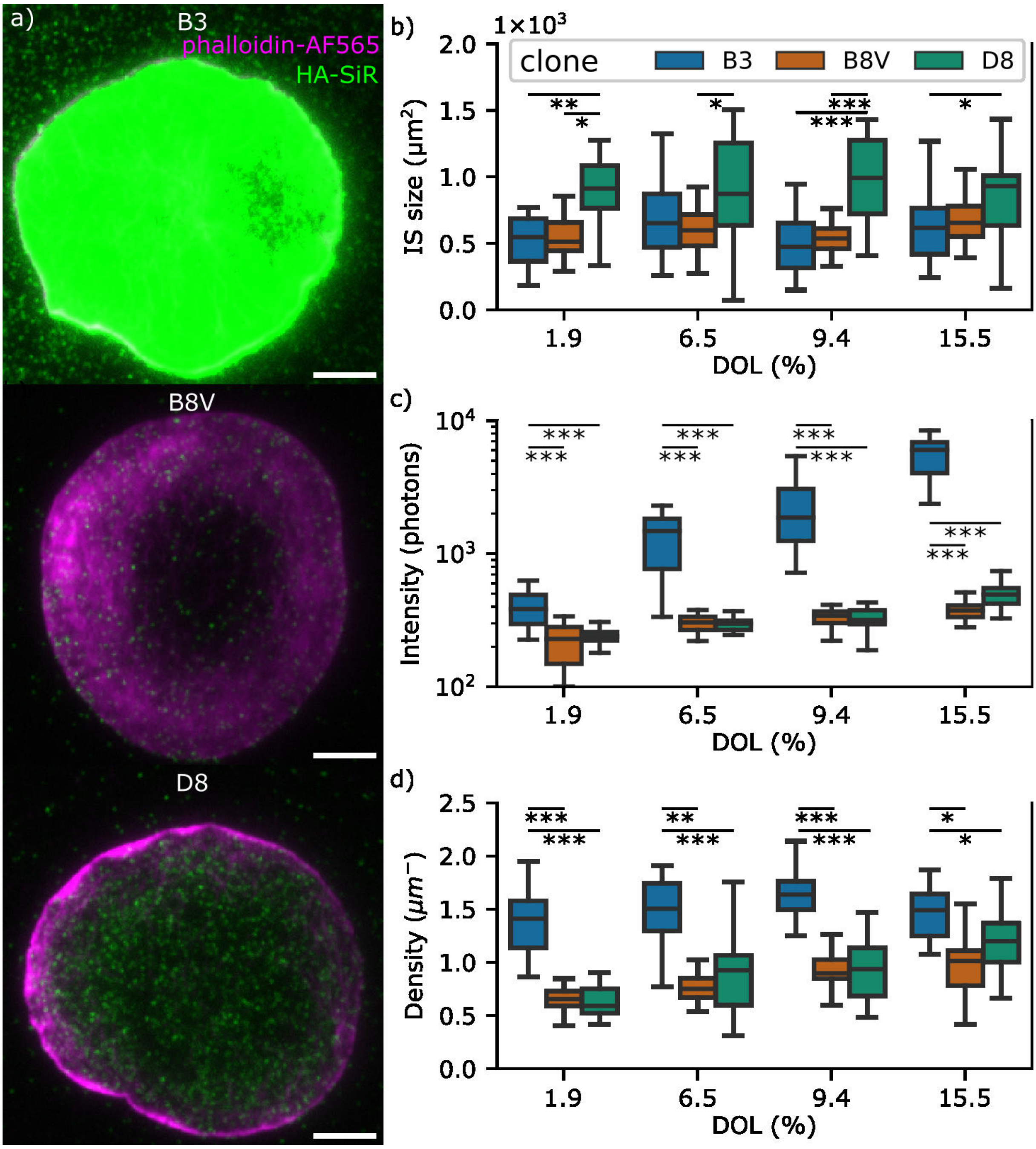

Fig. 5.12: SLP-76-HaloTag expression in single-cell clones. Determination of the characteristics of different single-cell clones of Jurakt cells expressing SLP-76-HaloTag stained with HA-SiR at different concentrations. a) Representative TIRFM images of each of the Jurkat clones with the highest DOL. Labelled SLP-76 is shown in green, and actin stained via phalloidin-Atto565 in magenta. b) IS area of the different cell clones after activation outlined by the actin stain. c) Intensity of the SLP-76-HaloTag clusters at as determined by localisation algorithm (ThunderSTORM) at different DOL as determined by ProDOL. d) Density of the SLP-76-HaloTag clusters at different DOL. Density was determined by dividing the number of localisations by the area of the IS . a) Scale bars are 5 µm. Boxplots show the values on a cell wide basis with $20 \leq n \leq 36$. Results of Dunn's test (post-hoc after Kruskal-Wallis test) with Bonferroni correction shown as: *-p<0.05, **-p<0.01, ***-p<0.001.

lowest (Fig. 5.12c). The density of clusters showed an increase with DOL for the D8 and B8V clones, but not for the B3 (Fig. 5.12d). The this is due to the inability to distinguish the individual clusters on cells that exhibited a high expression of SLP-76-HaloTag, and thus increased density within the IS, in the case of high labelling efficiency.

The amount of SLP-76-HaloTag was also assayed by flow cytometry to show that the difference between the cell clones is not due to differences in the recruitment of the proteins to the surface of the cells (Fig. SI 9).

From this point, the D8 clone was selected as the most appropriate choice for single-molecule experiments with the labelling concentration limited to between 0.5 nM and 1 nM HA-SiR to have the appropriate MC density. Western blot experiments were also conducted to evaluate the ratio between native (i.e. untagged) and tagged SLP-76, however, the amount of tagged protein D8 was too little to detect (Fig. SI 10).

5.2.3.3 Quantitative analysis of SLP-76 microclusters

Prior to live cell experiments, it would be beneficial to establish the stoichiometry of the SLP-76 MCs at different time points and as well as the general trend of recruitment.

For this purpose, synchronised activation experiments were conducted on T-cell activation. Jurkat cells of the D8 clone expressing SLP-76-HaloTag were deposited, washed, and then fixed after a set time to create a tight time window for cell contact with the coverslip. The cells' SLP-76 MC stoichiometries were examined from 30 s to 10 min by staining with HA-SiR, in addition to their CD3 phosphorylation and the area of their IS. Data consisted of three independent experiments with 36.0±1.6%, 21.3±1.2%, and 12.9±0.6% DOL, as measured with ProDOL. These percentages were used to correct the amounts of SLP-76-HaloTag estimated by both TIRFM and CoPS. In addition to the temporal differences during activation, the effects of different surface coating was reinspected. Cells on differently coated coverslips were examined after 5 min of contact with the surface (Fig. 5.13a).

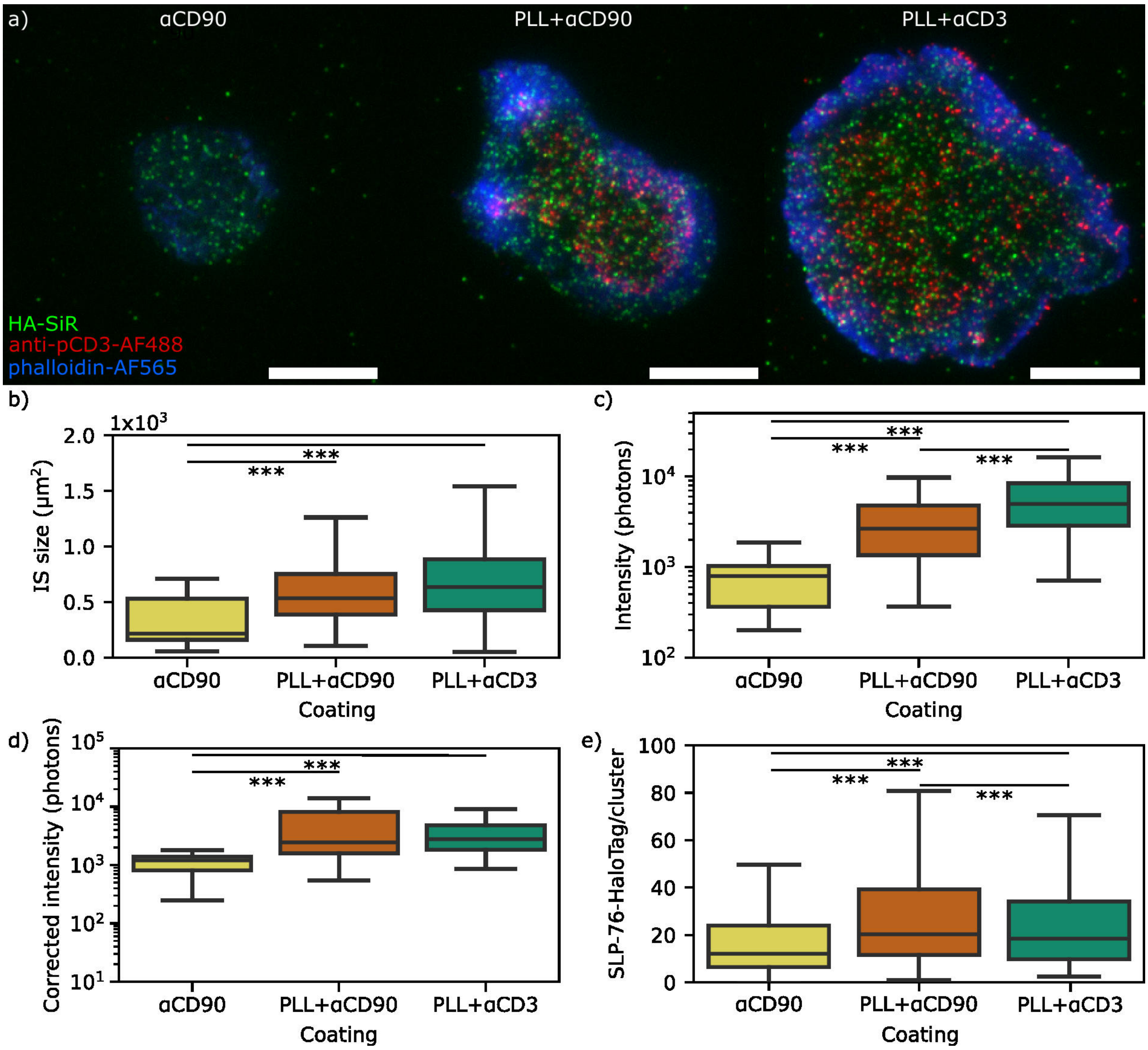

Fig. 5.13: Effects of different surface coatings on SLP-76 clustering. a) Representative TIRFM images of Jurkat cells with 5 min synchronised immobilisation on coverslips functionalised with anti-CD90 antibody, or PLL with either anti-CD90 or anti-CD3 antibodies. SLP-76-HaloTag was inspected by staining with HA-SiR (green). Activation was determined by anti-pY145-CD3 antibody conjugated to Alexa Fluor488 (AF488) (red) with a phalloidin-Atto565 (blue) as an actin stain. b) IS area determined by the actin stain. c) Intensity of the pCD3 signal determined by localisation algorithm (ThunderSTORM). d) Intensity of the SLP-76-HaloTag clusters determined by localisation algorithm (ThunderSTORM) and corrected with the DOL results from ProDOL. e) Number of HA-SiR-labelled SLP-76 molecules per cluster as determined by CoPS corrected with the DOL results from ProDOL. a) Scale bars are 10 µm. b)-d) Boxplots show the values on a cell wide basis with sample number in cells equaling n=26, 123, 117, from left to right. e) Boxplot shows values in a cluster-wide fashion with sample size n=550, 4083, 3848, from left to right. Results of Dunn's test (post-hoc after Kruskal-Wallis test) shown as: *-p<0.05, **-p<0.01, ***-p<0.001.

Looking at the IS area and the phosphorylation of CD3 shows that the presence of PLL corresponds to significant increase (p<0.001) in these activation markers (Fig. 5.13a and b). The presence of anti-CD3 antibodies increased the phosphorylation of CD3 additionally from 2.65±0.36 to 4.98±0.51×10^3 photons. The amount of SLP-76-HaloTag per cluster within the cells was measured by staining with HA-SiR. The intensity of the SLP-76 MCs on coverslips functionalised only with CD90 showed a significantly lower intensity ($p<0.001$) of the fluorescence of SLP-76 clusters - 1201±84 photons (median±SE), compared to the PLL coated slips which showed intensities of 2770±36 photons and 2444±37 photons for CD3 and CD90, respectively (Fig. 5.13d). The CoPS results agree that the lack of PLL results in a lower number of SLP-76 molecules per cluster - 12.0±1.1 (Fig. 5.13e). However, the CoPS analysis on the PLL coated coverslips showed an unlikely result where anti-CD90 antibody was significantly higher ($p<0.001$) than the CD3- 20.3±0.4 to 18.4±0.4. However, this might be attributed to overpowering the statistical test with too many data points.

The changes in stoichiometry of the SLP-76 MC were investigated in parallel using four different time points: 30 s, 90 s, 5 min and 10 min (Fig. 5.14a). We can track the activation of the Jurkat cells during these time points as the area of the IS increases from 295±26 µm^2 at 30 s to 828±31 µm^2 at 10 min ($p<0.001$) (Fig. 5.14b). The phosphorylation of CD3 also increased significantly with activation ($p<0.001$), but it peaks at 90 s with an intensity of 7.42±1.14×10^3 photons before decreasing to 3.92±0.51×10^3 photons (Fig. 5.14c). The CoPS analysis (Fig. 5.14e) was not in agreement with the intensity measurements (Fig. 5.14d) about the time with the highest amount of SLP-76 per MC changes. The intensity based measurement peaked at 10 min with a value of 3.88±0.33×10^3 photons, while the CoPS measurements peak with 20.3±0.6 copies of SLP-76-HaloTag. The other activation times result in values of approximately 2.5×10^3 photons and 18.5 molecules/MC, for the intensity and CoPS measurements, respectively.

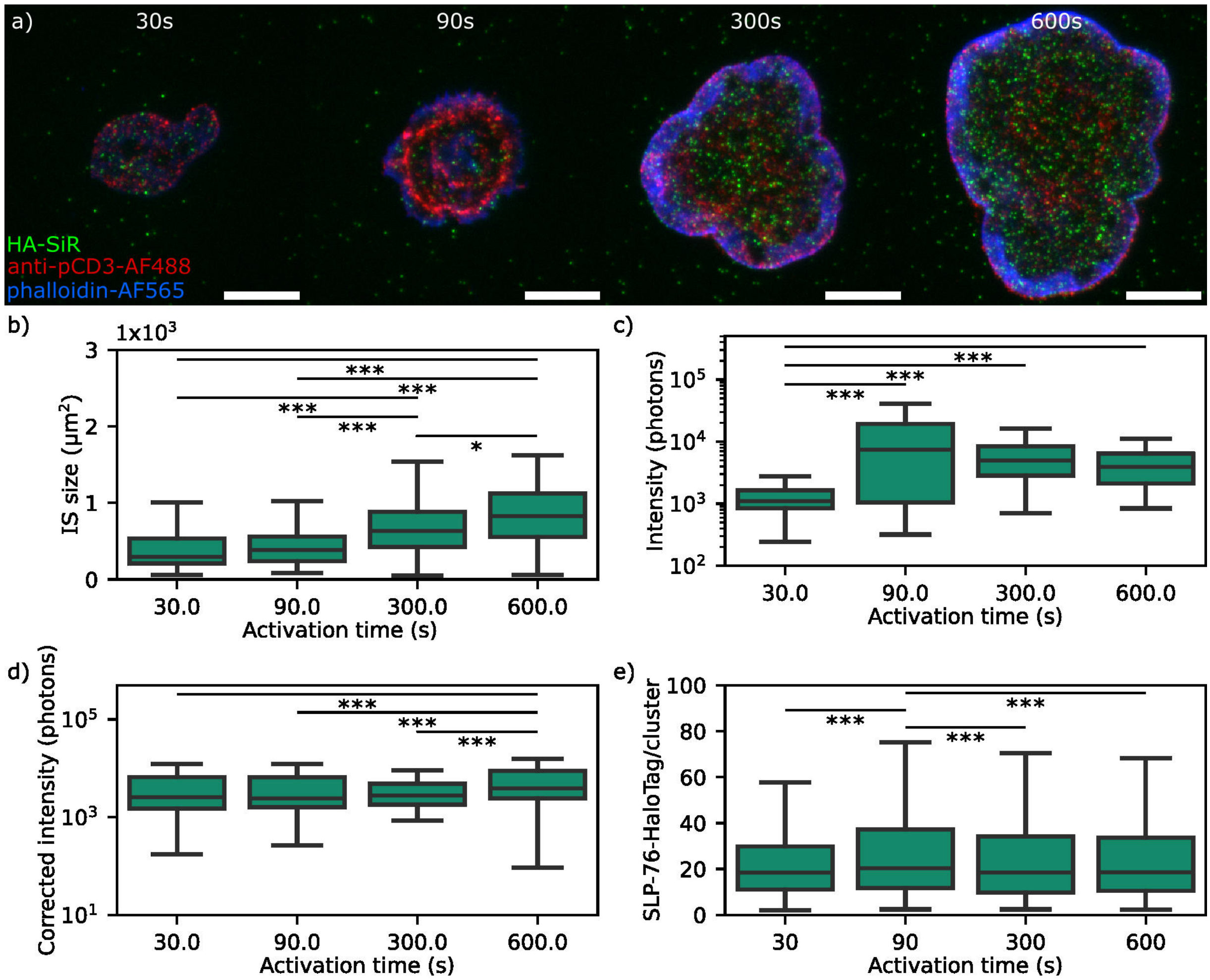

Fig. 5.14: Temporal differences in SLP-76 MC during activation. a) Representative TIRFM images of Jurkat cells allowed to activate for different times (30 s to 10 min) on PLL-coated coverslips fuctionalised with anti-CD3 antibodies. SLP-76-HaloTag was inspected by staining with HA-SiR (green). Activation was also determined by anti-pY145-CD3 antibody conjugated to Alexa Fluor488 (AF488) (red) with a phalloidin-Atto565 (blue) as an actin stain. b) IS surface area determined by the phalloidin signal. c) Intensity of the pCD3 signal determined by cluster localisation algorithm (ThunderSTORM). d) Intensity of the SLP-76-HaloTag clusters corrected with the DOL estimated by ProDOL. e) Number of SiR-labelled SLP-76 molecules per cluster as determined by CoPS corrected with the DOL. a) Scale bars are 10 µm. b)-d) Boxplots show the values on a cell wide basis with sample number in cells equaling n=133, 135, 117, 135, from left to right. e) Boxplots show values in a cluster-wide fashion with sample size n=1448, 2445, 3848, 4674, from left to right. Results of Dunn's test (post-hoc after Kruskal-Wallis test) with Bonferonni adjustment shown as: *-$p<0.05$, **-$p<0.01$, ***-$p<0.001$.

5.2.3.4 Imaging of SLP-76-Halo in live T cells during activation.

Having measured SLP-76 stoichiometry within fixed Jurkat cells in the previous section, an important comparison is to that of the live cellular context using CoPS, where dynamics of SLP-76 cluster diffusion and assembly are present. An important first step, however, was to determine to inspect the general trend of SLP-76 recruitment. To assay the underlying effects of photobleaching on these measurements a stroboscopic imaging method was applied. The slowest (10 s) sampling showed a consistent intensity

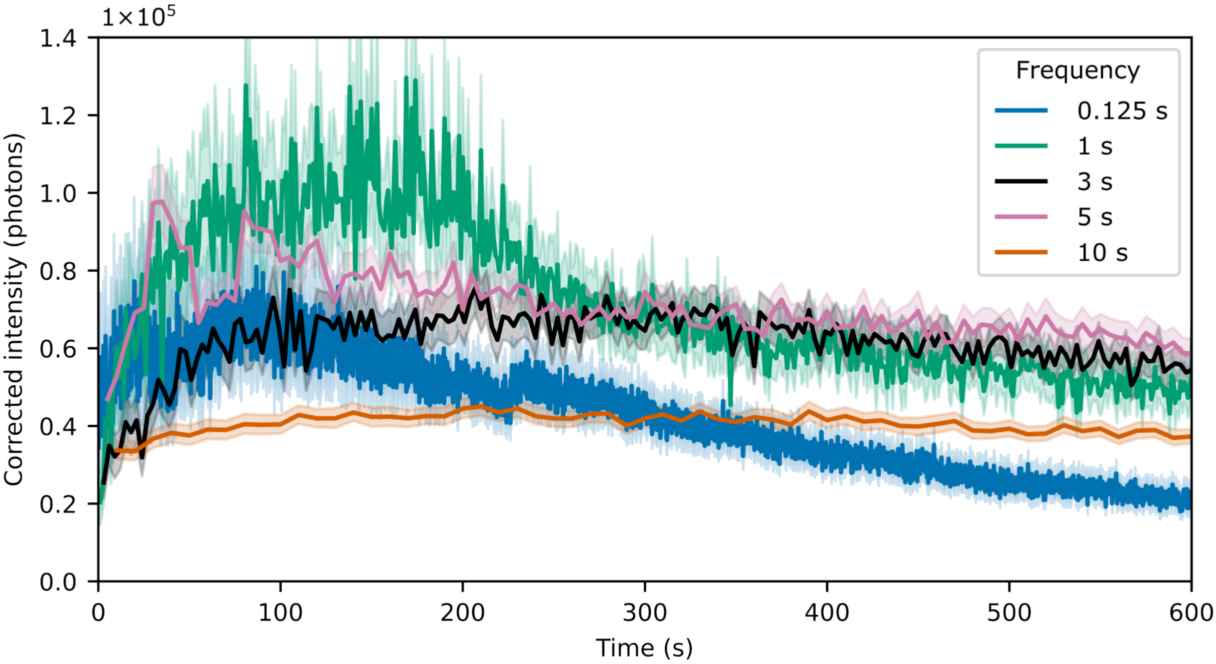

Fig. 5.15: Stroboscopic imaging of SLP-76-Halo. Intensities of SLP-76 MC corrected with the DOL estimated by ProDOL. The cells were labelled with 1 nM HA-SiR for 30 min. The different colours show the different frequencies of samplings. The shaded areas are the 95% CI.

around 3×10^4 photons. Interestingly, the continuous imaging, as well as the 1 s and 5 s sampling traces, exhibited a small peak between 30 s and 120 s, which could show that there is a slight increase on the presence of SLP-76 shortly after activation.

To determine if the surface coating changes the SLP-76 recruitment to the IS, single particle tracking was used to map the movement of SLP-76 MCs during activation of T cells on different surfaces (Fig. 5.16). Approximately, 15 min long traces were recorded with 124.6 ms frame integration time. The length of the tracks were shorter for the anti-CD90 antibody-only coating compared to the other ones containing PLL-0.48±0.04 s (Fig. 5.16a). This was a significant decrease ($p<0.05$) compared to the PLL with anti-CD3 antibody, which had trace times of 0.72±0.08 s. The tracks were then filtered to retain those containing 5 or more steps (0.625 s). Data from the PLL coated coverslip also had a significantly increased net movement than the surface with only anti-CD90 antibody at 305±56 nm ($p<0.01$) and 214±37 nm ($p<0.05$), for the ones with anti-CD90 and anti-CD3, respectively (Fig. 5.16b). The mean directional change the tracks for the PLL samples were decreased significantly ($p<0.05$) (Fig. 5.16c), and the confinement ratio was also increased. This was seen as a significant decrease for the CD90 compared to the sample with PLL and CD90 ($p<0.05$) (Fig. 5.16d).

Taken together the live cell experiments show that there may be small increase in the

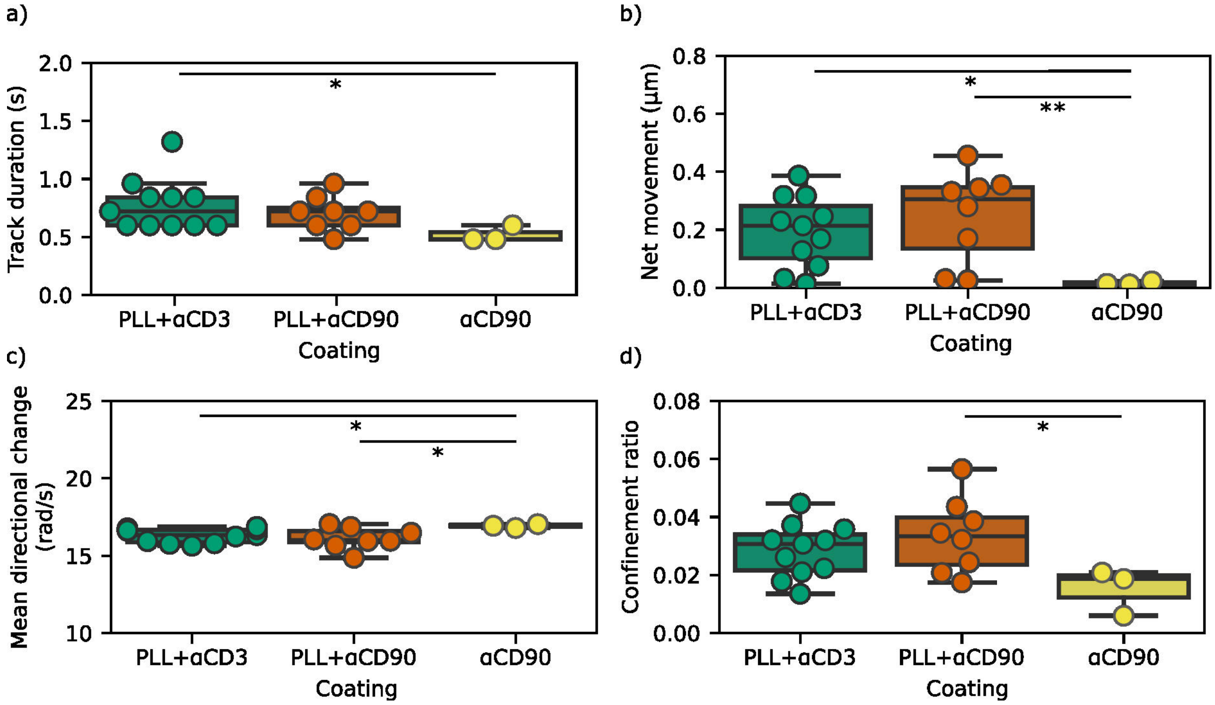

Fig. 5.16: Single particle tracking of SLP-76 microclusters. Single particle tracking of SLP-76 clusters in Jurkat cells immobilised on differently coated coverslips after staining with 1 nM HA-SiR for 30 min. a) Length of the traces of SLP-76 clusters before filtering. b) The net movement of the clusters from the initial position of the track. c) Directional change of the tracks per second. d) Confinement ratio of each trajectory. Sample size was 11 cells, 8 cells, and 3 cells, from left to right. Results of Dunn's test (post-hoc after Kruskal-Wallis test) shown as: *-p<0.05, **-p<0.01, ***-p<0.001.

SLP-76 stoichiometry (i.e., an increased number of SLP-76 in MCs) in the early stage of T cell activation (around 90 s), which could be overlooked in fixed cell experiments.

5.3 Discussion

Quantitative experiments in cells increase the difficulty of live cell protein complex stoichiometry measurements (i.e., additional dynamics of the protein complexes). Our ProDOL method solves one of these issues, the degree of labelling. We have shown that it can be applied for both pre- and post-fixation labelling. The method is also likely to work in live cells with simultaneous acquisitions in the reference and labelled channels. Imaging of the Jurkat cells revealed that the increase of labelling concentration increases to a saturation of the DOL at 50% with the higher values attributed to the increase of the non-specific labelling, which is yielded by the cellular debris which accumulates in the sample during the longer incubation times.

While live cell imaging of molecular complexes continues to be a difficult task, the nuclear pore complex remains a good molecular standard even for live cell imaging due to its slow lateral movement. Further, imaging buffers can improve fluorophore stability. Despite, AA showing no significant improvements to the photobleaching, there seems to be a visible decrease in the photoblinking of the fluorophores inside of the cell. Future work would benefit from screening of another common cell permeable component of ROXS buffers - Trolox (190). HEPES on the other hand did not show any change in the photophysics exhibited by the fluorophores. It is an important CO_2 buffer but in high concentrations it could result on cell toxicity due to changes in pH (171). It is important to acknowledge that both DMEM and FB contain folic acid, which degrades when exposed to high amounts of blue light and can lead to phototoxicity (191).

Investigation of T cell activation showed that the main activating factor in our system was most likely PLL. The activating property of PLL had previously been described by an article by Santos *et al.* (192). There the PLL resulted in the increase of the cell size and the restriction of movement of TCR MCs. This could also explain why the activatory and control antibody coating seemed to perform similarly when PLL coating was present. The lack of a directed movement in SLP-76 microclusters can also be due to the PLL coating, as the single-particle tracking results were in disagreement with publications using only antibody coating (189).

By inspecting the intensity corresponding to SLP-76 quantity in MCs at the early stages of activation we can observe a difference between fixed cell and dynamic live cell imaging. In Tashev *et al.* (92), fixed cells did not exhibit a considerable change of SLP-76 in MCs. It could be that the issue with our synchronisation protocol is the fixation of the cells with formaldehyde. The fixation process may be slow enough to allow the cell to enter the later stages of activation. If the recruitment of the SLP-76 is in fact quicker in earlier stages of activation this could hint at a negative regulation in late stages of T cell activation. Thus, the immobilised SLP-76 MCs, as well as ZAP70 MCs, could be an important target for a dynamic version of CoPS to assay.

Chapter 6

General Discussion

6.1 Conclusion

In this work a custom fluorescence microscopy setup was built. The confocal volume was calculated and thus the resolution of the confocal microscope side was determined to be around 300 nm. Parameters of the widefield part of the microscope were also established and the gain calibration was used throughout this project. The ability to count molecules based on fluorescence antibunching was cross validated with PBSA, both done on the same microscope. The microscope has since been used for multiple publications for its antibunching capabilities (92), as well as other the ability to perform other techniques (193, 194).

To move towards dynamic CoPS measurements two new versions of the analysis were implemented to the analysis pipeline. These were then applied to experimental data and their limitations were outlined. A problem with the high laser power on DNA origami was also identified when imaging Cy5-labelled imager strands and a fluorophore showing less DNA damage, Atto 643, was found. The kinetics of the DNA origami were also determined for the two types of imager strands and were determined to be appropriate for CoPS. However, the Atto 643 showed a susceptibility to photobleaching.

The live cell experiment part of the project showed not only that the NPC is an appropriate system for *in cellulo* single-molecule experiments, but also confirmed that the inclusion of molecules such as AA, can be used to improve the photoblinking of dyes in live cells.

An important outcome of this project was the validation of the accuracy of ProDOL, as well as its use in large studies of the labelling efficiency of protocols. This method provides a simple quick way to determine the degree of labelling of protein tags. Thus, resolving one of the major problems with quantitative microscopy. ProDOL can be applied in a variety of studies to determine the labelling efficiency prior to experiments. SLP-76 stoichiometry was shown to remain mostly constant in microcluster (MC) from 30 s to 10 min of activation on a PLL-coated coverslip in fixed cells. However, in live cells there might be a slight increase in the early stages of T cell activation. In this experimental system the SLP-76 clusters remained still enough, but too short-lived for CoPS measurements. To improve this a higher degree of labelling could be used or perhaps changing the system towards ZAP70. A plasmid was developed by Kassandra Malassi in our lab, however, problems with the expression could not be solved within the time constraint of this PhD.

6.2 Outlook

With new commercial microscope systems antibunching methods such as CoPS, can become more user-friendly, and therefore more widely applied. One of the main limitations of CoPS is the necessity for single-photon detectors, which can record events at a MHz time resolution. Currently this limits laboratories to using single-point single-photon avalanche diodes (SPADs), and thus constrains CoPS to point measurements. This significantly limits the functionality of the technique. However, with the development of new generation SPAD arrays this issue might be resolved in the future. This would mean not only increasing the throughput of the experiment, but also combining the antibunching measurements with single-molecule tracking to increase its applicability with live cells.

Another big issue with CoPS that can be addressed is the stability of the dyes used. Previously in Ta, *et al.* (91) a study into the brightness and the stability of dyes was performed. However, this study was performed prior to the development of newer Janelia Fluor (JF) dyes (195), which might prove to have higher brightness and photobleaching quantum yield. This would allow CoPS to count faster and to higher numbers of emitters. A study of newly produced dyes might greatly benefit the field as a whole.

These dyes can then be used on imager strands in DNA origami as shown in Chap. 4 to determine the generation of reactive oxygen species (ROS). This can be done better with reporter dyes which show the changes of environment. These can also be attached on the imager strands. The dyes can also be inspected for their cell membrane permeability and their labelling efficiency with ProDOL. If membrane permeable the dyes can be used in an assay to determine the effects of live cell media.

As already shown in Chap. 5 additions of ascorbic acid (AA) can be used to decrease the photoblinking dyes. The promising new dyes can be investigated for the influence of AA, as well as Trolox.

The study of the T cells have also shown that the PLL is the prominent contributor to activation. Despite the benefit of having SLP-76 clusters being immobilised, a new version of the coating needs to be established which features only the anti-CD3 activatory antibodies to increase biological relevancy. If the SLP-76 clusters move laterally too quickly for CoPS, then ZAP70 can be investigated as a potential new target, which is stationary, but also exhibit the cycling of cytosolic proteins.

Despite this project not being able to reach the ultimate goal of determination of the kinetics of clustering in live cells, it outlined the difficulties and proposed solutions which would greatly benefit CoPS as a counting technique. Hopefully, the direction outlined in this text can in the future be used to bring CoPS to the final goal of assaying molecular clusters in live cells.

Chapter 7

References

1. Alberts B, Johnson A, Lewis J, Raff M, Roberts K, Walter P. Protein Function. Garland Science; 2002. Available from: `https://www.ncbi.nlm.nih.gov/books/NBK26911/`.

2. Sykulev Y, Joo M, Vturina I, Tsomides TJ, Eisen HN. Evidence that a single peptide-MHC complex on a target cell can elicit a cytolytic T cell response. Immunity. 1996;4(6):565-71.

3. Cebecauer M, Spitaler M, Sergé A, Magee AI. Signalling complexes and clusters: functional advantages and methodological hurdles. Journal of Cell Science. 2010 2;123(3):309-20.

4. Graham I, Duke T. The logical repertoire of ligand-binding proteins. Physical Biology. 2005 8;2(3):159.

5. Monks CRF, Freiberg BA, Kupfer H, Sciaky N, Kupfer A. Three-dimensional segregation of supramolecular activation clusters in T cells. Nature 1998 395:6697. 1998 9;395(6697):82-6.

6. Koretzky GA, Abtahian F, Silverman MA. SLP76 and SLP65: complex regulation of signalling in lymphocytes and beyond. Nature Reviews Immunology. 2006 1;6(1):67-78.

7. Hummert J, Tashev SA, Herten DP. An update on molecular counting in fluorescence microscopy. The International Journal of Biochemistry & Cell Biology. 2021;135:105978.
8. Balagopalan L, Raychaudhuri K, Samelson LE. Microclusters as T Cell Signaling Hubs: Structure, Kinetics, and Regulation. Frontiers in Cell and Developmental Biology. 2021 1;8:608530.
9. Freire E, Mayorga OL, Straume M. Isothermal Titration. Analytical Chemistry. 1990 9;62(18):950A-959A.
10. Zhu X, Gao T. Spectrometry. Nano-inspired Biosensors for Protein Assay with Clinical Applications. 2019 1:237-64.
11. Griffin GD, Stratis-Cullum DN, McKnight TE. Biosensors. Encyclopedia of Microbiology. 2019 1:542-74.
12. Baker H. IX. An account of Mr. Leeuwenhoek's microscopes. Philosophical Transactions of the Royal Society of London. 1740;41(458).
13. Wolbarsht ML. Micrographia or Some Physiological Descriptions of Minute Bodies Made by Magnifying Glasses with Observations and Inquiries Thereupon. Robert Hooke . The Quarterly Review of Biology. 1963;38(1):115-6.
14. Wang X, Huang SC, Huang TX, Su HS, Zhong JH, Zeng ZC, et al. Tip-enhanced Raman spectroscopy for surfaces and interfaces. Chemical Society Reviews. 2017 7;46(13):4020-41.
15. Pluta M. Advanced light microscopy / Vol. 1, Principles and basic properties. PWN; 1988.
16. Thorn K. A quick guide to light microscopy in cell biology. Molecular Biology of the Cell. 2016 1;27(2):219-22.
17. Selinummi J, Ruusuvuori P, Podolsky I, Ozinsky A, Gold E, Yli-Harja O, et al. Bright Field Microscopy as an Alternative to Whole Cell Fluorescence in Automated Analysis of Macrophage Images. PLOS ONE. 2009 10;4(10):e7497.

18. Heimstädt O. Das fluoreszenzmikroskop. Z Wiss Mikrosk. 1911;28(330-337):14.

19. Wollman AJM, Nudd R, Hedlund EG, Leake MC. From animaculum to single molecules: 300 years of the light microscope. Open Biology. 2015 4;5(4).

20. Zimmermann T. Spectral Imaging and Linear Unmixing in Light Microscopy. In: Rietdorf J, editor. Microscopy Techniques. Berlin, Heidelberg: Springer Berlin Heidelberg; 2005. p. 245-65.

21. Lichtman JW, Conchello JA. Fluorescence microscopy. Nature Methods. 2005 12;2(12):910-9.

22. Smith B, Winefordner JD, Omenetto N. Atomic fluorescence of sodium under continuous-wave laser excitation. Journal of Applied Physics. 1977 7;48(7):2676-80.

23. Martin RB, Richardson FS. Lanthanides as probes for calcium in biological systems. Quarterly Reviews of Biophysics. 1979;12(2):181-209.

24. Frederick J, Herschel W. ’AμoρΦωτα No. I. On a Case of Superficial Colour Presented by a Homogeneous Liquid Internally Colourless; 1845.

25. Bagatolli LA. Fluorescence Spectroscopy: Basic Foundations and Methods. In: Analytical Techniques in the Pharmaceutical Sciences. Springer, New York, NY; 2016. p. 29-59.

26. Jabłoński A. Efficiency of Anti-Stokes Fluorescence in Dyes. Nature. 1933;131(3319):839-40.

27. Mondal PP, Diaspro A. Basics of Fluorescence and Photophysics. In: Fundamentals of Fluorescence Microscopy. Springer, Dordrecht; 2014. p. 111-34.

28. Nagashima K, Velan SS. Understanding the singlet and triplet states in magnetic resonance. Concepts in Magnetic Resonance Part A: Bridging Education and Research. 2013 9;42(5):165-81.

29. Straughan BP, Walker S. Fluorescence and Phosphorescence Spectroscopy. Spectroscopy. 1976:161-98.

30. Berezin MY, Achilefu S. Fluorescence lifetime measurements and biological imaging. Chem Rev. 2010;110(5):2641-84.

31. Lakowicz JR. Introduction to Fluorescence. Principles of Fluorescence Spectroscopy. 2006;3:1-26.

32. Heupel M, Thiel E. Fluorescence Reduction by a Triplet-State Population. Journal of Fluorescence. 1997;7(4):371-5.

33. Stuhr R, Bayer P, von Wangelin AJ. The Diverse Modes of Oxygen Reactivity in Life & Chemistry. Chemsuschem. 2022 12;15(24):202201323-4.

34. Gijzeman OLJ, Kaufman F, Porter G. Oxygen quenching of aromatic triplet states in solution. Part 1. Journal of the Chemical Society, Faraday Transactions 2: Molecular and Chemical Physics. 1973 1;69(0):708-20.

35. Croce AC, Bottiroli G. Autofluorescence Spectroscopy and Imaging: A Tool for Biomedical Research and Diagnosis. European Journal of Histochemistry : EJH. 2014 10;58(4):320-37.

36. Shilova ON, Shilov ES, Deyev SM. The effect of trypan blue treatment on autofluorescence of fixed cells. Cytometry Part A : the journal of the International Society for Analytical Cytology. 2017 9;91(9):917-25.

37. Zheng Q, Juette MF, Jockusch S, Wasserman MR, Zhou Z, Altman RB, et al. Ultra-Stable Organic Fluorophores for Single-Molecule Research. Chemical Society Reviews. 2014 2;43(4):1044-56.

38. Weiss J. Fluorescence and Oxidation in Conjugated Ring Systems. Nature. 1940;145(3680):744-5.

39. Lakowicz JR. Fluorophores. Principles of Fluorescence Spectroscopy. 2006:63-95.

40. Lovell TC, Branchaud BP, Jasti R. An Organic Chemist's Guide to Fluorophores – Understanding Common and Newer Non-Planar Fluorescent Molecules for Biological Applications. European Journal of Organic Chemistry. 2024 3;27(9):e202301196.

41. Schwartz A, Wang L, Early E, Gaigalas A, Zhang YZ, Marti GE, et al. Quantitating Fluorescence Intensity from Fluorophore: The Definition of MESF Assignment. Journal of Research of the National Institute of Standards and Technology. 2002;107(1):83.
42. Lakowicz JR. Single-Molecule Detection. Principles of Fluorescence Spectroscopy. 2006:757-95.
43. Fu Y, Finney NS. Small-molecule fluorescent probes and their design. RSC Advances. 2018 8;8(51):29051-61.
44. Breusegem SY, Clegg RM, Loontiens FG. Base-sequence specificity of Hoechst 33258 and DAPI binding to five (A/T)4 DNA sites with kinetic evidence for more than one high-affinity Hoechst 33258-AATT complex. Journal of Molecular Biology. 2002 2;315(5):1049-61.
45. Zhitomirsky B, Farber H, Assaraf YG. LysoTracker and MitoTracker Red are transport substrates of P-glycoprotein: implications for anticancer drug design evading multidrug resistance. Journal of Cellular and Molecular Medicine. 2018 4;22(4):2131-41.
46. Hoppe-Seyler F, Butz K. Peptide aptamers: Powerful new tools for molecular medicine. Journal of Molecular Medicine. 2000 9;78(8):426-30.
47. Shangguan D, Meng L, Cao ZC, Xiao Z, Fang X, Li Y, et al. Identification of liver cancer-specific aptamers using whole live cells. Analytical Chemistry. 2008 2;80(3):721-8.
48. Vinkenborg JL, Mayer G, Famulok M. Aptamer-Based Affinity Labeling of Proteins. Angewandte Chemie International Edition. 2012 9;51(36):9176-80.
49. Lengsfeld AM, Löw I, Wieland T, Dancker P, Hasselbach W. Interaction of Phalloidin with Actin. Proceedings of the National Academy of Sciences of the United States of America. 1974;71(7):2803-7.
50. Elia N. Using unnatural amino acids to selectively label proteins for cellular imaging: a cell biologist viewpoint. The Febs Journal. 2021 2;288(4):1107-17.

51. Shimomura O, Johnson FH, Saiga Y. Extraction, purification and properties of aequorin, a bioluminescent protein from the luminous hydromedusan, Aequorea. Journal of Cellular and Comparative Physiology. 1962;59:223-39.

52. Sample V, Newman RH, Zhang J. The structure and function of fluorescent proteins. Chemical Society Reviews. 2009 9;38(10):2852-64.

53. Yang F, Moss LG, Phillips GN. The molecular structure of green fluorescent protein. Nature Biotechnology. 1996;14(10):1246-51.

54. Rodriguez EA, Campbell RE, Lin JY, Lin MZ, Miyawaki A, Palmer AE, et al. The growing and glowing toolbox of fluorescent and photoactive proteins. Trends in Biochemical Sciences. 2017 2;42(2):111-29.

55. Nemet I, Ropelewski P, Imanishi Y. Applications of phototransformable fluorescent proteins for tracking dynamics of cellular components. Photochemical and Photobiological Sciences. 2015 8;14(10):1787-806.

56. Zhou XX, Lin MZ. Photoswitchable Fluorescent Proteins: Ten Years of Colorful Chemistry and Exciting Applications. Current Opinion in Chemical Biology. 2013 8;17(4):682-90.

57. Keppler A, Gendreizig S, Gronemeyer T, Pick H, Vogel H, Johnsson K. A general method for the covalent labeling of fusion proteins with small molecules in vivo. Nature Biotechnology. 2003 1;21(1):86-9.

58. Gautier A, Juillerat A, Heinis C, Corrêa IR, Kindermann M, Beaufils F, et al. An Engineered Protein Tag for Multiprotein Labeling in Living Cells. Chemistry & Biology. 2008 2;15(2):128-36.

59. Los GV, Encell LP, McDougall MG, Hartzell DD, Karassina N, Zimprich C, et al. HaloTag: A novel protein labeling technology for cell imaging and protein analysis. ACS Chemical Biology. 2008 6;3(6):373-82.

60. Grussmayer KS, Yserentant K, Herten DP. Photons in - numbers out: perspectives in quantitative fluorescence microscopy for in situ protein counting. Methods Appl Fluoresc. 2019;7(1):12003.

61. Rodimova SA, Meleshina AV, Kalabusheva EP, Dashinimaev EB, Reunov DG, Torgomyan HG, et al. Metabolic activity and intracellular pH in induced pluripotent stem cells differentiating in dermal and epidermal directions. Methods and Applications in Fluorescence. 2019 9;7(4):044002.

62. Barkauskas DS, Medley G, Liang X, Mohammed YH, Thorling CA, Wang H, et al. Using in vivo multiphoton fluorescence lifetime imaging to unravel disease-specific changes in the liver redox state. Methods and Applications in Fluorescence. 2020 6;8(3):034003.

63. Shashkova S, Leake MC. Single-molecule fluorescence microscopy review: shedding new light on old problems. Bioscience Reports. 2017 8;37(4):20170031.

64. Sanderson MJ, Smith I, Parker I, Bootman MD. Fluorescence microscopy. Cold Spring Harbor Protocols. 2014 10;2014(10):1042-65.

65. Hell SW. Toward fluorescence nanoscopy. Nature Biotechnology 2003 21:11. 2003 10;21(11):1347-55.

66. Lelek M, Gyparaki MT, Beliu G, Schueder F, Griffié J, Manley S, et al. Single-molecule localization microscopy. Nature Reviews Methods Primers 2021 1:1. 2021 6;1(1):1-27.

67. Abbe E. Beiträge zur Theorie des Mikroskops und der mikroskopischen Wahrnehmung: I. Die Construction von Mikroskopen auf Grund der Theorie. Archiv für mikroskopische Anatomie. 1873 12;9(1):413-8.

68. Kulaitis G, Munk A, Werner F. What is resolution? A statistical minimax testing perspective on super-resolution microscopy. Annals of Statistics. 2020 5;49(4):2292-312.

69. Jungmann R, Steinhauer C, Scheible M, Kuzyk A, Tinnefeld P, Simmel FC. Single-molecule kinetics and super-resolution microscopy by fluorescence imaging of transient binding on DNA origami. Nano Lett. 2010;10(11):4756-61.

70. Wichmann J, Hell SW. Breaking the diffraction resolution limit by stimulated emission: stimulated-emission-depletion fluorescence microscopy. Optics Letters. 1994 6;19(11):780-2.

71. Rust MJ, Bates M, Zhuang X. Stochastic optical reconstruction microscopy (STORM) provides sub-diffraction-limit image resolution. Nature Methods. 2006 10;3(10):793-6.

72. Funatsu T, Harada Y, Tokunaga M, Saito K, Yanagida T. Imaging of single fluorescent molecules and individual ATP turnovers by single myosin molecules in aqueous solution. Nature 1995 374:6522. 1995;374(6522):555-9.

73. Lu HP. Single-Molecule Enzymatic Dynamics. Science. 1998 12;282(5395):1877-82.

74. Schmidt T, Schütz GJ, Baumgartner W, Gruber HJ, Schindler H. Imaging of single molecule diffusion. Proceedings of the National Academy of Sciences of the United States of America. 1996 4;93(7):2926-9.

75. Cutrale F, Rodriguez D, Hortigüela V, Chiu CL, Otterstrom J, Mieruszynski S, et al. Using enhanced number and brightness to measure protein oligomerization dynamics in live cells. Nature Protocols 2019 14:2. 2019 1;14(2):616-38.

76. Thevathasan JV, Kahnwald M, Cieśliński K, Hoess P, Peneti SK, Reitberger M, et al. Nuclear pores as versatile reference standards for quantitative superresolution microscopy. Nature Methods 2019 16:10. 2019 9;16(10):1045-53.

77. Rosenfeld N, Perkins TJ, Alon U, Elowitz MB, Swain PS. A Fluctuation Method to Quantify In Vivo Fluorescence Data. Biophysical Journal. 2006 7;91(2):759-66.

78. Ulbrich MH, Isacoff EY. Subunit counting in membrane-bound proteins. Nature Methods. 2007 3;4(4):319-21.

79. McGuire H, Aurousseau MRP, Bowie D, Bluncks R. Automating Single Subunit Counting of Membrane Proteins in Mammalian Cells. The Journal of Biological Chemistry. 2012 10;287(43):35912-21.

80. Cordes T, Maiser A, Steinhauer C, Schermelleh L, Tinnefeld P. Mechanisms and advancement of antifading agents for fluorescence microscopy and single-molecule spectroscopy. Physical Chemistry Chemical Physics. 2011 4;13(14):6699-709.

81. Jungmann R, Avendaño MS, Dai M, Woehrstein JB, Agasti SS, Feiger Z, et al. Quantitative Super-Resolution Imaging with qPAINT using Transient Binding Analysis. Nature Methods. 2016 5;13(5):439-42.

82. Tsekouras K, Custer TC, Jashnsaz H, Walter NG, Pressé S. A novel method to accurately locate and count large numbers of steps by photobleaching. Molecular Biology of the Cell. 2016 11;27(22):3601-15.

83. Betzig E, Patterson GH, Sougrat R, Lindwasser OW, Olenych S, Bonifacino JS, et al. Imaging intracellular fluorescent proteins at nanometer resolution. Science. 2006 9;313(5793):1642-5.

84. Sharonov A, Hochstrasser RM. Wide-field subdiffraction imaging by accumulated binding of diffusing probes. Proceedings of the National Academy of Sciences of the United States of America. 2006 12;103(50):18911-6.

85. Patel L, Williamson D, Owen DM, Cohen EAK. Blinking statistics and molecular counting in direct stochastic reconstruction microscopy (dSTORM). Bioinformatics. 2021 9;37(17):2730-7.

86. Paul H. Photon antibunching. Reviews of Modern Physics. 1982 10;54(4):1061.

87. Ly S, Petrlova J, Huser T, Fore S, Gao T, Voss J, et al. Stoichiometry of reconstituted high-density lipoproteins in the hydrated state determined by photon antibunching. Biophysical Journal. 2011 8;101(4):970-5.

88. Fox AM. 6.4 Hanbury Brown-Twiss experiments with photons. In: Quantum Optics: An Introduction. vol. 15. Oxford university press; 2006. p. 113-5.

89. Tinnefeld P, Müller C, Sauer M. Time-varying photon probability distribution of individual molecules at room temperature. Chemical Physics Letters. 2001 9;345(3-4):252-8.

90. Basché T, Moerner WE, Orrit M, Talon H. Photon antibunching in the fluorescence of a single dye molecule trapped in a solid. Physical Review Letters. 1992 9;69(10):1516.

91. Ta H, Wolfrum J, Herten DP. An extended scheme for counting fluorescent molecules by photon-antibunching. Laser Physics. 2010 1;20(1):119-24.

92. Tashev SA, Euchner J, Yserentant K, Hänselmann S, Hild F, Chmielewicz W, et al. A General Method to Accurately Count Molecular Complexes and Determine the Degree of Labelling in Cells Using Protein Tags. bioRxiv. 2023:2023.09.08.556847.

93. Jimenez A, Friedl K, Leterrier C. About samples, giving examples: Optimized Single Molecule Localization Microscopy. Methods (San Diego, Calif). 2020 3;174:100-14.

94. Edelstein A, Amodaj N, Hoover K, Vale R, Stuurman N. Computer Control of Microscopes Using µManager. Current Protocols in Molecular Biology. 2010 10;92(1):1-14.

95. Bunnell SC, Kapoor V, Trible RP, Zhang W, Samelson LE. Dynamic actin polymerization drives T cell receptor-induced spreading: A role for the signal transduction adaptor LAT. Immunity. 2001 3;14(3):315-29.

96. Virtanen P, Gommers R, Oliphant TE, Haberland M, Reddy T, Cournapeau D, et al. SciPy 1.0: Fundamental Algorithms for Scientific
}Computing in Python. Nature Methods. 2020;17:261-72.

97. Tinevez JY, Perry N, Schindelin J, Hoopes GM, Reynolds GD, Laplantine E, et al. TrackMate: An open and extensible platform for single-particle tracking. Methods. 2017 2;115:80-90.

98. Ries J. SMAP: a modular super-resolution microscopy analysis platform for SMLM data. Nature Methods. 2020 9;17(9):870-2.

99. Arganda-Carreras I, Kaynig V, Rueden C, Eliceiri KW, Schindelin J, Cardona A, et al. Trainable Weka Segmentation: a machine learning tool for microscopy pixel classification. Bioinformatics. 2017 8;33(15):2424-6.

100. Courtney A, Alvey LM, Merces GOT, Burke N, Pickering M. The Flexiscope: a low cost, flexible, convertible and modular microscope with automated scanning and micromanipulation. Royal Society Open Science. 2020 3;7(3):191949.

101. Gibson GM, Archibald R, Main M, Kallepalli A. Modular light sources for microscopy and beyond (ModLight). HardwareX. 2023 3;13:e00385.

102. Ma H, Fu R, Xu J, Liu Y. A simple and cost-effective setup for super-resolution localization microscopy. Scientific Reports 2017 7:1. 2017 5;7(1):1-9.

103. Hedley GJ, Schröder T, Steiner F, Eder T, Hofmann FJ, Bange S, et al. Picosecond time-resolved photon antibunching measures nanoscale exciton motion and the true number of chromophores. Nature Communications. 2021 2;12(1):1-10.

104. Schmidt R, Weihs T, Wurm CA, Jansen I, Rehman J, Sahl SJ, et al. MINFLUX nanometer-scale 3D imaging and microsecond-range tracking on a common fluorescence microscope. Nature Communications. 2021 3;12(1):1-12.

105. Minski M. Microscopy apparatus; 1961. Available from: `https://cir.nii.ac.jp/crid/1571698600407014784`.

106. Minsky M. Memoir on inventing the confocal scanning microscope. Scanning. 1988 1;10(4):128-38.

107. Rüttinger S, Buschmann V, Krämer B, Erdmann R, MacDonald R, Koberling F. Comparison and accuracy of methods to determine the confocal volume for quantitative fluorescence correlation spectroscopy. Journal of Microscopy. 2008 11;232(2):343-52.

108. Webb DJ, Brown CM. Epi-Fluorescence Microscopy. Methods in Molecular Biology (Clifton, NJ). 2013;931:29.

109. Fish KN. Total Internal Reflection Fluorescence (TIRF) Microscopy. Current Protocols in Cytometry. 2009;0 12(SUPPL.50):Unit12.18.

110. Tokunaga M, Imamoto N, Sakata-Sogawa K. Highly inclined thin illumination enables clear single-molecule imaging in cells. Nature Methods 2008 5:2. 2008 1;5(2):159-61.

111. Broda H, Van Gooch VD, Taylor W, Aiuto N, Hastings JW. Acquisition of Circadian Bioluminescence Data in Gonyaulax and an Effect of the Measurement Procedure on the Period of the Rhythm. Journal of Biological Rhythms. 1986 9;1(3):251-63.

112. Mewies M, McIntire WS, Scrutton NS. Covalent attachment of flavin adenine dinucleotide (FAD) and flavin mononucleotide (FMN) to enzymes: The current state of affairs. Protein Science. 1998;7(1):7-20.

113. Slepian J. Hot Cathode Tube. US Pat. 1923;1450(265):18.

114. Lubsandorzhiev BK. On the history of photomultiplier tube invention. Nuclear Instruments and Methods in Physics Research Section A: Accelerators, Spectrometers, Detectors and Associated Equipment. 2006 11;567(1):236-8.

115. Hertz H. Ueber einen Einfluss des ultravioletten Lichtes auf die electrische Entladung. Annalen der Physik. 1887 1;267(8):983-1000.

116. Polyakov SV. Photomultiplier Tubes. In: Experimental Methods in the Physical Sciences. vol. 45. Academic Press; 2013. p. 69-82.

117. Einstein A. Über einen die Erzeugung und Verwandlung des Lichtes betreffenden heuristischen Gesichtspunkt. Annalen der Physik. 2005 2;14(S1):164-81.

118. Iams H, Salzberg B. The Secondary Emission Phototube. Proceedings of the Institute of Radio Engineers. 1935;23(1):55-64.

119. Donati S, Tambosso T. Single-Photon Detectors: From Traditional PMT to Solid-State SPAD-Based Technology. IEEE Journal of Selected Topics in Quantum Electronics. 2014 11;20(6):204-11.

120. Cova S, Ghioni M, Itzler MA, Bienfang JC, Restelli A. Semiconductor-Based Detectors. Experimental Methods in the Physical Sciences. 2013 1;45:83-146.

121. Oldham WG, Samuelson RR, Antognetti P. Triggering Phenomena in Avalanche Diodes. IEEE Transactions on Electron Devices. 1972;19(9):1056-60.

122. Mcintyre RJ. On the Avalanche Initiation Probability of Avalanche Diodes Above the Breakdown Voltage. IEEE Transactions on Electron Devices. 1973;20(7):637-41.

123. Zappa F, Tisa S, Tosi A, Cova S. Principles and features of single-photon avalanche diode arrays. Sensors and Actuators A: Physical. 2007 10;140(1):103-12.

124. Cova S, Lacaita A, Ripamonti G. Trapping Phenomena in Avalanche Photodiodes on Nanosecond Scale. IEEE Electron Device Letters. 1991;12(12):685-7.

125. Intermite G, McCarthy A, Warburton RE, Ren X, Villa F, Lussana R, et al. Fill-factor improvement of Si CMOS single-photon avalanche diode detector arrays by integration of diffractive microlens arrays. Optics Express. 2015 12;23(26):33777-91.

126. Cusini I, Berretta D, Conca E, Incoronato A, Madonini F, Maurina AA, et al. Historical Perspectives, State of Art and Research Trends of SPAD Arrays and Their Applications (Part II: SPAD Arrays). Frontiers in Physics. 2022 7;10:906671.

127. Nyquist H. Certain Topics in Telegraph Transmission Theory. Transactions of The American Institute of Electrical Engineers. 1928 4;47(2):617-44.

128. Shannon CE. Communication in the Presence of Noise. Proceedings of the IRE. 1949;37(1):10-21.

129. Tulloch S, Miranda QC. Technical Note 1: Introduction to EMCCDs. Tenerife: QUCAM; 2009. Available from: `http://www.qucam.com/assets/tn1.pdf`.

130. Van Vliet LJ, Boddeke FR, Sudar D, Young IT. Image detectors for digital image microscopy. John Wiley and Sons, Chichester (UK); 1998.

131. Kawai N, Kawahito S. Noise analysis of high-gain, low-noise column readout circuits for CMOS image sensors. IEEE Transactions on Electron Devices. 2004 2;51(2):185-94.

132. Qiu P, Mao YN, Lu XM, Xiang E, Jiang XJ. Evaluation of a scientific CMOS camera for astronomical observations. Research in Astronomy and Astrophysics. 2013 5;13(5):615.

133. Long F, Huang ZL, Zeng S. Localization-based super-resolution microscopy with an sCMOS camera Part II: Experimental methodology for comparing sCMOS with EMCCD cameras. Optics Express. 2012 7;20(16):17741-59.

134. Dussault D, Hoess P. Noise performance comparison of ICCD with CCD and EMCCD cameras. In: Infrared Systems and Photoelectronic Technology. vol. 5563. SPIE; 2004. p. 195-204.

135. Ryan DP, Dunlap MK, Gelfand MP, Werner JH, Van Orden AK, Goodwin PM. A gain series method for accurate EMCCD calibration. Scientific Reports. 2021 9;11(1):1-10.

136. Rothemund PWK. Folding DNA to create nanoscale shapes and patterns. Nature. 2006 3;440(7082):297-302.

137. Han W, Cheng W, Zhan Q. Design and alignment strategies of 4f systems used in the vectorial optical field generator. Applied Optics. 2015 3;54(9):2275-8.

138. Lang M, Rudolf F, Stelling J. Use of YouScope to Implement Systematic Microscopy Protocols. Current Protocols in Molecular Biology. 2012 4;98(1):1-14.

139. Lakowicz JR. Fluorescence Correlation Spectroscopy. In: Principles of Fluorescence Spectroscopy. 3rd ed. Springer; 2006. p. 798-840.

140. Power RM, Tschanz A, Zimmermann T, Ries J. Build and operation of a custom 3D, multicolor, single-molecule localization microscope. Nature Protocols 2024. 2024 5:1-59.

141. Loidolt-Krueger M. New Confocal Microscope for Quantitative Fluorescence Lifetime Imaging with Improved Reproducibility. Microscopy Today. 2023 2;31(1):24-31.

142. Ali MH, Imperiali B. Protein oligomerization: how and why. Bioorganic & Medicinal Chemistry. 2005 9;13(17):5013-20.

143. Xie ZR, Chen J, Wu Y. Multiscale Model for the Assembly Kinetics of Protein Complexes. Journal of Physical Chemistry B. 2016 2;120(4):621-32.

144. Duke T, Graham I. Equilibrium mechanisms of receptor clustering. Progress in Biophysics and Molecular Biology. 2009 9;100(1-3):18-24.

145. Pierce MM, Raman CS, Nall BT. Isothermal Titration Calorimetry of Protein–Protein Interactions. Methods. 1999 10;19(2):213-21.

146. Barison N, Lambers J, Hurwitz R, Kolbe M. Interaction of MxiG with the cytosolic complex of the type III secretion system controls Shigella virulence. The FASEB Journal. 2012 4;26(4):1717-26.

147. Benabdelhak H, Kiontke S, Horn C, Ernst R, Blight MA, Holland IB, et al. A Specific Interaction Between the NBD of the ABC-transporter HlyB and a C-Terminal Fragment of its Transport Substrate Haemolysin A. Journal of Molecular Biology. 2003 4;327(5):1169-79.

148. Liao J. Develop quantitative FRET (qFRET) technology as a high-throughput universal assay platform for basic quantitative biomedical and translational research and development. Med-X. 2023 12;1(1):1-19.

149. Xu Y, Piston DW, Johnson CH. A bioluminescence resonance energy transfer (BRET) system: Application to interacting circadian clock proteins. Proceedings of the National Academy of Sciences of the United States of America. 1999 1;96(1):151-6.

150. Liao J, Madahar V, Dang R, Jiang L. Quantitative FRET (qFRET) Technology for the Determination of Protein–Protein Interaction Affinity in Solution. Molecules. 2021 10;26(21):6339.

151. Michelman-Ribeiro A, Mazza D, Rosales T, Stasevich TJ, Boukari H, Rishi V, et al. Direct Measurement of Association and Dissociation Rates of DNA Binding in Live Cells by Fluorescence Correlation Spectroscopy. Biophysical Journal. 2009 7;97(1):337.

152. Mouttou A, Bremaud E, Noero J, Dibsy R, Arone C, Mak J, et al. Quantifying membrane binding and diffusion with fluorescence correlation spectroscopy diffusion laws. Biophysical Journal. 2023 6;122(11):2216-29.

153. Bauer J, Reichl A, Tinnefeld P. Kinetic Referencing Allows Identification of Epigenetic Cytosine Modifications by Single-Molecule Hybridization Kinetics and Superresolution DNA-PAINT Microscopy. ACS Nano. 2024 1;18(2):1496-503.

154. Ester M, Kriegel HP, Sander J, Xu X. A density-based algorithm for discovering clusters in large spatial databases with noise. KDD'96: Proceedings of the Second International Conference on Knowledge Discovery and Data Mining. 1996;96(34):226-31.

155. Eklund AS, Ganji M, Gavins G, Seitz O, Jungmann R. Peptide-PAINT Super-Resolution Imaging Using Transient Coiled Coil Interactions. Nano Letters. 2020 9;20(9):6732-7.

156. Oi C, Gidden Z, Holyoake L, Kantelberg O, Mochrie S, Horrocks MH, et al. LIVE-PAINT allows super-resolution microscopy inside living cells using reversible peptide-protein interactions. Communications Biology. 2020 8;3(1):1-10.

157. Schueder F, Stein J, Stehr F, Auer A, Sperl B, Strauss MT, et al. An order of magnitude faster DNA-PAINT imaging by optimized sequence design and buffer conditions. Nature Methods. 2019 10;16(11):1101-4.

158. Chung KKH, Zhang Z, Kidd P, Zhang Y, Williams ND, Rollins B, et al. Fluorogenic DNA-PAINT for faster, low-background super-resolution imaging. Nature Methods. 2022 5;19(5):554-9.

159. Jensen EC. Overview of Live-Cell Imaging: Requirements and Methods Used. The Anatomical Record: Advances in Integrative Anatomy and Evolutionary Biology. 2013 1;296(1):1-8.

160. Icha J, Weber M, Waters JC, Norden C. Phototoxicity in live fluorescence microscopy, and how to avoid it. Bioessays. 2017;39(8):1700003.

161. Cole R. Live-cell imaging. Cell Adhesion & Migration. 2014 9;8(5):452-9.

162. Ettinger A, Wittmann T. Fluorescence live cell imaging. Methods in Cell Biology. 2014;123:77-94.

163. Hellmeier J, Strauss S, Xu S, Masullo LA, Unterauer EM, Kowalewski R, et al. Quantification of absolute labeling efficiency at the single-protein level. Nature Methods 2024. 2024 4:1-6.

164. Hoebe RA, Van Der Voort HTM, Stap J, Van Noorden CJF, Manders EMM. Quantitative determination of the reduction of phototoxicity and photobleaching by controlled light exposure microscopy. Journal of Microscopy. 2008 7;231(1):9-20.

165. Reinhardt SCM, Masullo LA, Baudrexel I, Steen PR, Kowalewski R, Eklund AS, et al. Ångström-resolution fluorescence microscopy. Nature. 2023 5;617(7962):711-6.

166. Jones SA, Shim SH, He J, Zhuang X. Fast three-dimensional super-resolution imaging of live cells. Nature methods. 2011 6;8(6):499.

167. Jung SR, Deng Y, Kushmerick C, Asbury CL, Hille B, Koh DS. Minimizing ATP depletion by oxygen scavengers for single-molecule fluorescence imaging in live cells. Proceedings of the National Academy of Sciences of the United States of America. 2018 6;115(25):E5706-15.

168. Barry DJ, Durkin CH, Abella JV, Way M. Open source software for quantification of cell migration, protrusions, and fluorescence intensities. Journal of Cell Biology. 2015 4;209(1):163-80.

169. Harada T, Hata S, Takagi R, Komori T, Fukuyama M, Chinen T, et al. An antioxidant screen identifies ascorbic acid for prevention of light-induced mitotic prolongation in live cell imaging. Communications Biology. 2023 11;6(1):1-12.

170. Giannone G, Hosy E, Sibarita JB, Choquet D, Cognet L. High-content super-resolution imaging of live cell by uPAINT. Methods in Molecular Biology. 2013;950:95-110.

171. Michl J, Park KC, Swietach P. Evidence-based guidelines for controlling pH in mammalian live-cell culture systems. Communications Biology. 2019 12;2(1):1-12.

172. Dustin ML, Chakraborty AK, Shaw AS. Understanding the Structure and Function of the Immunological Synapse. Cold Spring Harbor Perspectives in Biology. 2010;2(10):a002311.

173. Yi J, Wu XS, Crites T, Hammer JA. Actin retrograde flow and actomyosin II arc contraction drive receptor cluster dynamics at the immunological synapse in Jurkat T cells. Molecular biology of the cell. 2012 3;23(5):834-52.

174. Alarcón B, Mestre D, Martínez-Martín N. The immunological synapse: a cause or consequence of T-cell receptor triggering? Immunology. 2011 8;133(4):420-5.

175. Dustin ML. The immunological synapse. Cancer immunology research. 2014 11;2(11):1023-33.

176. Palacios EH, Weiss A. Function of the Src-family kinases, Lck and Fyn, in T-cell development and activation. Oncogene. 2004 10;23(48):7990-8000.

177. Sheng R, Jung DJ, Silkov A, Kim H, Singaram I, Wang ZG, et al. Lipids Regulate Lck Protein Activity through Their Interactions with the Lck Src Homology 2 Domain. The Journal of Biological Chemistry. 2016 8;291(34):17639.

178. Wang H, Kadlecek TA, Au-Yeung BB, Goodfellow HES, Hsu LY, Freedman TS, et al. ZAP-70: An Essential Kinase in T-cell Signaling. Cold Spring Harbor Perspectives in Biology. 2010 5;2(5):a002279.

179. Garçon F, Patton DT, Emery JL, Hirsch E, Rottapel R, Sasaki T, et al. CD28 provides T-cell costimulation and enhances PI3K activity at the immune synapse independently of its capacity to interact with the p85/p110 heterodimer. Blood. 2008 2;111(3):1464-71.

180. Esensten JH, Helou YA, Chopra G, Weiss A, Bluestone JA. CD28 costimulation: from mechanism to therapy. Immunity. 2016 5;44(5):973.

181. Skånland SS, Moltu K, Berge T, Aandahl EM, Taskén K. T-cell co-stimulation through the CD2 and CD28 co-receptors induces distinct signalling responses. Biochemical Journal. 2014 6;460(3):399-410.

182. Bubeck Wardenburg J, Pappu R, Bu JY, Mayer B, Chernoff J, Straus D, et al. Regulation of PAK activation and the T cell cytoskeleton by the linker protein SLP-76. Immunity. 1998;9(5):607-16.

183. Germain RN. T-cell signaling: The importance of receptor clustering. Current Biology. 1997 10;7(10):R640-4.

184. Reich Z, Boniface JJ, Lyons DS, Borochov N, Wachtel EJ, Davis MM. Ligand-specific oligomerization of T-cell receptor molecules. Nature. 1997 6;387(6633):617-20.

185. Rossboth B, Arnold AM, Ta H, Platzer R, Kellner F, Huppa JB, et al. TCRs are randomly distributed on the plasma membrane of resting antigen-experienced T cells. Nature Immunology. 2018 7;19(8):821-7.

186. Hu YS, Cang H, Lillemeier BF. Superresolution imaging reveals nanometer- and micrometer-scale spatial distributions of T-cell receptors in lymph nodes. Proceedings of the National Academy of Sciences of the United States of America. 2016 6;113(26):7201-6.

187. Varma R, Campi G, Yokosuka T, Saito T, Dustin ML. T Cell Receptor-Proximal Signals Are Sustained in Peripheral Microclusters and Terminated in the Central Supramolecular Activation Cluster. Immunity. 2006 7;25(1):117.

188. Ma Y, Lim YJ, Benda A, Lou J, Goyette J, Gaus K. Clustering of the ζ-Chain Can Initiate T Cell Receptor Signaling. International Journal of Molecular Sciences. 2020 5;21(10):3498.

189. Bunnell SC, Hong DI, Kardon JR, Yamazaki T, McGlade CJ, Barr VA, et al. T cell receptor ligation induces the formation of dynamically regulated signaling assemblies. The Journal of Cell Biology. 2002 9;158(7):1263-75.

190. Distelmaier F, Valsecchi F, Forkink M, Van Emst-De Vries S, Swarts HG, Rodenburg RJT, et al. Trolox-Sensitive Reactive Oxygen Species Regulate Mitochondrial Morphology, Oxidative Phosphorylation and Cytosolic Calcium Handling in Healthy Cells. Antioxidants & Redox Signaling. 2012 12;17(12):1657.

191. Mukherjee S, Klarenbeek J, Oualid E, Van Den Broek B. "Radical" differences between two FLIM microscopes affect interpretation of cell signaling dynamics. iScience. 2024;27(7):110268.

192. Santos AM, Ponjavic A, Fritzsche M, Fernandes RA, De La Serna JB, Wilcock MJ, et al. Capturing resting T cells: the perils of PLL. Nature Immunology 2018 19:3. 2018 2;19(3):203-5.

193. Hummert J, Yserentant K, Fink T, Euchner J, Ho YX, Tashev SA, et al. Photobleaching step analysis for robust determination of protein complex stoichiometries. Mol Biol Cell. 2021;32(21):ar35.

194. Muzzopappa F, Hummert J, Anfossi M, Tashev SA, Herten DP, Erdel F. Detecting and quantifying liquid–liquid phase separation in living cells by model-free calibrated half-bleaching. Nature Communications. 2022;13(1):7787.

195. Grimm JB, Muthusamy AK, Liang Y, Brown TA, Lemon WC, Patel R, et al. A general method to fine-tune fluorophores for live-cell and in vivo imaging. Nature Methods. 2017 9;14(10):987-94.

Chapter 8

Appendices

8.1 Equations

8.1.1 CoPS

Equations of the mathematical model for different multiple detection events (mDEs) fitted by the CoPS library where p is the detection probability of detection of a photon emitted by a single fluorophore, p_{bg} is the detection probability of a photon emitted by the background and n is the number of emitters.

$$(1-p)^n \times (1-p_{bg})$$

8.1: Zero order mDE probability with background correction.

$$4 \times \left(-\frac{3}{4}p+1\right)^n \times \left(-\frac{3}{4}p_{bg}+1\right) - 4 \times (1-p)^n \times (1-p_{bg})$$

8.2: First order mDE probability with background correction.

$$\begin{aligned}&6 \times \left(-\frac{1}{2}p+1\right)^n \times \left(-\frac{1}{2}p_{bg}+1\right) + 6 \times (1-p)^n \times (1-p_{bg})\\&- 12 \times \left(-\frac{3}{4}p+1\right)^n \times \left(-\frac{3}{4}p_{bg}+1\right)\end{aligned}$$

8.3: Second order mDE probability with background correction.

$$\begin{aligned}&4 \times \left(-\frac{1}{4}p+1\right)^n \times \left(-\frac{1}{4}p_{bg}+1\right) - 4 \times (1-p)^n \times (1-p_{bg})\\&+ 12 \times \left(-\frac{3}{4}p+1\right)^n \times \left(-\frac{3}{4}p_{bg}+1\right) - 12 \times \left(-\frac{1}{2}p+1\right)^n \times \left(-\frac{1}{2}p_{bg}+1\right)\end{aligned}$$

8.4: Third order mDE probability with background correction..

$$\begin{aligned}&1 + (1-p)^n \times (1-p_{bg}) - 4 \times \left(-\frac{3}{4}p+1\right)^n \times \left(-\frac{3}{4}p_{bg}+1\right)\\&+ 6 \times \left(-\frac{1}{2}p+1\right)^n \times \left(-\frac{1}{2}p_{bg}+1\right) - 4 \times \left(-\frac{1}{4}p+1\right)^n \times \left(-\frac{1}{4}p_{bg}+1\right)\end{aligned}$$

8.5: Fourth order mDE probability with background correction.

8.2 Figures

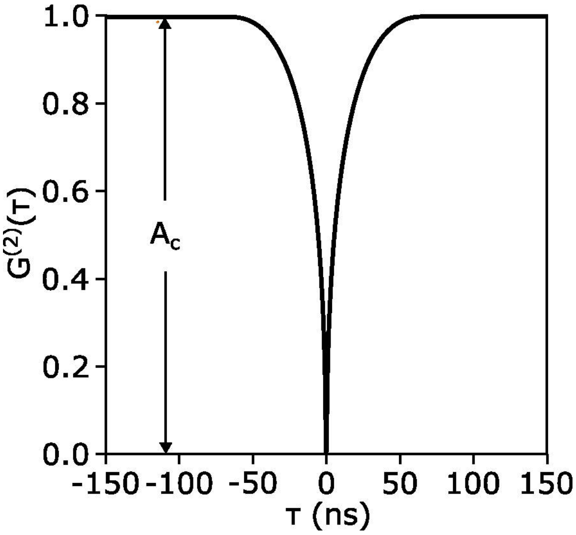

Fig. SI 1: Second order correlation with CW laser excitation. Second order correlation function $G^{(2)}(\tau)$ of the emission from a single emitter excited with a CW laser. A_c is the amplitude of the central dip at $G^{(2)}(0)$. The number of emitters n can be calculated by $n = \frac{1}{A_c}$.

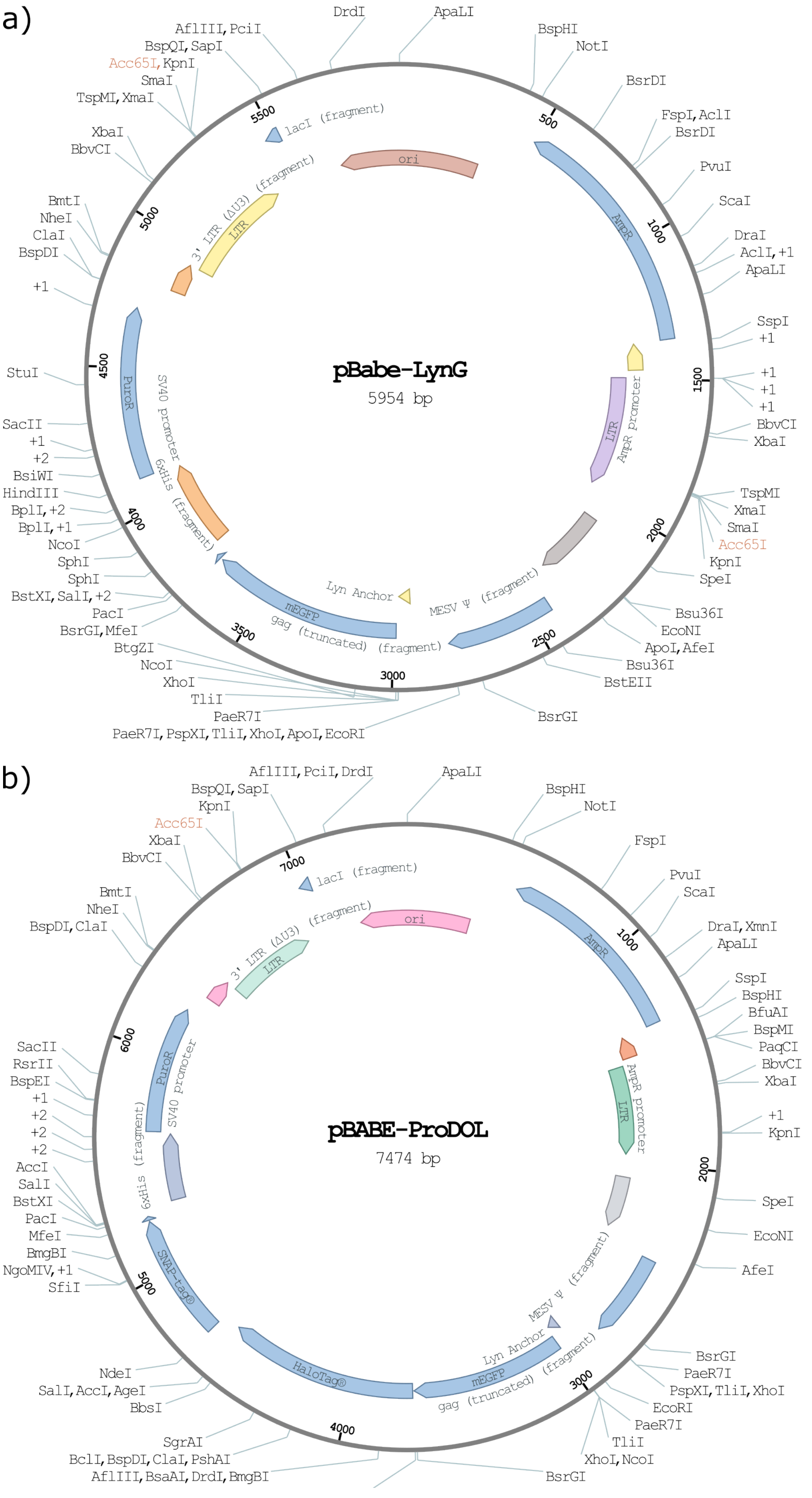

[h]

Fig. SI 2: Maps of the LynG and ProDOL plasmids. Plasmid maps containing the LynG (a) and ProDOL (b) constructs. Both are made out of the pBABE scaffold and contain PuroR- a puromycin resistance gene, for expression-based selection. The pBABE-LynG (#206867) and pBABE-ProDOL (#206866) are available on addgene.com.

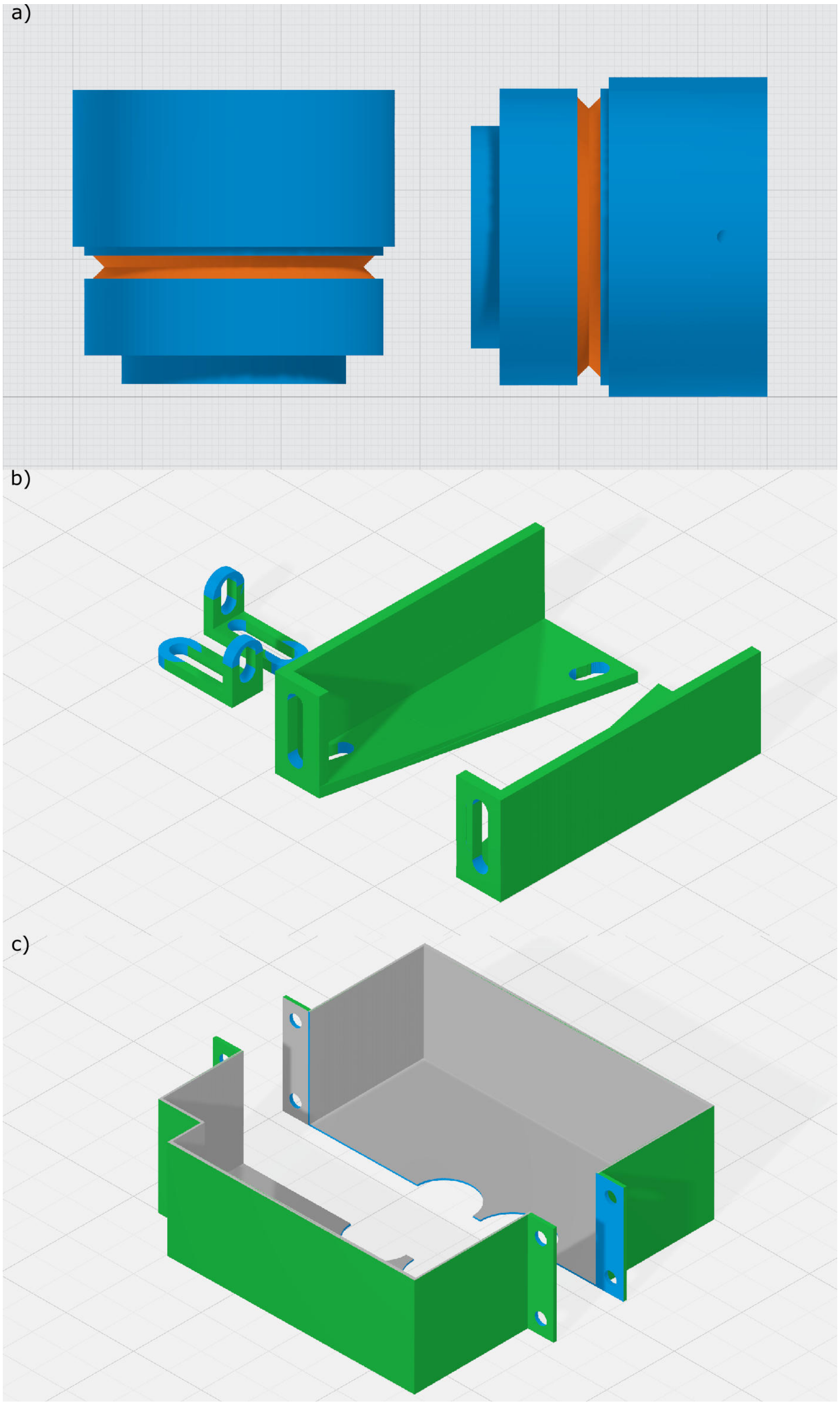

Fig. SI 3: Custom designed 3D-printed components. Render of the custom-designed 3D printed components of the CoPS-TIRF microscope. a) Shortened camera adapter for a Nikon Ti port. The major grids are 1 cm and the minor grids 1 mm. b) Holders for the Nikon Ti body to the dampening table. c) Skirt around the objective to ensure light insulation. b) and c) The major grids are 2 cm and the minor grids 1 cm.

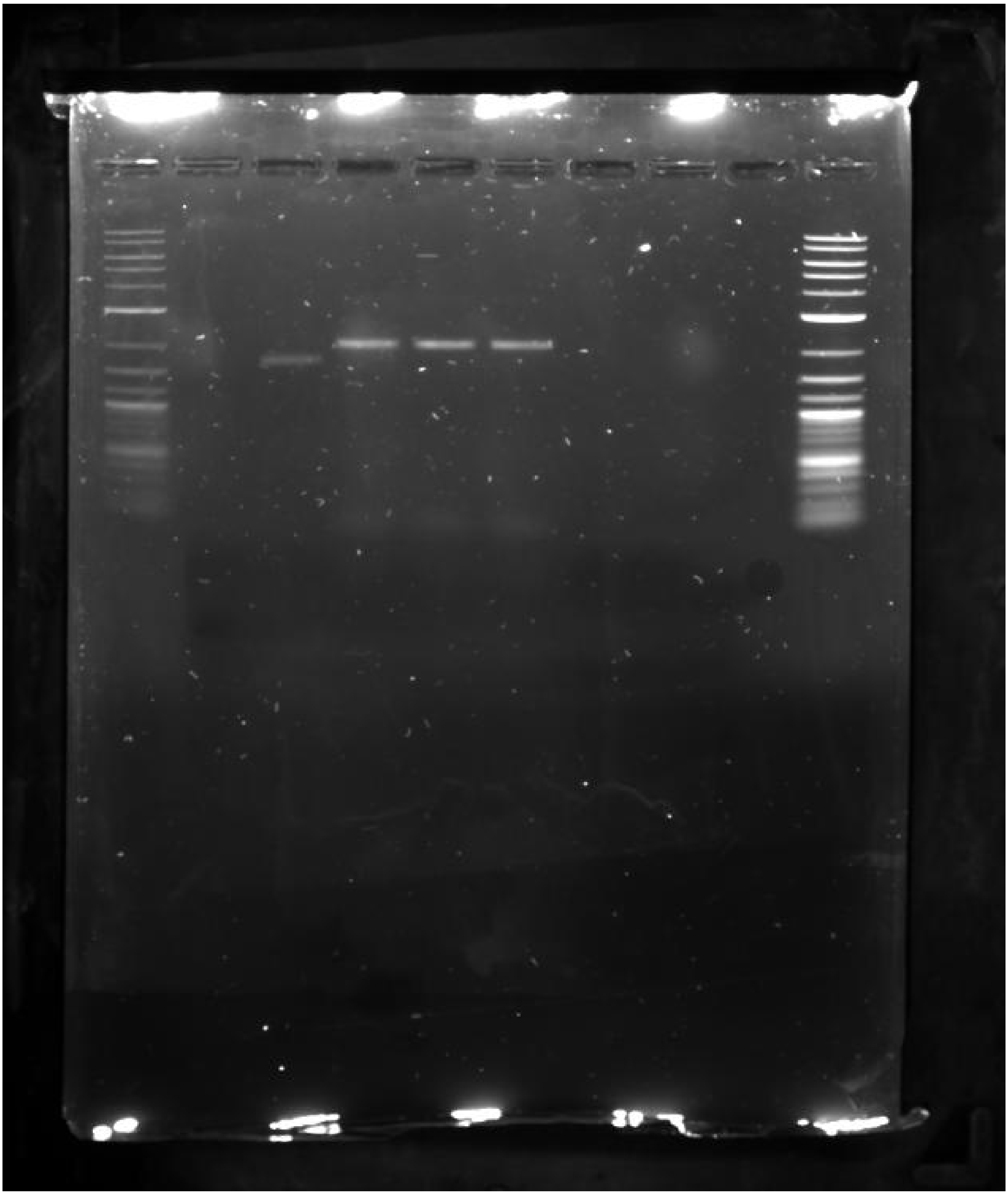

Fig. SI 4: Full gel of the DNA electrophoresis of NRO samples. The original unedited version of the full agarose gel featuring the scaffold, the three NRO samples flanked by two 1kb ladders.

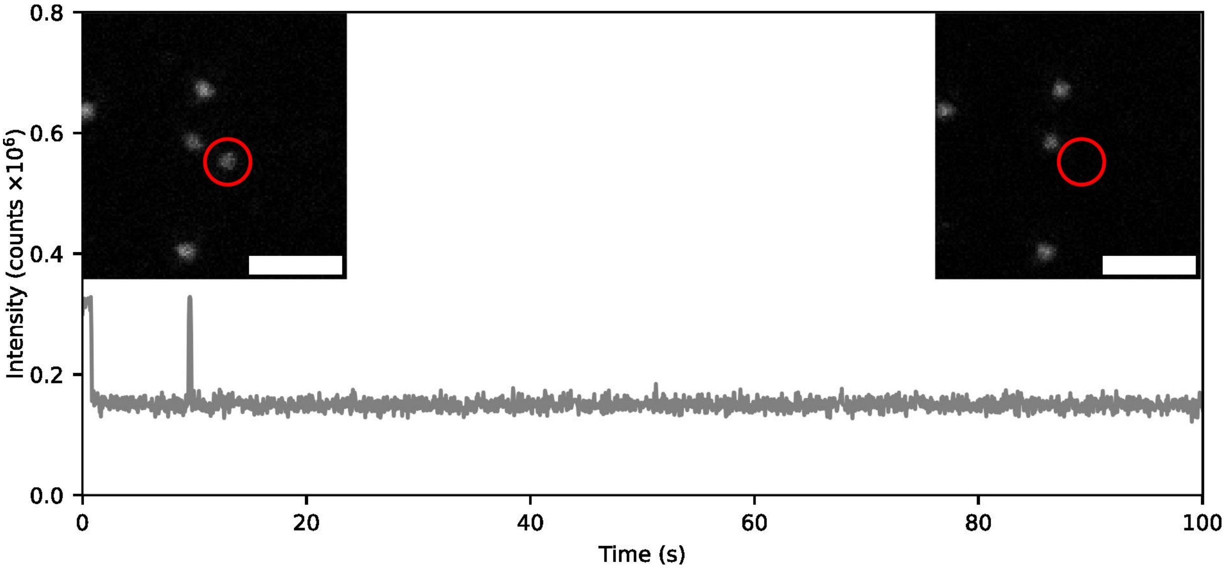

Fig. SI 5: Example of damage on 1xS1 origami labelled with a Atto 643 imager strands. Intensity trace from a 1xS1 NRO incubated with 1 nM 9 nt imager strands labelled with Atto 643. Traces are shown in gray. Images of the reference channel before and after the trace was recorded is shown with the origami from which the data was collected circled in red. Trace shows two quick binding events before going dark to the rest of the 10 min recording. Entire trace not shown.

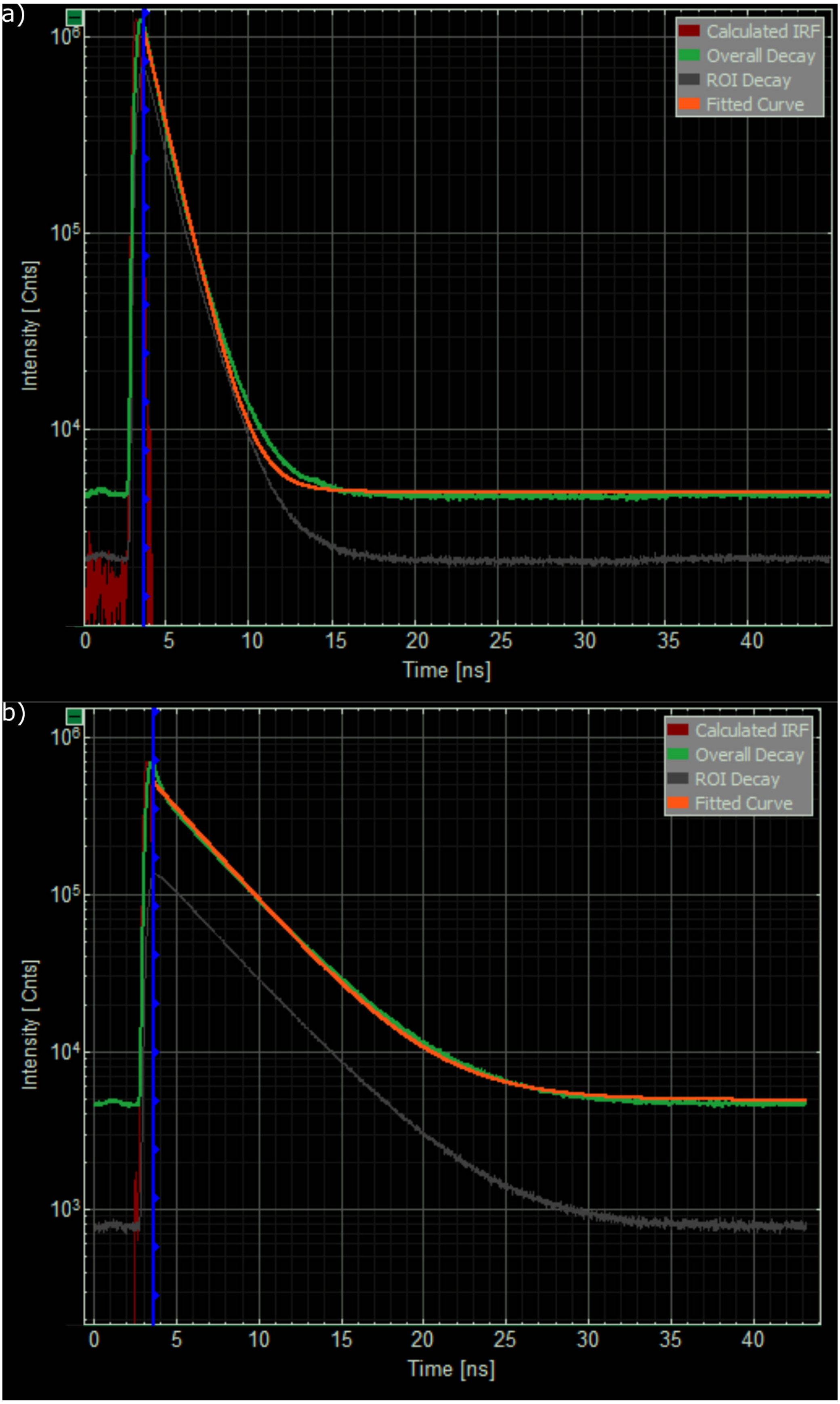

Fig. SI 6: Fluorescence lifetime decays of Cy5 and Atto643 labelled DNA strands. Representitive decays of the fluorescence (green) of the (a) Cy5 and (b) Atto643. The instrument response function (IRF) (red) was determined by the SymPhoTime64 software and the fit (orange) was calculated on the data after the IRF (grey).

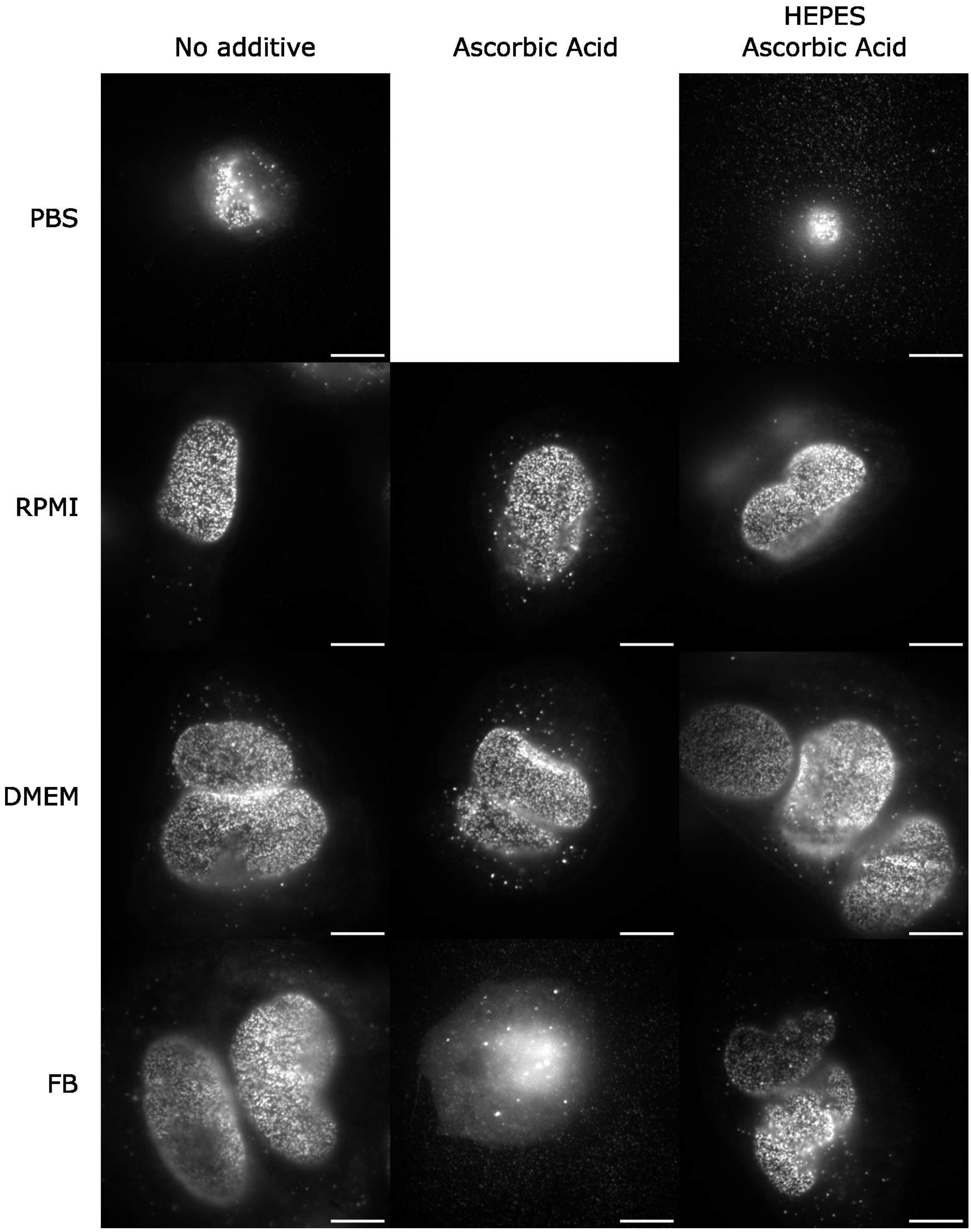

Fig. SI 7: Live staining of NUP107-SNAP stained with BG-SiR. Representative images of live U2OS cells stained with BG-SiR and imaged inside different media. FB- FluoroBright.

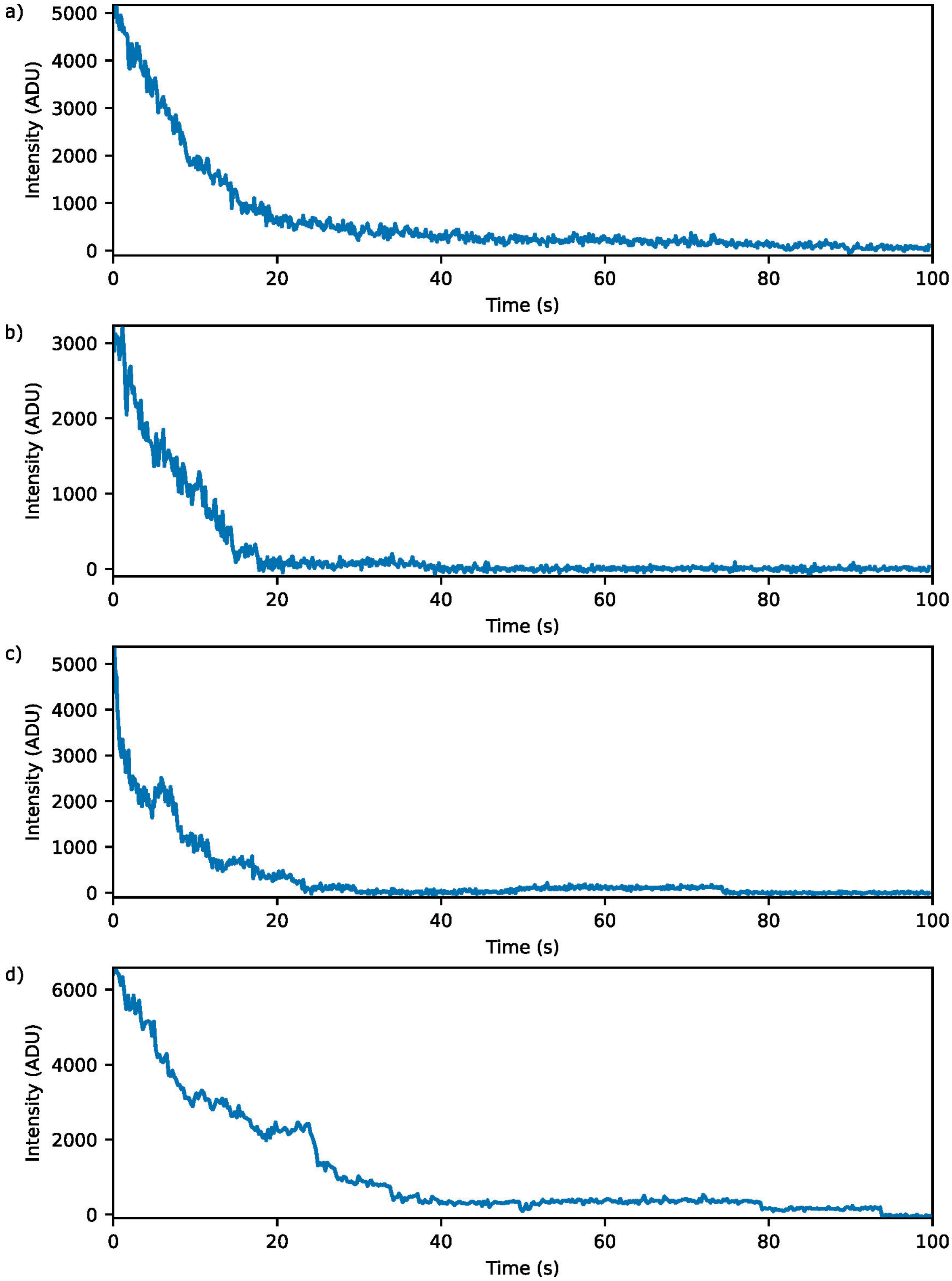

Fig. SI 8: Intensity fluctuations in the different imaging media. Representative intensity traces of the SiR-labelled Nup107-SNAP-tag. a) DMEM, b) DMEM with the addition of AA, c) DMEM with AA and HEPES, d) ROXS buffer.

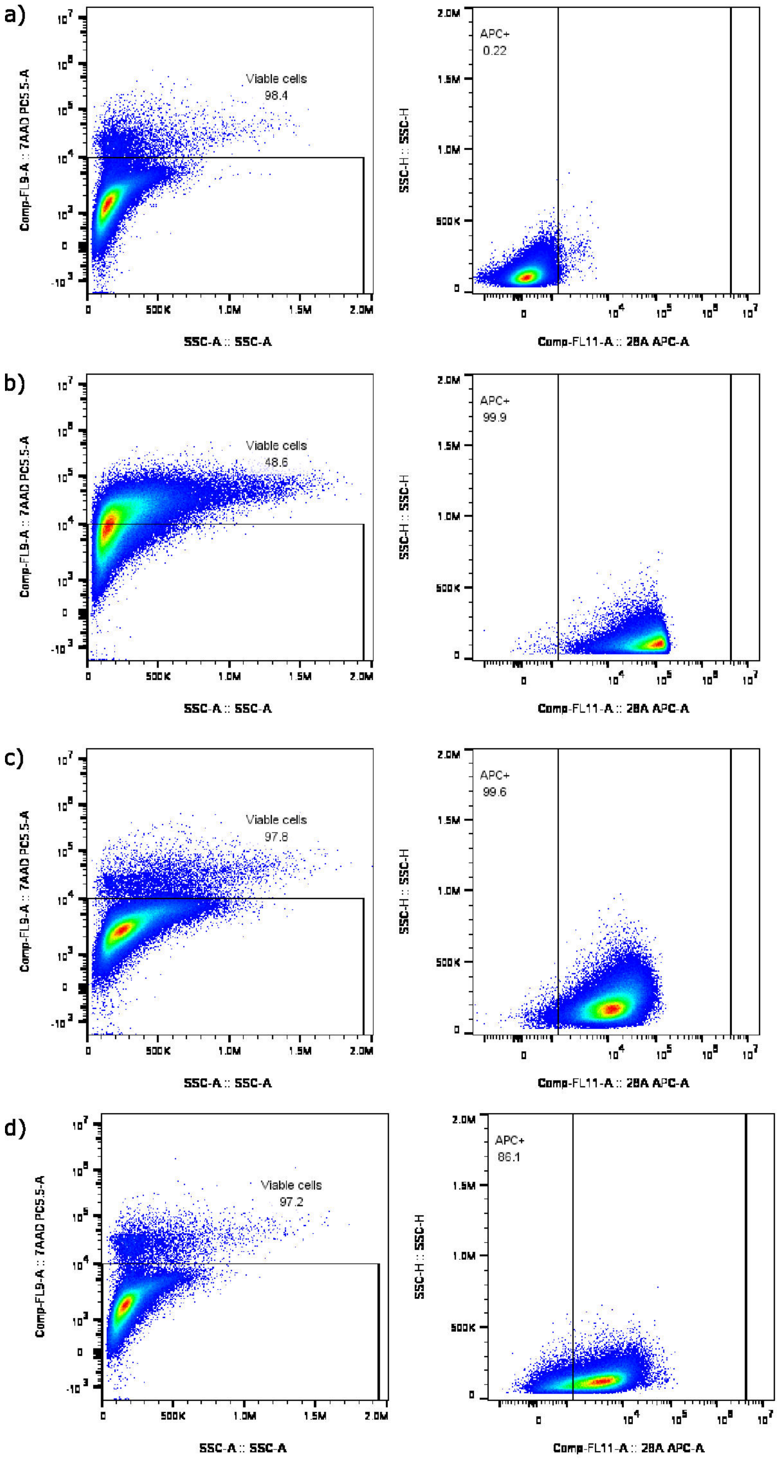

Fig. SI 9: Flow cytometry of Jurkat clones expressing SLP-76-HaloTag. Flow cytometry of a) wild type, b) B3, c) B8V, d) D8 Jurkat cells performed by Danielle Lezama. The left panel shows the viability of the different clones assayed with 7AAD (y axis) against side scatter (x axis). Right panel is the amount of SLP-76-HaloTag stained with 1 nM HA-SiR (x axis) against side scatter (y axis).

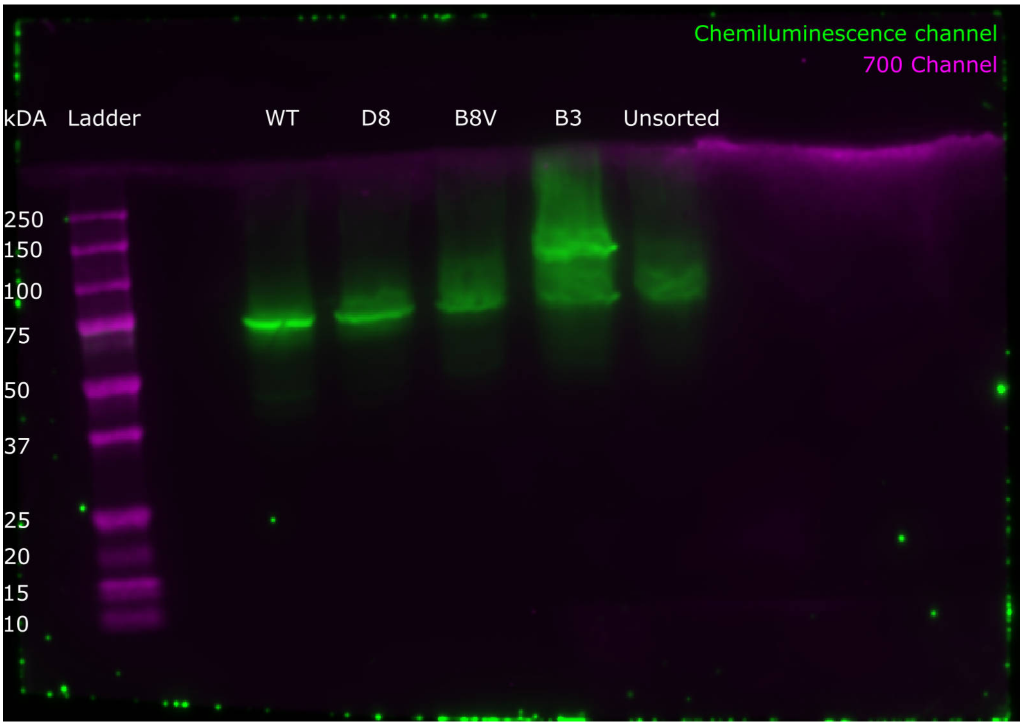

Fig. SI 10: Western blot of Jurkat clones expressing SLP-76-HaloTag. The ladder was detected in the 700 channel (magenta) and the samples were developed by horseradish peroxidase (HRP) in the chemiluminescence channel (green). The samples ran on the gel are shown above. The unsorted sample is the original stable cell line before single cell cloning.

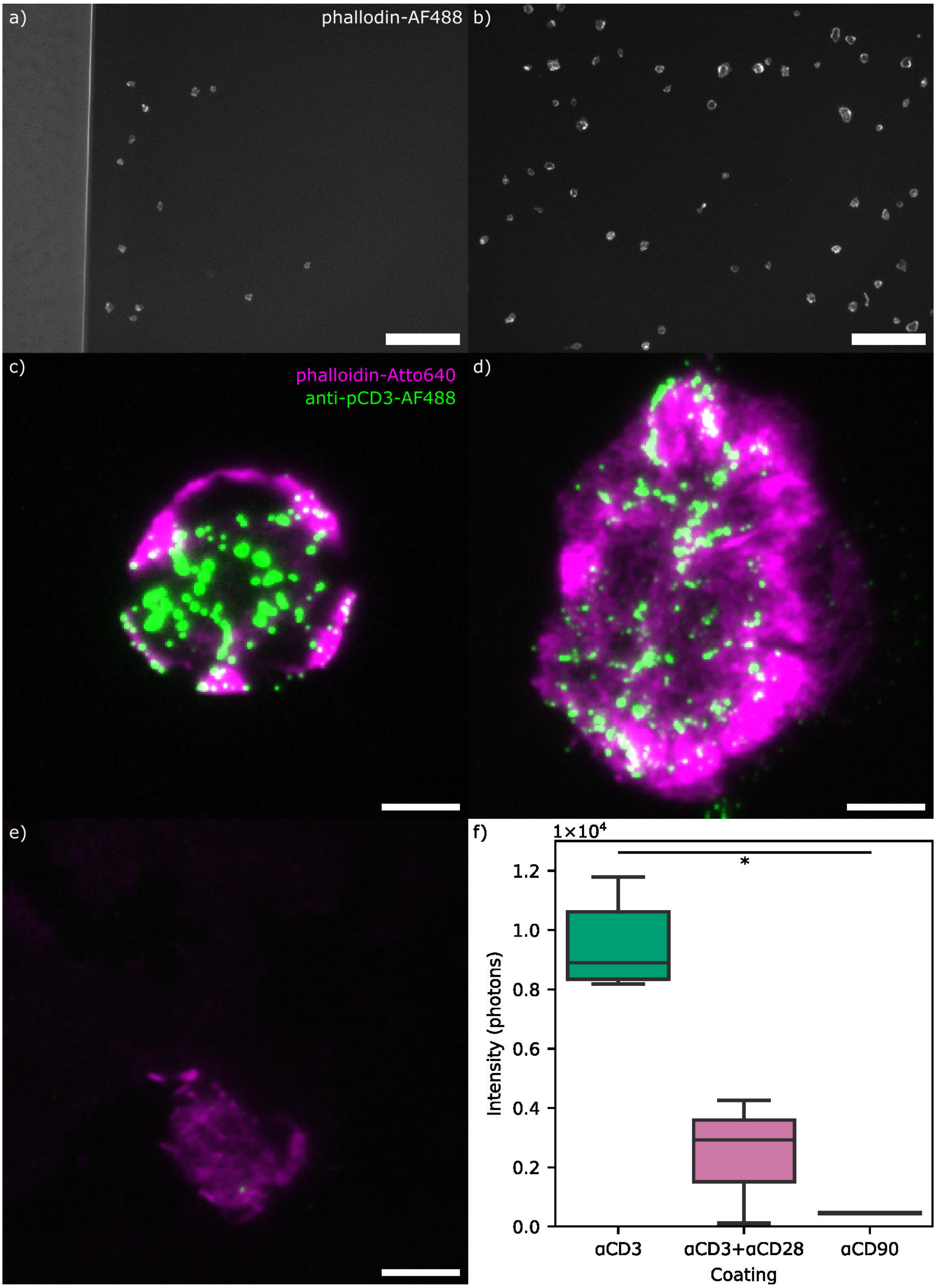

Fig. SI 11: Activation of T cells on antibody coated coverslips. Difference in Jurkat cell density after immobilisation on anti-CD90 antibody coated coverslips without PLL (a) and with PLL (b). Scale bar 200 µm. Activation levels were observed for anti-CD3 antibody (c), anti-CD3 antobody plus anti-CD28 antibody (d), and anti-CD90 antibody (e) coating. pCD3 was labelled via AF488 conjugated antibodies and the actin was stained with phalloidin-AF647. f) Comparison of the activation of the T cells via the intensity of the CD3 signal. Results of Dunn's test with Bonferroni correction shown as: *-$p<0.05$. Boxplot shows the data in a cell-wide fashion with the n=5, 7, and 2 from left to right.

8.3 Table

8.3.1 DNA origami

Tab. SI 1: S2 docking sites. Sequences written from 5'- to 3'-end. The three S2 docking strands contain a 21 nucleotide (nt) overhang on the 3'-end for binding the reference imagers (green) for colocalization. For immobilization, the biotinylated staple strands are modified with biotin on the 3'-end. The helix number to which the 5' and the 3' end belong are written. The number in the brackets is the position in those helices.

S2 Docking site staple strands	**5'-end**	**3'-end**
GCAAGGCCTCACCAGTAGCACCATGGGCTTGATAACATTCCTAACTTCTCATA	5[160]	6[144]
TTGACAGGCCACCACCAGAGCCGCGATTTGTATAACATTCCTAACTTCTCATA	3[160]	4[144]
GATGGTTTGAACGAGTAGTAAATTTACCATTATAACATTCCTAACTTCTCATA	6[143]	5[159]

Tab. SI 2: Unmodified staple strands of the NRO DNA origami. List of the unmodified staple strands. Sequences written from 5'- to 3'-end. The helix number to which the 5' and the 3' end belong are written. The number in the brackets is the position in those helices.

Unmodified staple strands	**5'-end**	**3'-end**
CATAAATCTTTGAATACCAAGTGTTAGAAC	17[224]	19[223]
AAGCCTGGTACGAGCCGGAAGCATAGATGATG	20[143]	19[159]
TCATTCAGATGCGATTTTAAGAACAGGCATAG	5[96]	7[95]
GCCATCAAGCTCATTTTTTAACCACAAATCCA	16[143]	15[159]
TATAACTAACAAAGAACGCGAGAACGCCAA	16[175]	14[176]
TTGCTCCTTTCAAATATCGCGTTTGAGGGGGT	10[111]	8[112]
GTATAGCAAACAGTTAATGCCCAATCCTCA	1[224]	3[223]
AAAGTCACAAAATAAACAGCCAGCGTTTTA	9[224]	11[223]
GGCCTTGAAGAGCCACCACCCTCAGAAACCAT	3[192]	5[191]
TTAACGTCTAACATAAAAACAGGTAACGGA	10[175]	8[176]
AGTATAAAGTTCAGCTAATGCAGATGTCTTTC	14[239]	12[240]
GATGTGCTTCAGGAAGATCGCACAATGTGA	18[79]	16[80]

Continued on next page

Tab. SI 2: Staple strands of the DNA origami (continued).

Unmodified staple strands	5'-end	3'-end
TCAAATATAACCTCCGGCTTAGGTAACAATTT	15[192]	17[191]
TTTCGGAAGTGCCGTCGAGAGGGTGAGTTTCG	2[207]	0[208]
GAGGGTAGGATTCAAAAGGGTGAGACATCCAA	14[111]	12[112]
TATTAAGAAGCGGGGTTTTGCTCGTAGCAT	2[175]	0[176]
GCCCTTCAGAGTCCACTATTAAAGGGTGCCGT	21[64]	23[63]
ATGCAGATACATAACGGGAATCGTCATAAATAAAGCAAAG	7[56]	9[63]
AGCCAGCAATTGAGGAAGGTTATCATCATTTT	22[207]	20[208]
TAAATGAATTTTCTGTATGGGATTAATTTCTT	0[111]	1[95]
AAACAGCTTTTTGCGGGATCGTCAACACTAAA	1[96]	3[95]
CGGATTCTGACGACAGTATCGGCCGCAAGGCGATTAAGTT	16[63]	18[56]
GCAATTCACATATTCCTGATTATCAAAGTGTA	19[160]	20[144]
GCGCAGACAAGAGGCAAAAGAATCCCTCAG	4[79]	2[80]
AGAGAGAAAAAAATGAAAATAGCAAGCAAACT	9[160]	10[144]
GACAAAAGGTAAAGTAATCGCCATATTTAACAAAACTTTT	13[184]	15[191]
ACACTCATCCATGTTACTTAGCCGAAAGCTGC	3[96]	5[95]
CTACCATAGTTTGAGTAACATTTAAAATAT	19[224]	21[223]
TATATTTTGTCATTGCCTGAGAGTGGAAGATTGTATAAGC	13[64]	15[71]
CGGATTGCAGAGCTTAATTGCTGAAACGAGTA	9[64]	11[63]
TAAATCATATAACCTGTTTAGCTAACCTTTAA	12[111]	10[112]
GTACCGCAATTCTAAGAACGCGAGTATTATTT	12[207]	10[208]

Continued on next page

Tab. SI 2: Staple strands of the DNA origami (continued).

Unmodified staple strands	5'-end	3'-end
TCTTCGCTGCACCGCTTCTGGTGCGGCCTTCC	18[111]	16[112]
GATTTAGTCAATAAAGCCTCAGAGAACCCTCA	11[64]	13[63]
GCAAGGCCTCACCAGTAGCACCATGGGCTTGA	5[160]	6[144]
ATTACCTTTGAATAAGGCTTGCCCAAATCCGC	6[111]	4[112]
CTTATCATTCCCGACTTGCGGGAGCCTAATTT	12[239]	10[240]
TTATACCACCAAATCAACGTAACGAACGAG	6[79]	4[80]
GTAATAAGTTAGGCAGAGGCATTTATGATATT	13[160]	14[144]
CAACCGTTTCAAATCACCATCAATTCGAGCCA	14[143]	13[159]
GATGGTTTGAACGAGTAGTAAATTTACCATTA	6[143]	5[159]
GCACAGACAATATTTTTGAATGGGGTCAGTA	23[224]	22[240]
AGCAAGCGTAGGGTTGAGTGTTGTAGGGAGCC	21[96]	23[95]
TCCACAGACAGCCCTCATAGTTAGCGTAACGA	0[175]	0[144]
TCACCAGTACAAACTACAACGCCTAGTACCAG	0[207]	1[191]
ATTATACTAAGAAACCACCAGAAGTCAACAGT	19[192]	21[191]
TAAGAGCAAATGTTTAGACTGGATAGGAAGCC	7[96]	9[95]
ATACATACCGAGGAAACGCAATAAGAAGCGCATTAGACGG	7[192]	9[199]
CAACTGTTGCGCCATTCGCCATTCAAACATCA	18[143]	17[159]
GATGGCTTATCAAAAAGATTAAGAGCGTCC	10[79]	8[80]
TAGGTAAACTATTTTTGAGAGATCAAACGTTA	13[96]	15[95]
AGGCAAAGGGAAGGGCGATCGGCAATTCCA	17[128]	19[127]

Continued on next page

Tab. SI 2: Staple strands of the DNA origami (continued).

Unmodified staple strands	5'-end	3'-end
ATTATCATTCAATATAATCCTGACAATTAC	20[175]	18[176]
GAAATTATTGCCTTTAGCGTCAGACCGGAACC	6[239]	4[240]
AATGGTCAACAGGCAAGGCAAAGAGTAATGTG	11[96]	13[95]
CCAATAGCTCATCGTAGGAATCATGGCATCAA	11[160]	12[144]
ATACCCAACAGTATGTTAGCAAATTAGAGC	8[175]	6[176]
ATAAGGGAACCGGATATTCATTACGTCAGGACGTTGGGAA	4[63]	6[56]
CACCAGAAAGGTTGAGGCAGGTCATGAAAG	4[175]	2[176]
ATCCCAATGAGAATTAACTGAACAGTTACCAG	10[207]	8[208]
CATGTAATAGAATATAAAGTACCAAGCCGT	14[175]	12[176]
CCAACAGGAGCGAACCAGACCGGAGCCTTTAC	10[143]	9[159]
GCTATCAGAAATGCAATGCCTGAATTAGCA	14[79]	12[80]
GACCTGCTCTTTGACCCCCAGCGAGGGAGTTA	4[111]	2[112]
AGGAACCCATGTACCGTAACACTTGATATAA	0[239]	1[223]
CAGCGAAACTTGCTTTCGAGGTGTTGCTAA	2[79]	0[80]
GCTTTCCGATTACGCCAGCTGGCGGCTGTTTC	17[96]	19[95]
ACAACTTTCAACAGTTTCAGCGGATGTATCGG	0[79]	1[63]
CAGCAAAAGGAAACGTCACCAATGAGCCGC	6[175]	4[176]
ACCTTTTTATTTTAGTTAATTTCATAGGGCTT	16[207]	14[208]
CGATAGCATTGAGCCATTTGGGAACGTAGAAA	5[192]	7[191]
GCCCGAGAGTCCACGCTGGTTTGCAGCTAACT	22[111]	20[112]

Continued on next page

Tab. SI 2: Staple strands of the DNA origami (continued).

Unmodified staple strands	5'-end	3'-end
ATTTTAAAATCAAAATTATTTGCACGGATTCG	20[239]	18[240]
ACCTTGCTTGGTCAGTTGGCAAAGAGCGGA	22[175]	20[176]
CTGAGCAAAAATTAATTACATTTTGGGTTA	18[175]	16[176]
CCTGATTGCAATATATGTGAGTGATCAATAGT	18[239]	16[240]
TCAATATCGAACCTCAAATATCAATTCCGAAA	21[160]	22[144]
AAAGGCCGGAGACAGCTAGCTGATAAATTAATTTTTGT	13[120]	15[127]
CTTTAGGGCCTGCAACAGTGCCAATACGTG	21[224]	23[223]
AATAGTAAACACTATCATAACCCTCATTGTGA	8[111]	6[112]
TCACCGACGCACCGTAATCAGTAGCAGAACCG	6[207]	4[208]
GCCCGTATCCGGAATAGGTGTATCAGCCCAAT	2[239]	0[240]
TGTAGCCATTAAAATTCGCATTAAATGCCGGA	16[111]	14[112]
TCGGCAAATCCTGTTTGATGGTGGACCCTCAA	22[143]	21[159]
TGACAACTCGCTGAGGCTTGCATTATACCA	1[128]	3[127]
CCACCCTCTATTCACAAACAAATACCTGCCTA	4[207]	2[208]
CCCGATTTAGAGCTTGACGGGGAAAAAGAATA	23[96]	22[112]
AAGTAAGCAGACACCACGGAATAATATTGACG	8[239]	6[240]
AAATTAAGTTGACCATTAGATACTTTTGCG	12[79]	10[80]
CACATTAAAATTGTTATCCGCTCATGCGGGCC	20[111]	18[112]
TTAAAGCCAGAGCCGCCACCCTCGACAGAA	3[224]	5[223]
ATATTCGGAACCATCGCCCACGCAGAGAAGGA	2[143]	1[159]

Continued on next page

Tab. SI 2: Staple strands of the DNA origami (continued).

Unmodified staple strands	5'-end	3'-end
TTCTACTACGCGAGCTGAAAAGGTTACCGCGC	12[143]	11[159]
AACGTGGCGAGAAAGGAAGGGAAACCAGTAA	23[128]	23[159]
GAATTTATTTAATGGTTTGAAATATTCTTACC	16[239]	14[240]
AGCGCGATGATAAATTGTGTCGTGACGAGA	3[128]	5[127]
AACGCAAAGATAGCCGAACAAACCCTGAAC	7[224]	9[223]
AGAAAACAAAGAAGATGATGAAACAGGCTGCG	17[160]	18[144]
CGCGCAGATTACCTTTTTTAATGGGAGAGACT	18[207]	16[208]
CACAACAGGTGCCTAATGAGTGCCCAGCAG	19[128]	21[127]
GCGGAACATCTGAATAATGGAAGGTACAAAAT	20[207]	18[208]
TAAAAGGGACATTCTGGCCAACAAAGCATC	23[160]	22[176]
AATTGAGAATTCTGTCCAGACGACTAAACCAA	14[207]	12[208]
GCGAAAAATCCCTTATAAATCAAGCCGGCG	21[128]	23[127]
AACACCAAATTTCAACTTTAATCGTTTACC	5[128]	7[127]
TAAATCAAAATAATTCGCGTCTCGGAAACC	15[128]	17[127]
GAAACGATAGAAGGCTTATCCGGTCTCATCGAGAACAAGC	10[191]	12[184]
GCCTCCCTCAGAATGGAAAGCGCAGTAACAGT	4[239]	2[240]
GCGAACCTCCAAGAACGGGTATGACAATAA	11[224]	13[223]
TTAGGATTGGCTGAGACTCCTCAATAACCGAT	1[160]	2[144]
ATCGCAAGTATGTAAATGCTGATGATAGGAAC	15[160]	16[144]
GCGGATAACCTATTATTCTGAAACAGACGATT	1[192]	3[191]

Continued on next page

Tab. SI 2: Staple strands of the DNA origami (continued).

Unmodified staple strands	5’-end	3’-end
AAGGAAACATAAAGGTGGCAACATTATCACCG	8[207]	6[208]
ACCCTTCTGACCTGAAAGCGTAAGACGCTGAG	23[192]	22[208]
ATATTTTGGCTTTCATCAACATTATCCAGCCA	15[96]	17[95]
TCAAGTTTCATTAAAGGTGAATATAAAAGA	5[224]	7[223]
TCTAAAGTTTTGTCGTCTTTCCAGCCGACAA	0[143]	1[127]
TTCCAGTCGTAATCATGGTCATAAAAGGGG	20[79]	18[80]
AAAGCACTAAATCGGAACCCTAATCCAGTT	23[64]	22[80]
AATACTGCCCAAAAGGAATTACGTGGCTCA	8[79]	6[80]
TTTATCAGGACAGCATCGGAACGACACCAACCTAAAACGA	1[64]	3[71]
TTGACAGGCCACCACCAGAGCCGCGATTTGTA	3[160]	4[144]
CTGTGTGATTGCGTTGCGCTCACTAGAGTTGC	19[96]	21[95]
GCGAGTAAAAATATTTAAATTGTTACAAAG	16[79]	14[80]
TAGAGAGTTATTTTCATTTGGGGATAGTAGTAGCATTA	10[127]	12[120]
CGAAAGACTTTGATAAGAGGTCATATTTCGCA	9[96]	11[95]
TCATCGCCAACAAAGTACAACGGACGCCAGCA	4[143]	3[159]
TTAACACCAGCACTAACAACTAATCGTTATTA	22[239]	20[240]
TTATTACGAAGAACTGGCATGATTGCGAGAGG	7[160]	8[144]
GCCAGTTAGAGGGTAATTGAGCGCTTTAAGAA	10[239]	8[240]
ACAACATGCCAACGCTCAACAGTCTTCTGA	13[224]	15[223]
CATTTGAAGGCGAATTATTCATTTTTGTTTGG	17[192]	19[191]

Continued on next page

Tab. SI 2: Staple strands of the DNA origami (continued).

Unmodified staple strands	5'-end	3'-end
TGAAAGGAGCAAATGAAAAATCTAGAGATAGA	21[192]	23[191]
TGGAACAACCGCCTGGCCCTGAGGCCCGCT	22[79]	20[80]
TACCGAGCTCGAATTCGGGAAACCTGTCGTGCAGCTGATT	19[56]	21[63]
GTTTATTTTGTCACAATCTTACCGAAGCCCTTTAATATCA	7[248]	9[255]
ACAAACGGAAAAGCCCCAAAAACACTGGAGCA	16[47]	14[48]
GTTTATCAATATGCGTTATACAAACCGACCGTGTGATAAA	13[256]	15[263]
ACGGCTACAAAAGGAGCCTTTAATGTGAGAAT	2[47]	0[48]
GACCAACTAATGCCACTACGAAGGGGGTAGCA	4[47]	2[48]
AAGGCCGCTGATACCGATAGTTGCGACGTTAG	2[111]	0[112]
CTCCAACGCAGTGAGACGGGCAACCAGCTGCA	22[47]	20[48]
ACCGATTGTCGGCATTTTCGGTCATAATCA	6[271]	4[272]
CAGAAGATTAGATAATACATTTGTCGACAA	22[271]	20[272]
TGCATCTTTCCCAGTCACGACGGCCTGCAG	17[32]	19[31]
TTAGTATCACAATAGATAAGTCCACGAGCA	14[271]	12[272]
GTTTTAACTTAGTACCGCCACCCAGAGCCA	2[271]	0[272]
TTAATGAACTAGAGGATCCCCGGGGGGTAACG	20[47]	18[48]
CTTTTACAAAATCGTCGCTATTAGCGATAG	18[271]	16[272]
ATCCCCCTATACCACATTCAACTAGAAAAATC	8[47]	6[48]
AGAAAGGAACAACTAAAGGAATTCAAAAAAA	0[47]	1[31]
TTTTATTTAAGCAAATCAGATATTTTTTGT	12[175]	10[176]

Continued on next page

Tab. SI 2: Staple strands of the DNA origami (continued).

Unmodified staple strands	5'-end	3'-end
AGCCACCACTGTAGCGCGTTTTCAAGGGAGGGAAGGTAAA	4[255]	6[248]
AACAAGAGGGATAAAAATTTTTAGCATAAAGC	14[47]	12[48]
GCCGTCAAAAAACAGAGGTGAGGCCTATTAGT	21[256]	23[255]
TGTAGAAATCAAGATTAGTTGCTCTTACCA	12[271]	10[272]
GAGAGATAGAGCGTCTTTCCAGAGGTTTTGAA	9[256]	11[255]
CCACCCTCATTTTCAGGGATAGCAACCGTACT	0[271]	1[255]
CTTTAATGCGCGAACTGATAGCCCCACCAG	23[256]	22[272]
CCAGGGTTGCCAGTTTGAGGGGACCCGTGGGA	18[47]	16[48]
CAAATCAAGTTTTTTGGGGTCGAAACGTGGA	23[32]	22[48]
ACGCTAACACCCACAAGAATTGAAAATAGC	10[271]	8[272]
CTTTTGCAGATAAAAACCAAAATAAAGACTCC	8[143]	7[159]
TACGTTAAAGTAATCTTGACAAGAACCGAACT	6[47]	4[48]
TAATCAGCGGATTGACCGTAATCGTAACCG	15[32]	17[31]
TTTTCACTCAAAGGGCGAAAAACCATCACC	21[32]	23[31]
GCCTTAAACCAATCAATAATCGGCACGCGCCT	11[256]	13[255]
AATAGCTATCAATAGAAAATTCAACATTCA	8[271]	6[272]
CATCAAGTAAAACGAACTAACGAGTTGAGA	5[32]	7[31]
CAGGAGGTGGGGTCAGTGCCTTGAGTCTCTGAATTTACCG	1[256]	3[263]
AAATCACCTTCCAGTAAGCGTCAGTAATAA	4[271]	2[272]
CTCGTATTAGAAATTGCGTAGATACAGTAC	20[271]	18[272]

Continued on next page

Tab. SI 2: Staple strands of the DNA origami (continued).

Unmodified staple strands	5'-end	3'-end
TTTACCCCAACATGTTTTAAATTTCCATAT	9[32]	11[31]
CCTAAATCAAAATCATAGGTCTAAACAGTA	15[224]	17[223]
GTCGACTTCGGCCAACGCGCGGGGTTTTTC	19[32]	21[31]
CGTAAAACAGAAATAAAAATCCTTTGCCCGAAAGATTAGA	19[248]	21[255]
AGGCTCCAGAGGCTTTGAGGACACGGGTAA	1[32]	3[31]
GAGAAGAGATAACCTTGCTTCTGTTCGGGAGAAACAATAA	16[255]	18[248]
TTTAGGACAAATGCTTTAAACAATCAGGTC	7[32]	9[31]
AATACGTTTGAAAGAGGACAGACTGACCTT	3[32]	5[31]
CTTAGATTTAAGGCGTTAAATAAAGCCTGT	16[271]	14[272]
TAAATCGGGATTCCCAATTCTGCGATATAATG	12[47]	10[48]
AACAGTTTTGTACCAAAAACATTTTATTTC	11[32]	13[31]
CTGTAGCTTGACTATTATAGTCAGTTCATTGA	10[47]	8[48]
AGACGACAAAGAAGTTTTGCCATAATTCGAGCTTCAA	7[128]	9[135]
AACGCAAAATCGATGAACGGTACCGGTTGA	13[32]	15[31]

S1 Docking site staple strands	5’-end	3’-end	1xS1	2xS1	5xS1
AATTGAGAATTCTGTCCAGACGACTAAACCAATTTCCTCTACCACCTACATCAC	14[207]	12[208]			X
CTGAGCAAAAATTAATTACATTTTGGGTTATTTCCTCTACCACCTACATCAC	18[175]	16[176]			X
CCAATAGCTCATCGTAGGAATCATGGCATCAATTTCCTCTACCACCTACATCAC	11[160]	12[144]	X	X	X
TTAACGTCTAACATAAAAACAGGTAACGGATTTCCTCTACCACCTACATCAC	10[175]	8[176]			X
CATGTAATAGAATATAAAGTACCAAGCCGTTTCCTCTACCACCTACATCAC	14[175]	12[176]		X	X

Tab. SI 3: S1 docking sites. External S1 docking strands of the NRO DNA Origami, which serve to bind imager strands. Sequences written from 5’- to 3’-end. The S1 docking site docking strands have a single-strand overhang of 22 nt on their 3’-end (red). The helix number to which the 5’ and the 3’ end are written. The number in the brackets is the position in those helices. The presence in each of the new rectangular origami (NRO) version have been shown with X.

8.3.2 Laser intensity

Tab. SI 4: Laser intensity for 640 nm laser. Laser power corresponding to the percentage set in software was calculated via a power meter measurement before the objective and then corrected via the objective transmissible percentage.

Power (%)	Before objective(mW)	After objective (W/cm^2)
1	0.4	1.8
2	0.8	3.6
3	1.2	5.4
5	2.1	9.5
10	4.3	19.5
15	6.5	29.4
20	8.7	39.4
25	10.8	48.9
30	13	58.9
40	17.4	78.8
50	21.7	98.2
60	26	117.7
70	30.5	138.1
80	34.9	158.0
90	39.5	178.8
100	43.8	198.3

Tab. SI 5: Laser intensity for 561 nm laser. Laser power corresponding to the percentage set in software was calculated via a power meter measurement before the objective and then corrected via the objective transmissible percentage.

Power (%)	Before objective(mW)	After objective (W/cm^2)
1	0.18	0.8
2	0.36	1.6
3	0.53	2.4
5	1	4.5
10	2.1	9.5
15	3.1	14.0
20	4.1	18.6
25	5.2	23.5
30	6.3	28.5
40	8.4	38.0
50	10.5	47.5
60	12.7	57.5
70	14.7	66.5
80	16.8	76.1
90	19	86.0
100	21.2	96.0

Tab. SI 6: Laser intensity for 488 nm laser. Laser power corresponding to the percentage set in software was calculated via a power meter measurement before the objective and then corrected via the objective transmissible percentage.

Power (%)	Before objective(mW)	After objective (W/cm^2)
1	0.39	1.8
2	0.66	3.0
3	0.95	4.3
5	1.5	6.8
10	2.9	13.1
15	4.3	19.5
20	5.8	26.3
25	7.2	32.6
30	8.6	38.9
40	11.4	51.6
50	14.2	64.3
60	17	77.0
70	19.8	89.6
80	22.6	102.3
90	25.5	115.4
100	28.2	127.7

Tab. SI 7: Laser intensity for 405 nm laser. Laser power corresponding to the percentage set in software was calculated via a power meter measurement before the objective and then corrected via the objective transmissible percentage.

Power (%)	Before objective(mW)	After objective (W/cm^2)
1	0.3	1.4
2	0.65	2.9
3	0.95	4.3
5	1.56	7.1
10	3	13.6
15	4.4	19.9
20	6.1	27.6
25	7.7	34.9
30	9.3	42.1
40	12.3	55.7
50	14.5	65.6
60	18.5	83.8
70	21.8	98.7
80	25	113.2
90	28.2	127.7
100	31.5	142.6